Thèse
pour obtenir le grade de
Docteur de l'Ecole Normale Supérieure de Lyon
Discipline : Chimie Physique
Ecole Doctorale de Chimie de Lyon

Dissertation
zur Erlangung des Doktorgrades
an der Fakultät für Physik
der Universität Bielefeld

Numerical Simulations of a Smectic Lamellar Phase of Amphiphilic Molecules

présentée par
vorgelegt von
Claire Loison

27/06/2003

Jury :	Prof. A. Ajdari	ESPCI, Paris	rapporteur
	Prof. K. Binder	Univ. Mainz	rapporteur
	Prof. L. Bocquet	Univ. Lyon 1	examinateur
	Prof. M. Klein	Pennsylvania Univ.	invité
	Prof. M. Mareschal	Univ. Libre de Bruxelles	directeur de thèse
	Prof. J. Rädler	Univ. München	examinateur
	Prof. F. Schmid	Univ. Bielefeld	directrice de thèse

Contents

Contents

Summary

This thesis deals with the liquid crystalline lamellar phase L_α built by amphiphilic molecules in aqueous solutions, and its interaction with macromolecules. We perform molecular dynamics simulations to study thermal fluctuations and defects appearing in a stack of parallel amphiphilic bilayers separated by layers of solvent. The idealized, coarse-grained model represents the solvent with soft spheres and the amphiphiles with bead-and-spring tetramers (two solvophilic beads and two solvophobic beads). The algorithm used for this thesis describes the lamellar phase in the isobaric isothermal ensemble without surface tension $(N, P, T, \gamma = 0)$.

First, we verify that the model exhibits a liquid-crystalline lamellar phase, which we characterize. In a second part, we study the elasticity of this smectic lamellar phase. The position fluctuation spectra of the bilayers are computed, and compared to the predictions of the "Discrete Harmonic"(DH) theory for the elasticity of smectic phases. The bilayer fluctuations observed in the simulation of a stack of fifteen bilayers are well described by the DH-theory, so that the two elastic constants -the bending rigidity K_c and the smectic compressibility modulus B- can be computed.

Then, we investigate the point defects appearing in the smectic because of thermal fluctuations. It turns out that transient pores spontaneously nucleate in the bilayers of the lamellar phase. On the contrary, necks and passages between the bilayers are rarely detected. The size and shape distributions of the pores are investigated. The relationship between their area a and their contour length c is well described by the scaling law $a \propto c^{2/3}$ - the same scaling as two dimensional closed random walks. Additionally, the surface tension is zero. Therefore we consider that the energy of a pore depends explicitly only on the contour length of the pore. The effective free energy of individual pores and the line tension of the pore edge are then estimated from the contour-length distribution. Besides, a time-dependent analysis shows that the displacement of the pores within the bilayers during their life-time is very limited.

In the last chapter of this thesis, we investigate a lamellar phase doped by a solvent-soluble flexible linear polymer inserted between two bilayers. Two polymer types were simulated: adsorbing or non-adsorbing. In both cases, the interactions between the bilayers are softened in the presence of a polymer. However, the conformations of the chain strongly depend on the interactions between the polymer and the bilayers: An adsorbing polymer remains aligned with the bilayers and confined in the thin solvent layer, whereas a non-adsorbing polymer condenses into a globule. Contrarily to standard hypothesis, a non-adsorbing polymer locally modifies the interlamellar spacing, and triggers the formation of pores in its vicinity.

Summary

Résumé (French summary)

Cette thèse traite de la phase lamellaire smectique (L_α) formée par des molécules amphiphiles en solution aqueuse, ainsi que de son interaction avec des macromolécules. Cette phase est constituée d'un empilement de bicouches d'amphiphiles, parallèles les unes aux autres, et séparées par des couches de solvant.

Le but de la thèse est d'étudier les fluctuations thermiques et les défauts au sein d'une phase L_α par dynamique moléculaire. Nous utilisons un modèle mésoscopique, représentant le solvant par des sphères molles et les molécules amphiphiles par des tétramères (deux sphères solvophiles et deux sphères solvophobes liées par des ressorts). L'algorithme de dynamique moléculaire utilisé pour cette thèse décrit la phase lamellaire dans l'ensemble isobare isotherme sans tension de surface (NPT$\gamma = 0$).

Tout d'abord, nous vérifions que le modèle présente une phase L_α stable, et nous la caractérisons. Ensuite, nous comparons les fluctuations de positions des bicouches à des prédictions de la théorie "Discrete Harmonic" (DH) de l'élasticité des smectiques. Les fluctuations de positions des membranes étudiées par la simulation d'un empilement de quinze bicouches sont en accord avec la théorie DH, ce qui permet de mesurer les constantes élastiques de la phase L_α modèle (le module de compressibilité B et le module de rigidité de courbure moyenne K_c).

Ensuite nous étudions les défauts ponctuels qui apparaissent dans la phase smectique à cause des fluctuations thermiques. Des pores transitoires nucléent spontanément dans les bicouches. Par contre, des connections ou passages entre les bicouches ne sont que rarement détectés. Les distributions de taille et de forme des pores sont étudiées. La dépendance de l'aire des pores a en fonction de la longueur du contour c est bien décrite par la relation $a \propto c^{2/3}$ (la même loi d'échelle est obtenue pour une marche alléatoire fermée en deux dimensions). De plus, dans le cas présent, la tension de surface est nulle. Il est donc raisonnable de supposer que l'énergie associée à la formation d'un pore ne dépend explicitement que de la longueur de son contour. Cette énergie, ainsi que la tension de ligne, sont alors déduites de la distribution de probabilité du périmètre des pores. Par ailleurs, une étude de l'évolution temporelle des pores montre qu'ils ne se déplacent que très peu au sein de la membrane durant leur durée de vie.

Dans le dernier chapitre, nous étudions une phase lamellaire dopée par un polymère linéaire flexible. Ce polymère, soluble dans le solvant, est inséré entre deux lamelles. Deux types de polymères ont été simulés : polymères adsorbants, et non adsorbants. Dans les deux cas, les interactions effectives entre les membranes sont modifiées par la présence du polymère. Par contre, la conformation du polymère dépend radicalement des interactions du polymère avec les amphiphiles : un polymère adsorbé reste parallèle aux membranes, confiné dans le solvant, alors qu'un polymère non adsorbé se condense en un

Résumé (French summary)

globule. Contrairement aux hypothèses habituelles, le polymère non adsorbé perturbe localement la distance interlamellaire et favorise l'apparition de pores dans son voisinage.

Zusammenfassung (German summary)

Diese Arbeit behandelt die flüssig-kristalline lamellare Phase (die sogenannte L_α Phase), die amphiphile Moleküle in wässriger Lösung ausbilden. Diese lamellare Phase besteht aus mehrere Lagen paralleler amphiphiler Doppelschichten, die durch Lösungsmittel voneinander getrennt sind. Wir studieren mittels Molekulardynamiksimulationen die thermischen Fluktuationen der Doppelschichten und die Defekte, die in der lamellaren Phase auftreten köennen, und die Auswirkungen eines Makromoleküls, das zwischen die Doppelschichten gesetzt wird.

In dem zugrundeliegenden, idealisierten "coarse-grained" Modell werden das Lösungsmittel als weiche Kugeln und die Amphiphile als Tetramere (zwei hydrophile Kugeln und zwei hydrophobe Kugeln) repräsentiert. Der Algorithmus, der in dieser Arbeit verwendet wird, beschreibt die lamellare Phase im isobaren isothermen Ensemble ohne Oberflächenspannung ($NPT, \gamma = 0$).

Zuerst verifizieren wir, daß das Modell tatsächlich eine stabile L_α Phase bildet, und charakterisieren ihre flüssig-kristalline Struktur.

Um die Elastizität der lamellaren Phase zu untersuchen, berechnen wir die Fluktuationsspektren der Positionen von den Doppelschichten und vergleichen sie mit den Vorhersagen der "Discrete Harmonic Theory" (DH) für die Elastizität der smektischen Phasen. Die Ergebnisse der Simulation, die mit einem Stapel von fünfzehn Doppelschichten durchgeführt wurde, stimmen mit der DH Theorie überein. Daher können die elastischen Konstanten (Steifigkeitsmodul K_c und smektischer Kompressionsmodul B) berechnet werden.

Nachfolgend betrachten wir lokale Defekte, die auf Grund thermischer Fluktuationen erscheinen. Kurzlebige Poren treten spontan in den Doppelschichten der lamellaren Phase auf. Im Gegensatz dazu werden Verbindungen oder Durchgänge zwischen den Doppelschichten selten beobachtet. Die Verteilungen von Größe und Form der Poren werden bestimmt. Das Verhältnis zwischen Fläche der Poren a und ihrer Konturlänge c wird durch das Skalengesetz $a \propto c^{2/3}$ beschrieben (ein analoges Skalengesetz gilt für zweidimensionale geschlossene Irrfahrten). Zusätzlich ist die Oberflächenspannung null. Wir nehmen dann an, daß die Energie einer einzelnen Pore nur von ihrer Konturlänge abhängt. Diese Energie und die Linienspannung des Porenrandes werden mittels der Verteilung für die Konturlänge geschätzt. Zusätzlich zeigt eine zeitabhängige Analyse, daß die Poren innerhalb ihrer Lebensdauer nicht nennenswert diffundieren.

Schließlich wird eine lamellare Phase untersucht, in der ein hydrophiles, flexibles, lineares Polymer zwischen zwei Doppelschichten eingesetzt wurde. Zwei Typen von Polymeren werden simuliert: adsorbierende und nicht-adsorbierende. In beiden Fälle werden die Wechselwirkungen zwischen den Doppelschichten in Anwesenheit des Polymer

verändert. Die Konformation des Polymers hängt allerdings stark von den Wechselwirkungen zwischen dem Polymer und den Amphiphilen ab: Ein adsorbierendes Polymer verbleibt während der gesamten Simulation in der dünnen Lösungsmittelschicht zwischen den beiden Doppelschichten. Ein nicht-adsorbierendes Polymer dagegen kondensiert in einen kompakten Tropfen". Im Gegensatz zu den übliches Annahmen ändert ein nicht-adsorbierendes Polymer lokal den interlamellaren Abstand und erzeugt Poren in der Doppelschicht in seiner Nähe.

Introduction

The subject of this thesis is the pure and polymer-doped L_α lamellar phase of amphiphilic molecules. The following pages introduce amphiphilic molecules, describe the L_α lamellar phase and explain the scope of this thesis.

Amphiphilic molecules

The term amphiphilic is composed of two greek roots: "amphi"for "both sides"and "philia"for love. It is used to describe molecules composed of two covalently bonded parts with different affinities. Some examples of amphiphilic molecules are given in Table 0.1. Soaps (*e.g.* SDS) are soluble in both oil and water, they contain both a hydrophilic, water-loving head and a hydrophobic, oil-loving tail. Lipids, which are found in almost all living organisms, compose another broad class of amphiphiles (e.g. DPPC).

Because of their particular solubility properties, amphiphilic molecules are widely used as detergents, and in cosmetics, pharmaceutical or food formulations. They play a crucial role in the formation of emulsions, foams, colloidal suspensions and coatings because they increase the spreading and wetting properties of liquids by reducing their surface tension.

Beside their ambivalent solubility property, amphiphiles exhibit another very interesting behavior: in solution, they self-assemble into a large variety of phases ordered on a nanometer-to-micrometer length-scale (mesophases), *e.g.* lamellar phases. Amphiphiles are therefore used in the synthesis of technical materials. For example, mesophases of amphiphiles can be successfully polymerized [88]. The resulting solids may exhibit the same structure as the soft amphiphilic solutions and be used as precise filters, catalysts, or medical drips. The self-assembly of amphiphilic molecules in an aqueous environment is also a fundamental process for living organisms: the basic substance of cell membranes is a self-assembled sheet of lipids [66].

Schematically, in aqueous solutions, the polar heads of the amphiphiles favor a molecular dispersion, whereas their hydrophobic tails favor a phase separation. As a compromise, the amphiphilic molecules self-assemble into colloidal aggregates: spherical micelles, tubular micelles, or planar bilayers (see Fig. 0.1).

When the concentration is low, the amphiphiles form spherical micelles. The smallest concentration at which micelles can be detected is called the critical micellar concentration (CMC), and can be as small as 10^{-10} M! In diluted solutions, micelles have an inner part containing the lipidic tails, and an outer shell containing the head groups, directed toward the solvent. In concentrated solutions, the micelles are inverted: The inner part

structure of the amphiphile	CMC
$C_{12}H_{25}OSO_3^-$ Na^+	$8.1 \times 10^{-3}(25°C)$
Sodiumdodecylsulfate (SDS) : anionic	
$C_{12}H_{25}N(CH_3)_3^+$ Br^-	$1.5 \times 10^{-2}(25°C)$
Dodecylammonium Bromide (DAB) : cationic	
$(C_{15}H_{31}COO)\,CHCH_2OPO_3CH_2CH_2NMe_3$	$5 \times 10^{-10}(41°C)$
$(C_{15}H_{31}COOCH_2)$	
Dipalmitoylphosphatidylcholine (DPPC) : zwitterionic	
$C_{12}H_{25}\,(OCH_2CH_2)_6\,OH$	$8.7 \times 10^{-2}(25°C)$
Hexaethylene glycol dodecyether ($C_{12}E_6$) : neutral	

Table 0.1: Examples of amphiphilic molecules. The temperature at which the critical micellar concentration (CMC) is measured is given in parenthesis (the definition of the CMC is in the text). In the small pictures, the disks represent the hydrophilic heads, and the zig-zag tails represent hydrocarbon or fluorocarbon chains.

direct micelle   cylindrical micelle   bilayer   inverted micelle

~nm   μm   μm   ~nm
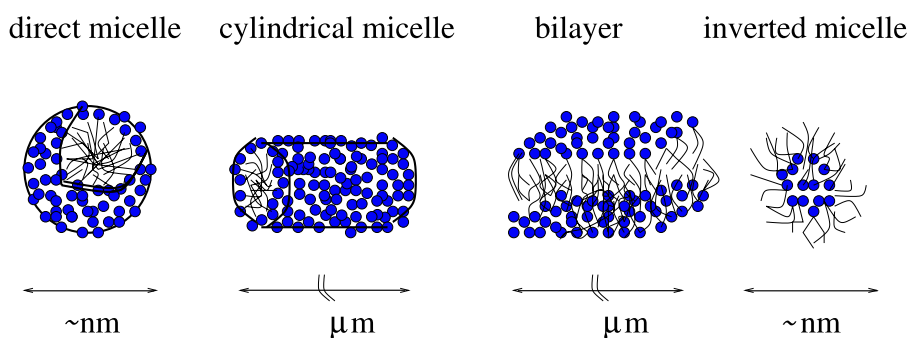
Figure 0.1: Aggregates of amphiphilic molecules.

of the micelles is composed of the hydrophilic heads, and the external shell is composed of the tails.

Bilayers appear at intermediate concentrations. They consist of two one-molecule thick layers, the monolayers. Within each monolayer, all the amphiphiles point their hydrophobic part in the same direction, forming a sheet with one hydrophobic side, and one hydrophilic side. In aqueous solvent, the hydrophobic sides of the two monolayers face each other, so that they are inside the bilayer, shielded from the aqueous solvent by the polar heads.

Diblock-copolymers exhibit self-assembling properties similar to those of soaps or lipids. For example, they form micelles and bilayers. Polymers are large molecules synthesized by bonding covalently together a large number of relatively small molecules (the monomers). A simple case is the linear homopolymer: a long chain of identical

monomers. Diblock-copolymers are composed of two linear homopolymers linked by a covalent bond. In this thesis, we consider short amphiphilic molecules (about twelve carbon atoms), so we deal with soaps or lipids rather than with block-copolymers.

The L_α lamellar phase

Phase diagrams of amphiphiles exhibit many phases: each one of the aggregates mentioned previously may self-assemble into several different mesophases. For example, bilayers self-assemble into several lamellar phases - among which the L_α phase, which is the subject of this thesis.

The relevant parameters to describe the phase diagram of aqueous solutions of amphiphiles are the concentration of the amphiphiles and the temperature. For ionic components, the ionic strength of the solvent has to be taken into account as well.
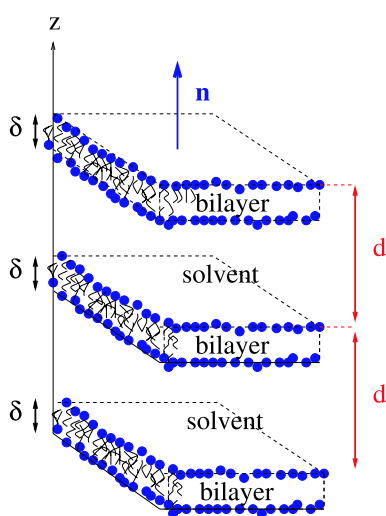
Figure 0.2: Structure of a binary lamellar phase, with the thickness δ of the parallel bilayers and its periodicity d. The unitary vector **n**, called the director, shows the average orientation of the amphiphilic molecules. In the L_α lamellar phase, **n** is also perpendicular to the lamellae.

A lamellar phase is a stack of bilayers, parallel to each other, separated by layers of solvent (see Fig. 0.2). The periodicity d of the lamellar phase may vary from dozens to thousands of Ångstroms [49]. Among the numerous lamellar phases observed experimentally (see Fig. 0.3), three types are distinguished: crystalline phases, gel phases, and a liquid crystalline phase denoted L_α.

In the L_α lamellar phase (see Fig. 0.3 E), the polar heads are not ordered, and the amphiphiles diffuse quite freely in each monolayer. There is no order in the fatty chains either (they are melted). The L_α phase is a smectic liquid crystal: parallel to the planes of the bilayers, the molecules are distributed as in a liquid; perpendicularly to the bilayers, there is a long-range positional order.

Motivation and scope of the thesis

Many common biological phenomena (*e.g.* the fusion of two membranes, the exocytose, and the interactions of biomembranes with carbohydrates) involve local structural changes in the amphiphilic bilayer composing biomembranes. The L_α phase has proven
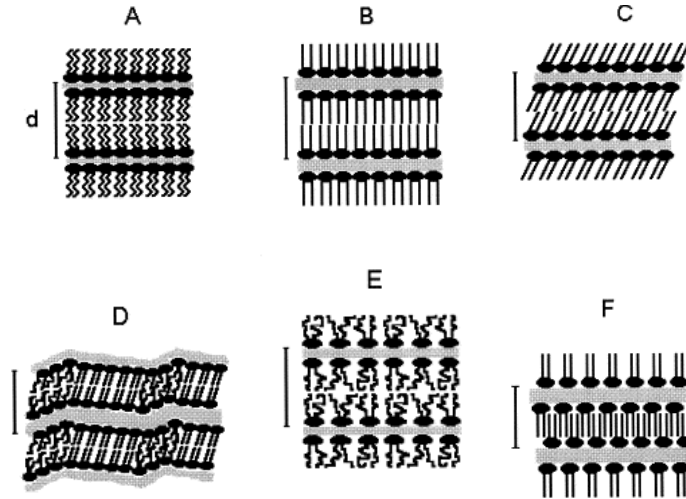
Figure 0.3: Schematic views of some lamellar phases found in phosphatidyl-cholines/water lamellar phases: (A) crystalline L_c; (B) gel untilted chains, L_β; (C) gel tilted chains, L'_β; (D) rippled gel, P'_β; (E) liquid crystalline, L_α. (F) fully interdigitated gel, L_α. Reproduced from [96]. The phosphatidyl-cholines are lipids found in biological membranes.

to be a good experimental and theoretical model to study amphiphilic bilayers, and their interactions with polymers [152, 105]. Nevertheless, the interactions of polymers with amphiphilic bilayers are still poorly understood: How do polymers influence the mechanism of fusion between membranes [162]? How do large hydrophilic polymers permeate through biomembranes [185, 186]?

Furthermore, the technical applications of artificial doped L_α phases are numerous, for instance new biological materials [92], new meso-structured solids obtained from the polymerization of soft mesophases [36, 117], anisotropic solvents for specific measurements (*e.g.* NMR [160, 9]). Some relevant questions are still only partly answered. What are the effective interactions between inclusions in smectics [195, 60, 172]? What are the conformations of molecules embedded in a lamellar phase [39]? To answer these questions, one needs to know the local and transient conformations of the lamellar phase. In this thesis, we shall focus our interest on:

- The position fluctuations of the bilayers: The influence of a guest molecule on the lamellar phase strongly depend on its ability to deform. How does the lamellar phase release the constraint imposed by an inclusion? It depends on its elastic properties. Results on the elastic properties of the simulated lamellar phase are presented in Chapter 3.

- Pores in the bilayers of the L_α phase: experimentally, pores are difficult to observe directly. Nevertheless, many experimental observations are easier to understand

if we assume the presence of pores in amphiphilic bilayers (*e.g.* the permeation of molecules through bilayers [67, 169, 210, 118]). With molecular dynamics simulations, one can study transient pores appearing in the bilayers (see Chapter 4).

- The influence of a polymer inclusion on these fluctuations and defects: Experimental studies of doped lamellar phase give a lot of information on the bilayers [17, 44, 57, 42, 64, 152, 92]. Less information is available about inclusions[92, 152, 150]. Results on the conformations of a polymer inserted in the simulated lamellar phase are presented in Chapter 5.

A coarse-grained model studied by computer simulations

Polymer-L_α complexes exhibit several characteristic time- and length-scales. The lamellar domains are typically one micrometer large, whereas the size of the head-group of an amphiphilic molecule is about one nanometer. Fig. 0.4 illustrates the large range of length-scales appearing in doped lamellar phases. The time-scales also span several
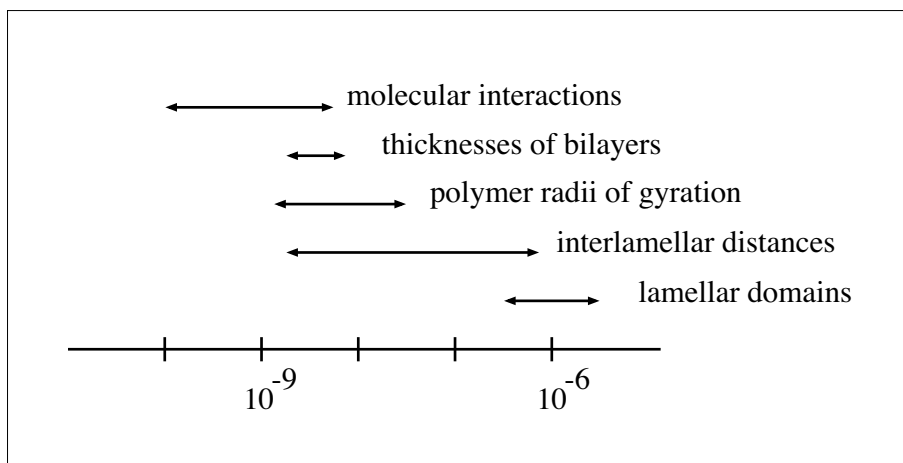
Figure 0.4: Characteristic length-scales (in meters) in doped lamellar phases.

orders of magnitude (see Fig. 0.5).

Various models have been used to describe the lamellar phase on different time- and length-scales, from all-atoms models to mesoscopic models describing the bilayers as continuous elastic surfaces. The coarse-grained molecular model used in this thesis was obtained by neglecting atomic details and considering only the amphiphilic properties of the molecules. It is an extension of a model proposed by Grest and Kremer in 1986 [73]. Since then, it has been extensively used to study polymers [97, 47] and, more recently, to study the rheological properties of amphiphilic dimers [182, 75].

The coarse-graining enables us to obtain information about the structure of the L_α phase at time scales and length scales around ten nanoseconds and ten nanometers,
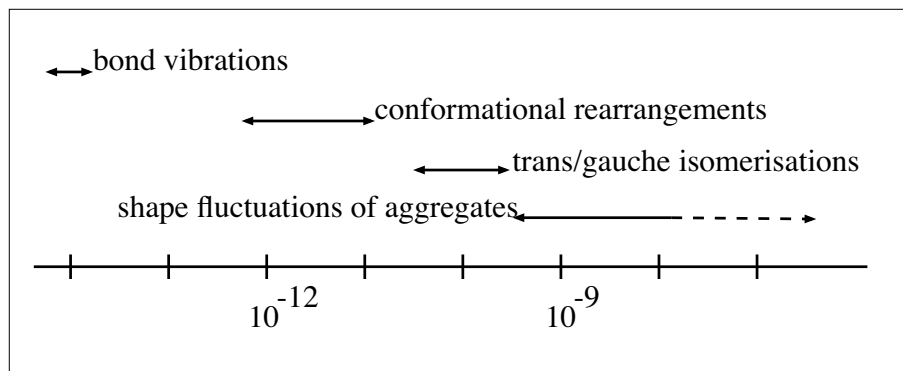
Figure 0.5: Characteristic times (in seconds) of common types of motion in amphiphilic bilayers.

which is suited to study the position fluctuations of the bilayers, the appearance of some point defects, and the conformations of a confined polymer. The size of the membranes simulated for this work is similar to the size reported in the most recent publications on bilayers with coarse-grained models [126, 176] (thousands of amphiphilic molecules per bilayer). These previous simulations of amphiphilic bilayers have described one or two bilayers, whereas the calculations of this thesis simulate stacks of five and fifteen bilayers. The contribution of the present work is not only to simulate much larger systems, but also to investigate the interactions between the bilayers, and the effect of a polymer confined between these bilayers.

To study an off-lattice coarse-grained molecular model, computer simulations have proven to be an efficient method [73, 182]. The advantage offered by molecular dynamics is that very few assumptions are done on the type of defects which may appear in the lamellar phase, or on the conformation of the guest polymer. In this sense, the numerical simulations are considered here as experiments "in silico"[106].

Organization of the thesis

This thesis is organized in five chapters.

In the first chapter, the simulation model is introduced, as well as the method to study it (molecular dynamics simulations). I use a coarse-grained, off-lattice model describing a binary solution containing a solvent and amphiphilic molecules: a fluid of soft beads stands for the solvent, and tetramers stand for the amphiphiles - two solvophilic beads linked to two solvophobic beads. The simulation algorithm, optimized for the scope of this thesis, describes the lamellar phase in the isobaric isothermal ensemble without surface tension ($N, P, T, \gamma = 0$), and with periodic boundary conditions. Then, I show that the model is suited to simulate the liquid crystalline structure of the lamellar phase (Chapter 2). In Chapter 3, the position-fluctuations of the bilayers are compared to

the predictions of the "Discrete Harmonic"theory for the elasticity of smectics [80, 144, 102, 141, 110]. Chapter 4 contains results on point defects in the L_α phase. Pores spontaneously nucleate in the lamellar phase. We shall investigate the size, shape, lifetime, and the spatial distribution of these pores. Last but not least, Chapter 5 deals with the interaction of a polymer with the lamellar phase. A single linear homopolymer, represented by a bead-and-spring chain, is inserted into the simulated lamellar phase. It is soluble in the solvent layer of the lamellar phase, but not in the hydrophobic part of the bilayers. The simulations provide information on the conformations of the polymer, and on the influence of the polymer on the lamellar phase. Finally, the conclusion discusses the principal results of this thesis and proposes some perspectives.

Introduction

1 Simulation of smectics: model and method

This chapter presents the model of the doped lamellar phase, and the method used to study it: numerical simulations.

1.1 Off-lattice, coarse-grained model

1.1.1 Models of lamellar phases

Molecular dynamics simulations of lipid bilayers which include atomic details have been performed for about three decades [190, 52, 59]. Recent publications report simulations of several hundred of lipids in thousands of water molecules [114, 99]. The available scales in time and space are still limited compared to many biochemical processes, but the performance is increasing enormously, thanks to the parallelization of simulation codes and to faster algorithms. Ten years ago, atomic models permitted to describe the different conformations of molecules in the solid, gel and liquid phases of lipid bilayers [79]. Since then, atomic molecular dynamics simulations have even been used to investigate the interactions of amphiphilic bilayers with other molecules. Due to the complexity of biological membranes, the number of interesting systems which can be simulated is huge: mixtures of lipids, adsorption of peptides, inclusion of cholesterol (see Fig. 1.1 A, from [32]), inclusion of membrane proteins, diffusion of ions, *etc.*

Limiting the accuracy of the calculations by cutting-off the potentials at about $1\,\mathrm{nm}$ permits to study a bilayer during longer times (256 DPPC during $0.5\,\mu\mathrm{s}$ [113]) or to simulate more molecules (2000 DPPC for $16\,\mathrm{ns}$ [114]).

Coarse-grained molecular models are obtained by neglecting atomic details and keeping only the structure of the molecules. The coarse-grained "molecules" are typically derived from the "realistic" molecules by grouping some atoms together into beads interacting *via* effective potentials. The electrostatic interactions and the dihedral angle potentials are often neglected. For example, a molecule of hexane C_6H_{14} is possibly coarse-grained into a chain of six "united-atoms" interacting via the popular $6-12$ Lennard-Jones radial pair-potential (6-12 LJ) ([201] and Ref. in it).

$$\mathcal{V}_{\mathrm{LJ}}(r) = 4\epsilon \left[\left(\frac{\sigma}{r} \right)^{12} - \left(\frac{\sigma}{r} \right)^{6} \right]$$

where ϵ is the potential depth, and σ a typical length for the interaction. The essential
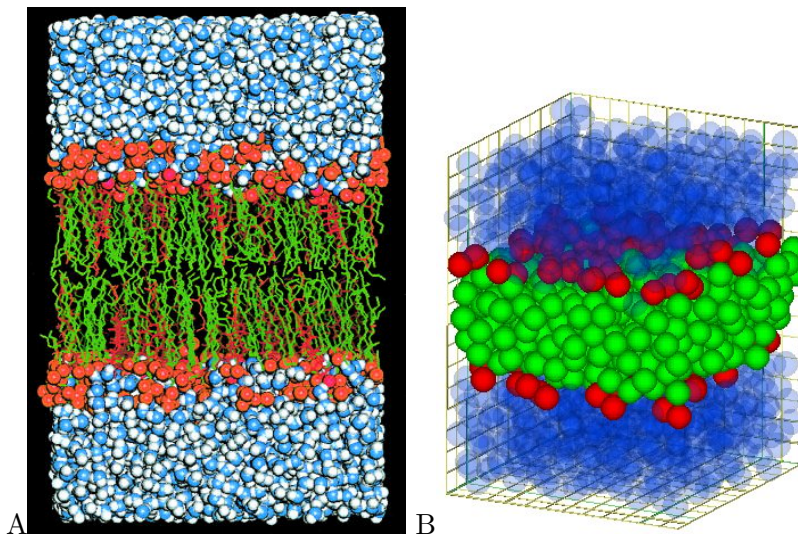
Figure 1.1: A: Atomic model of a bilayer: 108 molecules of DPPC, 5 301 molecules of water and 54 molecules of cholesterol [32]. B: Molecular coarse-grained model of a bilayer with ht_4 amphiphiles (one head-bead linked to a chain of four tail beads) [69].

features of Lennard-Jones potentials are a soft repulsion at small distances ($r \leq 2^{1/6}\sigma$), and a short-ranged attraction ($\mathcal{V}_{\mathrm{LJ}} \propto -r^{-6}$).

Shelley *et al.* [174, 173] proposed a coarse-grained model of dimyristoylphosphati-dylcholine (DMPC). One amphiphile of more than 100 atoms was reduced to 13 units interacting *via* Lennard-Jones-type potentials (6-12 LJ, but also 4-6 LJ, among others). In this case, the coarse-grained simulations cost about 400 times less computer time than the all-atoms simulations.

Further simplified models describe the interactions between the amphiphilic molecules only qualitatively, but much more generally (see Fig. 1.1 B, from [69]). The main components included in these models are: (i) the amphiphilic structure, (ii) the internal degrees of freedom of the molecules, and (iii) the interactions between amphiphiles and solvent molecules. For example, short amphiphilic oligomers composed of hydrophobic tail-beads linked to hydrophilic head-beads self-assemble into micelles or bilayers, whose shape fluctuations can be studied by numerical simulations [180, 69, 129].

Lattice models also have proven to be very successful to reproduce the phase diagram of amphiphilic solutions [100, 33]. Müller *et al.* explored the mechanical stability of model membranes composed of diblock-copolymers dissolved in bulk homopolymers using lattice Monte Carlo simulations [127, 126], and compared the results to those of self-consistent-field theory.

By neglecting additionally the internal degrees of freedom of the amphiphilic molecules, Leibler *et al.* could simulate a unilamellar vesicle (see Fig. 1.2 A, from [103]).

Finally, a different class of models neglects even the amphiphilic character of the

molecules, to focus on the properties of membranes built by amphiphilic molecules. The membranes are represented as a undulating surfaces. Triangulated elastic surfaces, for instance, have proven to be a good model to study the shape fluctuation of vesicles (see Fig. 1.2 B, from [71]) or the proliferation of pores in bilayers [175, 177].
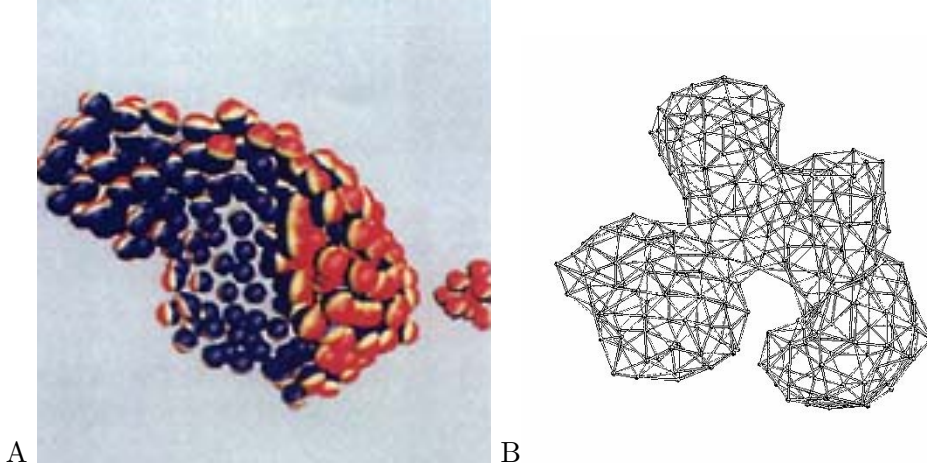
Figure 1.2: A: Model of a bilayer as an assembly of spheres composed of three parts: one hydrophobic, in the center (yellow), and two hydrophilic at the poles (red and blue) [103]. B: Model of bilayer as a triangulated surface with fluctuating topology [71].

1.1.2 Definition of the model

The model used in this thesis is an extension of a coarse-grained off-lattice model proposed by Grest and Kremer in 1986 [73], which has been used extensively to simulate polymers [97, 47]. It has been extended recently to study the rheologic properties of amphiphilic dimers [182, 75]. The model resembles the one used by Goetz *et al.* [69] (see Fig. 1.1 B): it is a coarse-grained off-lattice molecular model. The amphiphiles are represented by tetrameric chains composed of two hydrophobic tail beads and two hydrophilic head beads, denoted by *hhtt* or h_2t_2. The polymer is a simple linear chain of hydrophilic beads (see Fig.1.3). Chemical details, long-range interactions or chain stiffness are not incorporated in the model.

The forces derive from radial, short-ranged pair potentials. The beads interact through a soft repulsion and a short-ranged attraction characterized by two parameters: a length defining the range of the interaction σ, and an energy defining the depth of the potential ϵ. The units are the following: for the energies k_BT, for the lengths σ, and for the mass of the beads, m. These units lead to the time unit $\tau = (m\sigma^2/k_BT)^{1/2}$.

A bead represents approximatively three alkyl groups, or eventually three water molecules. The orders of magnitude of the units are then $k_BT \simeq 10^{-21}\,J$, $m \simeq 10^{-25}\,kg$, and $\sigma \simeq 5\,\mathring{A}$ [174]. The time unit is approximatively one picosecond ($\tau \simeq 10^{-12}\,\mathrm{s}$).
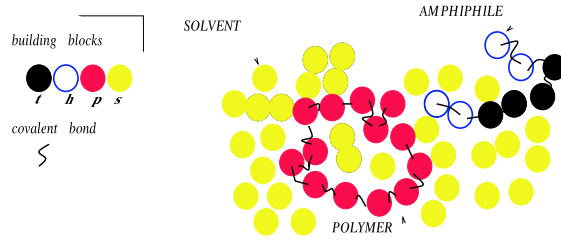
Figure 1.3: Molecules of the model: solvent beads, amphiphiles and polymers. They are composed of four sorts of beads: solvent beads, tail beads, heads beads and polymer beads.
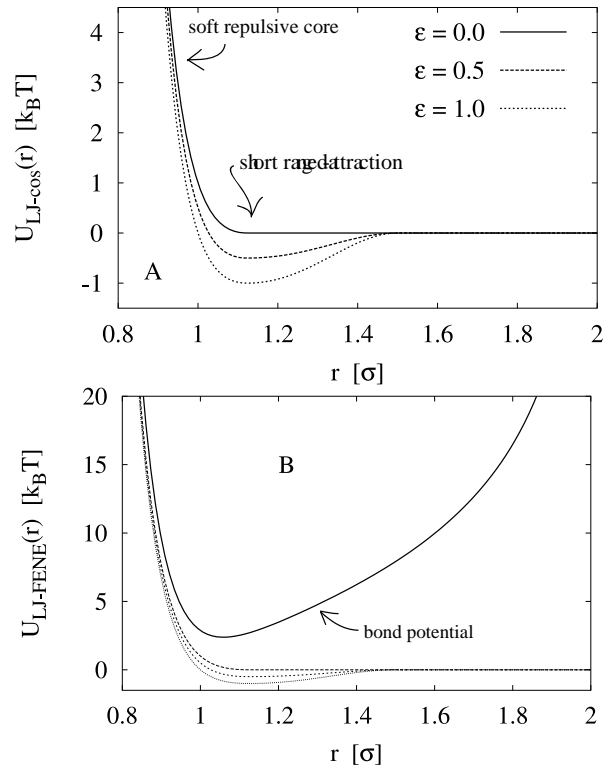
Figure 1.4: Radial pair potentials as a function of the inter-particle distance. **A**: Potential of interaction between beads that are not connected: $U_{\text{LJ-cos}}$. **B**: Potential of interaction between connected beads: $U_{\text{LJ-FENE}}$ (solid line). The potentials of non-connected pairs are represented as well (dashed line).

	solvent	head	tail	polymer
solvent	ϵ	ϵ	0	ϵ
head	ϵ	ϵ	0	ϵ
tail	0	0	ϵ	0
polymer	ϵ	ϵ	0	ϵ

Table 1.1: Potential depths for the non-bonded interacting beads. In most cases, $\epsilon = 1.1\,k_B T$

Force fields

Unconnected beads interact via the $LJ - cos$ potential, defined by

$$U_{\text{LJ-cos}}(r) = \begin{cases} 4k_B T \left[\left(\frac{\sigma}{r}\right)^{12} - \left(\frac{\sigma}{r}\right)^{6} + \frac{1}{4} \right] - \epsilon & \text{if } r \leq 2^{1/6}\sigma \\ \frac{\epsilon}{2} \left[cos(\alpha r^2 + \beta) - 1 \right] & \text{if } 2^{1/6}\sigma \leq r \leq r_c \\ 0 & \text{if } r_c \leq r \end{cases} , \qquad (1.1)$$

where σ is the unit of length, $\alpha = \pi/r_c^2 - 2^{1/3}\sigma^2$ and $\beta = 2\pi - r_c^2\alpha$. The cutoff is chosen at $r_c = 1.5\,\sigma$ (see Fig. 1.4 A for an illustration). The minimum of potential ($r \simeq 1.16\,\sigma$) and the cut-off ($r = 1.5\,\sigma$) are independent of the potential depth ϵ. At $\epsilon = 0$, the potential is strictly repulsive.

The potential depths of the several interactions between unconnected beads are collected in Table 1.1.

Connected beads repel each other with the same soft-core potential as non-bonded beads, but at larger distance, the interaction is attractive through a "finite extendable non-linear elastic"(FENE) potential (see Fig. 1.4 B).

$$U_{\text{LJ-FENE}}(r) = \begin{cases} 4k_B T \left[\left(\frac{\sigma}{r}\right)^{12} - \left(\frac{\sigma}{r}\right)^{6} \right] - \left(\frac{\kappa r_b^2}{2}\right) \ln \left[1 - \left(\frac{r}{r_b}\right)^2 \right] & \text{if } r \leq r_b \\ \infty & \text{if } r_b \leq r \end{cases} . \qquad (1.2)$$

The parameters used for in this thesis are $r_b = 2.0\,\sigma$ and $\kappa = 7.0\,k_B T \cdot \sigma^{-2}$, as in [47].

Truncation of the potentials

The potentials of the model are cut off at $1.5\,\sigma$ or $2\,\sigma$: This permits to optimize the simulation code by using the so-called neighbor-lists and cell-lists [1, 63]. The principle is explained in the following.

If every particle interacts with every other particle of the simulation box, the number of interactions is proportional to $N(N - 1)/2$, where N is the number of bead in the simulation box. If the potential is short-ranged and the density is fixed, the number of interactions increases no longer quadratically, but linearly with N. As most of the time of computation is spent calculating the forces, reducing the cut-off r_c significantly speeds up the calculations.

Still, the number of distances to check remains $N(N-1)/2$. To speed up the calculations even more, the algorithm uses the so-called neighbor-lists combined with cell-lists [63, 1].

The principle of the neighbor-lists (also named Verlet list) is the following: A list of pairs of particles at the distance r that are close enough to interact is stored ($r \leq r_c$). For the calculation of the forces, instead of testing $N(N-1)/2$ distances at each time step, the algorithm directly uses the list of interacting neighbors. The key point is that pairs of particles which are at the distance r slightly larger than the cutoff r_c are also stored in the neighbor-list ($r \leq r_c + d_s$, where d_s is a "distance of security"). Thus the neighbor-list does not have to be updated at each time-step, and much computation time is saved.

Additionally, the construction of the neighbor-lists is optimized by cell-lists: the space is divided into cells, in which the particles are sorted. The lists of cells whose particles may interact is set up only once, at the beginning of the simulation. During the simulation, for each Verlet list update, only the pairs of particles belonging to the pairs of cells registered in the cell-list are checked. The computational time decreases because the construction of the list becomes much cheaper than $N(N-1)/2$ checks of distances.

Finally, the program is implemented with an optimized domain-decomposition scheme, to run the simulations in parallel [148, 182].

Besides these technical considerations, the truncation of the potentials strongly influences the properties of the system. For instance, the critical temperature of the Lennard-Jones fluid decreases from $k_B T_c/\epsilon = 1.316$ to 1.085 when the potential is cutoff at $2.5\,\sigma$ and shifted to get a continuous potential [1]. Additionally, as the model does not include long-range interactions, in particular non-screened electrostatic forces, the study is restricted to neutral lamellar phases - or to charged lamellar phases where the long-range interactions are screened by a solvent with a high dielectric constant.

1.1.3 Phenomenology of the model

As the phase diagram of the model is complex, I outline here only the essential features relevant to this thesis. For pedagogical reasons, the details of the simulations are not discussed here (for more details, see Section 1.2).

The solvent: a simple fluid

The solvent beads repel each other at short distance ($r \leq 2^{1/6}\,\sigma$), and attract each other at intermediate distance ($2^{1/6}\,\sigma \leq r \leq 1.5\,\sigma$), as depicted in Fig. 1.4 A. Despite the cutoff of the potential, the pure solvent is similar to a Lennard-Jones fluid. Its phase diagram is expected to be composed of a gas phase, a fluid phase and one or more crystalline phases. For this thesis, the gas phase is not relevant.

To detect approximatively the fluid-to-solid phase transition of the solvent, I studied its density ρ as a function of the potential depth ϵ, with a simulation in the constant-NPT ensemble (see Fig. 1.5). As expected, the density increases when the potential becomes more attractive (increasing ϵ). The abrupt increase of the density indicates the
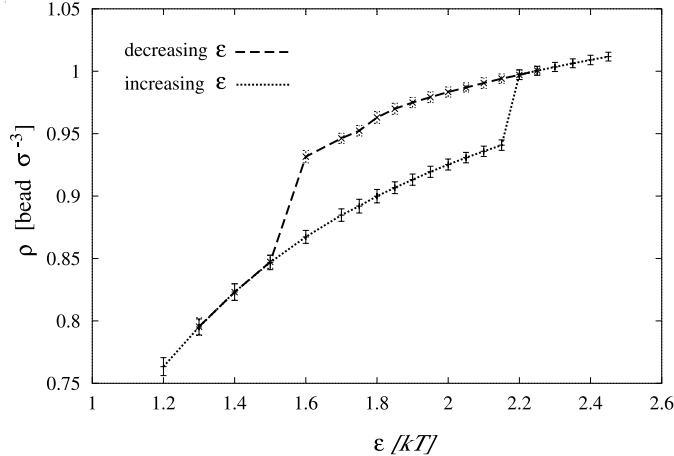
Figure 1.5: Density of the solvent as a function of the potential-depth in NPT ensemble ($N = 1\,000$ beads, $P = 1\,k_BT \cdot \sigma^{-3}$).

fluid-to-solid transition. Since the transition is first-order, we observe hysteresis when the potential depth is decreased again.

The minimum density at which the solid is observed is about 0.93 beads per unit volume. To ensure that the system remains fluid, one simulates it at a density close to 0.85 beads per unit volume.

Pure amphiphiles: the order-disorder transition

The amphiphiles are represented by chains of two tail beads and two heads beads. The tail-head pairs repel each other at short distance, whereas the head-head or tail-tail pairs additionally attract each other at intermediate distances. If they were not connected to each other, the heads and tails would demix for ϵ larger than $0.6\,k_BT$ [182]. In the case of connected chains, increasing the potential depth ϵ drives a self-assembly. For pure amphiphilic systems, two phases have been observed. Two snapshots in Fig. 1.6 represent a pure h_2t_2 system in the disordered phase (small ϵ) and in the ordered liquid crystalline lamellar phase (large ϵ).

Quantitatively, the transition between the two phases can be detected by an abrupt variation of the nematic order parameter S (defined in Section 2.1.2). The transition occurs around $\epsilon = 0.8\,k_BT$ (see Fig. 1.6). As the transition is first-order, the system exhibits hysteresis.

To simulate the lamellar phase, I have chosen the value $\epsilon = 1.1\,k_BT$. The density 0.85 beads per unit volume corresponds then to a pressure of $3.0\,k_BT \cdot \sigma^{-3}$.

More generally, other amphiphilic oligomers h_nt_m may self-assemble into a smectic A. For example, dimers undergo the order-disorder transition at the potential depth $\epsilon = 1.2\,k_BT$. I have chosen to simulate tetramers because they are small, symmetric (monolayers have no spontaneous curvature), and their lamellar phase is stable relative

7
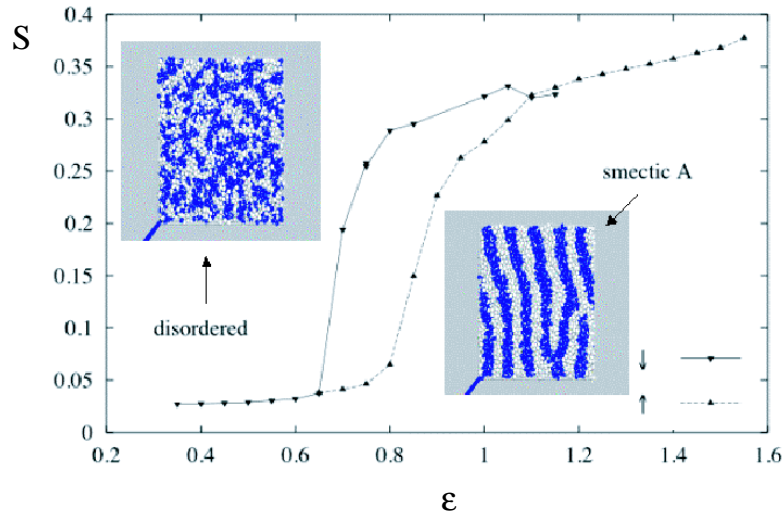
Figure 1.6: Nematic order parameter S vs. potential depth ϵ in a system of 8192 tetramers $h_2 t_2$ simulated in the constant-NVT ensemble ($\rho = 0.85$ beads $\cdot \sigma^{-3}$). The potential depth ϵ is increased or decreased of $0.05\,k_B T$ every $10\,000\,\tau$. During the first $2\,000\,\tau$ the system relaxes; the following $8\,000\,\tau$ are used for the measurement.

to the addition of a small amount of solvent, contrarily to the lamellar phase of dimers.

Dilution of the lamellar phase

In the present model, the heads of the amphiphiles attract the solvent, the tails do not. When solvent is added to a pure amphiphilic lamellar phase, it accumulates between the amphiphilic bilayers. With the chosen parameters ($\epsilon = 1.1\,k_B T$, $P = 2.9\,k_B T \cdot \sigma^{-3}$), if the amount of solvent exceeds 25 % of solvent (bead percentage), the lamellar phase is destroyed, and a disordered phase appears. Consequently, a single fluid bilayer of the tetrameric amphiphiles in a large amount of solvent is not stable. It breaks down to form micelles.

The lamellar phases simulated in this thesis contain 20% of solvent (bead percentage). Fig. 1.7 illustrates the self-assembly of the lamellar phase at this composition, after an instantaneous increase of ϵ ($\epsilon = 0.8\,k_B T$ to $1.1\,k_B T$, at constant $P = 2.9\,k_B T \cdot \sigma^{-3}$). The self-assembly observed in Fig. 1.7 shows that for 20% of solvent beads, and for the parameters $\epsilon = 1.1\,k_B T$, $P = 2.9\,k_B T \cdot \sigma^{-3}$, the lamellar phase is stable.
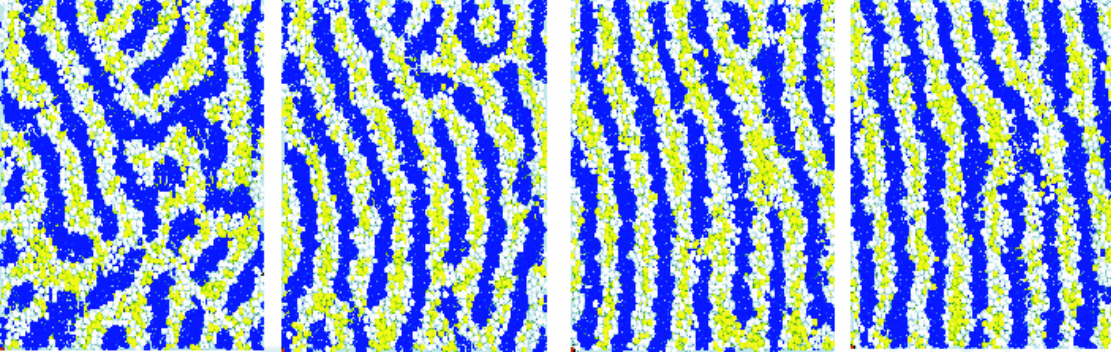
Figure 1.7: Time evolution of $30\,720$ amphiphilic tetramers with $30\,720$ solvent beads, after a change in the segregation parameter from $0.8\,k_B T$ to $1.1\,k_B T$ at the pressure $2.9\,k_B T \cdot \sigma^{-3}$ (the simulations are done in the constant-NPT ensemble with no surface tension described in Section 1.2.3). From left to right, the snapshots represent the system at $10\,000\,\tau$, $20\,000\,\tau$, $30\,000\,\tau$, and $40\,000\,\tau$ after the quench. Tail-beads are blue, head-beads are white and solvent beads are yellow.

The polymer: a linear self-avoiding chain

Polymers are modeled by flexible linear chains of beads. Because of the soft-core interaction between polymer beads, the polymer is "self-avoiding". For non-bonded pairs, the polymer-polymer interactions are identical to solvent-solvent or polymer-solvent interactions. Taking the same potential depth between the polymer and the solvent as for the polymer-polymer and solvent-solvent interactions ($\epsilon_{PP} = \epsilon_{SS} = \epsilon_{SP}$) should ensure that the polymer is in a good solvent[1]. To verify that the single polymer chains are effectively swollen coils in the pure solvent, I computed their squared radius of gyration

$$R_g^2 = \frac{1}{N} \sum_{i=1}^{N} |\mathbf{r}_i - \mathbf{r}_{CM}|^2 \quad \text{with} \quad \mathbf{r}_{CM} = \frac{1}{N} \sum_{i=1}^{N} \mathbf{r}_i, \qquad (1.3)$$

where $\mathbf{r}_i$ is the position of the bead i in the chain of N beads. I studied the dependance of R_g^2 upon the length N of the chain ($N = 40$ to 400). Fig. 1.8 displays the square of the radii of gyration as a function of N with $\epsilon_{SP} = 1.1\,k_B T$. The fit of the equation $R_g^2 \propto N^{2\nu}$ to the simulation data yields $\nu = 0.57 \pm 0.01$, which is lower than Flory's theoretical prediction for an infinite polymer in good solvent ($\nu = 0.59$) [58], but larger than $1/2$. Therefore, we can consider that the polymer is in a good solvent.

---

[1] Simulations of a single polymer chain in explicit athermal and good solvents have been reported in the literature with similar potentials [142, 47, 143, 48]. Besides, I estimated approximatively the θ-point at $\epsilon_{SP} = 1.0 \pm 0.03\,k_B T$ for $\epsilon_{PP} = \epsilon_{SS} = 1.1\,k_B T$, by computing the structure factor averaged over all directions $S(|k|)$ of chains of $N = 40$ to 400 with $\epsilon_{SP} = 0.7$ to $1.3\,k_B T$, and estimating ν by fitting the data with the equation $S(|k|) \propto |k|^{-1/\nu}$ in the intermediate regime ($R_g^{-1} \leq k \leq \sigma^{-1}$).
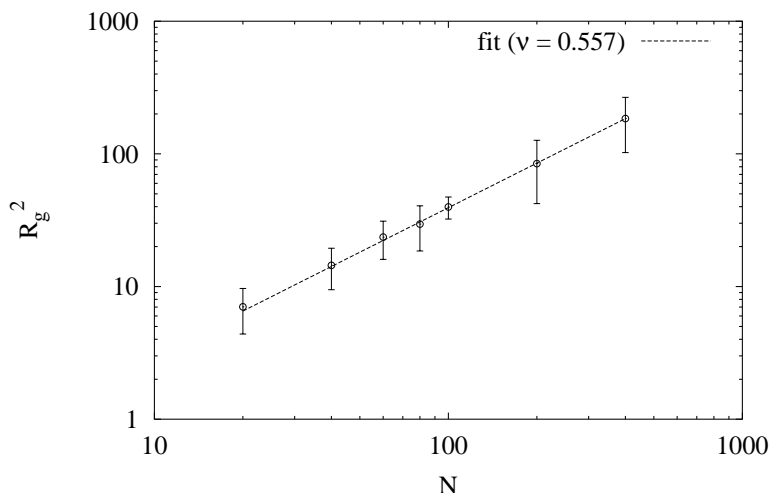
Figure 1.8: Square of the radius of gyration *vs.* chain length in a log-log plot. The single polymer chains were simulated in explicit solvent, with a total number of beads of $32\,000$, in a cubic box in the NPT ensemble at $P = 2.9\,k_B T \cdot \sigma^3$ for $20\,000\,\tau$ ($\rho = 0.85 \pm 0.01\,\text{bead} \cdot \sigma^{-3}$). The interactions between polymer chains were negligible up to $N = 100$. For $N = 200$ and 400, the end-to-end distance of the polymer was only slightly smaller than the dimension of the simulation box.

1.2 Method: numerical simulations

1.2.1 General introduction

This introduction outlines briefly the important concepts of statistical physics and numerical simulations used for this thesis[2]. Here, as in the whole thesis, we deal with a classical system, without relativistic or quantum effects.

Classical statistical mechanics.

Chemical and physical analyses provide a lot of information about the detailed structure of matter at an atomic level. This "atomic" description of matter inspired the model of the lamellar phase of amphiphiles doped with a polymer: the smectic is modeled as an ensemble of particles interacting with each other. A single configuration is defined by hundreds of thousands of variables: the positions and velocities of the particles.

On the other hand, our daily experience demonstrates that in most cases, only a

---

[2] Detailed descriptions are found for example in the books or review articles by Chandler [29], Kubo [98], Goldstein [70], Risken [158], Gardiner [65] (about statistical physics and stochastic), Allen and Tildesley [1], Frenkel and Smit [63], Binder [12, 13], Tuckerman[192], also with Martyna and Berne[193] (about numerical simulations).

handful of parameters is necessary to describe a material on a macroscopic scale. For a lamellar phase of amphiphiles, the composition, the temperature and the pressure may be sufficient to define the state of the system.

Statistical mechanics is the method of choice to study our model because it links these points of view, allowing us to compute macroscopic properties of a huge number of molecules from the interactions between them.

Gibbs introduced the term "statistical mechanics"in 1884 to name a new discipline developed among others by Maxwell and Boltzmann. In 1902, he published a general framework for the statistical description of N identical interacting particles. The theory introduces the notions of a microstate of the system, and a thermodynamical ensemble of microstates. The positions and velocities of the N particles define a microstate - a point $\mathbf{x} = \{\mathbf{r}^N, \mathbf{p}^N\}$ in a $6N$-dimensional space, named the phase-space Ω. Some macroscopic properties (the volume of the particles, their energy, the pressure in the system, the temperature, *etc.*) can be expressed as a function of $\mathbf{x}$. For example, the internal energy $\mathcal{U}$ of N point particles of masses m_i defined by the positions and impulses $\{\mathbf{r}_i, \mathbf{p}_i\}_{i=1,..,N}$, interacting through a potential $\mathcal{V}(\{\mathbf{r}_i\})$ is

$$\mathcal{U}(\{\mathbf{r}_i, \mathbf{p}_i\}) = \mathcal{V}(\{\mathbf{r}_i\}) + \sum_{i=1}^{N} \frac{\mathbf{p}_i^2}{2m_i}.$$

All the microstates leading to the same macroscopic properties (temperature, pressure, *etc.*.) form a so-called thermodynamic ensemble. The ensemble of microstates is characterized by the probability $\rho(\mathbf{x})d\mathbf{x}$ that a microstate is found in the volume of phase space defined by the vectors $\mathbf{x}, \mathbf{x} + d\mathbf{x}$.

Originally, Gibbs treated three ensembles of identical point particles confined in a fixed volume (V). He calculated their probability density function from the second law of thermodynamics.

- (N, V, E): the microcanonical ensemble describing an isolated system with a constant energy E ; then $\rho^{(NVE)}(\mathbf{x}) \propto \delta(\mathcal{U}(\mathbf{x}) - E)$, where $\mathcal{U}(\mathbf{x})$ is the internal energy of the microstate. All microstates with the energy E have the same probability.

- (N, V, T): the canonical ensemble describing a system in contact with a heat bath at a constant temperature T; then $\rho^{(NVT)}(\mathbf{x}) \propto e^{-\beta\mathcal{U}(\mathbf{x})}$, where β is $1/(k_B T)$ and k_B the Boltzmann's constant. The probability of existence depends on the value of the internal energy only.

- (μ, V, T): the grand canonical ensemble describing a system in contact with a heat bath at a constant temperature T and a particle-reservoir at a constant chemical potential μ; then $\rho^{(\mu VT)}(\mathbf{x}) \propto e^{-\beta\mathcal{U}(\mathbf{x})+\beta\mu N}$, where μ is the chemical potential, conjugated variable of the number of particles N.

This approach has been generalized to describe other thermodynamical ensembles. Thermodynamical ensembles describing the smectic phase depend on more than three parameters, for instance the concentrations of each species, the dimensions of the container perpendicular, and parallel to the layers, and the temperature (see Sect. 7).

One fundamental assumption of the calculations of this thesis is the ergodicity hypothesis, stating that the observable $\bar{A}$ measured as a mean value over the time of observation (see Eq. 1.4) equals the ensemble average $\langle A \rangle$ defined by Eq. 1.5.

$$\bar{A} \;\; = \;\; \lim_{\tau \to \infty} \frac{1}{\tau} \int_0^\tau \mathrm{d}t \; A(t), \tag{1.4}$$

$$\langle A \rangle \;\; = \;\; \int_\Omega \mathrm{d}\mathbf{x} \; \rho(\mathbf{x}) \; A(\mathbf{x}). \tag{1.5}$$

One cannot prove that the simulated smectic phase is ergodic. For gas and simple liquids, the ergodicity hypothesis has been generally accepted. For complex fluids, like liquid crystals, the ergodicity is supposed to be true far from the solid states or gel states.

Finally, to predict the observable $\bar{A}$ in a thermodynamic ensemble defined by $\rho(\mathbf{x})$, one computes the ensemble average $\langle A \rangle$ (Eq. 1.5).

The analytical calculation of a high-dimensional integral over the phase space is rarely possible, so one calculates the integral numerically. The algorithm can be summarized as follows:

1. generate an ensemble of n microstates $\{\mathbf{x}_j\}_{j=1,n}$ with a sampling probability $\mathcal{P}(\mathbf{x})$.

2. for each generated microstate, calculate the macroscopic observables $A(\mathbf{x}_j)$.

3. calculate the average

$$\langle A \rangle \simeq \frac{1}{n} \sum_{j=1}^n A(\mathbf{x}_j) \frac{\rho(\mathbf{x_j})}{\mathcal{P}(\mathbf{x_j})}. \tag{1.6}$$

The sampling probability $\mathcal{P}(\mathbf{x})$ is an important variable of the algorithm. A uniform probability is inefficient because the microstates with a significant probability of existence fill a tiny proportion of the phase-space, whose dimension may reach several hundreds of thousands. So importance-sampling (non-uniform $\mathcal{P}$) is necessary. Sampling the phase space directly with the probability distribution of the ensemble of interest is judicious if the energy landscape is quite "smooth". On the contrary, if the energy landscape has several deep minima, a sampling probability different from the equilibrium one may increase the accuracy of the method.

Physicists and chemists use often two classes of sampling methods: Monte Carlo calculations and Molecular Dynamics simulations. These two methods can been interpreted as recipes to construct iteratively a ensemble of microstates in the phase space, with a probability distribution converging towards a chosen probability distribution. The first microstate is taken arbitrarily, in a region where the density of state is not too low. Then, each microstate is deduced from the preceding microstate(s) according to rules which ensure the convergence of the probability density.

In the next sections, I introduce the general ideas underlying molecular dynamics, Langevin dynamics, and Monte Carlo methods. The details and the derivation of the algorithm used for this thesis are given in Sections 1.2.2 and 1.2.3.

Molecular dynamics.

An "intuitive" choice to construct a trajectory in phase-space is to follow the time evolution of the system. The trajectories of N particles interacting through a potential $\mathcal{V}(\mathbf{r}^N)$ are described by Newton's law

$$m_i \frac{\mathrm{d}^2 \mathbf{r}_i}{\mathrm{d}t^2} = \mathbf{f}_i \quad \text{where} \quad i = 1, ..., N \quad \text{and} \quad \mathbf{f}_i = -\nabla_{\mathbf{r}_i} \mathcal{V}(\mathbf{r}^N), \tag{1.7}$$

where m_i the mass of the particle i, $\mathbf{r}_i$ its position and $\mathbf{f}_i$ the force it undergoes. These equations of motion describe a Hamiltonian dynamics. The Hamiltonian $\mathcal{H}$ is a constant of the motion.

$$\mathcal{H}(\{\mathbf{r}^N, \mathbf{p}^N\}) = \mathcal{V}(\{\mathbf{r}^N\}) + \mathcal{K}(\{\mathbf{p}^N\}), \tag{1.8}$$

where $\mathcal{K}(\{\mathbf{p}^N\}) = \sum_{i=1}^N \frac{\mathbf{p}_i^2}{2m_i}$ is the kinetic energy of the system. For an ergodic system, the trajectories determined by Newton's laws sample eventually the microcanonical ensemble (N,V,E).

For many-body systems, Eq. 1.7 has no simple analytical solutions. It is discretized in time to be integrated numerically. The integration scheme should be stable and efficient. For instance, the simple and popular velocity-Verlet algorithm can be derived from the Taylor expansion in time of the coordinates, up to the third power of the time step (noted Δt) [3].

$$\mathbf{v}_i(t + \Delta t/2) \simeq \mathbf{v}_i(t - \Delta t/2) + \frac{\mathbf{f}_i(t)}{m_i} \Delta t, \tag{1.9}$$

$$\mathbf{r}_i(t + \Delta t) \simeq \mathbf{r}_i(t) + \mathbf{v}_i(t + \Delta t/2) \Delta t, \tag{1.10}$$

where i is the particle index. I have used an integration scheme very similar to the velocity-Verlet algorithm (see Sect. 11 for details). As the exact equations of motion conserve the Hamiltonian $\mathcal{H}$, a negligible drift of the internal energy is one of the criteria for a good integrator.

Extensions of molecular dynamics describe other ensembles than the microcanonical one. For example, Andersen published a method to simulate in the isobaric isoenthalpic ensemble (N,P,H) [2]. He defines an extended phase-space, composed of the usual positions and velocities of the particles, plus two new variables: the volume, and its time derivative $\dot{V}$. The Hamiltonian is extended with a potential energy (PV) and a fictitious kinetic energy for the volume $(Q\dot{V}^2/2)$:

$$\mathcal{H}^{ext} = \mathcal{K} + \mathcal{V} + PV + Q\dot{V}^2/2, \tag{1.11}$$

where Q is a fictitious mass. The pressure P is a fixed parameter of the system, whereas the volume varies according to equations of motion derived from the extended Hamiltonian. Similarly to the microcanonical case, the equations of motion for the particles and the volume are deduced from the conservation of the extended Hamiltonian. Admitting that the fictitious kinetic energy of the volume is negligible compared to the kinetic energy of the particles, the enthalpy H $\sim \langle \mathcal{H}^{ext} \rangle$ is a constant of motion, and the ensemble generated is isoenthalpic.

---

[3]for comments and comparison with other integration schemes, see [63, 12].

Langevin dynamics.

Langevin dynamics is a handy solution to simulate a system described by a Hamiltonian $\mathcal{H}$ in the canonical ensemble.

Langevin and Brownian dynamics are inspired by the erratic agitation of pollen floating on water observed by Brown in 1827. Einstein, in 1905, gave a theoretical explanation for the Brownian motion: it is caused by the incessant impacts of the atoms of the liquid on the particles.

Generally, Langevin dynamics is used to describe the "slow" dynamics of a system, forgetting the "fast" dynamics of some degrees of freedom. The main idea is that at sufficiently long time-scales, the motion of the Brownian particles can be described by stochastic differential equations. The effect of the "bath" is then modeled by a friction force proportional to the velocity $\mathbf{v}_i$ of the particle i and a random force $\boldsymbol{\eta}_i$. These forces are added to the deterministic forces deriving from the Hamiltonian (see Eq. 1.12). The velocity Verlet algorithm simulating a Hamiltonian dynamics can be extended to the so-called Euler algorithm, which produces a Langevin dynamics [91]:

$$
\begin{aligned}
\mathbf{v}_i(t + \Delta t/2) &\simeq \mathbf{v}_i(t - \Delta t/2) + [\mathbf{F}_i(t) - \gamma \mathbf{v}_i(t - \Delta t/2) + \boldsymbol{\eta}_i(t)] \frac{\Delta t}{m_i}, &(1.12) \\
\mathbf{r}_i(t + \Delta t) &\simeq \mathbf{r}_i(t) + \mathbf{v}_i(t + \Delta t/2) \Delta t, &(1.13)
\end{aligned}
$$

where i is the particle index. The noises on the several degrees of freedom are uncorrelated. The implicit fast degrees of freedom exchange energy with the slow degrees of freedom. To ensure that the probability distribution of microstates generated by this dynamics converges towards the canonical probability distribution with the expected temperature T, the intensity of the noises and the friction coefficient are linked through

$$
\langle \eta_i^\alpha(t) \rangle_t = 0, \tag{1.14}
$$

$$
\langle \eta_i^\alpha(t).\eta_j^\beta(t + \tau) \rangle_t = 2 k_B T \gamma \; \delta(\tau) \delta_{ij} \; \delta_{\alpha\beta}, \tag{1.15}
$$

where i and j denote the particle indices, α and β the directions of space. The notation $\langle \cdot \rangle_t$ denotes a time average[4].

Other methods are available to simulate in the canonical ensemble [1, 63]. One advantage of Langevin dynamics is the simplicity of its implementation, and its stability even for large time steps (0.01τ). One disadvantage is that it is not time-reversible.

Monte Carlo method.

Extensive use of random numbers inspired the name Monte Carlo for a technique to calculate high-dimensional integrals. The method is attractive because the convergence of the integration does not depend on the dimension of the integral; moreover, it allows to invent almost any Markov process in the phase-space, disregarding the time-evolution of the system.

---

[4]We use the notations of a continuous time evolution here, but of course the time is still discretized, and the average over the time is a sum. The delta function for the time interval τ, $\delta(\tau)$, is a simplified notation for the Kronecker symbol $\delta_{0n}/(\Delta t)$ where n is the integer $\tau/(\Delta t)$.

The algorithm iteratively constructs a Markov chain in phase space[5]. One step of the random walk is composed of two stages. First, the trial move: the new state $\mathbf{x}_j$ is constructed with the probability $\alpha(i \to j)$ from the preceding old state $\mathbf{x}_i$. The trial moves must permit to visit eventually any state from any other state of the phase space to guaranty the ergodicity. Second, the trial move is accepted with an acceptance probability noted $acc(i \to j)$. The transition probability to displace the initial state $\mathbf{x}_i$ towards the new state $\mathbf{x}_j$, noted $\pi(i \to j)$, is the product of the probability of the independent stages (Eq. 1.16). The probability to remain at the same place is the probability that no move is successful (see Eq. 1.17).

$$\text{if } i \neq j, \quad \pi(i \to j) = \alpha(i \to j) \; acc(i \to j), \tag{1.16}$$
$$\text{else} \quad \pi(i \to i) = 1 - \sum_{j \neq i} \pi(i \to j). \tag{1.17}$$

The transition probabilities π have to be constructed such that the equilibrium probability distribution $\mathcal{P}(\mathbf{x})$ is a steady state of the dynamics: at equilibrium, the number of states leaving any particular state $\mathbf{x}_i$ equals the number of states arriving at $\mathbf{x}_i$ from all other states in the system

$$\forall i, \quad \sum_j \mathcal{P}(\mathbf{x}_i)\pi(i \to j) = \sum_j \mathcal{P}(\mathbf{x}_j)\pi(j \to i). \tag{1.18}$$

where i and j are state indices. Several transition probabilities fulfilling Eq. 1.18 can be invented. Similarly, several couples of trial and acceptance probabilities are valid. Writing a Monte Carlo algorithm becomes more straightforward if one imposes the so-called detailed-balance. This condition, stronger than the general balance (Eq. 1.18), imposes each net current between any pair of states to vanish:

$$\forall \{i, j\}, \quad \mathcal{P}(\mathbf{x}_i)\pi(i \to j) = \mathcal{P}(\mathbf{x}_j)\pi(j \to i). \tag{1.19}$$

Metropolis proposed a general solution fulfilling detailed-balance: a symmetric "trial-move" probability (Eq. 1.20), associated with the acceptance probability given by Eq. 1.21.

$$\alpha(i \to j) = \alpha(j \to i), \tag{1.20}$$
$$acc(i \to j) = \max\left\{1, \frac{\mathcal{P}(\mathbf{x}_j)}{\mathcal{P}(\mathbf{x}_i)}\right\}. \tag{1.21}$$

1.2.2 Simulation of smectics

The properties of an infinite system do not depend on the thermodynamic ensemble in which they are studied. Yet, in numerical simulations the number of molecules is limited, so that the choice of the thermodynamic ensemble and boundary conditions influences the efficiency and the results of the simulations. In the present section, I emphasize some particularities of the simulations of smectic phases.

---

[5] Actually when Monte Carlo calculations are used to generate the canonical ensemble, the velocities and positions are considered as independent variables. The dependancies of the density distribution on the velocities and on the positions can be separated. The Monte Carlo method is used to construct a Markov chain in the space of the positions. The distribution of the velocities is supposed to equal Boltzmann's distribution.

Shape of the simulation box, orientation of the layers

To study the bulk properties of a system with simulations in a finite box, one usually uses periodic boundary conditions[6]. The symmetry operations of the simulation box are then imposed to the system. To avoid artifacts, one chooses a symmetry group for the simulation box included in the symmetry group of the simulated system. Of course, for simple liquids, whose symmetry group contains all symmetry operations, there are no limitations. For crystals or liquid crystals, the possibilities are reduced.

The smectic A is invariant with respect to translations $\mathbf{t}$ along the director, with $\mathbf{t} = id\mathbf{n}$ where the d is the interlamellar distance, i an integer and $\mathbf{n}$ the director of the smectic. It is also invariant with respect to all rotations and translations in a plane perpendicular to the director (space group $T(2) \times D_{\infty h}$). The simulation box used in this thesis is an orthorhombic simulation box. It fits the symmetry of smectic A phases: z-axis of the box aligned with the director, and the x- and y-directions are in the plane of the layers (see 1.9). To include the box translation $\mathbf{L}_z$ in the symmetry group of the
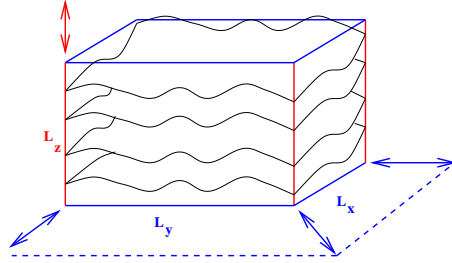
Figure 1.9: Choice of the box geometry relative to the smectic phase.

smectic, the box dimension L_z must be a multiple of d. If this condition is not fulfilled, the lamellar phase undergoes stress. To release the constraint, it may adopt a geometry different from the one depicted in Fig 1.9. As an illustration, Fig. 1.10 shows snapshots of the equilibration of a lamellar phase set up by hand in a simulation box with the correct symmetry, but an arbitrary interlamellar distance. The initial configuration is composed of four bilayers of tetramers $h_2 t_2$ without solvent, on a cubic lattice with a density of 0.85 beads per unit volume. The director is along the z-axis. The normal pressure is then $-0.16\,k_B T{\cdot}\sigma^{-3}$, and the tangential pressure $6.62\,k_B T{\cdot}\sigma^{-3}$ ($\epsilon = 1.1\,k_B T$). During the equilibration, the constraint of the fixed box triggers defects and undulations which destroy the lamellar phase. After more than $10\,000\,\tau$, the number of defects has decreased, but the director is no longer along the box axis. The onset of undulations due

---

[6] The simulated system is a part of an infinite periodic system, including the N beads of the simulation box at the position $\mathbf{r}_i$, plus their copies, with identical velocities, at the positions $\mathbf{r}_i + n_x \mathbf{L}_x + n_y \mathbf{L}_y + n_z \mathbf{L}_z$ (n_x, n_y, n_z are integers and $\mathbf{L}_x, \mathbf{L}_y, \mathbf{L}_z$ the vectors defining the simulation box and the periodicity of the system). The number of beads of the system is constant even if the beads may cross the limit of the simulation box: when a bead leaves the simulation box, a copy of it enters it on the other side of the simulation box, with an identical velocity. The interactions between the particles in the simulation box and their copies are taken into account in the algorithm.
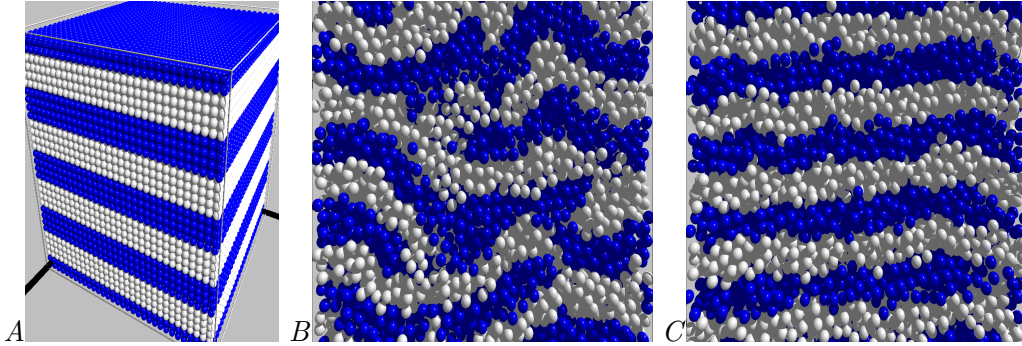
Figure 1.10: Equilibration in a fixed simulation box. *A*: Initial configuration (see text for explanations) *B* and *C*: Time evolution of lamellae of h_2t_2 amphiphilic tetramers, in the canonical ensemble at time 350 and $12\,050\,\tau$.

to a small compression or extension of the lamellar phase in the direction of the smectic was studied by Soddeman *et al.* [182, 181, 75]. If the simulation box is large enough, the lamellar phase almost always finds an orientation fitting in an arbitrary orthorhombic box [182][7].

Constraints on the simulation box

When solids are simulated, there are less choices for the simulation box symmetry. Allotropic varieties whose symmetry is incompatible with the symmetry of the simulation box are destabilized. To avoid such artifacts, Parrinello and Rahman proposed a method to simulate solids in a *fully flexible* simulation box [137, 138]. Depending on the stress tensor of the system, both the dimensions and the shape of the box are modified. The stress is minimized and the box symmetry fits to the symmetry of the crystalline phase during the calculations. No constraints are imposed on the simulation box. In a liquid, the compressibility modulus is low, and the stress tensor is subject to large fluctuations when particles diffuse through the boundaries [4]. If one uses Parrinello and Rahman's method, it may be difficult to stabilize the fluctuating box. Usually, simple liquids are simulated in a *fixed* simulation box.

For the case of the smectic A, the semi-crystalline positional ordering in the direction of the director results in a high compressibility modulus. One can therefore let L_z vary according to the method proposed by Parrinello and Rahman. But in the direction perpendicular to the director, the smectic behaves like a liquid, and the box must be stabilized. In this thesis, the dimensions parallel to the lamellae, L_x and L_y, vary, but the ratio $L_x/L_y = \alpha$ is kept constant.

---

[7] Given the box dimensions $L_{x,y,z}$ and the interlamellar distance d, if one can find three integers m_x, m_y, m_z fulfilling $d^2 = m_x^2/L_x^2 + m_y^2/L_y^2 + m_z^2/L_z^2$, then a solution for the director exist: $n_\alpha = (d/L_\alpha)m_\alpha$, where α denotes the directions x, y, z [182]. The number of solutions increases with the size of the simulation box.

Fig. 1.11 illustrate the advantages of fluctuating boundaries with snapshots of the equilibration of a configuation with the same initial conditions as in Fig. 1.10, but with a flexible simulation box (with $L_x/L_y = \alpha$ kept constant). In this algorithm, the box
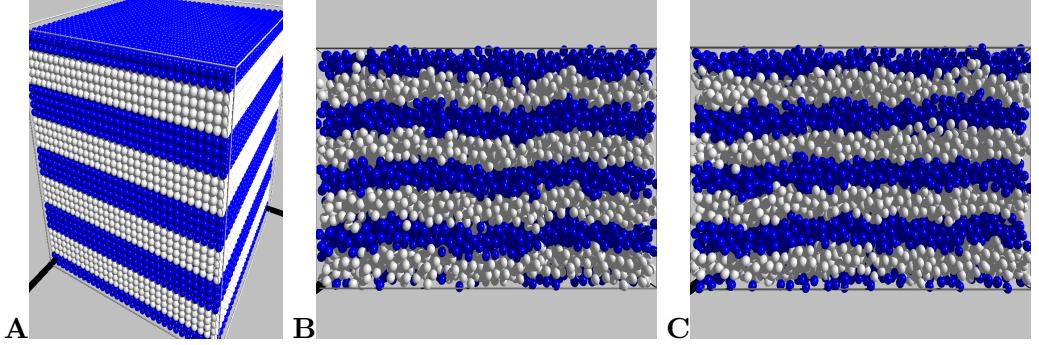
Figure 1.11: Equilibration in a flexible simulation box. **A**: same initial configuration as in Fig. 1.10. **B** and **C**: Time evolution of lamellae of A2B2 amphiphiles, in the canonical ensemble (fixed volume and temperature), with a flexible box and an isotropic average pressure tensor, at time $350\,\tau$ and $1\,850\tau$ of simulation. The configuration stays stable for later times.

dimensions are modified at each time step. The variations of the box dimensions depend on the pressure in the system (for more details see Sect. 1.2.3). During the whole simulation, the director remains aligned in the initial direction (with small direction fluctuations), while the box dimensions adjust to the equilibrium interlamellar spacing. The orientation of the director is not constrained, but the fluctuating boundaries enable the system to equilibrate easily and to circumvent the high energy barrier of a reorientation of the lamellae.

The comparison between the two simulations (Fig. 1.11 and Fig. 1.10) shows that a flexible simulation box has two advantages: first the equilibration is rapid; second, the orientation of the bilayers is stabilized. Moreover, the interlamellar distance does not have to be known before the simulations. For these reasons, I have chosen to simulate in a flexible simulation box - despite the higher computational cost.

In the following, the director of the lamellar phase is assumed to point along the z-axis.

Pressure tensor in smectic A

In this section, I define the pressure P as the themodynamical variable conjugated of the volume, and give a microscopic expression $\mathcal{P}$ of the pressure tensor. To simplify the notation, in this section, the system is supposed to be composed of N identical particles defined by their positions $\mathbf{r}_i$ and impulses $\mathbf{p}_i$, interacting through the potential $\mathcal{V}(\mathbf{r})$. The generalization to a system with several kind of particles is straightforward. The potential is written as a sum of radial pair potential $\mathcal{V}(\mathbf{r}^N) = \sum_{i \neq j} \mathcal{V}_{ij}(r_{ij})$ with the interparticle distance $r_{ij} = |\mathbf{r}_i - \mathbf{r}_j|$.

The partition function of the system in the canonical ensemble is

$$Z(N,V,T) = e^{-\beta F(N,V,T)} = \frac{1}{\Lambda^{3N} N!} \int d\mathbf{r}^N e^{-\beta \mathcal{V}(\mathbf{r}^N)}, \tag{1.22}$$

where $\Lambda = h/\sqrt{2\pi m k_B T}$ is de Broglie's wavelength and h, Planck's constant.

The pressure is defined as the derivative of the free energy of the system with respect to the volume:

$$P = -\left(\frac{\partial F}{\partial V}\right)_{T,N}. \tag{1.23}$$

The pressure P can be rewritten as the derivative of the partition function with respect to the volume V

$$P = \frac{1}{\beta Z}\left(\frac{\partial Z}{\partial V}\right)_{T,N}. \tag{1.24}$$

To give a microscopic expression of the pressure, one must specify how the change of volume affects the positions of the particles. One considers usually that the coordinates are subjected to a homogenous re-scaling: when the volume increases by dV, all coordinates of the particles are multiplied with $1 + dV/V$. In other words, the derivative of Z with respect to the volume is done with the expression

$$Z(N,V,T) = e^{-\beta F(N,V,T)} = \frac{V^{3N}}{\Lambda^{3N} N!} \int d\mathbf{s}^N e^{-\beta \mathcal{V}(V^{1/3}\mathbf{s}^N)}, \tag{1.25}$$

where the relative positions $\mathbf{s}_i = \mathbf{r}_i V^{-1/3}$ are kept constant during the volume expansion. The derivation leads then to the usual microscopic expression of the pressure

$$\mathcal{P} = \frac{N k_B T}{V} + \frac{1}{3V} \sum_{i=1}^{N} \mathbf{r}_i \cdot \mathbf{f}_i, \tag{1.26}$$

where f_i is the force on the particle i

$$\mathbf{f}_i = -\sum_{j \neq i} \left(\frac{\partial \mathcal{V}_{ij}}{\partial r}\right) \frac{\mathbf{r}_{ij}}{r_{ij}}. \tag{1.27}$$

The vector $\mathbf{r}_{ij}$ is $\mathbf{r}_i - \mathbf{r}_j$ and r_{ij} is its norm. In molecular dynamics simulation, the pressure P is computed as a ensemble average of the instantaneous pressure $\mathcal{P}$:

$$P = \langle \mathcal{P} \rangle. \tag{1.28}$$

In the case of an anisotropic system, like the lamellar phase, it is informative to separate the deformations of the volume between dilatations parallel to the plane of the bilayers and those perpendicular to it. For example, the derivative relative to the volume can be done with a re-scaling of the z-coordinates only, keeping the x and y coordinates constant during the volume expansion.

$$P_{\alpha\alpha} = \frac{L_\alpha}{V}\left(\frac{\partial F}{\partial L_\alpha}\right)_{N,T,L_\beta}, \tag{1.29}$$

where α denotes a direction of space and β the dimensions of space different from α. One defines then the pressures normal and tangential to the bilayers:

$$P_n = P_{zz} \text{ and } P_t = \frac{P_{xx} + P_{yy}}{2}. \tag{1.30}$$

To calculate the microscopic expression of $P_{\alpha\alpha}$, the coordinates of the particles are re-scaled in the three directions of space separately. The derivation of the partition function is then done after the change of variables

$$r_i^\alpha = L_\alpha s_i^\alpha,$$

where α denotes the directions x, y, z. The result is

$$\mathcal{P}_{\alpha\alpha} = \frac{L_\alpha}{V}\left(\frac{\partial F}{\partial L_\alpha}\right)_{N,T,L_\beta} = \frac{Nk_BT}{V} + \frac{1}{V}\sum_{i=1}^{N} r_i^\alpha \; f_i^\alpha, \tag{1.31}$$

where α denotes a direction of space and β the dimensions of space different from α. For an isotropic system, the three components of the pressure equal. For an anisotropic system under stress, they may differ. In the case of the lamellar phase, x- and y-directions are equivalent, so that the x and y component equal at equilibrium ($P_{xx} = P_{yy}$).

The microscopic expression of the pressure can alternatively be derived from a mechanical definition: the force per unit area acting on the surface of a system with surfaces normal to the directions x, y, z. The microscopic expression of the pressure tensor is then deduced from the virial theorem [1] and reads

$$\mathcal{P}^{\alpha\beta}V = \sum_{i=1}^{N}\left\langle m_i v_i^\alpha v_i^\beta \delta_{\alpha\beta} + r_i^\alpha f_i^\beta \right\rangle, \tag{1.32}$$

where the upper-scripts α and β denote the direction of space x, y, z. The index α refers to the normal axis of the surface on which the force acts, and β denotes the direction of the force itself. The diagonal components correspond to the forces "trying to"change the dimensions of the system. The off-diagonal elements correspond to forces "trying to"change the shape of the system. In the fluid lamellar phase, there is not shear rigidity, so the non-diagonal components of the pressure tensor vanish in thermal equilibrium. The average pressure tensor has the form

$$P = \begin{pmatrix} P_t & 0 & 0 \\ 0 & P_t & 0 \\ 0 & 0 & P_n \end{pmatrix} \tag{1.33}$$

If there is no external stress imposed to the system, $P_n = P_t$.

Microscopic expression for the surface tension

A microscopic expression of the surface tension can be derived following the same steps as for the pressure.

The free energy F of the system is written as a function of the number of particles N, the temperature T, the volume V and the projected area of the bilayers A (see Fig. 1.9). The surface tension is defined as the derivative of the free energy relative to the area, at fixed temperature, pressure, volume, and number of particles:

$$\gamma = \left(\frac{\partial F}{\partial A}\right)_{T,V,N} = -\frac{1}{\beta Z}\left(\frac{\partial Z}{\partial A}\right)_{T,V,N}. \tag{1.34}$$

To calculate a microscopic expression of γ, one must find a deformation of the system which changes the area $A = L_x L_y$, and conserves the volume $V = L_x L_y L_z$. The solution proposed by Buff [25] is to re-scale the particle coordinates according to

$$x_i = \sqrt{A}s_{ix} \; ; \; y_i = \sqrt{A}s_{iy} \; ; \; z_i = s_{iz}/A. \tag{1.35}$$

and to keep the rescaled variables $\mathbf{s}_i$ constant during the derivation of the partition function Z relative to A. The derivation yields the following microscopic expression of the surface tension:

$$\gamma = L_z(\mathcal{P}_n - \mathcal{P}_t), \tag{1.36}$$

where $\mathcal{P}_n$ and $\mathcal{P}_t$ are the instantaneous pressure components normal and tangential to the layers (see Eqs. 1.31 and 1.30).

The re-scaling proposed here is intrinsically linked to the symmetry of the lamellar phase. For other symmetries, for example when there are curved interfaces in the system, Eq. 1.36 is not valid [7].

Ensemble of simulation

In the microcanonical ensemble, a smectic phase containing solvent and amphiphilic molecules is described by five intensive variables: the internal energy, the number N_s of solvent molecules, the number N_a of amphiphilic molecules, the projected area A of the layers, and the dimension L_z of the simulation box along the director.

I decided to simulate in an isothermal ensemble with constant number of particles, and with no surface tension. This choice is motivated by the hope that this ensemble should reproduce the bulk properties of a small patch among a lamellar domain, as sketched in Fig. 1.12[8].

If we conserve the number of molecules of solvent and amphiphiles (constant -N_s, N_a), and control the temperature (constant-T), several ensembles are possible. I have listed in Table 1.2 the possible thermodynamical ensembles with a flexible simulation box, separating the fixed parameters and their fluctuating conjugated variables.

To compute the surface tension of the whole system, one uses the expressions given in the fourth column of Table 1.2. The ensembles (3) and (4) permit to impose a zero surface tension on the system. Using the ensembles (1) and (2), one must first find a set

---

[8] As it is difficult to measure the surface tension of amphiphilic bilayers or lamellar phase, it is also difficult to know which surface tension really corresponds to a given experimental setup. Several arguments have been published on the correct surface tension to impose in simulations [53, 3, 85, 108, 54].
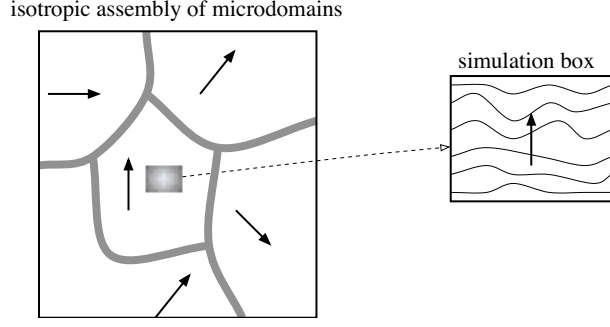
Figure 1.12: Sketch of a lamellar phase composed of microdomains, and of the simulation box extracted among one of those domains. The arrows represent the directors of the different domains.

ensemble	fixed parameters	fluctuating variable	γ
(1)	A, P_n	$L_z, \mathcal{P}_{xx}, \mathcal{P}_{yy}$	$\langle L_z[P_n - \mathcal{P}_{xx} + \mathcal{P}_{yy}/2]\rangle$
(2)	P_t, L_z	$A, \mathcal{P}_{zz}$	$\langle L_z[\mathcal{P}_{zz} - P_t]\rangle$
(3)	$V, P_n - P_t$	L_z, A	$\langle L_z\rangle(P_n - P_t)$
(4)	P_n, P_t	L_z, A	$\langle L_z\rangle(P_n - P_t)$

Table 1.2: Several thermodynamical ensembles of simulation for the smectic phase; the thermodynamic variables are fixed (at least on average), and their conjugates are fluctuating. In any case, the temperature and the numbers of particles are fixed.

of parameters leading to a zero surface tension, which implies more calculation time. As the smectic-isotropic transition is a first-order transition, the use of a constant-volume ensemble may keep the system at a density where it would like to phase separate into two bulk phases of different densities, but is prevented of doing so by finite size effects, therefore I eliminate the ensemble (3). To conclude, I have chosen the ensemble (4): the $(N, P_n, T, \gamma = 0)$ ensemble which permits to control the surface tension, and which is compatible with the constraints imposed on the shape of the simulation box.

The debate about which ensemble should be used to simulate single bilayer began about one decade ago and seems to be still open [31, 53, 209, 191, 85, 54, 114]. Merz remarked about it in 1997[119]: "although this debate has garnered much attention in the past year (97), it is still unclear whether it is an issue of major practical importance [...]. At this time, it appears that either the (N, P, T) or the (N, P_n, T, γ) ensemble is suitable for simulation bilayers".

1.2.3 $(N, P, T, \gamma = 0)$ algorithm

The algorithm used in this thesis was adapted from the "Langevin piston method" proposed by Kolb *et al.* [91] and Feller *et al.* [209] to simulate a fluid in the isobaric isothermal ensemble (constant-NPT) [91, 209]. I modified the algorithm to simulate the lamellar

phase in the isobaric isothermal ensemble imposing a zero surface tension $(NPT, \gamma = 0)$ with a fixed ratio L_x/L_y.

As in Section 1.2.2, the instantaneous pressure tensor is noted $\mathcal{P}_{\alpha\beta}$, and computed with Eq. 1.32. The pressures components that are parameters of the Hamiltonian are noted $P_{\alpha\beta}$.

In the following chapter, the algorithm generating the isobaric isoenthalpic ensemble with no surface tension are derived according to an extended Hamiltonian dynamics. Then, enthalpy fluctuations are incorporated into the equation of motions, in order to derive an algorithm describing the (N, P_n, T, γ) ensemble.

Rescaled variables

Parrinello and Rahman have written a general algorithm which does not constrain the simulation box at all [136]. The geometry of the simulation box is described by the matrix $\hat{h}$, containing the vectors defining the box. Their notations include nine new parameters[9]. For an orthorhombic simulation box, the matrix $\hat{h}$ is diagonal:

$$\hat{h} = \begin{pmatrix} L_x & 0 & 0 \\ 0 & L_y & 0 \\ 0 & 0 & L_z \end{pmatrix}. \tag{1.37}$$

I use their matrix notations even though the matrices are often diagonal to recall that the pressure is a tensor which may be not diagonal if the system is not equilibrated. Following the derivation of [136], the positions and momenta of the particles, $\mathbf{r}_i$ and $\mathbf{p}_i$ are rescaled with the dimensions of the box into dimensionless coordinates $\mathbf{s}_i$ and $\dot{s}_{i\alpha}$:

$$\forall i : \mathbf{r}_i = \hat{h}\mathbf{s}_i \quad \Leftrightarrow \quad \forall i, \forall \alpha : s_{i\alpha} = \frac{r_{i\alpha}}{L_\alpha}, \tag{1.38}$$

$$\forall i : \mathbf{v}_i = \hat{h}\dot{\mathbf{s}}_i + \dot{\hat{h}}\mathbf{s}_i \quad ; \quad \forall i, \forall i\alpha : \dot{s}_{i\alpha} = \frac{v_{i\alpha}}{L_\alpha} + s_{i\alpha}\frac{\dot{L}_\alpha}{L_\alpha}, \tag{1.39}$$

where the subscript i labels the particle and the subscript α labels the directions x, y, z.

Extended Lagrangian and Hamiltonian

The kinetic and potential energies of the box are appended to the microcanonical Lagrangian.

$$\mathcal{L}(\mathbf{s}_i, \dot{\mathbf{s}}_i, \hat{h}, \dot{h}) = \left\{ \mathcal{K}^{part}(\dot{\mathbf{s}}_i, \hat{h}) - \mathcal{V}^{part}(\mathbf{s}_i, \hat{h}) \right\} + \left\{ \mathcal{K}^{box}(\hat{h}, \dot{h}) - \mathcal{V}^{box}(\hat{h}) \right\}. \tag{1.40}$$

---

[9]To let the box fluctuate in shape and size but to avoid including the degrees of freedom for free rotation, Souza et al. [184] restricted the number of box parameters to six: the six scalar products between the vectors defining the box

with the following energies for the particles[10] :

$$\mathcal{K}^{part}(\dot{\mathbf{s}}_i, \hat{h}) = \sum_i \frac{m_i}{2} \left(\dot{\mathbf{s}}'_i \ \hat{h}'\hat{h} \ \dot{\mathbf{s}}_i \right) \quad and \quad \mathcal{V}^{part}(\vec{s}_i, \hat{h}) = \sum_{i,j>i} v_{ij}(|r_{ij}|). \tag{1.41}$$

The potential energy of the box determines the thermodynamic ensemble of the simulations. For an isobaric ensemble, the potential energy is the product of the pressure with the volume. The surface energy is proportional to the surface tension γ.

$$\mathcal{V}^{box}(\hat{h}) = P \prod_\alpha L_\alpha + \gamma L_x L_y. \tag{1.42}$$

As I have chosen to impose no surface tension, this last term vanishes.

The kinetic energy of the box has no influence on the equilibrium state as long as it is negligible compared to the kinetic energy of the system of particles. Yet, it influences the dynamics of the box and, indirectly, the dynamics of the whole system [156, 157]. Parrinello and Rahman expressed the kinetic energy of the walls $\mathcal{K}^{box}(\hat{h}, \dot{\hat{h}})$ is as if they had the mass Q [136][11] .The mass Q has no direct physical meaning, but it defines the time-scale of the fluctuations of the box dimensions.

$$\mathcal{K}^{box}(\hat{h}, \dot{\hat{h}}) = \frac{Q}{2} \sum_{\alpha \in \{x,y,z\}} \dot{L}_\alpha^2 \tag{1.45}$$

I modified the original formula given by Parrinello and Rahman, to consider the constraint on the ratio L_x/L_y. In this case, only two additional variables L_y and L_z are necessary:

$$\mathcal{K}^{box}(\hat{h}, \dot{\hat{h}}) = \frac{Q}{2} \left(2\dot{L}_y^2 + \dot{L}_z^2 \right). \tag{1.46}$$

The extended Lagrangian $\mathcal{L}(\dot{\mathbf{s}}_i, \mathbf{s}_i, \dot{L}_y, \dot{L}_z, L_y, L_z)$ is then

$$\mathcal{L} = \left\{ \sum_{i,\alpha} \frac{L_\alpha^2}{2} m_i \dot{s_{i\alpha}}^2 - \sum_{i,j>i} v_{ij}(|r_{ij}|) \right\} + \left\{ \frac{Q}{2} \left(2\dot{L}_y^2 + \dot{L}_z^2 \right) - P \prod_\alpha L_\alpha \right\}. \tag{1.47}$$

---

[10]The coupling term between $\dot{L}_\alpha$ and $s_{i\alpha}$ disappeared in the expression of the kinetic energy of the particles $\mathcal{K}^{part}$ (Eq.1.41). This Lagrangian does not yield Newton's equations of motion, but the trajectories permit to calculate averages corresponding to the isothermal-isobaric ensemble [2].

[11]Andersen proposed another expression of kinetic energy:

$$\mathcal{K}^{box}(\dot{\mathbf{s}}_i, \hat{h}) = \frac{Q}{2} \dot{V}^2 = \frac{QV^2}{2} \left(\sum_\alpha \dot{L}_\alpha/L_\alpha \right)^2. \tag{1.43}$$

This expression couples the dimension of the box and their derivatives in the kinetic energy, so no simple simplectic algorithm can be found. Ray [156, 157] proposed another way of writing it which respects the virial theorem and equals the form proposed by Andersen if the simulation box is cubic:

$$\mathcal{K}^{box}(\dot{\mathbf{s}}_i, \hat{h}) = \frac{Q}{2} \sum_\alpha \dot{L}_\alpha^2 L_\alpha^4. \tag{1.44}$$

The momenta coupled to the positions and to the box length are defined as usual for Hamiltonian dynamics:

$$\pi_{i\alpha} \;\doteq\; \frac{\partial \mathcal{L}}{\partial \dot{\mathbf{s}}_{i\alpha}} \;\Rightarrow\; \forall i, \forall \alpha : \pi_{i\alpha} = L_\alpha^2 m_i \dot{s}_{i\alpha}, \tag{1.48}$$

$$\Pi_\alpha \;\doteq\; \frac{\partial \mathcal{L}}{\partial \dot{L}_\alpha} \;\Rightarrow\; \Pi_z = Q\dot{L}_z; \Pi_y = 2Q\dot{L}_y. \tag{1.49}$$

The extended Hamiltonian $\mathcal{H}(\pi_i, \mathbf{s}_i, L_\alpha, \Pi_\alpha)$ reads

$$\mathcal{H} \;\doteq\; -\mathcal{L} + \sum_i \mathbf{s}_i.\pi_i + L_z\Pi_z + L_y\Pi_y, \tag{1.50}$$

$$= \sum_{i,\alpha} \frac{1}{2m_i} \frac{\pi_{i\alpha}^2}{L_\alpha^2} + \sum_{i,j>i} v_{ij}(|r_{ij}|) + \frac{1}{2Q}\left(\frac{\Pi_y^2}{2} + \Pi_z^2\right) + P\prod_\alpha L_\alpha. \tag{1.51}$$

The Hamiltonian of the system is a constant of motion and determines the ensemble of simulation.

Constant-(N, P, H, γ) algorithm

The algorithm is justified by Liouville's equation [63], describing the time evolution of the probability density function $\rho(\mathbf{x}, t)$:

$$\frac{d\rho(\mathbf{x}, t)}{dt} = i\hat{L}\rho(\mathbf{x}, t), \tag{1.52}$$

where $\hat{L}$ is the Liouville operator, and $\rho(\mathbf{x}, t)$ the probability density function. In the case of molecular dynamics, the probability density is a delta function in phase space: $\rho(\mathbf{x}, t) = \delta(\mathbf{x} - \mathbf{X}(t))$, where $X(t)$ define the trajectory in phase space. The Liouville operator $\hat{L}$ depends on the Hamiltonian according to

$$i\hat{L} = -\sum_{i\alpha} \left\{ \frac{\partial \mathcal{H}}{\partial \pi_{i\alpha}} \frac{\partial}{\partial \mathbf{s}_{i\alpha}} - \frac{\partial \mathcal{H}}{\partial \mathbf{s}_\alpha} i \frac{\partial}{\partial \pi_{i\alpha}} \right\} - \sum_{\alpha \in \{z,y\}} \left\{ \frac{\partial \mathcal{H}}{\partial \Pi_\alpha} \frac{\partial}{\partial L_\alpha} - \frac{\partial \mathcal{H}}{\partial L_\alpha} \frac{\partial}{\partial \Pi_\alpha} \right\}. \tag{1.53}$$

The Liouville equation (Eq. 1.52) cannot be integrated in a simple analytical form, because the Liouville operator depends implicitly on the time, *via* the velocities and forces. For this reason, the integration up to the time t is done iteratively, in N_s steps, calculating and applying the Liouville operator N_s times. The time evolution of the position $\mathbf{X}(t)$ in phase space is written as

$$\mathbf{X}(t) \approx \left[\prod_{m=1}^{N_s} e^{i\hat{L}_m \Delta t}\right] \mathbf{X}(0) \;\; \text{with} \;\; \Delta t \to 0, \tag{1.54}$$

where $\Delta t = t/N_s$ is the time-step of the integration. According to Trotter's theorem, the energy error is of the order of $(\Delta t)^2$ and does not diverge when the total time increases

[63]. For each time step, the action of the Liouville operator is separated into four components ($\hat{L}_1$ to $\hat{L}_4$) corresponding to the separated actions on the positions ($\hat{L}_1$), the particle momenta ($\hat{L}_4$), the box dimension ($\hat{L}_2$) and box momenta ($\hat{L}_3$).

For the particles position and momenta, the evolution operator reads

$$i\hat{L}^{part} = \overbrace{-\sum_{i,\alpha} \dot{s}_{i\alpha} \frac{\partial}{\partial s_{i\alpha}}}^{\hat{L}_1} + \overbrace{\sum_{i,\alpha} \dot{\pi}_{i\alpha} \frac{\partial}{\partial \pi_{i\alpha}}}^{\hat{L}_4}, \tag{1.55}$$

where the time derivative are deduced from the the Hamiltonian: for all i and for all α,

$$\dot{s}_{i\alpha} = \frac{\partial \mathcal{H}}{\partial \pi_{i\alpha}} \quad \Rightarrow \quad \dot{s}_{i\alpha} = \frac{\pi_{i\alpha}}{L_\alpha^2 m_i}, \tag{1.56}$$

$$\dot{\pi}_{i\alpha} = -\frac{\partial \mathcal{H}}{\partial s_{i\alpha}} \quad \Rightarrow \quad \dot{s}_{i\alpha} = L_\alpha \sum_{j \neq i} f_{ij}^\alpha. \tag{1.57}$$

Similarly, for the box variables, the evolution operator reads

$$i\hat{L}^{box} = \overbrace{-\dot{L}_z \frac{\partial}{\partial L_z} - \dot{L}_y \frac{\partial}{\partial L_y}}^{\hat{L}_2} + \overbrace{\dot{\Pi}_z \frac{\partial}{\partial \Pi_z} + \dot{\Pi}_y \frac{\partial}{\partial \Pi_y}}^{\hat{L}_3}, \tag{1.58}$$

where the time derivative are deduced from the Hamiltonian:

$$\dot{L}_z = \frac{\partial \mathcal{H}}{\partial \Pi_z} \quad \Rightarrow \quad \dot{L}_z = \frac{\Pi_z}{Q}, \tag{1.59}$$

$$\dot{\Pi}_z = -\frac{\partial \mathcal{H}}{\partial L_z} \quad \Rightarrow \quad \dot{\Pi}_z = \frac{V}{L_z} \left[\mathcal{P}_{zz} - P\right], \tag{1.60}$$

and

$$\dot{L}_y = \frac{\partial \mathcal{H}}{\partial \Pi_y} \quad \Rightarrow \quad \dot{L}_y = \frac{\Pi_y}{2Q}, \tag{1.61}$$

$$\dot{\Pi}_y = -\frac{\partial \mathcal{H}}{\partial L_y} \quad \Rightarrow \quad \dot{\Pi}_y = 2\frac{V}{L_y} \left[\frac{1}{2}\left(\mathcal{P}_{yy} + \mathcal{P}_{xx}\right) - P\right]. \tag{1.62}$$

Time reversibility is an important criterion for the stability of the algorithm. At this point, in order to guarantee the time reversibility of the algorithm, each time step is decomposed according to[12]

$$e^{i\hat{L}\Delta t} = e^{i\hat{L}_4\Delta t/2} \, e^{i\hat{L}_3\Delta t/2} \, e^{i\hat{L}_2\Delta t/2} \, e^{i\hat{L}_1\Delta t} \, e^{i\hat{L}_2\Delta t/2} \, e^{i\hat{L}_3\Delta t/2} \, e^{i\hat{L}_4\Delta t/2}. \tag{1.63}$$

According to the equation

$$e^{a\frac{\partial}{\partial x}} f(x) = f(x+a), \tag{1.64}$$

the effects of the several Liouville operators are shifts in phase space. The decomposition given by Eq. 1.63 results in the following algorithm:

---

[12]Depending on the system, other decompositions are possible. I kept the one tested by Kolb *et al.*.

1. $\pi_i \leftarrow \pi_i + \hat{h}\frac{\Delta t}{2}\mathbf{f}_i$

2. $\Pi_z \leftarrow \Pi_z + \frac{\Delta t}{2}\frac{V}{L_z}(\mathcal{P}_{zz} - P)$

   $\Pi_y \leftarrow \Pi_y + \frac{\Delta t}{2}\frac{V}{L_y}[(\mathcal{P}_{yy} + \mathcal{P}_{xx}) - 2P]$

3. $L_z \leftarrow L_z + \frac{\Delta t}{2}\frac{\Pi_z}{Q}$

   $L_y \leftarrow L_y + \frac{\Delta t}{2}\frac{\Pi_y}{2Q}$

   $L_x \leftarrow \alpha L_y$

4. $\mathbf{s}_i \leftarrow \mathbf{s}_i + \frac{\Delta t}{\hat{h}^2 m_i}\pi_i$

5. $L_z \leftarrow L_z + \frac{\Delta t}{2}\frac{\Pi_z}{Q}$

   $L_y \leftarrow L_y + \frac{\Delta t}{2}\frac{\Pi_y}{2Q}$

   $L_x \leftarrow \alpha L_y$

6. new forces and pressure are calculated

7. $\Pi_z \leftarrow \Pi_z + \frac{\Delta t}{2}\frac{V}{L_z}(\mathcal{P}_{zz} - P)$

   $\Pi_y \leftarrow \Pi_y + \frac{\Delta t}{2}\frac{V}{L_y}[(\mathcal{P}_{yy} + \mathcal{P}_{xx}) - 2P]$

8. $\pi_i \leftarrow \pi_i + \hat{h}\frac{\Delta t}{2}\mathbf{f}_i$

The force $\mathbf{f_i}$ is the force exerted on the particle i by all the other particles.

Langevin thermostat

The previous equations of motion generate trajectories representative of the isobaric-isoenthalpic ensemble. To simulate the system in the isobaric-isothermal ensemble, a thermostat is introduced. In this thesis, the enthalpy fluctuations are included in the system via a Langevin thermostat. The algorithm is justified by the Smoluchowski equation:

$$\frac{d\rho(\mathbf{x}, t)}{dt} = i\hat{L}_{FP}\ \rho(\mathbf{x}, t). \tag{1.65}$$

In the case of Langevin dynamics, the evolution operator (or Fokker-Planck operator) takes the form

$$\hat{L}_{FP} = \hat{L} + \sum_{i,\alpha}\left(\frac{\gamma_p}{L_\alpha m_i}\pi_{i\alpha}\right)\frac{\partial}{\partial \pi_{i\alpha}} + k_B T \gamma_p \sum_{i,\alpha}\frac{\partial^2}{\partial \pi_{i\alpha}^2}\ , \tag{1.66}$$

where $\hat{L}$ is the Liouville operator corresponding to the Hamiltonian dynamics (see Eq. 1.53), and Eq. 1.65 ensures that the probability distribution function $\rho(\mathbf{x})$ converges towards Boltzmann's distribution $\rho(\mathbf{x}) \propto e^{-\beta\mathcal{H}(\mathbf{x})}$.

One possibility to construct a trajectory (discretized in time), fulfilling Eq. 1.65 with $\hat{L}_{FP}$ defined by Eq. 1.66 is to replace the force on the particle i, $\mathbf{f}_i$, by [91]

$$\mathbf{f}_i - \frac{\gamma_p \hat{h}^{-1}}{m_i}\pi_i, +\eta_i(t)$$

with

$$\langle \eta_{i\alpha}(t) \rangle = 0 \;\; ; \;\; \langle \eta_{i\alpha}(t)\eta_{j\beta}(t') \rangle = 2k_BT\gamma_p \;\; \delta_{ij} \; \delta_{\alpha\beta} \; \delta(t-t').$$

In the algorithm used for this thesis, the energy fluctuation of the beads also thermostate the walls of the box.

Ensemble of simulation

In this subsection, we shall verify that the ensemble generated by the equations of motion is isobaric and isothermal. The demonstration is inspired by Andersen [2].

Suppose we want to calculate the mean value of an observables F. As the simulation is done with re-scaled variables, we define the function G, depending on the rescaled variables s_i and π_i taking the same values as F. G is defined as follows:

$$G(s_{i\alpha} = r_{i\alpha}/L_\alpha, \pi_{i\alpha} = m_i v_{i\alpha}L_\alpha, L_\alpha) = F(r_{i\alpha}, p_{i\alpha}). \tag{1.67}$$

The trajectory in phase space defines a probability density of state proportional to the Boltzmann distribution $e^{-\beta\mathcal{H}(\mathbf{x})}$, with the extended Hamiltonian $\mathcal{H}(\mathbf{x})$ defined by Eq. 1.51. Integrating on the phase space leads to the expectation value of G

$$\bar{G} = \frac{1}{N!\mathcal{Q}} \int_0^{\infty}{}^{(3)L_x=L_y} dL_\alpha \int_0^1{}^{(3N)} ds_{i\alpha} \int_{-\infty}^{\infty}{}^{(3N)} d\pi_{i\alpha} G(\mathbf{x})e^{-\beta\mathcal{H}(\mathbf{x})}, \tag{1.68}$$

with

$$\mathcal{Q} = \frac{1}{N!} \int_0^{\infty}{}^{(3)L_x=L_y} dL_\alpha \int_0^1{}^{(3N)} ds_{i\alpha} \int_{-\infty}^{\infty}{}^{(3N)} d\pi_{i\alpha} e^{-\beta\mathcal{H}(\mathbf{x})}. \tag{1.69}$$

The upperscripts above the integrals denote the dimension of the integration space, and an eventual constraint on the integration. Because G does not depend on Π_α, the quadratic contributions of Π_α in the Hamiltonian can be integrated separately in both the numerator and denominator.

$$\prod_{\alpha=y,z} \int_{-\infty}^{\infty} d\Pi_\alpha e^{-\beta\frac{1}{2Q}\sum_\alpha \Pi_\alpha^2} = 2k_BT\pi Q. \tag{1.70}$$

The rest of the integral is

$$\bar{G} = \frac{\int_0^{\infty}{}^{(3)L_x=L_y} dL_\alpha \int_0^1{}^{(3N)} ds_{i\alpha} \int_{-\infty}^{\infty}{}^{(3N)} d\pi_{i\alpha} G(s_{i\alpha}, \pi_{i\alpha}, L_\alpha)e^{-\beta H(s_{i\alpha}, \pi_{i\alpha}, L_\alpha)}}{\int_0^{\infty}{}^{(3)L_x=L_y} dL_\alpha \int_0^1{}^{(3N)} ds_{i\alpha} \int_{-\infty}^{\infty}{}^{(3N)} d\pi_{i\alpha} e^{-\beta H(s_{i\alpha}, \pi_{i\alpha}, L_\alpha)}}, \tag{1.71}$$

where H is the enthalpy of the system:

$$H(s_{i\alpha}, \pi_{i\alpha}, L_\alpha) = \mathcal{U} + PV = \sum_{i,\alpha} \frac{1}{2m_i} \frac{\pi_{i\alpha}^2}{L_\alpha^2} + \sum_{i,j>i} v_{ij}(|r_{ij}|) + P \prod_{\alpha=x,y,z} L_\alpha. \qquad (1.72)$$

Finally, a change of the variable $ds_{i\alpha}\, d\pi_{i\alpha} = dr_{i\alpha}\, dp_{i\alpha}$ shows that the computed average over G yields the isobaric-isothermic average of F:

$$\bar{G} = \frac{\int_0^\infty {}^{L_x=L_y} dV e^{-\beta PV} \int_0^\infty {}^{(3N)} dr_{i\alpha} \int_{-\infty}^\infty {}^{(3N)} dp_{i\alpha} F(r_{i\alpha}, p_{i\alpha}) e^{-\beta\mathcal{U}(r_{i\alpha},p_{i\alpha})}}{\int_0^\infty dV e^{-\beta PV} \int_0^\infty {}^{(3N)} dr_{i\alpha} \int_{-\infty}^\infty {}^{(3N)} dp_{i\alpha} e^{-\beta\mathcal{U}(s_{i\alpha},\pi_{i\alpha})}}. \qquad (1.73)$$

Example of equilibration

To illustrate the algorithm described previously, an example of equilibration of a lamellar phase in the constant-$(NPT, \gamma = 0)$ ensemble is presented here. The initial configuration is the same as in the previous example of this chapter, shown in Fig. 1.10. Four bilayers of tetramers h_2t_2 without solvent are placed on a cubic lattice. The director is along the z-axis. The normal pressure is $-0.16\, k_B T \cdot \sigma^{-3}$ and the tangential pressure is $6.62\, k_B T \cdot \sigma^{-3}$ ($\epsilon = 1.1\, k_B T$).

For the early begining of the equilibration, I have chosen a small time step $\Delta t = 0.001\, \tau$ and a large fictitious mass $Q = 1\, m$ because the intial configuration is far from e-quilibrium. The displacement of walls of the simulation box minimizes the discrepancy between the diagonal component of the pressure tensor and the imposed pressure $P = 2.9\, k_B T \cdot \sigma^{-3}$. The early time evolution of the box dimension is plotted in figure 1.13. As the initial normal pressure ($-0.16\, k_B T \cdot \sigma^{-3}$) is much lower than the imposed pressure, the dimension L_z decreases; similarly, the high tangential pressure ($6.62\, k_B T \cdot \sigma^{-3}$) imposes the dimensions L_x and L_y to increase. The values are stabilized after a time of about $100\, \tau$. For larger times, the system is simulated with a larger time step $\Delta t = 0.005\, \tau$ and a lower piston mass $Q = 0.1\, m$. It turns out that the box dimensions, and pressure components have already converged at $t = 100\, \tau$.

Figure 1.14 shows the evolutions of the pressure components at the beginning of the simulation.

In the algorithm, only the mean value of the tangential pressures, $\mathcal{P}_t = (\mathcal{P}_{xx} + \mathcal{P}_{yy})/2$, is taken into account. Fig. 1.14 shows that the individual pressure components P_{xx} and P_{yy} effectively equal. Analogously, even if no constraint are imposed on the non-diagonal terms of the pressure, they vanish when the local equilibrium has been reached: P_{xy}/P and the other analogous ratios are less than a few percents.
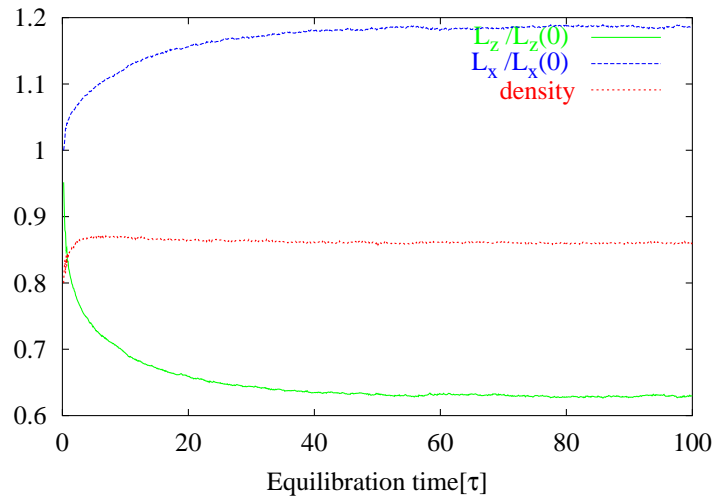
Figure 1.13: Time evolution of the box dimensions(relatively to the values at $t = 0$) and of the density. The initial box is a cube ($L_x = L_y = L_z \simeq 35\,\sigma$), and the initial density is 0.85 beads per unit volume.
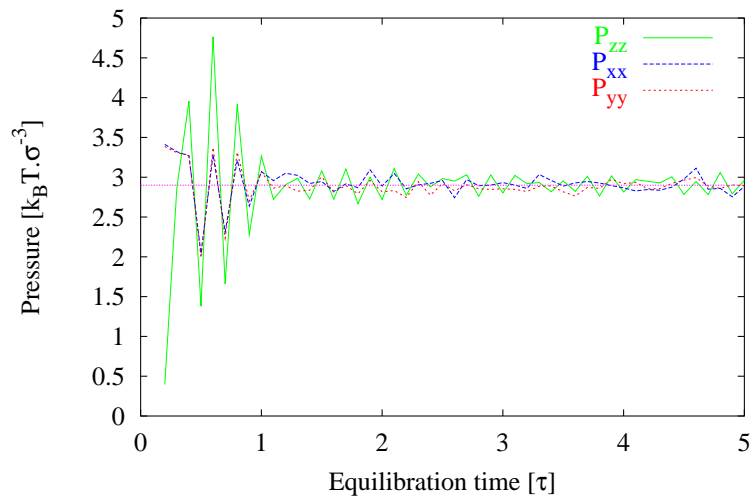
Figure 1.14: Time evolution of the pressure components during the same equilibration as in Fig. 1.13 (note the difference of scales on the x-axis).

2 Characterization of the smectic phase

Before studying the fluctuations and defects of bilayers in the smectic phase, one should first characterize the equilibrium structure of the simulated lamellar phase. This is done in this chapter. In Section 2.1, the self-assembly of the amphiphiles into a smectic A phase is examined by investigating the variation of *ad hoc* orientational and translational order parameters. Section 2.2 describes the equilibrium structure of the lamellar phases by its density, composition and pressure profiles along the director of the smectic.

2.1 Smectic ordering

2.1.1 Qualitative approach

Fig. 2.1 shows the pair correlation function of tail beads, $g_{tt}(r)$ computed in the disordered state and in the lamellar phase. At short distances, the local fluid structure
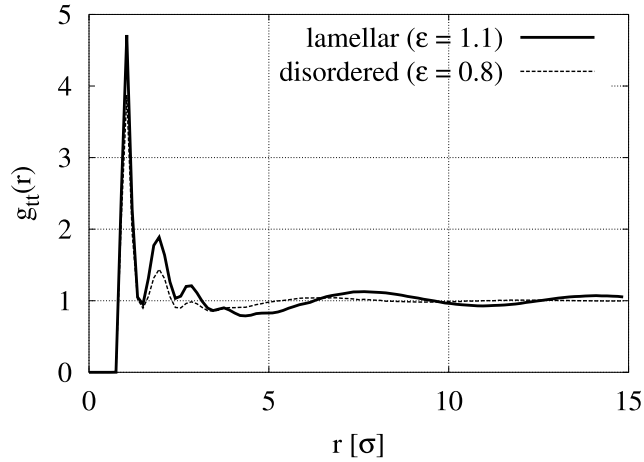
Figure 2.1: Pair correlation function for the tail beads *vs.* the distance between the beads r at $P = 2.9\,k_BT \cdot \sigma^{-3}$ for a typical system of $10\,240$ h_2t_2 tetramers and $10\,240$ solvent beads, simulated in NPT ensemble with isotropic pressure tensor.

dominates over the ocillations of $g_{tt}(r)$ in both phases. The larger peak comes from both bonded and non-bonded pair of tail beads. At intermediate distances, the difference

between the two structures appears. In the lamellar phase, the pair correlation function exhibits small oscillations which are absent in the disordered phase (the periodicity corresponds actually to the inter-layer distance). This smooth structure of the fluid on intermediate length scales is typical of a liquid crystalline phase.

Chandrasekhar [30] defines a liquid crystal as: "a state of aggregation intermediate between the crystalline solid and the amorphous liquid. As a rule, a substance which is strongly anisotropic in some of its properties and yet exhibits a certain degree of fluidity". The macroscopic anisotropy of the liquid crystal emerges from an inhomogeneous or anisotropic distribution of the molecules.

For example, in nematics, the molecules show a long range orientational order. The average direction in which the molecules point is the director **n**. A snapshot of the ht bonds of a typical configuration of the stack of five bilayers is displayed in Fig. 2.2 A. It suggests that such a long-range orientation correlation is found in the simulated lamellar phase. Fig. 2.2 A additionally reveals that the molecules arrange themselves
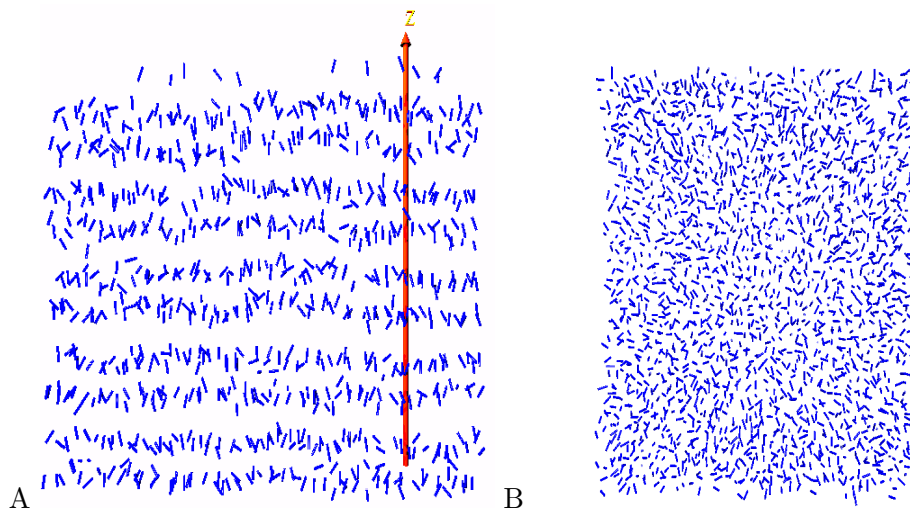
Figure 2.2: *A*: Side view ht bonds in a snapshot of 5 bilayers, and their director (z-direction of the simulation box). For clarity, only a slide of thickness 2σ is represented. *B*: Top view of ht bonds of one bilayer in a stack of 5 bilayers.

into bilayers. The lamellar phase is therefore more ordered that a nematic phase: both orientational and translational symmetries are broken. The density, composition and pressure profiles along the director are periodic, and symmetric relative to the mid-plane of the bilayers. Fig. 2.2 B is a top view on the ht bonds of the amphiphiles belonging to one of the five bilayers of Fig. 2.2 A. One guesses that within the bilayer, the ht bonds are randomly distributed.

For a quantitative approach, the breaking of symmetry is described with order parameters, which vanish in the more symmetric, less ordered phase, and are different from zero in the less symmetric, more ordered phase [179]. Phase transitions can be detected

through the variations of *ad hoc* order parameters.

2.1.2 Orientational order parameter

The nematic order parameter S measures the dispersion of the orientations of the molecules in the sample. It is computed as the largest eigenvalue or the nematic tensor $\hat{Q}$ [30, 41]

$$\hat{Q}_{\alpha,\beta} = \frac{1}{2N} \sum_{i=1}^{N} \left(3u_{i\alpha}u_{i\beta} - \delta_{\alpha\beta}\right), \text{ with } \alpha, \beta \in \ \{\text{x,y,z}\} \qquad (2.1)$$

where $\mathbf{u}_i$ is a unit vector describing the direction of the molecule i, δ the Kronecker symbol, and the sum ranges over all the N molecules. S equals 1 for perfectly aligned molecules, and 0 for a random configuration. The corresponding eigenvector is the director $\mathbf{n}$. I have chosen to take the direction of the molecules $\mathbf{u}_i$ along the *ht* bonds of the tetrameric amphiphiles *hhtt*, but other choices are possible and lead to similar results [74].

Fig. 2.3 shows the order parameter S as a function of the potential depth ϵ for a set of runs where ϵ was either increased from 0.82 to $1.0\,k_BT$ starting from a random configuration, or decreased from 1.1 to $0.82\,k_BT$ starting from a perfectly aligned lamellar phase. The order parameter jumps from 0 to about 0.38 when ϵ is increased, and back to 0 when ϵ is reduced. The jump and the presence of a hysteresis indicate a first order phase transition between an isotropic phase and an ordered phase [28].

2.1.3 Translational order parameter

Fig. 2.4 displays the average composition profiles along the director (z-direction). For each position z, I have taken as a reference the mid-plane position of the nearest membrane (the procedure to compute the positions of the membranes is described in Section 3.2.1). The tail-beads are segregated in the middle of the membrane, and the heads coat the tail layer, shielding it from the solvent. Such a composition profile is typical for the bilayer structure built by amphiphilic molecules (e.g. [69]). Here, the density profile of tail-beads happens to be close to a cosine function.

The translational symmetry breaking can be investigated through the density-density correlation functions along the director. I computed the density autocorrelation of the tail beads defined in Eq. 2.2 for the Z direction.

$$p_{tt}(Z) = \frac{1}{N_t(N_t-1)} \sum_{i\neq j} \frac{1}{dz} \int_{-\frac{dz}{2}}^{\frac{dz}{2}} \mathrm{d}z' \delta\left(\frac{|z_i - z_j| - [Z + z']}{L_z}\right), \qquad (2.2)$$

where N_t is the number of t beads, z_i and z_j are the coordinates of the beads i and j. The parameter $\mathrm{d}z$ is the thickness over which the correlations are averaged, L_z the box dimension in z-direction and δ the delta function.

Fig. 2.5 shows the density autocorrelation in the direction parallel and perpendicular to the director (z-direction).
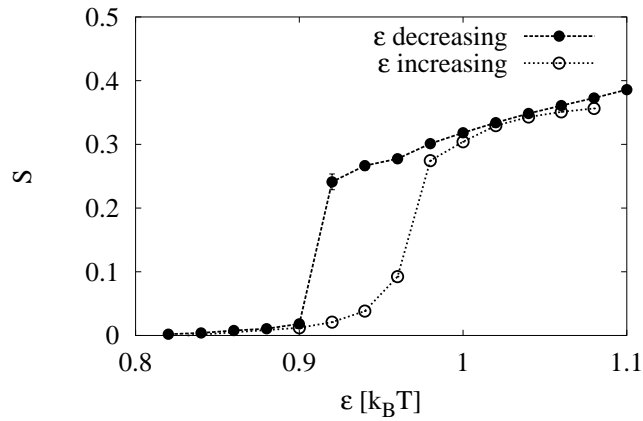
Figure 2.3: Nematic order parameter S *vs.* potential depth ϵ of a typical system of $10\,240$ h_2t_2 tetramers and $10\,240$ solvent beads, simulated in NPT ensemble with isotropic pressure tensor for $P = 2.9\,k_BT \cdot \sigma^{-3}$ and ϵ from $0.82\,k_BT$ to $1.1\,k_BT$ by steps of $0.02\,k_BT$, during $10\,000\,\tau$ (relaxation time of $5\,000\,\tau$ + computation time $5\,000\,\tau$). For the configurations generated during the increase of ϵ, some linear defects are still present during the production runs (after $5\,000\,\tau$ of relaxation), so that the order parameter measured is slightly lower than the value obtained with an initial lamellar configuration set by hand. The lines are just guides for the eyes.
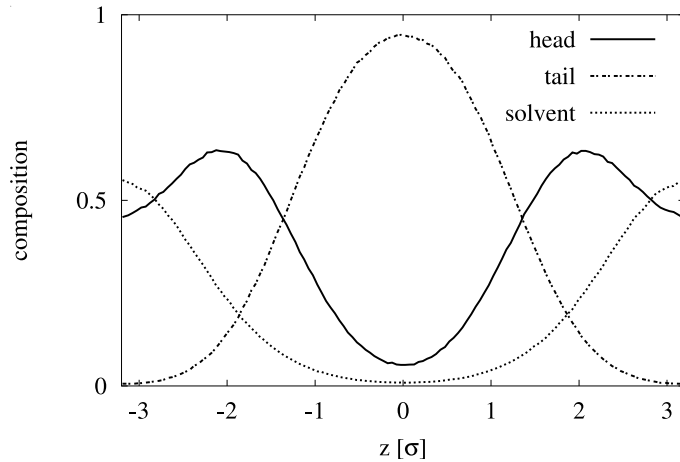
Figure 2.4: Composition profiles along the director, averaged over the 15 membranes. $z = 0$ corresponds to the mid-plane of the bilayers. The inter-lamellar distance is $d = 6.4\,\sigma$.

The density autocorrelation $p_{tt}(X)$ is constant: The layers are effectively perpendicular
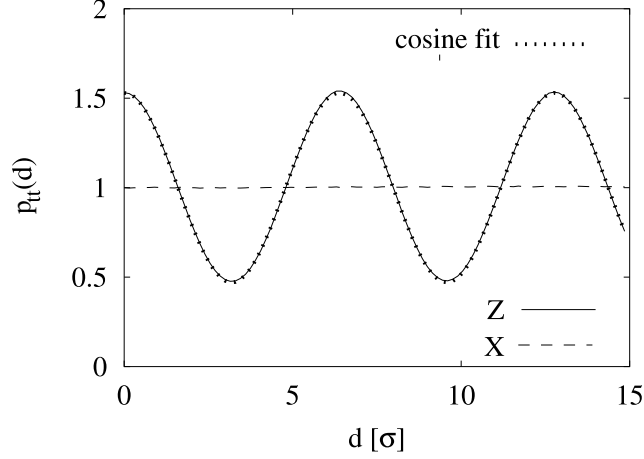
Figure 2.5: Autocorrelation functions of the density of tail beads in the plane of the bilayers (X) and along the director (Z), as a function of the distance between beads (for one configuration at $P = 2.9\,k_BT \cdot \sigma^{-3}$ and $\epsilon = 1.1\,k_BT$). The fit of the function $f(x) = 1 + \alpha\cos(2\pi x/d)$ to the autocorrelation in Z direction yields $\alpha = 0.52$ and $d = 6.38\,\sigma$.

to the director, and, on average, the translational symmetry is not broken in the plane of the bilayers. By contrast, $p_{tt}(Z)$ fluctuates significantly. In our case, $p_{tt}(Z)$ happens to be nicely fitted by a cosine function $1 + \alpha\cos(2\pi z/d)$, with a period d corresponding to the interlamellar distance. I have used the amplitude of the oscillations of $p_{tt}(Z)$, noted α, as an order parameter for the translational symmetry breaking. Fig. 2.6 shows that
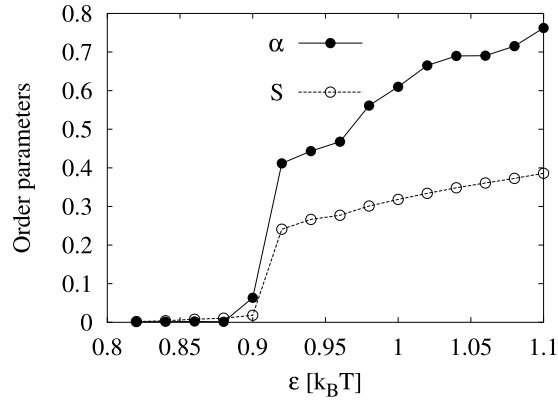
Figure 2.6: Nematic order parameter S and translational order parameter α *vs.* potential depth (decreasing ϵ), for the same simulations as in Fig. 2.3. The lines are guides for the eyes. The errors on S are about 0.01, on α about 0.05.

the behavior of the translational order parameter α as a function of ϵ is similar to the one of S: They are both different from zero in the ordered phase, and simultaneously jump to zero at $\epsilon = 0.92\,k_B T$. As expected for amphiphilic solutions, the coarse-grained model does not exhibit a nematic phase ($S \neq 0$ and $\alpha = 0$ in any direction) [125, 182].

A jump in the density accompanies the isotropic to smectic A transition (see Fig. 2.7).
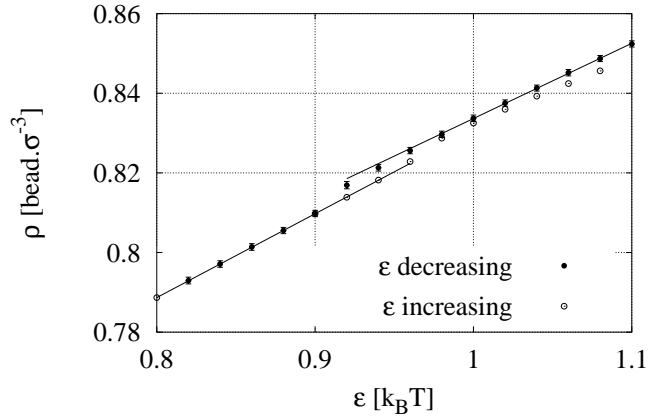
Figure 2.7: Density ρ *vs.* potential depth ϵ. The simulation data are the same as in Fig. 2.3. The lines are linear fits for the disordered phase and for the lamellar phase (decreasing ϵ).

2.1.4 Interlamellar distance

The interlamellar d is shown as a function of the potential depth in Fig. 2.8. It seems to increase linearly with the potential depth ϵ, which can be interpreted as a segregation factor. As we have seen in Fig. 2.7, the density nevertheless increases with ϵ. We conclude that the area per amphiphile in the bilayer decreases when ϵ increases. The opposite trends of the area per molecule and the interlamellar distance confirm the anisotropy of the lamellar phase.
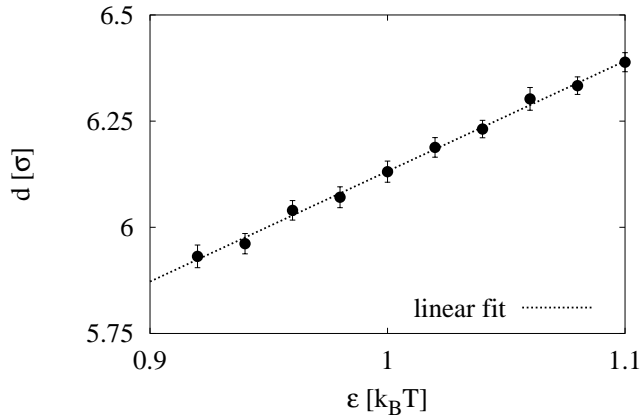
Figure 2.8: Interlamellar distance d *vs.* potential depth ϵ. The simulation data are the same as those for decreasing ϵ in Fig. 2.3.

2.2 Structure of the lamellar phase

In the previous section, we have seen that the amphiphiles self-assemble into a smectic A phase (L_α). Taking into account the phenomenology of the model presented in Section 1.1, I have chosen simulation parameters in the stability region of the lamellar phase: $\epsilon = 1.1\,k_BT$ and $P = 2.9\,k_BT \cdot \sigma^{-3}$ ($\rho \sim 0.852$ bead$\cdot\sigma^{-3}$) and 20 percent of solvent beads. In the following, I describe the equilibrium structure of the lamellar phase in these particular conditions.

2.2.1 Typical systems

The lamellar phase was simulated in the ($NPT, \gamma = 0$)-ensemble as described in Section 1.2. Two systems were studied. The small system contains five bilayers of about two thousands tetramers each, separated by thin layers of solvent (10 240 tetramers and 10 240 solvent beads). The large system is three times larger in z-direction: it contains fifteen bilayers of about two thousands tetramers each (30 720 tetramers and 30 720 solvent beads).

The rearrangement of lamellae from a random initial configuration requires at least $30\,000\,\tau$. Therefore I imposed the orientation of the lamellae, constructing by hand the initial configuration made of five or fifteen layers stacked in the z-direction. It first relaxed for $10\,000\,\tau$, during which the interlamellar distance adjusted to its equilibrium value and the shape of the flexible box changed accordingly. The equilibrated box dimensions were $L_x = L_y = 43.40 \pm 0.05\,\sigma$, $L_z = 95.7 \pm 0.2\,\sigma$ for the system of fifteen bilayers, and $L_x = L_y = 43.37 \pm 0.08\,\sigma$, $L_z = 31.9 \pm 0.1\,\sigma$ for the system of five bilayers[1]. As discussed in Section 1.2.2, thanks to the flexibility of the simulation box, the

---

[1]The averaged values are given with their standard deviation obtained from the production runs.

director remains basically aligned with the z-direction. Fig. 2.9 shows a snapshot of the equilibrated system of fifteen bilayers.
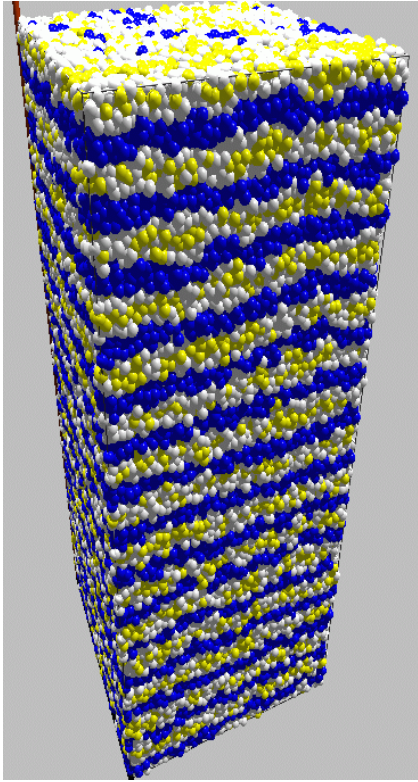
Figure 2.9: Snapshot of 30 720 amphiphilic tetramers h_2t_2 and 30 720 solvent beads. The blue beads are solvophobic (t-beads), the white beads are solvophilic (h-beads) and the solvent beads are yellow.

For the production runs, I have carried on the simulations of the lamellar systems at the potential depth $\epsilon = 1.1\,k_BT$ and the pressure $P = 2.9\,k_BT\cdot\sigma^{-3}$ during $100\,000\,\tau$. The calculations were done in the Computer Center of the Max Planck Society in Garching; they cost approximately 25 000 CPU-hours, which were parallelized on 16 to 32 IBM 'Power 4' processors with a clock frequency of 1.3 GHz and a maximal performance of 5.2 GFlops/s.

I checked that the diagonal terms of the pressure tensor were equal. The non-diagonal terms did not vanish exactly, but they were smaller than the error of the measure of the pressure (typically $\langle P_{xy}\rangle/\langle P_{xx}\rangle \sim 10^{-3}$). Similarly, I verified that the algorithm imposes a zero surface tension by computing the difference between the normal and tangential pressure components in the system (Eq. 2.3).

$$\gamma = \int_0^{L_z} [P_n(z) - P_t(z)]\mathrm{d}z. \tag{2.3}$$

Actually, the computed surface tension is not strictly zero: I obtained

$$\langle\gamma\rangle = -0.01 \pm 0.011\,k_BT\cdot\sigma^{-2}$$

per bilayer. The large standard deviation of the surface tension results from the high fluctuation of the pressure. The mean value of the surface tension is negligible: Previous simulation studies of bilayers with similar coarse-grained models [176] have shown that a change of less than 0.1% in the area per polar head relative to the equilibrium value leads to a surface tension of the order of $0.1\,k_B T{\cdot}\sigma^{-2}$. In other words, the area compressibility modulus of the bilayer is high ($200\,\mathrm{mN{\cdot}m^{-1}}$ for phosphatydylcholine lipid bilayers [155]). Compared to that value, the surface tension found in the simulated stack is negligible.

2.2.2 Anisotropy of the diffusion

The mean square displacements of the molecules were computed as a function of time. In the smectic phase, one can define a diffusion coefficient along the director (D_z) and perpendicular to it ($D_\perp$), with Eqs. 2.4 and 2.5.

$$D_z = \lim_{t\to\infty} \frac{1}{2t}\langle |z(t) - z(0)|^2\rangle, \tag{2.4}$$

$$D_\perp = \lim_{t\to\infty} \frac{1}{4t}\langle |x(t) - x(0)|^2 + |y(t) - y(0)|^2\rangle. \tag{2.5}$$

From a simulation of 5 bilayers in NVT ensemble during $10\,000\,\tau$, I computed diffusion coefficients of the order of 10^{-4} to $10^{-3}\,\sigma^2\cdot\tau^{-1}$ (see Table 2.1).

phase	$D_\perp$ solvent	D_z solvent	$D_\perp$ $h_2 t_2$	D_z $h_2 t_2$
isotropic ($\epsilon = 1.0 k_B T$)	47	47	25	25
lamellar ($\epsilon = 1.1 k_B T$)	42	4.5	20	1.0

Table 2.1: Diffusion coefficient of the solvent and of the amphiphilic tetramer in the lamellar phase and the isotropic phase (in units of $10^{-4}\,\sigma^2\cdot\tau^{-1}$) obtained for a simulation of $10\,000\,\tau$ of the small system (5 layers). The simulations are done in the NVT ensemble with $\rho = 0.85$ bead$\cdot\sigma^{-3}$ to avoid artifacts due to the box re-scaling. The thermostat is nevertheless included in the simulation.

In fact, the mean square displacement of the molecules along the director during the time of the simulation ($100\,000\,\tau$) is smaller than the square of the interlamellar distance. The values obtained for D_z are therefore only upper values.

To compare these results with a simple case, I simulated a system of $1\,000$ solvent beads in its fluid and crystalline phases. The diffusion coefficient of the solvent in the crystal is lower than $10^{-4}\,\sigma^2\cdot\tau^{-1}$, and in the simple fluid phase $3\cdot 10^{-2}\,\sigma^2\cdot\tau^{-1}$. As expected, the diffusion coefficients found for the liquid crystal range between those two extremes.

The diffusion constants of the solvent and the tetramers in the disordered phase and within the bilayers ($D_\perp$) are similar. In contrast, the diffusion coefficient perpendicular to the layers is one order of magnitude lower. These orders of magnitude agree with available experimental data: The lateral diffusion of lipids within a single bilayer are typically of the order of 5 to 20 μm$^2\cdot$s^{-1} [66, 183] or $10^{-4}\,\sigma^2\cdot\tau^{-1}$. In the lamellar phase, the diffusion perpendicular to the bilayers is about one order of magnitude lower than the diffusion parallel to the bilayers [37].

2.2.3 Density and composition profiles

As the smectic A phase is invariant with respect to a translation parallel to the plane of the bilayer, and to a rotation about the director of the layers, the local structure of the smectic layers can be characterized by the composition profiles across the layers. We have already studied composition profiles along the director in Fig. 2.4. They were obtained by a computation of the average densities in slabs perpendicular to z-direction, *i.e.* averaged over the whole surface $L_x L_y$.

Because of the position fluctuations of the bilayers, clearly visible on Fig. 2.2 A, the relatively smooth profiles of Fig. 2.4 do not represent the local composition profile. To account for the position fluctuations of the bilayers, I computed the local position of each membrane, $h_n(x, y)$ on a grid in the (x, y) plane and evaluated the local profile in the z-direction relative to those positions (the procedure to compute the positions of the membranes is described in Section 3.2.1). Fig. 2.10 A presents the resulting composition profiles. The inner part of the bilayer is around $z = 0$, and $d = 6.4\,\sigma$ is the mean interlamellar distance. The tails are highly segregated in the inner part of the bilayer, on a thickness about $2\,\sigma$ and the head segments shield the tails from the solvent. The width of the interface is about $1\,\sigma$. We deduce from Fig. 2.10 A that almost no solvent beads penetrate into the amphiphilic bilayer.

Fig. 2.10 B shows the local density profile across the bilayers (with the same calculation method as Fig. 2.10 A). The density profile dips twice, at the interface between head-rich and tail-rich domains ($|z| \sim 1.2\,\sigma$), where the repulsions dominate.

2.2.4 Pressure profiles

The pressure is the force per unit area exerted by the system on an imaginary or a real surface in contact with the system. For inhomogeneous systems, the pressure depends on the position and the orientation of the test surface, so that one defines a local pressure tensor $\mathbf{P}(\mathbf{R})$ corresponding to the force per unit of surface on an infinitesimal surface.

The translational and rotational invariances in the plane of the bilayers impose that the pressure tensor depends only on the coordinate along the director ($\mathbf{P}(z)$), and that the pressure components in the plane of the layers are equal. Additionally, the local pressure tensor in a smectic is diagonal, just as the global pressure tensor. The local pressure tensor is then described by the pressure normal to the layer (P_n), and the pressure tangential to the layer (P_t) with

$$\mathbf{P}(z) = P_t(z)(\mathbf{e}_x \mathbf{e}_x + \mathbf{e}_y \mathbf{e}_y) + P_t(z)\mathbf{e}_z \mathbf{e}_z. \tag{2.6}$$

In equilibrium, mechanical stability requires that the gradient of the pressure tensor vanishes [198]:

$$\nabla \cdot \mathbf{P} = \mathbf{0}. \tag{2.7}$$

In particular, the derivative along the director vanishes, so that the normal component of the pressure is constant:

$$\frac{\partial P_n}{\partial z} = 0 \Rightarrow P_n(z) = \text{const.} \tag{2.8}$$

A

B
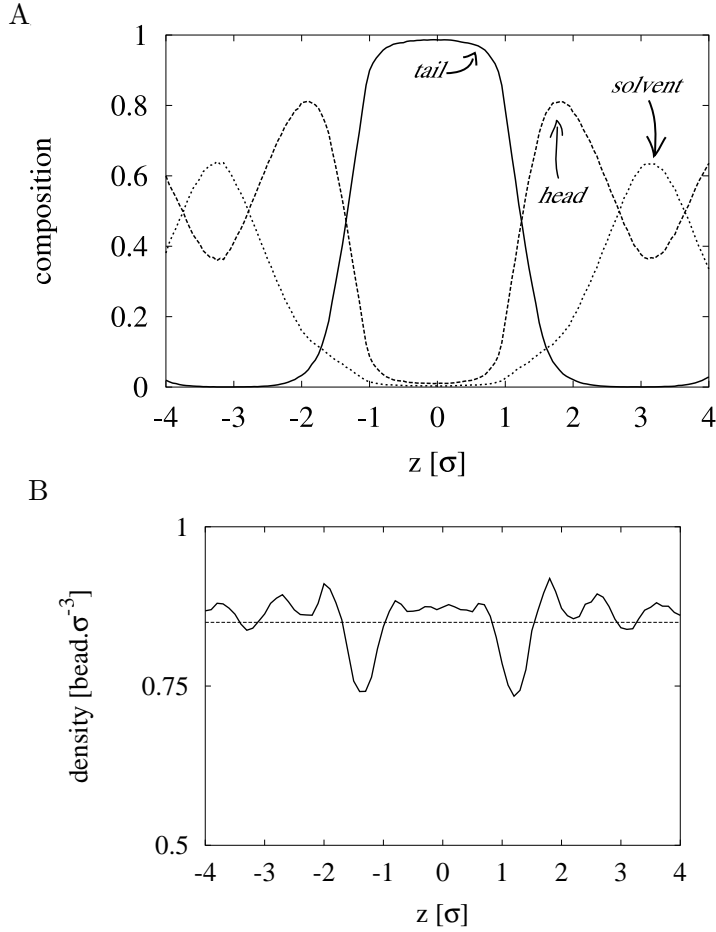
Figure 2.10: *A*: Composition profile across the bilayers. *B*: Bead density profile across the bilayers. The thick solid line is the density profile, the thin dashed line is the mean value.

Finally, in the liquid crystalline phase with a planar geometry, the pressure tensor is reduced to the calculation of the tangential pressure profile along the director, $P_t(z)$. This profile is not uniquely defined [7], and several conventions have been compared (*e.g.* [108] and [198] and Ref. in it).

Pressure profiles across amphiphilic bilayers were investigated with all-atoms model of amphiphiles [200, 108] and with coarse-grained models [69, 176]. The results depend strongly on the details of the model and the convention used to compute the pressure profile. In the following, I present results obtained using the Irving-Kirkwood convention [82], which has been proven to give good results for anisotropic phases with planar

geometries [198, 7]. The normal and tangential pressure components read

$$P_n(z) = k_B T \rho(z) + \frac{1}{A} \left\langle \sum_{\{i,j\}} f_{ij}^z \, z_{ij} \, w(z, z_i, z_j) \right\rangle, \tag{2.9}$$

and

$$P_t(z) = k_B T \rho(z) + \frac{1}{2A} \left\langle \sum_{\{i,j\}} \left[f_{ij}^x \, x_{ij} + f_{ij}^y \, y_{ij} \right] \, w(z, z_i, z_j) \right\rangle, \tag{2.10}$$

where $\rho(z)$ denotes the density at the height z averaged over $x-$ and $y-$directions, A the area of the plane in tangential direction, z_i and z_j the coordinates of the particles along the director, $z_{ij} = z_i - z_j$, $\mathbf{f}_{ij}$ the force exerted by the particle j on the particle i, and $w(z, z_i, z_j)$ a weight depending on the position of the particles relative to the surface $\mathrm{d}\mathbf{A}$. The weight $w(z, z_i, z_j)$ is $|z_{ij}|^{-1}$ if the line connecting the particles i and j passes through the surface, and zero elsewhere:

$$w(z, z_i, z_j) = \frac{1}{|z_{ij}|} \, \theta\left(\frac{z - z_i}{z_{ij}}\right) \, \theta\left(\frac{z_j - z}{z_{ij}}\right), \tag{2.11}$$

where θ denotes Heaviside's step function:

$$\theta(x) = \begin{cases} 0 & \text{if} \quad 0 > x, \\ 0.5 & \text{if} \quad x = 0, \\ 1 & \text{if} \quad 0 < x. \end{cases} \tag{2.12}$$
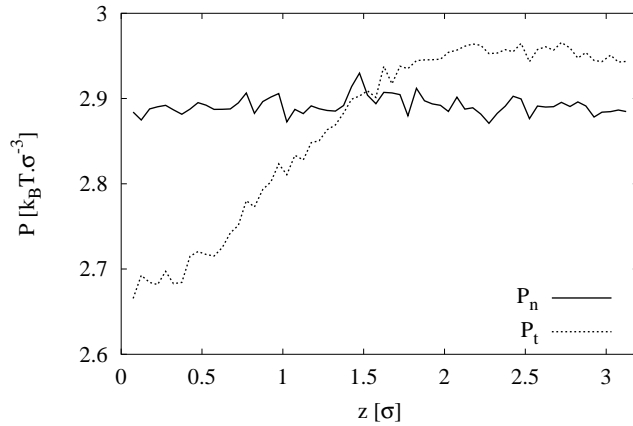
Figure 2.11: Normal and tangential pressure profiles across the bilayers.

Fig. 2.11 shows the pressure profiles along the director of the lamellar phase, computed with Eqs. 2.9 and 2.10 averaged over slabs of thickness $\Delta z = 0.25 \, \sigma$. The data are averaged over all 15 bilayers in the simulation box, and during about $100\,000 \, \tau$. As

expected, the normal pressure component remains approximatively constant. The errors on the pressure are of the same order of magnitude as the fluctuations of the profile $P_n(z)$ around its mean value ($0.05\,k_BT \cdot \sigma^{-3}$). The large error on the pressure profiles reflects the rapidly fluctuating forces acting on each bead.

The tangential pressure deviates significantly from its mean value. One possible interpretation of the profile is based on the concept of "opposing forces" in lipid bilayers [126]. The equilibrium results from a competition between two forces: the tendencies of hydrocarbon tails to aggregate in water, counterbalanced by the mutual repulsion of the head groups. The inner part of the membrane ($z \lesssim 1.5\,\sigma$) can be seen as a liquid layer of solvophobic beads with a surface tension favoring a low area/volume ratio of the inner part of the bilayer, and $P_n(z) - P_t(z) \geq 0$. On the contrary, the repulsive interactions favor a low ratio volume/surface of the interfacial region ($z \gtrsim 1.5\,\sigma$), and $P_n(z) - P_t(z) \leq 0$.

To summarize, we have seen that the coarse-grained model presented in Section 1.1 permits to simulate a smectic A phase of amphiphiles. I have studied the phase transition between a disordered phase and a smectic L_α phase of a relatively concentrated solution of amphiphiles. The results obtained for the simulated coarse-grained L_α phase agree with published results about amphiphilic bilayers, and provide a starting point for the study of the fluctuations and the defects in the lamellar phase.

3 Fluctuations of bilayers

The elasticity of a L_α phase is modified by the inclusion of polymers between the bilayers [23, 17]. In order to compare the situations in the presence and in the absence of polymer, we shall first investigate the elasticity of the pure smectic phase.

The position fluctuations of the bilayers in the lamellar stack were computed using the same simulation data of the L_α phase as in Chapter 2. We shall compare these simulation results to the predictions of a model describing the layers of the smectic as undulating surfaces [80, 144, 102, 141, 72, 110]. Finally, I suggest an analysis of the data that permits to determine the bending constant and the compressibility modulus of the smectic.

3.1 Elasticity of the lamellar phase

The theory to which we shall compare the simulation results is based on the Helfrich and Canham Hamiltonian (HC) [78, 27], for the bending energy of a single fluid bilayer. The "Discrete Harmonic" model (DH), describing smectic phases, [80, 144, 102, 141, 72, 110] additionally incorporates the interactions between the bilayers *via* an harmonic potential.

This section begins with a reminder of the HC Hamiltonian for a single bilayer, and the resulting position fluctuations spectrum. The interactions between the membranes of the lamellar phase are then included in the model, and their influence on the position fluctuations is investigated.

3.1.1 Elasticity of single bilayers

Deformation modes

The elasticity of a bilayer can be characterized by its response to several mechanical stresses, for example to the stretching, bending, sliding or shearing, sketched in Fig. 3.1.

The energy necessary to alter the shape of a bilayer depends on the deformation mode. Fluid bilayers do not resist shearing along their mid-plane. Depending on the shear direction, either the monolayers slide on each other, or the polar heads reorder within the plane (see Fig. 3.1: sliding and shearing). Such deformations do not cost much energy. In this thesis, we shall not investigate shear deformations. By contrast, stretching a bilayer involves very high energies. Bending demands intermediate energies, of the order of $k_B T$ [50]. As a consequence, under normal conditions, amphiphilic bilayers behave like undulating membranes with a fixed area per molecule.
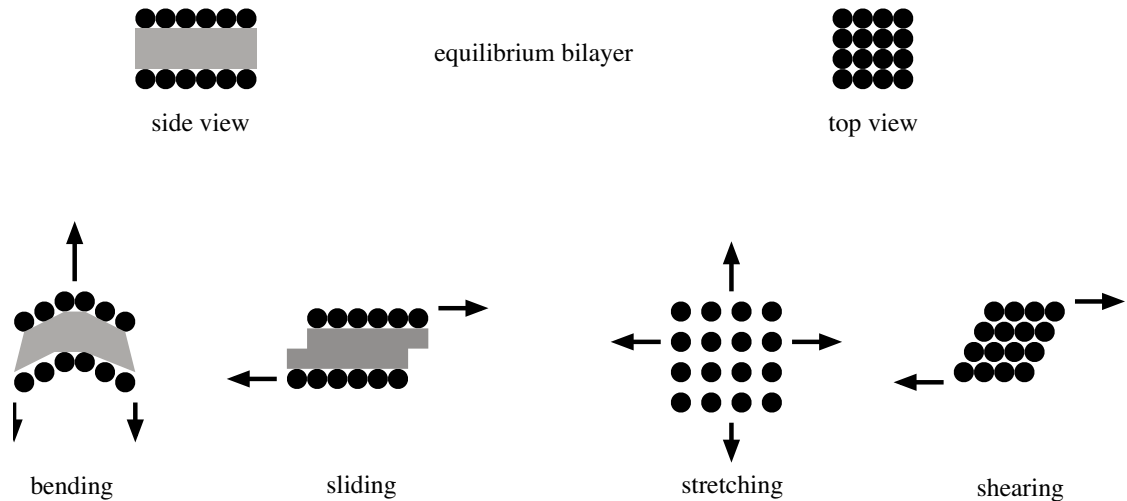
Figure 3.1: Sketches of the deformations of a bilayer. The disks represent hydrophilic heads, and the rectangles represent the hydrophobic tails.

The micropipette technique permits to study experimentally the bending and stretching deformations of a single bilayer. The advantages of this experimental setup are its high precision, and the possibility to test the reversibility of the deformations. By analyzing micropipette experiments on giant unilamellar vesicles, Evans *et al.* [50, 128, 51] could measure the elastic constants of amphiphilic bilayers. The principle of the experiment is the following: a pipette of a few micrometers is approached towards a vesicle until it comes in contact with it. Then, a suction in the pipette deforms the vesicle and increases its area. During the experiment, the bilayer is observed with an optical microscope, which permits to measure the area of the vesicle as a function of the pressure in the micropipette (see Fig. 3.2, from [155]). The fluctuations of the bilayers with wavelengths smaller than the microscope resolution (approximately 10^{-7} m) are not resolved. Calibration measurements are used to convert the pressure in the micropipette into a tension exerted on the bilayer. The area-*vs.*-tension curves are then interpreted. Two regimes are observed [50, 155, 61].

When the tension is low (0.001-0.5 mN/m), the vesicle is flaccid and the membrane fluctuates on length-scales invisible on micrographs. The difference between the observed area and the microscopic area due to unresolved fluctuations, named excess area, depends on the tension exerted on the vesicle. Increasing the tension reduces the excess area by reducing the amplitudes of the fluctuations. In this so-called entropic-tense regime, the analysis of the data permits to measure the bending constant K_c of the bilayers (defined in the following chapter).

The so-called stretched-tense regime is found for high tensions (≥ 0.5 mN/m), when the excess area is negligible. In this regime, the area per molecule increases. The data
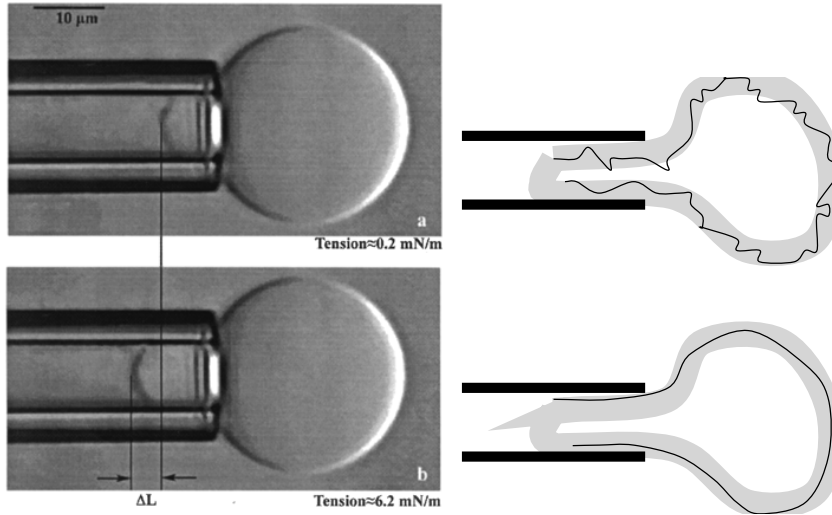
Figure 3.2: **Left**: Video micrographs of a vesicle area expansion test. (a) The vesicle at low tension. (b) The vesicle at high tension. The change in the projection length δL_p is proportional to the change in the apparent surface area ΔA. The volume inside the vesicle is constant during the suction. From [155]. **Right**: Sketches of the two stretching regimes. The thick line is the observed membrane, whereas the thin dark line represent the microscopic fluctuations of the membrane. At a low tension, the entropic-tense regime, at high tension, the stretch-tense regime. Inspired by [61].

permit to measure the area-compressibility of the bilayer, defined as

$$\tau = K_A \frac{\mathrm{d}A}{A},$$

where τ is the tension applied to the tensed bilayer, $\mathrm{d}A$ the subsequent increases of observed area, and A the observed area at equilibrium. The area compressibility of lipid bilayers can be as high as $200\,\mathrm{mN/m}$ (typical order of magnitude obtained for phosphatidylcholines [155, 61]). Therefore, fluid bilayers under normal conditions are usually considered as incompressible, and are said to be "saturated"[163]: If more amphiphiles are added to the bilayer, the total surface of the bilayer increases, whereas the area per molecules remains constants.

The next paragraph describes the Helfrich and Canham model for a saturated undulating membrane.

The Helfrich and Canham Hamiltonian of an undulating bilayer

Helfrich [78] and Canham [27] neglected the thickness of the membrane (δ) and all molecular details: They modeled the membrane as an undulating regular surface, and

proposed a phenomenological expression for its energy as a functional of its local curvatures.

Their arguments apply on the length-scales ζ larger than the thickness of the bilayer, $\zeta \gg \delta$. Of course, the geometry and area of the surface depends on ζ. In the following, we shall choose ζ as small as possible. Recent molecular dynamic simulations [114, 68] and this work have shown that the theory is appropriate for ζ larger than few thicknesses of the bilayer (see Sect. 3.1.2).

The effective Hamiltonian is a quadratic expansion in the principal curvatures of the surface c_1 and c_2

$$H = \int_S dS \left[\gamma + \frac{\kappa}{2}(c_1 + c_2 - c_0)^2 + \bar{\kappa} c_1 c_2 \right], \tag{3.1}$$

where the integral is over the whole surface of the membrane (S), γ is the surface tension of the membrane, c_0 is the spontaneous curvature. The parameters κ and $\bar{\kappa}$ are the elastic moduli of the mean and Gaussian curvatures (see Fig. 3.3).
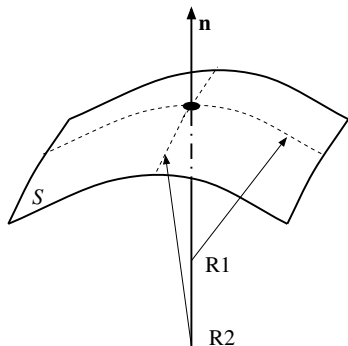
Figure 3.3: The principal curvatures measure the maximum and minimum bending of the surface. They are the inverses of the minimum and maximum radii of discs tangent to the surface.

The interfacial tension γ, or surface tension, has the unit of an energy per unit area. Jähnig [85] argued that in a flaccid vesicle, the surface tension of the bilayer should be zero because the area per polar head can be optimized independently of the other thermodynamical parameters (*i.e* the number of amphiphiles and the form of the vesicle). We shall assume in the following that

$$\gamma = 0. \tag{3.2}$$

The spontaneous curvature c_0 is different from zero in most biological cell membranes with different compositions in the two monolayers. On the contrary, in artificial bilayers, this asymmetry is generally absent. We shall assume in the following that

$$c_0 = 0. \tag{3.3}$$

The elastic modulus κ describes the rigidity of the membrane at the length-scale ζ, it modulates the amplitudes of the fluctuations of the membranes around their ground state. Its value is always positive, and varies between a few $k_B T$ for flexible membranes and 20 $k_B T$ for rigid membranes.

The observation of biconcave vesicles for bilayers with $c_0 = 0$ is a strong argument for the existence of the the saddle-splay term involving the Gaussian rigidity coefficient $\bar{\kappa}$. The energy $\bar{\kappa}$ may be positive or negative and determines the preferred topology of the bilayer.

As we are interested in the lamellar phase, I shall now briefly discuss the domain of stability of the planar geometry for a membrane with no spontaneous curvature[1]. Since the compressibility of bilayers is very high, we suppose that the area of the surface is fixed, and the surface tension zero. According to the Gauss-Bonnet theorem, the integral over the entire surface of the Gaussian curvature $c_1 c_2$ is proportional to the Euler characteristic χ of the surface, a topologically invariant property of a surface depending on the genus g of the surface. In two dimensions, the genus is the number of holes.

$$\int_A dS c_1 c_2 = 2\pi\chi = 4\pi(1 - g).$$

If $\bar{\kappa}$ is positive, then the energy of the surface decreases when the genus increases. Typically, a sponge phase is favorable. If $\bar{\kappa}$ is negative, then low genuses are favorable. The surface has a simple shape like a vesicle or a flat sheet. In particular, the elastic energy is $4\pi(2\kappa + \bar{\kappa})$ for a spherical vesicle and zero for the flat membrane. In brief, we obtained the following results:

$$\bar{\kappa} > 0 \Rightarrow \text{sponge phase,}$$

$$\bar{\kappa} < 0 \quad \text{and} \quad -2\kappa > \bar{\kappa} \Rightarrow \text{vesicle,}$$

$$\bar{\kappa} < 0 \quad \text{and} \quad -2\kappa < \bar{\kappa} \Rightarrow \text{flat membrane.}$$

Thermal fluctuations of a single flat membrane

As already mentioned, the energy needed to bend the membrane is of the order of $k_B T$ (at length-scales of several membrane thicknesses). Thus, the thermal energy suffices to excite some undulation modes. Thermal fluctuations play an important role in the physics of bilayers; for instance, the undulations give rise to steric repulsions between adjacent layers in the lamellar phase [163].

In the following, the position fluctuations are derived for a planar sheet with small deviations around the flat ground state ($-2\kappa < \bar{\kappa} < 0$). We shall use Monge's representation (for the notations, see Fig. 3.4): the planar ground state is perpendicular to the z-axis, and position of the membrane is given by the equation $z - h(x, y) = 0$ for x and y defined on the projected area $A_p = L_x L_y$. As we consider only an almost planar membrane, the topology of the membrane is fixed; the integral of the Gaussian curvature is neglected in the calculations. In Monge's representation, the mean curvature is given by the expression [163]

$$c_1 + c_2 = \frac{(1 + h_x^2)h_{yy} + (1 + h_y^2)h_{xx} - 2h_x h_y h_{xy}}{2(1 + h_x^2 + h_y^2)^{3/2}} \simeq \frac{1}{2}(h_{xx} + h_{yy}). \tag{3.4}$$

---

[1]A complete mathematical description and experimental observations of the various morphology of vesicles can be found in [171, 19].
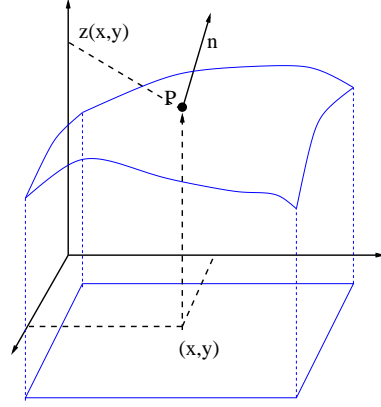
Figure 3.4: Sketch of the Monge representation of a surface.

Therefore, the HC Hamiltonian can be rewritten as

$$\mathcal{H} = \int_A \mathrm{d}x\mathrm{d}y \left[\frac{K_c}{2} \left(h_{xx} + h_{yy} \right)^2 \right],$$ (3.5)

where $K_c = \kappa/4$ is the bending constant of the membrane. The spectrum of fluctuations is given by the amplitude of $\tilde{h}(q_x, q_y)$, the two dimensional Fourier transformation of $h(x, y)$: [2]

$$\tilde{h}(\mathbf{q}_\perp) = \int_A d^2\mathbf{r}\ h(\mathbf{r})e^{i\mathbf{r}\cdot\mathbf{q}_\perp} \quad \text{and} \quad h(\mathbf{r}) = \frac{1}{A} \sum_{\mathbf{q}_\perp} \tilde{h}(\mathbf{q}_\perp)e^{-i\mathbf{r}\cdot\mathbf{q}_\perp},$$ (3.6)

where the vectors are in the plane perpendicular to the z-axis: $\mathbf{r} = (x, y)$ and $\mathbf{q}_\perp = (q_x, q_y)$. As the position of the membrane $h(\mathbf{r})$ is real, its Fourier transform $\tilde{h}(\mathbf{q}_\perp)$ is even, so that the free energy can be written as a sum over half of the vectors $\mathbf{q}_\perp$ only; the sum is then noted $\sum_{\mathbf{q}_\perp>0}$[3]. The Hamiltonian $\mathcal{H}$ reads in Fourier space

$$\mathcal{H} = \frac{2}{A} \sum_{\mathbf{q}_\perp>0} \frac{K_c}{2}q_\perp^4\ |\tilde{h}(\mathbf{q}_\perp)|^2.$$ (3.7)

Eq. 3.7 yields a Gaussian distribution for the real and imaginary parts of $\tilde{h}(q_\perp)$, $\Re\tilde{h}(q_\perp)$ and $\Im\tilde{h}(q_\perp)$, which are independent variables in the ensemble "$\mathbf{q}_\perp > 0$". The equipartition theorem applies and leads to the position fluctuation spectrum

$$\langle |\tilde{h}(q_\perp)|^2 \rangle = \frac{A\ k_B T}{K_c\ q_\perp^4}.$$ (3.8)

---

[2] For example $\sum_{\mathbf{q}_\perp}$: $q_x = \frac{\pi}{L_x}n_x$ with $n_x \in [-\frac{L_x}{a},\ \frac{L_x}{a}]$, and $q_y = \frac{\pi}{L_y}n_y$ with $n_y \in [-\frac{L_y}{a},\ \frac{L_y}{a}]$.
[3] For example: $\sum_{\mathbf{q}_\perp>0}$: $n_x \in [-\frac{L_x}{a},\ \frac{L_x}{a}]$ and $n_y \in [0,\ \frac{L_y}{a}]$ with a factor 1/2 for $n_y = 0$

Limits of the model

For small length scales, the configurations of individual molecules in the bilayer contribute to the position fluctuation of the surface [114]. The energy associated with the protrusions of single molecules out of the surface is not included in Helfrich's Hamiltonian. For length-scales of the order of the size of the molecules, the continuous theory is no longer valid.

The model is also not valid on very large length-scales because the bilayer can no longer be considered as flat. To quantify the length-scale on which the bilayer is flat, one calculates the orientational correlation function of the membrane [163]. The normal of the membrane in Monge's representation is written as:

$$\mathbf{n} = \frac{\mathbf{z} - h_x \mathbf{x} - h_y \mathbf{y}}{\sqrt{1 + h_x^2 + h_y^2}}. \tag{3.9}$$

The correlation decreases exponentially with ρ ($\rho = (x^2 + y^2)^{1/2}$):

$$\langle \mathbf{n}(\rho) \cdot \mathbf{n}(0) \rangle \propto e^{-\frac{\rho}{\zeta_p}} \text{ with } \zeta_p = \zeta \, e^{2\pi\beta K_c}. \tag{3.10}$$

The persistence length ζ_p is the length-scale under which the membrane can be considered as flat. In the simulations of this thesis, the typical order of magnitude for ζ_p is much larger than the simulation box ($L_x = L_y \simeq 40\,\sigma$ and $\beta K_c \simeq 4$).

As a conclusion, for length-scale larger than the bilayer thickness ($\sim 4\,\sigma$) the continuous model of the elastic theory and the simulation results should be comparable.

3.1.2 Thermal fluctuations in the lamellar phase

Previously, we modeled a floating bilayer as an elastic undulating membrane. The lamellar phase is a stack of such bilayers. The interactions between the bilayers contribute to the stability of the lamellar phase. The model of the elasticity of a lamellar phase proposed by Holyst [80] is obtained by adding to Helfrich's Hamiltonian a potential of interactions between bilayers. In the present section, this model will be used to derive the mean spectrum of position-fluctuations, the correlations between the fluctuation spectra, and the distribution of interlayer distances. In Sect. 3.2, we shall compare the theoretical predictions with the simulation results.

Deformations of the L_α phase

Under mechanical stress, or simply due to thermal fluctuations, the lamellar phase undergoes distortions [30, 28, 41]. These include compressions perpendicular to the director, the splay and the bend of the director (see Fig. 3.5). The energy penalty on the director bend (*i.e.* layer splay) is very high, because this mode imposes large variations of the interlayer distance. As already mentioned the thermal energy is sufficient to induce some splay to the director (*i.e.* to bend the lamellae). The energy of compression depends on the potential of interaction between the bilayers. This deformation has generally to be taken into account as well [28].

NOTATIONS
- splay of the director or layer bend

$$(\nabla.\mathbf{n})^2 \neq 0$$

- bend of the director or layer splay

$$(\mathbf{n} \times [\nabla \times \mathbf{n}])^2 \neq 0$$
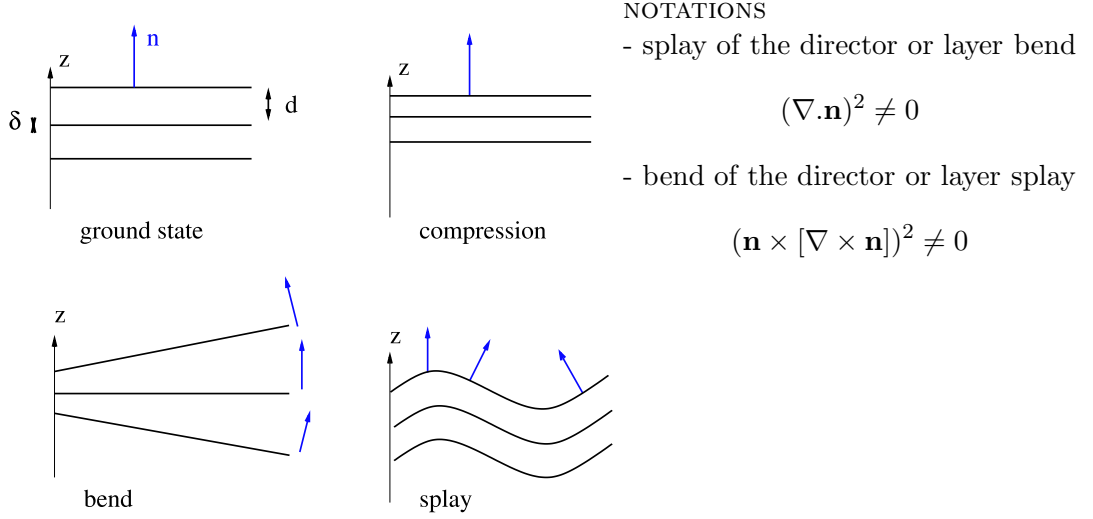
Figure 3.5: Ground state and elastic deformations around the ground state of the smectic A phase. The director may be splay or bend.

A simple model for the elasticity of the lamellar phase

In the following, I present the Discrete Harmonic model [80, 144, 102, 141, 72] to describe the elastic deformations of a L_α phase. It is based on Helfrich's and Canham's Hamiltonian for the single fluid bilayer. The interactions between the bilayers are modeled by a harmonic potential.

The system is described by a discrete set of layers, which are stacked in the z-direction and extend in the (x, y)-plane. The average interlayer distance is d. It is assumed that the position of the n-th layer can be described by a unique height function $z = h_n(x, y)$. The fluctuations about the mean position of the layer are characterized by the discrete displacement $u_n(x, y) = h_n(x, y) - nd$. Again, the surface tension γ of the bilayers is neglected.

The effective Hamiltonian for the smectic A is a direct generalization of Helfrich's Hamiltonian (Eq. 3.1). The interactions between the bilayers n and $n+j$ are taken into account in the free energy density *via* a term depending on the local displacement of both bilayers: $|u_{n+j}(x, y) - u_n(x, y)|$. In the Discrete Harmonic model, only interactions between adjacent layers are considered:

$$\mathcal{F}_{DH} = \sum_{n=0}^{N-1} \int_{A_p} \mathrm{d}x \, \mathrm{d}y \left[\frac{K_c}{2} \left(\frac{\partial^2 u_n}{\partial x^2} + \frac{\partial^2 u_n}{\partial y^2} \right)^2 + \frac{B}{2} (u_n - u_{n+1})^2 \right]. \qquad (3.11)$$

The sums run over the N membranes and their projected area A_p. The first term accounts for the bending energy of individual bilayers, and the second term approximates the free energy of compression. The elasticity of the smectic phase is thus characterized by two elastic constants: K_c, the bending modulus of a single membrane, and B, the compressibility modulus. The elastic constants define the in-plane correlation length $\xi = (K_c/B)^{1/4}$. As for single membranes, the integral over the Gaussian curvature $(u_{xx}u_{yy} - u_{xy}^2)$ has been neglected because the topology of the lamellar phase is supposed to be fixed. The so-called "Discrete Harmonic model"(DH) has proven to be very useful to interpret X-ray scattering data of highly oriented lamellar phases [102, 141, 110, 168] and to study the interfacial properties of thin film of lamellar phase [80, 144, 72].

To avoid confusion, I recall here also the hamiltonian proposed initially by De Gennes [41], which is the continuous version of the DH model.

$$\mathcal{F}_C = \int_V dv \left[\frac{\bar{B}}{2} u_z^2 + \frac{K}{2} (u_{xx} + u_{yy})^2 \right], \tag{3.12}$$

where the displacement field $u(x, y, z)$ takes the values of $u_n(x, y) = h_n(x, y) - nd$ for the discrete values $z = h_n(x, y)$, and some continuous intermediate values in-between. The integral is done over the whole volume V of the sample. The elasticity constants of single membranes B and K_c are linked to the bulk compression modulus $\bar{B}$ and the bulk bending modulus K by the simple relations $B = \bar{B}/d$ and $K_c = Kd$. The bulk elastic constants define the characteristic smectic length $\lambda = (K/\bar{B})^{1/2}$.

The compressibility coefficient B is linked to the effective pair potential between adjacent membranes, $V(d)$, via

$$B = \frac{\partial^2 V(d)}{\partial^2 d}. \tag{3.13}$$

Interactions between membranes

Four interactions between adjacent membranes are usually described [83, 49]: van der Waals attractions, electrostatic forces, hydration repulsions, and undulation repulsions. They depend on the periodicity d of the lamellar phase, on the thickness δ of the bilayers, and on the temperature. Experimentally, the thickness δ is fixed by the nature of the amphiphiles, whereas the periodicty d of the smectic may vary, depending on the concentration of the amphiphiles. The interaction potential, noted $V(d, \delta)$, is given per unit area of bilayer.

Hydration repulsions: when the lamellar phase is hydrated, each polar head is surrounded by several water molecules, and possibly by ionic compounds. When two bilayers are so close that the hydration layers deform, the displacement of water molecules and counter-ions costs energy. As this interaction decreases very rapidly, the potential is classically modeled by [153]

$$V_H(d, \delta) = H_0 e^{-\frac{d-\delta}{\lambda_H}}. \tag{3.14}$$

The range λ_H of the interaction is a few Ångstroms short. The prefactor H_0 is approximatively $4\,k_B T \cdot \mathring{A}^{-2}$. On the length-scale of our coarse-grained model, this interaction is not relevant.

van der Waals attractions: the permanent and induced dipolar interactions between two bilayers through the solvent are always attractive. An approximate expression for a solvent with monovalent ions is [111]

$$V_{VDW}(d,\delta) = \frac{A_H}{12\pi}\left(\frac{1}{(d-\delta)^2} + \frac{1}{(d+\delta)^2} - \frac{2}{d^2}\right). \qquad (3.15)$$

The Hamaker constant, A_H, is of the order of $k_B T$. At long distance, the potential decreases proportionally to d^{-4}.

As no long-ranged interaction is incorporated in our coarse-grained model, this interaction is not considered in the simulations.

Electrostatic interactions: for amphiphilic ionic compounds, electrostatic repulsions among the bilayer and between the bilayers are important. These interactions depend on the concentration of ions in the solvent and the valence of these ions.

For charged amphiphiles, with a solvent containing only the monovalent counter-ions of the amphiphiles, the bilayers repel each other. For large interlayer distances, the repulsion energy per unit area decreases like $(d-\delta)^{-1}$ [159]. For a solvent containing a high concentration of monovalent ions, and large interlayer distances, the electrostatic interactions are screened. Then, the bilayers undergo a repulsion deriving from a potential proportional to $\exp(-(d-\delta))$ [83].

In the case of multivalent ions, correlation effects may induce attraction between the two identically charged bilayers [130]. Such effects are still only partially understood.

In this thesis, no long-ranged interaction is incorporated in the coarse-grained model, so electrostatic interactions are not considered.

Undulation interactions: even neutral bilayers may build a diluted lamellar phase. This cannot be interpreted by van der Waals attractions only. Helfrich [78] showed that neighboring bilayers undergo an effective repulsion: when two fluctuating surfaces are approached, the number of accessible conformations is reduced for both of them. The subsequent entropy reduction costs a free energy inversely proportional to the bending energy of the bilayers:

$$V_{und}(d,\delta) = \frac{3\pi^2}{128}\frac{(k_B T)^2}{K_c(d-\delta)^2}. \qquad (3.16)$$

Other interactions. Both electrostatic effects and undulation interactions are modified by the presence of a complex solute. For example, if a polymer is included between the bilayers of a lamellar phase, elasticity constants of the smectic are modified [17]. Polymer may even absorb on the bilayers, and possibly bridge them. The potentials describing such interactions are highly non-linear.

If the amphiphiles are neutral, or if the solvent has a high dielectric constant, the lamellar phase is stabilized by undulation repulsions. The compressibility modulus associated to Helfrich interactions is

$$B_{und} = \frac{9\pi}{64} \frac{(k_B T)^2}{K_c (d-\delta)^4}.$$ (3.17)

We shall compare compressibility modulus B_{und} (Eq. 3.17) to the compressibility modulus resulting from the simulation analysis in Section 3.2.

In the simulations, steric interactions are present between the bilayers. Effective attractive interactions may also exist between the simulated bilayers: the heads groups of the amphiphiles and the solvent attract each other at intermediate distances. Additionally, at very short distances, direct attraction between the heads groups and the between the tails appear. These lead for example to fusion between bilayers.

In the following, we shall forget the details about the bilayer interactions, representing them by a global compressibility modulus B.

Position fluctuations spectrum - Discrete Harmonic model

The position fluctuations of u_n are conveniently studied in Fourier space, because the Fourier modes decouple and the equipartition theorem applies. We perform continuous Fourier transformations in the x- and y-directions, and a discrete Fourier transformation in the z-direction:

$$u(q_z, \mathbf{q}_\perp) = \sum_n u_n(\mathbf{q}_\perp) \, e^{-iq_z nd},$$ (3.18)

$$u_n(\mathbf{q}_\perp) = \int_A \mathrm{d}^2 r \, u_n(\mathbf{r}) \, e^{-i\mathbf{q}_\perp \cdot \mathbf{r}},$$ (3.19)

$$= \frac{1}{N} \sum_{q_z} u(q_z, \mathbf{q}_\perp) \, e^{+iq_z nd},$$ (3.20)

where q_z is the z-component of $\mathbf{q}$, and $\mathbf{q}_\perp$ the projection into the (x,y)-plane. In the simulations, the system is bounded by the box of dimensions L_x, L_y, L_z and periodic boundary conditions apply. The components of the vector $\mathbf{q}$ take only discrete values $q_\alpha = k_\alpha (2\pi)/L_\alpha$ with an integer k_α. The maximum number of independent z-components k_z is the number of bilayers $N = 5$ or 15. In x and y directions, the size of the simulation box is about $40 \, \sigma$. Using the equipartition theorem, we calculate the average amplitudes of fluctuations in large systems [163]:

$$\Rightarrow \langle |u(\mathbf{q}_\perp, q_z)|^2 \rangle = \frac{N L_x L_y \, k_B T}{2B \left[1 - \cos(q_z d)\right] + K_c \, q_\perp^4},$$ (3.21)

where the brackets $\langle \cdot \rangle$ denotes thermal averages.

Auto-correlation and cross-correlation of fluctuation spectra

Unfortunately, the statistical error of the simulation results for $\langle |u(\mathbf{q}_\perp, q_z)|^2 \rangle$ was too large to allow for a direct comparison with Eq. 3.21. Therefore, I resorted to studying the integrated quantities

$$s_n(\mathbf{q}_\perp) \;\doteq\; \frac{1}{N^2} \sum_{q_z} e^{iq_z nd} \langle |u(\mathbf{q}_\perp, q_z)|^2 \rangle, \tag{3.22}$$

$$= \;\frac{1}{N} \sum_{j=0}^{N-1} \langle u_j(\mathbf{q}_\perp).u_{n+j}(\mathbf{q}_\perp)^* \rangle. \tag{3.23}$$

The quantity $s_0(\mathbf{q}_\perp)$ describes correlations within membranes, whereas $s_n(\mathbf{q}_\perp)$ (at $n > 0$) characterizes correlations between membranes.

In an infinitely thick stack of bilayers, the sum can be replaced by an integral:

$$\sum_{q_z} \;\rightsquigarrow\; (Nd/2\pi) \int_0^{2\pi/d} \mathrm{d}q_z.$$

Inserting the equation 3.21 in Eq. 3.22, and using the formula

$$\frac{1}{2\pi} \int_0^{2\pi} d\tau \, \frac{e^{in\tau}}{a - \cos(\tau)} = \frac{(a - \sqrt{a^2 - 1})^n}{\sqrt{a^2 - 1}}, \tag{3.24}$$

one obtains

$$s_0(X) \;\overset{N \to \infty}{=}\; \frac{L_x L_y \, k_B T}{B \sqrt{X(X + 4)}}, \tag{3.25}$$

$$s_n(X) \;\overset{N \to \infty}{=}\; s_0(X) \cdot \left[1 + \frac{X}{2} - \frac{1}{2} \sqrt{X(X + 4)} \right]^n. \tag{3.26}$$

The dependence in $q_\perp$ has been included in the dimensionless parameter X

$$X = (\xi q_\perp)^4 \geq 0, \tag{3.27}$$

which also depends on the in-plane correlation length ($\xi = (K_c/B)^{1/4}$).

The ratios s_n/s_0 between cross-correlations s_n of membranes and the autocorrelation s_0 depend only on X. Fig. 3.6, representing $s_n(X)$ for $n = 0, 1, 2$ on a double logarithmic scale, shows two scaling regimes with a cross-over around $X_c = 1$ or $q_c = \xi^{-1}$.

If $q_\perp$ is much larger than q_c, the fluctuation spectrum s_0 of a single membrane is proportional to X^{-1} (or $q_\perp^{-4}$). This corresponds to the spectrum of a single isolated membrane without surface tension (Eq. 3.8). In this regime, the cross-correlations between different layers decay exponentially like X^{-n} with the interlamellar distance nd. The fluctuations of different membranes are basically uncorrelated, and the bilayers behave like free, unconstrained membranes.

In contrast, the regime $q_\perp \ll q_c$ is dominated by the coupling of compression modes with the bending fluctuations, where the fluctuation spectrum s_0 of single membranes is
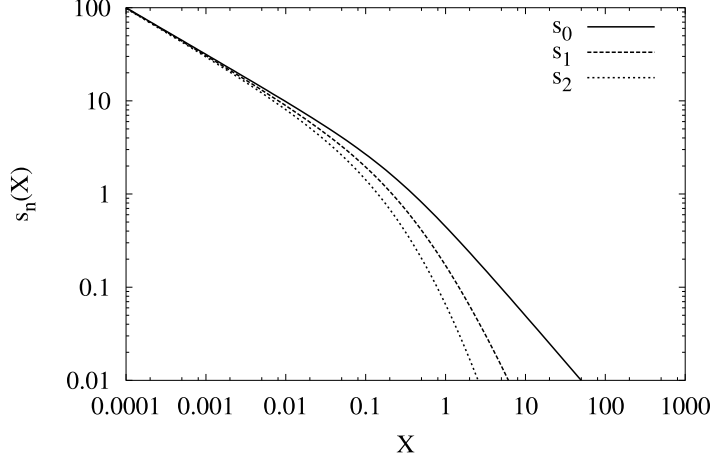
Figure 3.6: $s_n(X)$ for $n = 0, 1, 2$ in log-log scales as a function of the dimensionless variable X. For this graph, the common prefactor $(L_x L_y k_B T)/B$ is set to 1.

proportional to $X^{-1/2}$ (or $q_\perp^{-2}$). The fluctuations grow more slowly with the wavelength than those of free membranes, because the membranes are constrained in the stack. In the infinite wavelength limit ($X \to 0$), the ratios s_n/s_0 tend towards one, *i.e.* the fluctuations of the bilayers are coherent.

Height-height correlations

These results allow us to derive the height-height correlation function $\langle \delta u_n(r)^2 \rangle$, which is usually used to discuss X-ray scattering spectra [102, 141, 110]. It is defined by

$$\delta u_n(x, y)^2 \doteq \frac{1}{N} \sum_{j=0}^{N-1} |u_{j+n}(x, y) - u_j(0, 0)|^2. \tag{3.28}$$

With the change of variable $\tau = \sqrt{X}/2$, one obtains [102, 110]

$$\langle \delta u_n(r)^2 \rangle \stackrel{N \to \infty}{=} \frac{2\eta_1}{q_1^2} \int_0^\infty d\tau \, \frac{1 - J_0(\frac{r}{\xi}\sqrt{2\tau}) \cdot \left(\sqrt{1 + \tau^2} - \tau\right)^{2n}}{\tau\sqrt{1 + \tau^2}}, \tag{3.29}$$

where $r = \sqrt{x^2 + y^2}$, J_0 is the first Bessel function, q_1 is the position of the first diffraction peak ($q_1 = 2\pi/d$), and η_1 is the Caillé parameter [26] characterizing the width of the X-ray diffraction peaks of a highly aligned lamellar phase.

$$\eta_1 = \frac{k_B T}{8\sqrt{BK_c}} \frac{4\pi}{d^2}. \tag{3.30}$$

The upper limit of the integral 3.29 is actually $(\pi/2)^2\xi^2$, not ∞. In the limit of an infinite system, Eq. 3.29 is a good approximation [110].

3.2 Simulation results

After having recalled the discrete harmonic theory for the position fluctuations of the bilayers, I shall compare it to the simulation results.

3.2.1 Analysis of the configurations

The data used for the analysis of the position fluctuations of the bilayers are the same as in Chapter 2. As described in Sect. 2.2.1, the lamellar phase was simulated in the $(N, P, T, \gamma = 0)$-ensemble. The configurations are analyzed to find the positions $h_n(x, y)$ for each bilayer and each configuration. The main steps of the analysis are the following[4]:

1. The space is divided into $N_x N_y N_z$ cells of size (dx,dy,dz) with $N_x = N_y = 32, N_z \sim 96$. For a density of 0.85 particles per volume unit, $dx = dy \simeq 1.3\,\sigma$ and $dz \simeq 1.0\,\sigma$. From one configuration to the other, the size of the cell may vary because the dimensions the simulation box fluctuate. With these parameters, only a few beads occupy each cell.

2. The relative density of tail beads is averaged in each of those cells by counting the number of tail beads $N_{tail}(x, y, z)$ and the total number of particles $N_{tot}(x, y, z)$ in this cell: $\rho_{tail}(x, y, z) = N_{tail}(x, y, z)/N_{tot}(x, y, z)$. The distribution of relative density of tail beads is shown in Fig. 3.8.

3. The membranes are defined as the space where the relative density of tail-beads is higher than a threshold ($\rho_{tail}(x, y, z) > \rho_0$).

    a) The value of the threshold ρ_c is chosen at 80% of the maximum relative density of beads *i.e.*
    $$\rho_c = \max\{\frac{1}{A} \int_A \mathrm{d}x \, \mathrm{d}y \, \rho_{tail}(x, y, z)\}.$$

    As can be seen on the Fig. 3.8, only a few cells have a relative density between 0.5 and 0.9, so that the position of the threshold in this interval does not influence too much the results.

    b) The cells with $\rho_{tail}(x, y, z) \geq \rho_c$ are associated into clusters: two cells of membranes that share at least one vortex are attributed to the same cluster. Clusters whose size is smaller than $N_x N_y/4$ cells are considered as "small clusters" because of are too small to be a membrane. Larger clusters are said to be "membrane-cluster", and are considered as the inner part of a membrane[5].

---

[4] This algorithm is valid only if there are no topological defects in the lamellar phase. To take into account these defects, the algorithm is more complicated than presented in the text (see Section 4.1). I give some more technical details in footnotes.

[5] If there are no topological defects, there should be the same number of large clusters as membrane. A neck is defined as an ensemble of cells connecting two membranes. When it is removed, the two membranes are no longer connected. In term of topological analysis, when the neck is removed, a large cluster separates into two large clusters. To take into account necks, some more tests are
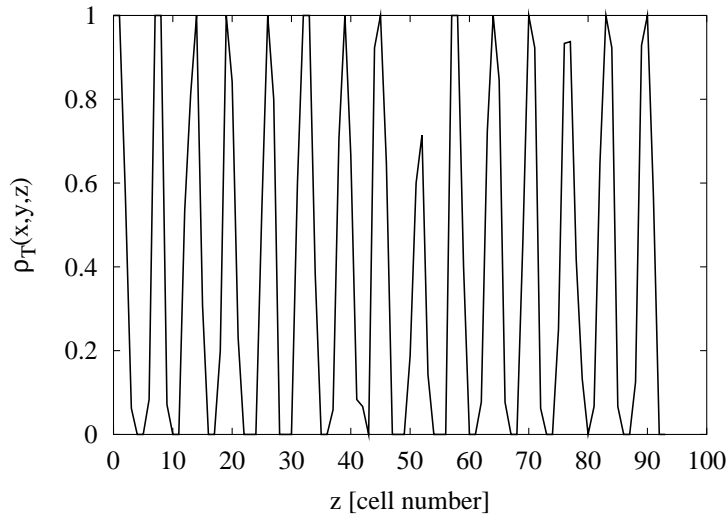
Figure 3.7: Typical profile of the relative density of tail beads (for an arbitrary position (x, y) in an arbitrary conformation), for the parameters $N_x = N_y = 32$ or $dx = dy \simeq 1.3\,\sigma$ and $dz \sim 1.0\,\sigma$.
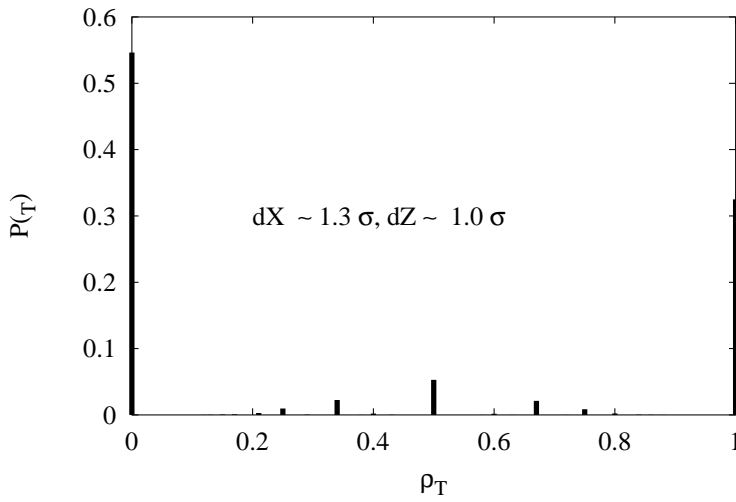
Figure 3.8: Distribution of the relative density of tail beads in the cells for the parameters $N_x = N_y = 32$ or $dx = dy \simeq 1.3\sigma$ and $dz \sim 1.0\sigma$. The configuration is the same as in Fig. 3.7.

---

included in the algorithm:

i. If the number of big clusters is higher than the number of membranes, the threshold is lowered and Point 3 is reiterated.

4. For each ach position (x, y), and for each peak of $\rho_{tail}(x, y, z)$ (see Fig. 3.7), the two heights $h_n^{min}(x, y)$ and $h_n^{max}(x, y)$ for which the density $\rho_{tail}(x, y, z)$ equals the threshold ρ_0 are estimated by a linear extrapolation. The value of the mean position and thickness are computed according to

$$h_n(x, y) = \frac{1}{2}\left[h_n^{max}(x, y) + h_n^{min}(x, y)\right], \tag{3.31}$$

$$t_n(x, y) = \frac{1}{2}\left[h_n^{max}(x, y) - h_n^{min}(x, y)\right]. \tag{3.32}$$

Position of the mean of the membrane
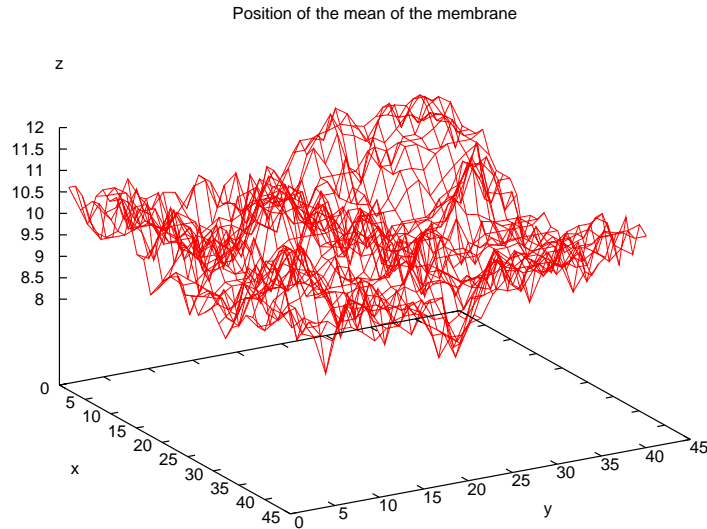
Figure 3.9: Typical conformation of the position $h_n(x, y)$ of a membrane in a stack of five membranes, determined with $N_x = 32$ and $N_y = 32$. See the text for explanation.

Some positions (x, y) may correspond to a hole of the membrane; in this case, one attributes to the hole the mean position of the membrane $(h_n^{hole}(x, y) = \bar{h}_n)$. [6]

ii. If the number of big clusters is lower than the number of membranes, the necks of amphiphiles are detected. A naïve algorithm to detect the necks would be to test for each cell if it is a neck, then to test for each pairs of neighboring cells, then for each three-cells-cluster, *etc.*. Actually, because the necks can be composed of more than ten cells, the algorithm has to be optimized. One possibility is to look first for cluster of cells situated in the solvent layers.

iii. When the number of big clusters equals the number of membranes, the position and thickness of the membranes are computed (see Point 4).

[6]If there is a neck between the neighboring membranes i and j, both $h_i(x, y)$ and $h_j(x, y)$ are set in the middle of the neck. For example, if $\bar{h}_j \leq \bar{h}_i$, then $h^{neck}(x, y) = \left[h_j^{min}(x, y) + h_i^{max}(x, y)\right]/2$.

5. The functions $u_n(x,y) = h_n(x,y) - \bar{h}_n$ undergo a two dimensional Fourier transform, yielding $u_n(q_x, q_y)$, as defined by Eq. 3.19. The correlations $s_0(q_x, q_y)$, $s_1(q_x, q_y)$, $s_2(q_x, q_y)$ of the resulting functions are calculated as in Eq. 3.23. Finally, the radial averages of $s_{0,1,2}(q_x, q_y)$, $s_{0,1,2}(q_\perp)$, are calculated by binning over wave-numbers on a grid independent of the dimension of the box. The ensemble averages of $s_{0,1,2}(q_\perp)$ are used to do the numerical analysis.

3.2.2 Interlayer distances

Let us begin with the distribution of inter-layer distances. The probability to find two membranes at the distance between δh and $\delta h + \delta d$ is written as $P(\delta h)\delta d$. To compute $P(\delta h)$, I measured the probability distribution of $|h_n(x,y) - h_{n+\Delta n}(x,y)|$ for all $n \in [1, N]$ and $\Delta n \in [1, N/2]$, and averaged the probability distribution over n and Δn. The resulting $P(\delta h)$ is shown in Fig. 3.10 for the several Δn in the system containing 15 bilayers.
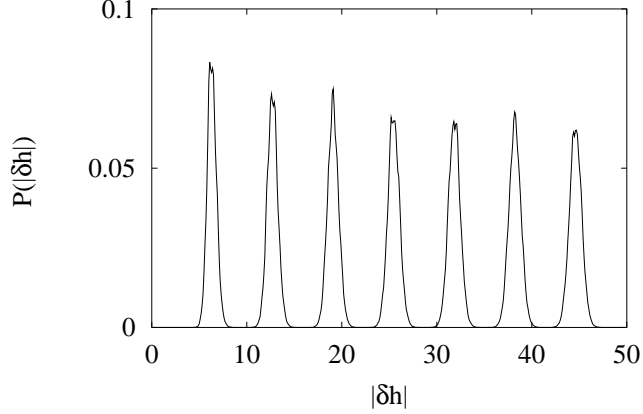
Figure 3.10: Distribution of distances between layers in a lamellar stack of 15 layers. The units for δh is σ, the units for $P(\delta h)$ is σ^{-1}.

The periodic arrangement of the peaks clearly reflects the smectic order of the membranes along the director. The nth peak corresponds to the distance between bilayers which are separated by n layer(s) of solvent. The mean values and variances of each peak are plotted as a function of n in Figures 3.11 and 3.12.

Not surprisingly, the mean interlamellar distances are proportional to n: $\langle |h_n(x,y) - h_0(x,y)| \rangle = nd$. The fitted mean interlamellar distance d equals $6.38\,\sigma$. The variances of each peak $|h_n(x,y) - h_0(x,y)|$ equal the height-height correlation function $\langle \delta u_n(r)^2 \rangle$ defined by Eq. 3.28 for $r = 0$. As shown in Fig. 3.12, the prediction of the DH model (Eq. 3.29) describes the lowest order peaks $n = 1, 2$ relatively well, giving a Caillé parameter of $\eta_1 = 0.055$. At larger n, a discrepancy appears between the theory and the simulation data. It can be attributed to finite size effects: in infinite systems, $\langle \delta u_n(0)^2 \rangle$ increases monotonously with n. On the contrary, in a finite system with periodic boundary conditions, it decreases for n larger than $N/2$ and reaches zero for $n = N$.

Figures 3.11 and 3.12 also display results obtained for systems with 5 layers in order to show the finite size effects. The interlamellar distance does not depend significantly on the system size. The variances are smaller in the smaller system, even for small n. Consequently, the Caillé parameter η_1 obtained for the small system ($\eta_1 = 0.050$) is slightly lower (10%) than the value obtained for the large system ($\eta_1 = 0.055$).
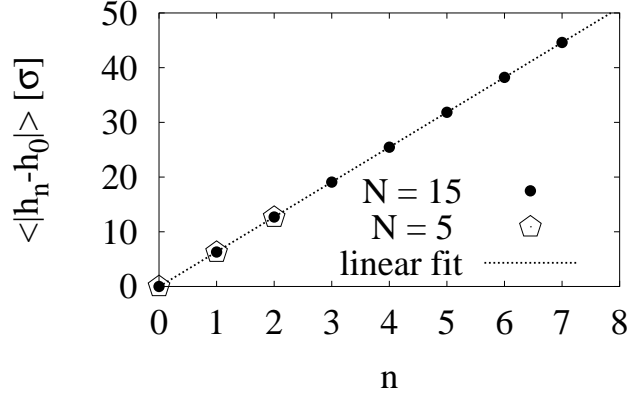
Figure 3.11: Mean inter-lamellar distance between bilayers separated by n solvent layers, $\langle |h_n(x,y) - h_0(x,y)| \rangle$, *vs.* n. The solid line is a linear fit.
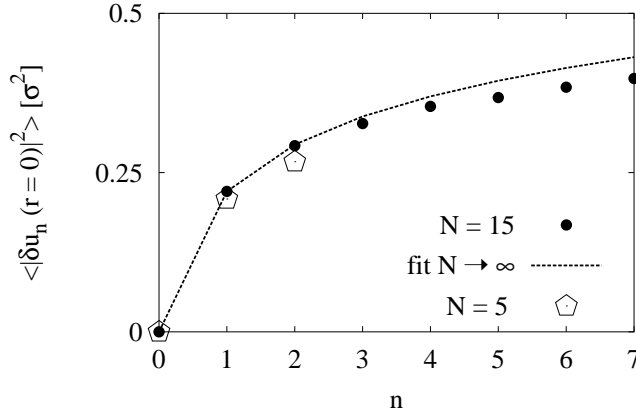
Figure 3.12: Variance of the distribution of inter-lamellar distances between bilayers sep-
arated by n layers of solvent. Data are shown for the large system (15 bi-
layers) and the small system (5 bilayers). The line is a fit of the data for
the large system to Eq. 3.29, with the prefactor $\eta_1/q_1^2 = 0.055$.

3.2.3 Cross-correlation spectra

To study the fluctuation spectra of the position fluctuations, I computed the quantities
$s_n(q_\perp)$ defined in Eq. 3.22, with $q_\perp^2 = q_x^2 + q_y^2$. Fig. 3.13 shows $s_n(q_\perp)/(L_x L_y)$ for
$n = 0, 1, 2$ as a function of $q_\perp$. Unfortunately, the autocorrelation time for the slowest
mode $(q_\perp = 0.1\,\sigma^{-1})$ is comparable to the total length of the simulations $(100\,000\,\tau)$, and
the results for this part of the spectrum are not significant. The correlation time drops
to $2\,500\,\tau$ for $q_\perp = 0.3\,\sigma^{-1}$. On the short-wavelength side, at $q_\perp \leq 1\,\sigma^{-1}$, the continuum
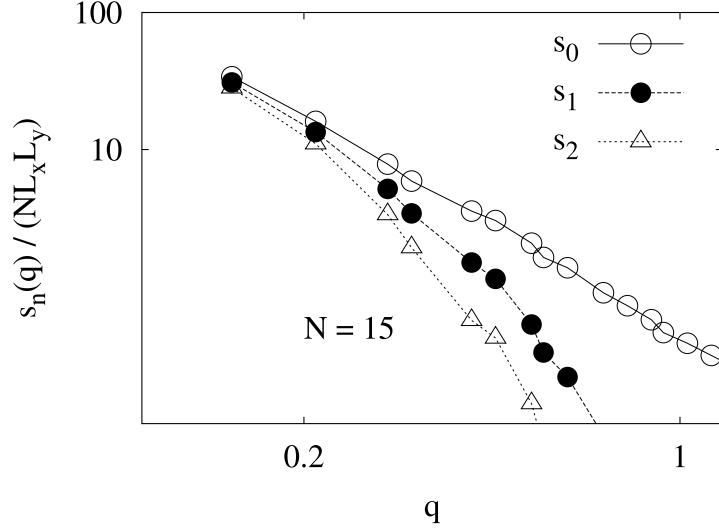
Figure 3.13: Correlation of fluctuation spectra of membrane positions for the system of 15 bilayers $s_n(q_\perp)/(L_x L_y)$ *vs.* $q_\perp$.

theory (Eq. 3.11) is no longer valid. The fluctuations of the membrane thickness then vary according to a $1/q_\perp^{-2}$ behavior [114]. This has be interpreted in terms of an effective surface tension caused by the protrusion of molecules out of the bilayer. In the present system, the protrusion regime is found at $q \simeq 0.8\,\sigma$, corresponding to a length scale of about $8\,\sigma$ (data not shown).

For these reasons, in the following, the data analysis is restricted to the range:

$$0.3\,\sigma^{-1} \leq q_\perp \leq 0.8\,\sigma^{-1}.$$

The direct fit of Eq. (3.25) to the data available for $s_0(q_\perp)$ in this regime turned out to be not very significant. Comparing the ratios s_1/s_0 and s_2/s_0 to the theoretical prediction (Eq. 3.26) was much more rewarding. For the big system (15 bilayers), the agreement between the simulation data and the theory is good (see Fig. 3.14).

I have fitted the results for s_1/s_0 and s_2/s_0 independently, with only one fit parameter ξ. Both fits give very similar values, and the two values yield $\xi = 2.34 \pm 0.01\,\sigma$.

In the small system (five bilayers), the infinite slab approximation $N \to \infty$ becomes very questionable, therefore I have compared $s_{1,2}/s_0$ to the discrete sum obtained by the numerical evaluation of Eq. 3.23 using the approximation given by Eq. 3.21 for the expression of $\langle |u_n(q_z, \mathbf{q}_\perp)|^2 \rangle$ valid for an infinite system. At first sight, the agreement seems reasonable (see Fig. 3.15). However, the in-plane correlation length ξ obtained in the fit, $\xi = 2.6 \pm 0.1\,\sigma$, is significantly larger than that calculated in the big system. Thus, it seems that the finite thickness of the simulated system in the direction of the director affects the elastic properties of the membranes.
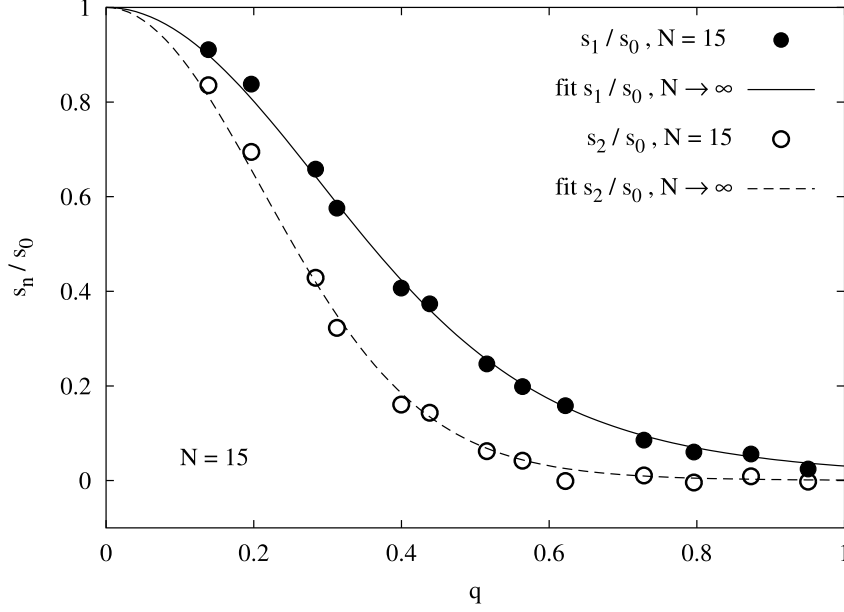
Figure 3.14: Ratio $s_{1,2}(q_\perp)/s_0(q_\perp)$ *vs.* wave vector $q_\perp$ in the system with 15 lamellae. The dots represent simulation data, and the solid lines are fits of Eq. 3.26 with $X = (\xi q_\perp)^4$ and $\xi_1 = 2.35\,\sigma$, $\xi_2 = 2.33\,\sigma$.

To check whether finite size effects also affect the surface tension of the system, I have re-analyzed the data with the surface tension γ as additional fit parameter. The theoretical result (Eq. 3.26) remains the same, but X has to be replaced by $X = \xi^4 q_\perp^4 + \gamma q_\perp^2/B$. Fitting $s_{1,2}/s_0$ with this new X gave $\gamma/B \sim 0.33\,\sigma^2, \xi = 2.35\,\sigma$ in the system with fifteen bilayers. However, given the quality of the data, a slab thickness of fifteen bilayers seems sufficient to obtain agreement with the DH-theory in the limit $N \to \infty$ and $\gamma \to 0$.

Knowing the interlamellar distance $d = 6.38 \pm 0.02\sigma$ and the elastic parameters $\eta_1 = 0.055$ and $\xi = 2.35\,\sigma$ in the large simulated system, we can calculate the bending energy $K_c = 4\,k_B T$ and the compressibility modulus $B = 0.13\,k_B T \cdot \sigma^{-4}$. The surface tension is then about $0.01\,k_B T \cdot \sigma^{-2}$ per bilayer, which we neglected.

3.2.4 Auto-correlation spectra

Knowing the elastic constants, we now turn back to re-inspect the spectrum $s_0(q_\perp)$ of correlations within single membranes. This allows us to compare $s_0(q_\perp)$ directly with the theoretical prediction (Eq. 3.25). The comparison between the prediction of Eq. 3.25 and the data is shown in Fig. 3.16. The discrete harmonic theory describes the data reasonably well.
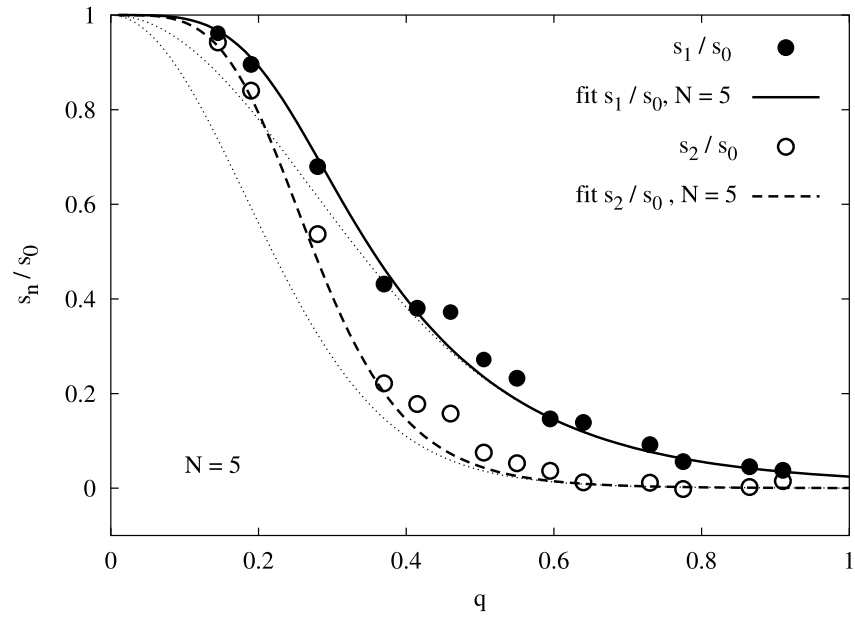
Figure 3.15: Ratio $s_{1,2}(q_\perp)/s_0(q_\perp)$ *vs.* wave vector $q_\perp$ in the system with 5 lamellae. The dots represent simulation data, and the solid lines are fits using the discrete summation of Eq. 3.23 with $\xi_1 = 2.5\,\sigma$, $\xi_2 = 2.7\,\sigma$. The curves obtained with the infinite slab approximation (see Eq. 3.26) and the same values of ξ are also shown for comparison (thin dotted lines) .
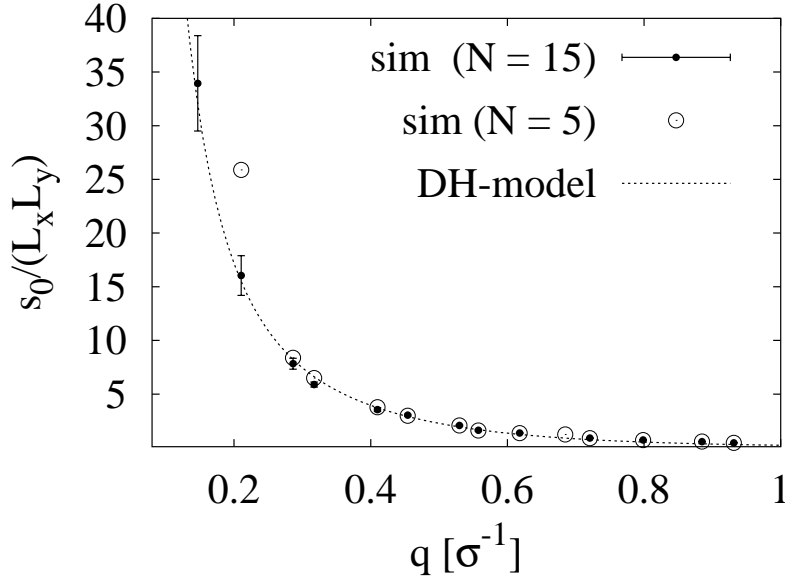
Figure 3.16: Autocorrelation spectra $s_0(q_\perp)/(L_x L_y)$ of the membranes in a stack of 5 or 15 layers. The solid line is the prediction of the "Discrete Harmonic" theory (Eq. 3.25) with the parameters $B = 0.13 \, k_B T \cdot \sigma^{-4}$, and $\xi = 2.35 \, \sigma$ $(\gamma = 0)$.

3.2.5 Discussion

In this chapter, the position fluctuations of the bilayers in a lamellar phase were investigated with molecular dynamics simulations, and compared to the "Discrete Harmonic" model of smectics [102].

The positions of the bilayers were deduced from the local density of tail beads. They have been analyzed both in real space (interlamellar distance distribution) and in Fourier space (auto- and cross-correlations of fluctuation spectra).

The agreement of the simulation results with the Discrete Harmonic theory proposed by Lei *et al.* [102] was reasonable for a simulated stack of fifteen bilayers. We observed finite size effects, and the agreement with the theory was less obvious for the small system. Qualitatively, the position fluctuations of the bilayers were more limited in the smaller system. The analysis of the fluctuations in real space was used to determine the Caillé parameter η_1 of the lamellar phase, and the analysis in Fourier space informed on the in-plane correlation length ξ. From η_1 and ξ, the elastic constants of the lamellar phase (B and K_c) were finally computed. In the simulated stack of fifteen bilayers, the compressibility modulus is $B = 0.13 \, k_B T \cdot \sigma^{-4}$, and the Caillé parameter is $\eta_1 = 0.055$.

Notably, the free membrane regime $q_\perp \xi \gg 1$ of the elastic theory, where the fluctuation spectrum s_0 is expected to scale like $s_0(q_\perp) \propto q_\perp^{-4}$, is never observed in our system. It turns out that the validity of the continuum approximation (Eq. 3.11) breaks down at wavevectors larger than $q_\perp \sim \xi^{-1}$. Obviously, increasing the system size or improving

the statistics to extend the spectrum to small $q_\perp$ will not change this situation. The in-plane correlation length ξ is so small that incoherent fluctuations of membranes cannot be observed.

We can compare these results to those obtained for a lamellar phase which is stabilized by the Helfrich interactions only. Inserting the bending energy $K_c = 4\,k_B T$ and the membrane thickness $\bar{t} = 4.4\,\sigma$, in Eqs 3.17 and 3.30, one obtains: $B^{\text{Helfrich}} = 0.007\,k_B T \cdot \sigma^{-4}$. Thus, the interactions between the bilayers simulated in the present thesis are much stiffer than those predicted by Helfrich's theory (B^{sim} is one order of magnitude largerof B^{Helfrich}). The discrepancy may result from the small size of the simulated system (we have seen that the Caillé parameter increases with the size of the system), or the high amphiphile concentration (Helfrich's theory is valid for large interlamellar distance relative to the membrane thickness). Finally, we have seen that during the total simulation time, the solvent does not diffuse between the different solvent layers (see Section 2.2.2). This constraint, which is not taken into account in Helfrich's calculations, may also increase the stiffness of the bilayers interactions, and diminish ξ.

4 Pores in the amphiphilic bilayers

Defects locally break the symmetry of an ordered medium. They are particularly important in non-equilibrium systems, but they may also appear at equilibrium because of thermal fluctuations, if their energy is of the same order of magnitude as the thermal energy (or lower). The number of defects may enormously increase near a phase transition [37, 81].

The smectic phase contains different kinds of defects [41, 28, 30], which can be classified in point defects and extended defects.

The extended defects of the L_α phase are observable with optical microscopy [6, 16]. In smectics, typical extended defects are focal conics, spherulites, disclinations and dislocations [41]. In addition, the bulk phase of smectics mostly consists of domains with different orientations of the director; the resulting domain boundaries are sources of several kinds of extended defects. Ingenious strategies have been designed to synthesize large lamellar domains without extended defects: "highly aligned lamellar phases"[167, 164, 37].

Highly aligned lamellar phases contain no extended defects, but point defects. Point defects involve fewer molecules than extended defects and are not visible in optical microscopy. They have been investigated using techniques such as freeze fracture electron microscopy, small angle neutron scattering, spin-labeling, birefringence measurements, x-ray scattering, NMR, and fluorescence recovery after photobleaching (see [37] and references in it). Point defects of the lamellar phase can be classified in pores in the bilayers, and necks or passages between two bilayers [19]. Topologically, pores connect solvent layers, necks connect amphiphilic bilayers, and passages connect both solvent layers and amphiphilic layers (see Fig. 4.1). Point defects are difficult to study experimentally

HOLE   NECK   PASSAGE
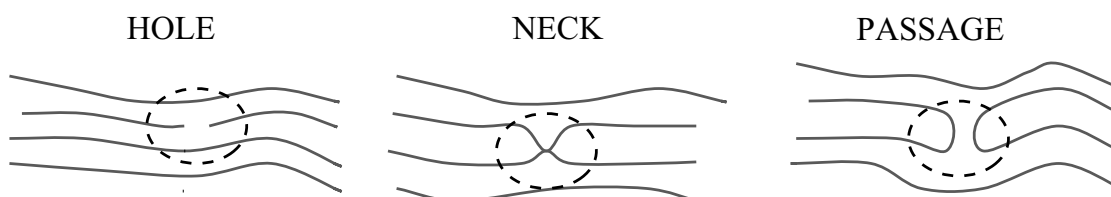
Figure 4.1: Point defects in smectics (inspired by [37]). The solid lines correspond to bilayers, the white background represents solvent regions; the dashed ellipses enclose the defects.

because of their small life-time and their small dimensions (less than millisecond and a

69

few nanometers [210, 118]). Moreover, several kinds of defects coexist. Yet, Constantin *et al.* [37] could distinguish passages from pores experimentally, by studying the diffusion anisotropy of dyes solubilized in a highly aligned lamellar phase.

Chapter 5 of this thesis, and recent publications [189, 162, 77], show that an embedded polymer triggers defects, *e.g.* local fusion, or pores in the bilayers. Therefore, the defects appearing because of thermal fluctuations *before* the insertion of the polymer must be characterized. As we shall see in Section 4.2, it turns out that the lamellar phase simulated for this thesis contains almost no necks or passages, but many pores.

Pores in bilayers play an important role in the diffusion of small molecules across lipid membranes [62, 101, 140], or the fusion of membranes [162, 77, 126]. Opening a transient pore in a biological membrane remains a challenge for drug delivery and gene therapy. The interest in pore formation has greatly increased with the development of electroporation: the application of a short, intense electric field allowing bulky hydrophilic molecules to permeate through lipid membranes. Numerical calculation methods - either with molecular models [112, 127, 81, 113, 207] or with density functional theories [131, 187] - have proven to be useful to describe the local structure of pores in bilayers.

This chapter is organized as follows. The first section presents the mechanism of pore formation proposed by Glaser [67], and the definition of the line tension associated to the formation of an edge around the pore [115]. Next, I outline the analysis of our simulation data: the algorithm detecting the pores, and the observables. In the third section, the results are presented. The spatial distribution of pores within the bilayers is investigated. The pores are then described through their size distribution, shape distribution, and composition profiles. Finally, an analysis of the time evolution of individual pores is presented; I estimate their life-time and briefly discuss the influence of the pores on the permeability of bilayers.

4.1 Background

4.1.1 Pores in bilayers: experiments

In a viscous solvent, like a mixture of water and glycerol, a pore in the bilayer of a unilamellar vesicle may become giant[1], and its dynamics slow enough to be recorded by a camera [169]. This situation is untypical: generally, transient pores can only be observed indirectly, for example through the high permeability of a bilayer.

The formation of pores in bilayers has been studied experimentally on single bilayers rather than on lamellar phases (cell membranes, artificial vesicles and black films). The permeability coefficient of a membrane can be determined experimentally from the decay times of concentration gradients, or by conductance measurements [112].

For unilamellar vesicles, the patch-clamp technique makes precise conductivity measurements possible, even as a function of time (see Fig. 4.2): patches as small as $10^{-8}\,\mathrm{m}^2$ can be examined every microsecond; the measured currents are then of the order of the nano-Ampere [15, 118]. The concentrations, the pressure, and the electrical poten-

---

[1]well, ...micrometers.

tial are controlled on both sides of the membrane. Typical permeability coefficients of
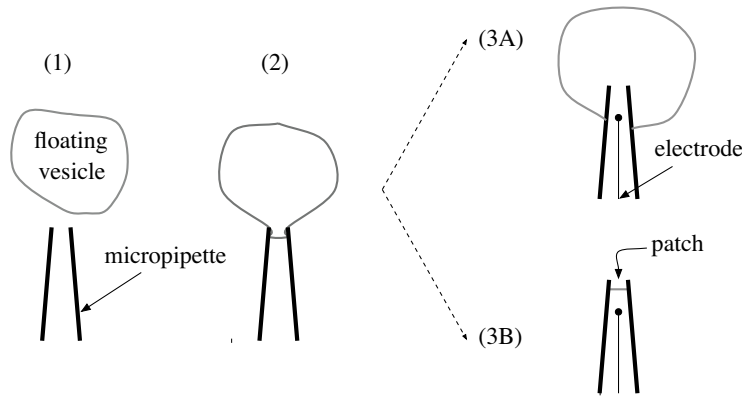
Figure 4.2: Sketch of the patch-clamp technique on a unilamellar vesicle. (1): A micropipette approaches the floating vesicle until it touches it. (2): A controlled depression applied inside the pipette sucks a tiny patch of the membrane into the pipette. (3A): Under a high suction, the patch breaks so that the pipette enters the inner part of the vesicle. (3B): If the pipette is gently pulled out, a tiny patch is cut out of the vesicle. A microelectrode inserted inside the micropipette permits conductivity measurements .

cations through lipid bilayers are of the order of 10^{-14} m·s^{-1}, corresponding to a flux of 10^{-16} mol·cm^{-2}·s^{-1}, or about one ion per second and per square micrometer of bilayer [132, 140].

The permeation process by which ions and small polar molecules cross the phospholipid bilayers is commonly interpreted in terms of two alternative theories: the solubility-diffusion mechanism and the pore mechanism [139]. These two mechanisms differ by the way how the permeability depends on the bilayer thickness [140].

According to the solubility-diffusion mechanism, the lipid bilayer is pictured as a thin slab of hydrophobic medium separating two aqueous phases, and acting as a diffusion barrier. To get from one aqueous phase to the other, the permeant must dissolve into the hydrophobic phase, diffuse across it, and dissolve into the second aqueous phase. Water and halide anions permeate through phospholipid bilayers by the solubility diffusion mechanism [139].

Bordi *et al.* [15] argued that the conductivity of artificial DMPE bilayers under 0.02M of potassium chloride at 20°C is too high to be attributed to a simple passive

diffusion of ions through the inner hydrophobic part of the bilayer. According to the pore mechanism, ions permeate across a bilayer through transient defects produced by thermal fluctuations. Passing through hydrated pores in the bilayers, the permeant circumvents the high energy cost required to penetrate into the hydrophobic region of the membrane. The pore mechanism is the dominant pathway for cations permeating thin bilayers. In particular, the leakage of protons through lipid membranes is attributed to transient pores [101, 140].

The pore mechanism is also evoked to explain the high permeability of lipid membranes under a mechanical, chemical or electrical stress [8, 62, 118]. In the presence of an electric field, the pores are possibly metastable. Melikov *et al.* [118] interpreted the fast transitions between different conductance levels of membrane patches as the opening and closing of single pores. They measured a pore life-time of 3 ms and a mean radius of approximately 1 nm.

Electroporation or sonication have found many applications in biology and medicine. For example, they are used to introduce bulky water-soluble molecules like RNA plasmides into cells: if the stress is not too intense or too long, the pores close off, and the cells survive.

To conclude, the existence of transient pores in lipid bilayers is accepted in the literature despite the experimental difficulties to observe them directly.

4.1.2 Formation of pores in single bilayers

Glaser proposed a simple model for thermally induced pores based on the general principle of nucleation theory [67]. The pore formation is divided into three stages (see Fig. 4.3): at room temperature, the bilayer thickness fluctuates and some hydrophobic tails happen to be exposed to the solvent (pre-hole). The solvent possibly spans the hydrophobic layer, creating a hydrophobic pore. If this pore expands, it becomes energetically favorable for the amphiphiles of the edge to reorient. The configurational rearrangement leads to a hydrophilic pore. The formation of pores is conceived as an

prepore   hydrophobic pore   hydrophilic pore
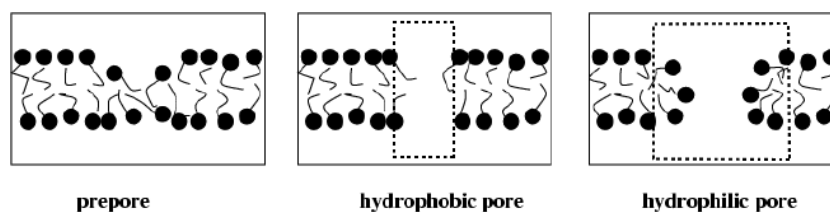
Figure 4.3: Schematic description of pre-holes, hydrophobic and hydrophilic pores in a bilayer (inspired from [67]). The disks are the hydrophilic heads groups, and the thin solid lines are the hydrophobic tails of the amphiphiles. The dashed rectangles emphasize the size of the pore.

activated process. The origin of the activation energy of pore formation in pure bilayers,

as opposed to the pore formation triggered by peptides or other molecules, is not clear [62, 177]. Glaser interpreted it as the energy needed to rearrange the conformation of the amphiphiles in the rim of the pore.

Studies of both hydrophilic [112, 127, 126, 131, 187] and hydrophobic [113, 207] pores were reported. Various theoretical studies, using methods as different as atomic molecular dynamic simulations [112], mesoscopic Monte Carlo calculations [127, 126] and density functional theories [131, 187] observed the spontaneous appearance of hydrophilic pores, but not the hydrophobic intermediates. Molecular dynamics simulations of hydrophobic pores [207] showed that the pores close off in a few picoseconds. As an alternative, it has been suggested [131, 127] that the pore formation may proceed via a simple modulation of the bilayer thickness.

In Section 4.3.1, density profiles across the pores are examined to determine the hydrophobic or hydrophilic nature of the pores in the simulated bilayers.

4.1.3 Energy of a hydrophilic pore

Listers [109] suggested that the appearance of a hydrophilic pore, of radius r in a membrane under lateral tension γ is associated with a reduction of energy $\gamma \pi r^2$ due to the release of surface tension, and with an increase of energy $2\pi r \lambda$ due to the energetic cost of the pore edge [177]. The parameter λ is the line tension of the edge. The net energy change is thus

$$E(r) = E_0 + 2\pi\lambda r - \gamma\pi r^2 \text{ with } r \geq r_{min}, \tag{4.1}$$

where the hydrophilic pore has a minimum radius r_{min}, corresponding approximatively to the thickness of the edge of the pore. Recently, Talanquer *et al.* [187] confirmed Eq. 4.1 using a density functional theory describing amphiphilic bilayers.

According to Eq. 4.1, a pore which has grown larger than the critical size ($r_c = \lambda/\gamma$), enlarges without bound, leading to bilayer rupture. For bilayers with no surface tension ($\gamma = 0$), the critical radius r_c tends toward infinity, and the membrane is stable despite the appearance of holes.

The surface tension exerted in micropipette experiments ranges from $10^{-3}\,\mathrm{mN \cdot m^{-1}}$ to $10\,\mathrm{mN \cdot m^{-1}}$ [155]. Direct experimental measurements of the line tension of lipid bilayers are difficult. Experimental values of line tension have been reported in the range of $1 \cdot 10^{-11}\,\mathrm{N}$ to $3 \cdot 10^{-11}\,\mathrm{N}$ [210, 124]. For hydrophilic pores, the line tension is interpreted as a sum of two terms [127, 115]: (i) The chemical potential of the amphiphiles necessary to form the rim of the pore (the amphiphilic molecules inside the dotted rectangle of Fig. 4.3); (ii) The energy cost of the configurational reorientation of the molecules in the rim. Both contributions are of the order of $5 \cdot 10^{-12}\,\mathrm{N}$ to $2 \cdot 10^{-11}\,\mathrm{N}$ under typical conditions. Therefore, the energy barrier $\pi\lambda^2/\gamma$ for the membrane rupture equals the thermal energy for a surface tension of about $100\,\mathrm{mN \cdot m^{-1}}$. Such a surface tension is not typical for biological systems under normal conditions.

Eq. 4.1 has been included in various models describing the proliferation of pores [62, 186, 175]. For example, Shillcock *et al.* [175, 177] studied the membrane rupture using Monte Carlo simulations based on Eq. 4.1, and showed that the rupture can be
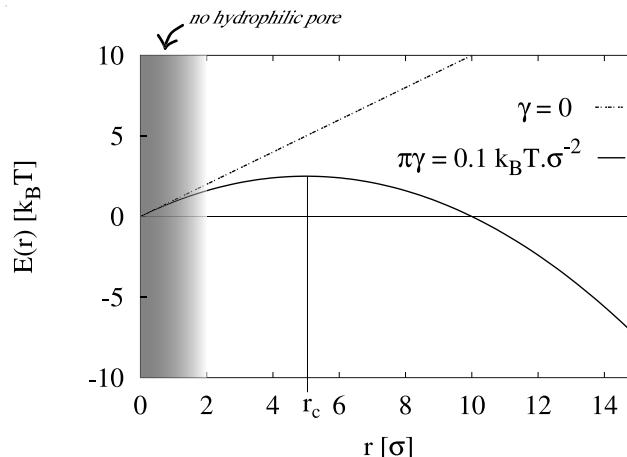
Figure 4.4: Excess free energy due to a single pore of radius r of line tension $2\pi\lambda = 1\ k_B T \cdot \sigma^{-1}$, for the surface tensions $\gamma = 0$ and $\pi\gamma = 0.1\ k_B T \cdot \sigma^{-2}$. For radii smaller than the minimum radius (shaded region), the hydrophilic pore does not exist.

triggered by a single large pore, or by the proliferation of small pores if the activation energy of pore formation is low.

4.2 Simulation details

This section outlines the algorithm which detects the pores in the bilayers, and the observables computed to study them.

The data were produced with the same simulation parameters as for the fluctuations of the bilayers in Chapter 3 (see Section 3.2). The small system contains 10 240 tetramers and 10 240 solvent beads, which form, at equilibrium, five bilayers of about 2 000 molecules each. The large system, three time larger in z-direction, is composed of fifteen bilayers of about 2 000 molecules each.

For the time-independent studies (Sections 4.2.1, 4.3.1, 4.3.3), I performed one run of $100\,000\,\tau$ for the large system; the results are based on the analysis of 400 configurations recorded every $250\,\tau$. For the time dependent studies (Section 4.3.4), I performed one run of $400\,\tau$ for the small system; the results are based on the analysis of 400 configurations recorded every $1\,\tau$.

4.2.1 Topological detection of defects

If the bilayers of the lamellar phase fluctuate only slightly around their mean planar position, their positions can be described in Monge representation with the functions $\{h_n(x,y)\}$ (see Fig. 3.4). If there is a point defect at the position (x,y) of the lamellae number n, the bilayer position position $h_n(x,y)$ is not defined *a priori*. So the presence

of defects makes the analysis of the simulation data with Monge representation difficult. On the other hand, topological fluctuations permit to detect the presence of defects [81].

I performed a simple topological analysis to detect *point* defects in the lamellar phase; it is based on the hypothesis that the system contains no *extended* defects.

As explained in Section 3.2, the density of the system is analyzed in a three dimensional rectangular grid. For each cell of the grid, whose volume is about $1.7\sigma^3$, the relative density of the tail bead $\rho_{tail}(x, y, z)$ is computed. The cells for which ρ_{tail} is larger than a threshold are grouped into three dimensional clusters[2]. A big cluster is defined as a "membrane-cluster" if its projected area on the plane of the bilayers is larger than one forth of the bilayer[3]. If the lamellar phase has no defects, the analysis yields one big "membrane-cluster" per bilayer. If there are fewer membrane-clusters than bilayers, one concludes that two membranes are linked with a neck or a passage, as sketched in Fig. 4.5. If there are more big clusters than bilayers, there may be an extended defect;
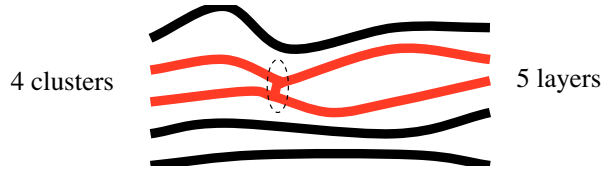
Figure 4.5: Example of the detection of a defect by a topological analysis. The number of bilayers is known; the number of clusters is computed. A discrepancy between the two reveals at least one topological defect in the system. The solid lines represent bilayers of membrane-clusters; and the white background represents the solvent regions.

Actually, this situation was not encountered.

The same topological analysis is done with grid cells which do not belong to the inner part of the bilayers. These cells, in which the fraction of tail beads is smaller than a threshold, are grouped into "solvent-clusters". If there are less solvent-clusters than solvent layers, there is a pore in one of the bilayers.

In fact, all the configurations generated had at least one pore. On the contrary, necks and passages were rarely detected (in about 5% of the configurations). Therefore, I focused the analysis on the pores in the bilayers.

4.2.2 Observables describing the pores

The previous topological analysis is quite straightforward, but it is only qualitative: it permits to detect the presence of defects in the whole system without informing on their number or position.

---

[2]Two cells belong to the same cluster if they share at least one vortex of the grid.

[3]Some small clusters may appear depending on the value of the threshold. The membrane-clusters were about 10 times larger than those small clusters.

Therefore I used a complementary analysis to detect the position of the pores. The algorithm is based on the one used to determine the positions and thicknesses of the lamellae (see Section 3.2.1). For each position (x, y), the tail-density $\rho_{tail}(x, y, z)$ oscillates as a function of z, with maxima corresponding to the inner part of the bilayers (see Fig. 3.7). For each membrane, a peak is expected. If a peak is missing, a pore is attributed to the corresponding membrane[4].

The pores of a given membrane of the lamellar system are recorded as an ensemble of N coordinates $\{\mathbf{r}_i\} = \{(x_i, y_i)\}$, defined on the grid of the analysis. Fig. 4.6 B shows a representative example of positions where a pore is detected. A snapshot of the corresponding membrane is displayed on the left panel of Fig. 4.6.
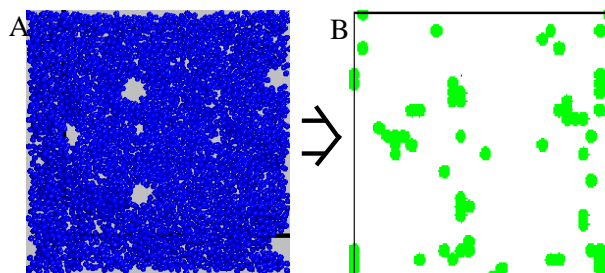
Figure 4.6:   *A*: Snapshot of the solvophobic beads of a bilayer (top view). *B*: Grid-positions where a pore was detected. The parameters of the analysis are the same as in Section 3.2: the projected area $L_x L_y$ is divided in $N_x \times N_y = 32 \times 32$ plaquettes with a surface of $\sim 1.7\,\sigma^2$. In the z-direction, the cells have a thickness of $dz \sim 1\,\sigma$.

For each membrane, the positions $\{(x_i, y_i)\}$ are grouped into two dimensional "pore-clusters". I have chosen to take the mesh of the grid rather small, in order to describe the shape fluctuations of the pores.

The areas and the contour lengths are computed with an algorithm calculating Minkowski functionals of a digital image (see Appendix 4.5). Those observables are approximative, because they are computed on a rectangular grid, which divides the projected area $L_x L_y$ into $N_x \times N_y = 32 \times 32$ plaquettes of dimensions dx and $dy = dx \sim 1.3\,\sigma$. The contour length is a multiple of the mesh size of the grid dx and the area is a multiple of $dx^2 \sim 1.7\,\sigma^2$.

The position of the pore is defined as the center of mass of the plaquettes belonging to the pore:

$$\mathbf{r}_{cm} = \frac{1}{n_p} \sum_{i=1}^{n_p} \mathbf{r}_i, \tag{4.2}$$

---

[4]The analysis is only valid if there are no necks. If there is a neck, the number of peaks is also reduced. I dealt with this problem by detecting the necks and removing them before determining the position of the pores. A neck is defined as a small number of cells of a membrane-cluster whose deletion divides the initial membrane-cluster into two membrane-clusters.

where n_p is the number of plaquettes belonging to the pore-cluster and $\mathbf{r}_i$ the position $\{x_i, y_i\}$ of the plaquette number i. The gyration matrix g is also computed:

$$g^{\alpha\beta} = g_0 + \frac{1}{n_p} \sum_{i=1}^{n_p} (r_i - r_{cm})^\alpha \cdot (r_i - r_{cm})^\beta \quad \text{with} \quad \alpha, \beta \in \{x, y, z\}, \qquad (4.3)$$

where g_0 is the gyration matrix of one plaquette. I approximated it by $1/4$ times the identity matrix.

4.3 Simulation results

4.3.1 Local structure

Composition profiles trough the holes.

Most theoretical studies of pore formation are based on the mechanism proposed by Glaser *et al.* [67] (see Sect. 4.1): First, thermal fluctuations overcome an energy barrier to create a small hydrophobic hole, then the amphiphiles of the edge change their conformation to form a hydrophilic pore. This reorganization was observed for example by Müller *et al.* [127, 126] in Monte Carlo simulations of amphiphilic diblock-copolymers.

The simulation data produced for this thesis also show this conformational reorganization. One first indication of the rearrangement into a hydrophilic pore is that the number of contacts between the tail-beads and the solvent-beads is the same in the pores and in an unperturbed bilayer.

To determine whether the pores are hydrophilic or hydrophobic, one investigates the composition profiles $\rho_{tail}(x, y, z)$, $\rho_{head}(x, y, z)$, $\rho_{solvent}(x, y, z)$ around the pores. For this analysis, only the pores whose area is between $4\,\sigma^2$ and $16\,\sigma^2$ are taken into account. The composition profiles are averaged over the directions around the center of the pore, with the center of the pore as origin. The result are composition profiles in radial coordinates $\rho(r, z)$, where r is the distance to the pore center, in the plane of the bilayer, and z the distance relative to the bilayer midplane. As the composition profiles are supposed to be symmetric relative to the mid-plane of the bilayer, I also averaged the profiles over the heights $+z$ and $-z$. In Fig. 4.7, the resulting averages are displayed as a function of r and $|z|$.

Far from the pore ($r \geq 5\,\sigma$), the bilayer structure is nicely visible: layers of solvent alternate with amphiphilic bilayers. Within the bilayer, the heads coat the tails. Closer to the pore, the density of tail beads decreases. A small pocket of solvent appears around the position $r \to 0$ and $z \sim 2\sigma$; the head-beads nevertheless shield the tail-beads. As a conclusion, the pores whose area is larger than $4\,\sigma$ are hydrophilic. Magnifying the contour profile of tail beads in the vicinity of the pore yields Fig. 4.8. We can see that the hydrophobic part of the bilayer is slightly thicker in the pore edge. This effect was predicted by May [115]. He calculated the form of the bilayer edge with a molecular model, by minimizing the conformational excess free energy of the amphiphiles of the edge, relative to the shape of the edge.
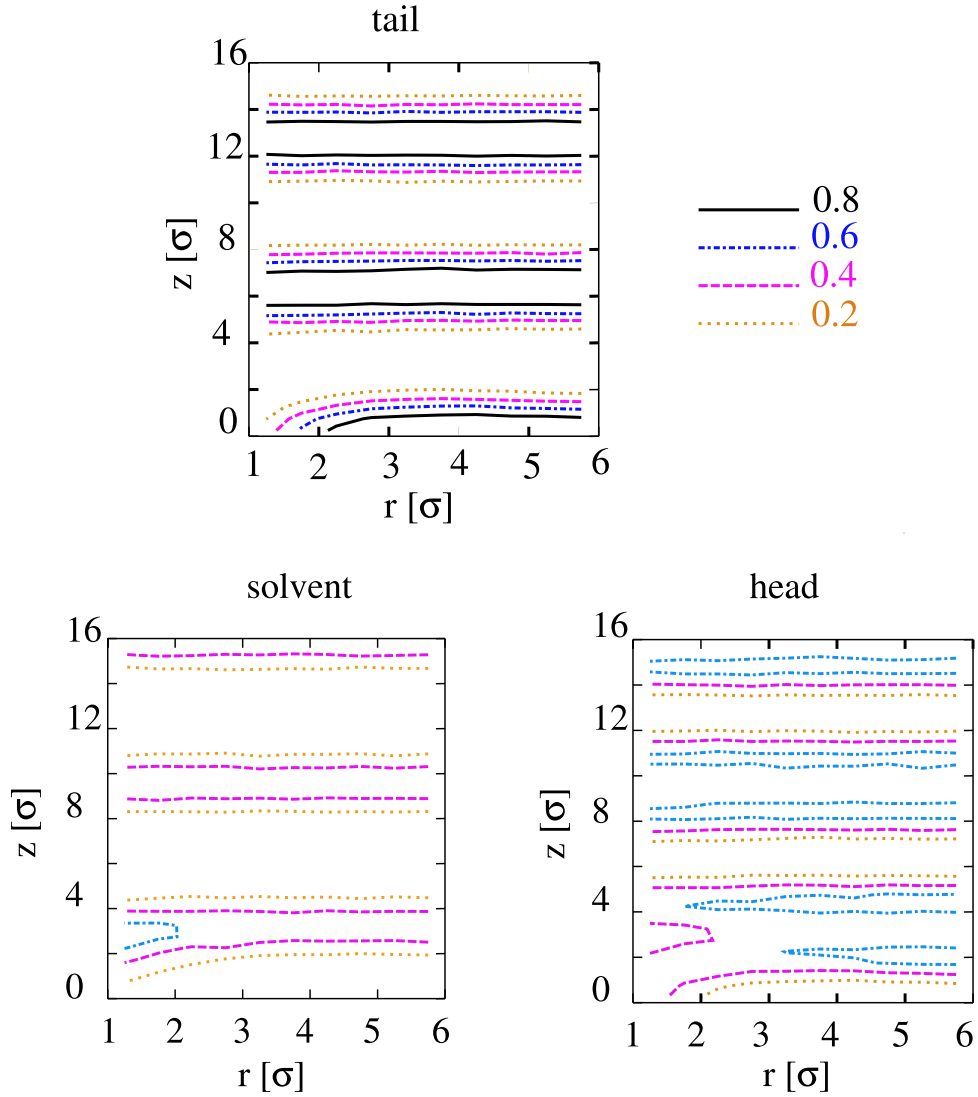
Figure 4.7: Compositions profiles around the center of pores whose area is between $4\,\sigma^2$ and $16\,\sigma^2$.

The rearrangement of the amphiphiles in large pores can also be observed on the orientation of the amphiphilic molecules around the pores. In Fig. 4.9, the middle bonds ht of amphiphiles h_2t_2 belonging to one bilayer are represented by color-coded cylinders: the colors range from blue for bonds aligned with the director, to red for bonds perpendicular to the director. The reorientation of the molecules in the pore edge described by Glaser occurs for large pores. Around smaller pores, the reorientation is not always clear. Because of the difficulty to localize exactly the edge of the pores, it was not possible to show any quantitative correlation between the local nematic order
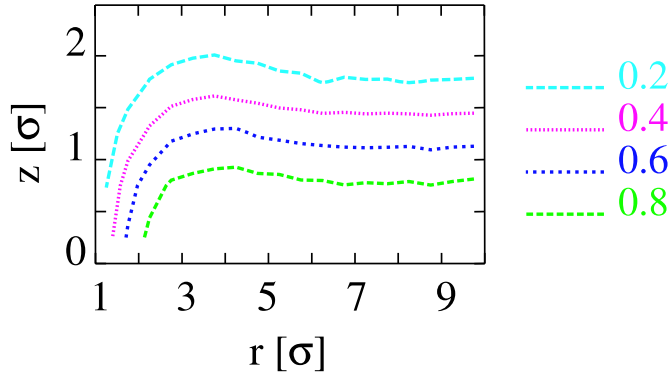
Figure 4.8: Compositions profile of the tail beads around the center of pores (enlargement of the panel of Fig. 4.7 corresponding to the tail beads density).
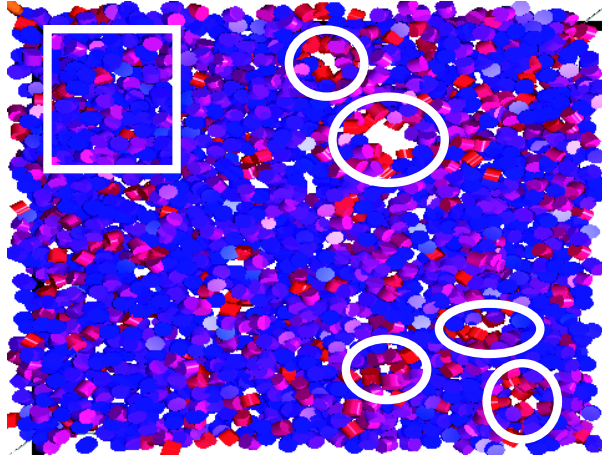
Figure 4.9: Snapshots of ht bonds in one bilayer (top view). The bond orientation is color-coded: blue for bonds aligned along the director, red for bonds perpendicular to it, and a gradient proportional to $\cos^2\theta$ for intermediate cases - θ is the angle between the bond and the director. The ellipses mark position of large pores, where the rearrangement can be observed. The rectangle encloses a region without pores.

parameter and the size of the pores.

Finally, the simulation data show that the number of solvent beads in the pore is proportional to the area of the pore (data not shown), following the equation $n_s = 0.2\,a$, where n_s is the number of solvent beads and a the area of the pore (in units of plaquette area). To contains one beads of solvent, the pore must then have an area a larger than $8.5\,\sigma^2$, *i.e.* a radius r larger than $1.6\,\sigma$. This length may serve as an estimate for the thickness of the edge thickness.

4.3.2 Spatial distribution

In each recorded snapshot, in each bilayer, the average number of pores is 9.9 ± 1.3. Their total area corresponds to approximatively 1% of the projected area $L_x L_y \sim 1850\,\sigma^2$ of the bilayer. Among the 10 pores, 5.7 ± 1.0 have the minimum size of one plaquette ($a \sim 1.7\,\sigma^2$).

Are these pores distributed randomly within a bilayer? To answer this question, we shall investigate the pair distribution function of the pores within each bilayer.

Pair correlation function
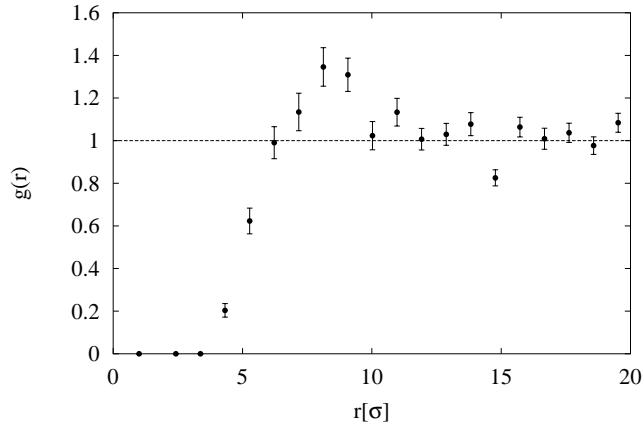
Figure 4.10: Pair correlation function between the centers of pores within the bilayers.

Because of the small number of pores per bilayer, the statistics on the pair correlation function is relatively poor. The correlation function displayed in Fig. 4.3.2 has been obtained from 100 configurations containing 15 bilayers recorded every $250\,\tau$. The correlations between the holes in different configurations are negligible (see Sect. 4.3.4), but there are correlations between the distributions of holes in the different bilayers of the same configuration. Those correlations are neglected in the analysis, so the error-bars plotted in Fig. 4.3.2 are underestimated.

Two qualitative trends are cleary visible: for large distances ($r \gtrsim 10\,\sigma$), no significant correlation is detected, whereas for small distances ($r \leq 7\,\sigma$), the correlation function drops from 1 to 0. One can interpret the depletion by an effective short-ranged repulsion between the pores. Let me recall that, due to the analysis, the pores undergo a "hard-core" repulsion: two pores can neither superpose, nor touch each other. For example, as the position of the pore is calculated on a grid of mesh $\sim 1.3\,\sigma$, two pore centers cannot be closer than $\sim 2.6\,\sigma$. In fact, $g(r)$ remains very small for $r \leq 4\,\sigma$. Two effects may contribute to the depletion at small distances: First, the pore edge may be relatively thick ($2\,\sigma$, which is close to the value $1.6\,\sigma$ estimated previously). Second, the pore size distribution is broad (see in Section 4.3.3).

Distribution of holes: Minkowski analysis

The pore distributions have also been analyzed with a complementary tool: Minkowski functionals. Minkowski functionals are used in various areas of mathematics and physics to analyze high-order correlations of spatial distributions. They find many applications in physics, *e.g.* the determination of fractal dimensions or the analysis of percolation threshold. The analysis presented here is inspired by Ref. [84], whose authors studied the spatial distribution of defects in a thin film of polymers. As discussed by Mecca and Michielsen [22, 116, 122], Minkowski functionals are complementary to spatial pair correlation functions because they contain information on many-points correlations.

The principle of the analysis is sketched in Figs. 4.11 and 4.12. A so-called germ is "attached" to each point. This germ is a geometrical form with a characteristic length l and orientation θ. I have chosen a square of area l^2 with a fixed orientation. Those

POINTS   *GERMS*   *PATTERN*
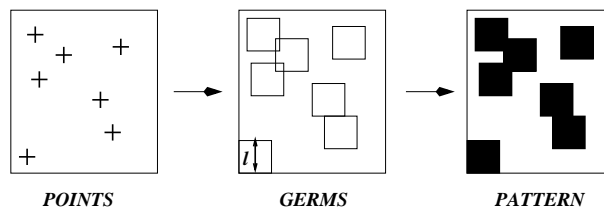
Figure 4.11: Principle of the construction of the pattern from a point distribution. The germs are oriented squares.

squares compose a pattern which is analyzed with Minkowski functionals using the algorithm published by Milchielsen [122] (see Appendix 4.5). In two dimensions, three Minkowski functionals are defined: the area A the contour length U and the Euler characteristic χ (see Fig. 4.12). In two dimensions, the Euler characteristic is the number of connected components minus the number of holes in those clusters. The dependence of

A   *U*   *X*
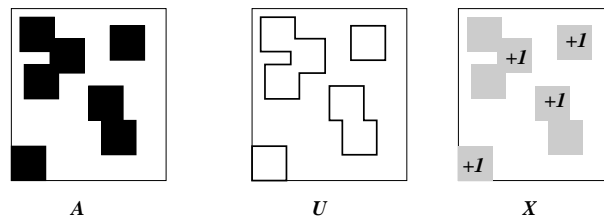
Figure 4.12: Illustration of the three Minkowski functionals of the two-dimensional pattern of Fig. 4.11: the area A, the contour length U, and Euler characteristic χ.

the Minkowski functionals on the length l contains information about the distribution of points.

In Appendix 4.5, the Minkowski analysis is tested on random sets of points. In par-

ticular, the influences of the density of points and of the self-avoidance between points
are investigated. One conclusion is that the algorithm shows relatively strong finite
size effects. As a consequence, I compared the simulation results to those of "random
self-avoiding sets of points"(RSA): ensembles of points whose coordinates have been
generated by a random number generator, under the condition that the points do not
superpose. For the analysis, RSA sets were generated on the same grid and with the
same density distribution as the ones of the pores. In Fig. 4.13, the dimensionless
Minkowski functionals m_0, m_1, m_2 (proportional respectively to A, U and χ) are shown
as a function of the dimensionless coverage factor $x = l^2 \rho$, where ρ is the density of
points (see Appendix 4.5 for more details). The error-bars are relatively large. The pore
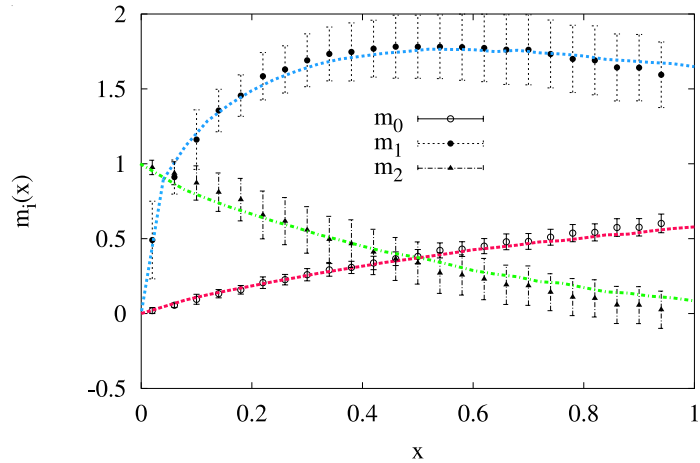
Figure 4.13: Minkowski analysis of the pore distribution. The symbols are the results
obtained with the distribution of pore centers in the bilayers. The curves
are obtained with RSA sets of points generated with the same density dis-
tributions as the one of the pores.

distributions are not significantly different from RSA sets of points. The small differ-
ences of the mean values between the simulation results and the RSA sets are compatible
with the short-ranged repulsion seen in the pair-correlation function (see Appendix 4.5
for a systematic study).

To conclude, the pores in the bilayers are not randomly distributed: they repel each
other at very short distances. The spatial pair correlation function between pores and
the Minkowski analysis are compatible with a simple model including only the intrinsic
hard-core repulsion between the pores.

4.3.3 Size and shape

The following section contains the results about the size and the shape of the pores in
the bilayers of the simulated lamellar phase.

The observables are the area of the pores, their contour length and their radius of

gyration; they are measured on a two dimensional grid as described in Sect. 4.2. The mesh size fluctuates: $dx = dy \sim 1.3 \pm 0.05\,\sigma$; one plaquette of the grid has then an area $dx \times dy \sim 1.7\,\sigma^2$. In the following, the notation "[plaquette]" indicates that the area is expressed in units of the plaquette area and the contour length in units of the mesh size.

Distributions of size and contour length

The probability distribution of the area of the pores, $P(a)$, is represented in Fig. 4.14 in a linear-log plot. As expected, the probability to find a pore decreases rapidly with
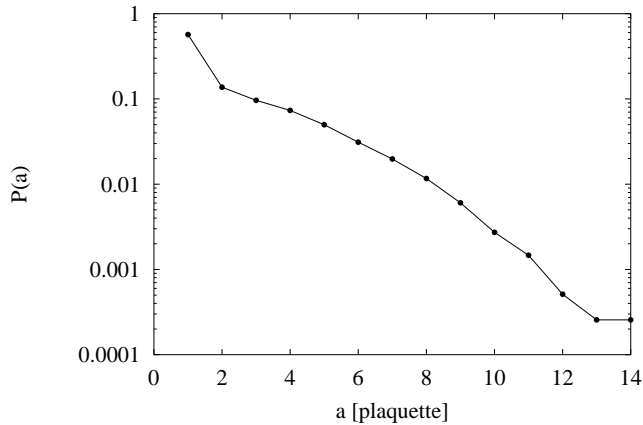
Figure 4.14: Probability distribution of the area of the holes in a semi-log plot.

the area a of the pore; 60% of the $\sim 20\,000$ holes detected have an area of only one plaquette ($\sim 1.7\,\sigma^2$) and less than 10 % extend over more that 4 plaquettes ($\sim 7\,\sigma^2$). The area distribution monotonously decreases in the accessible range, with no evidence for a preferred pore size. The observed pores are not equilibrium structures of a stable perforated lamellar phase, but are due to thermal fluctuations in the stable bilayers of the smectic.

The probability distribution of the contour length, $P(c)$, is shown in Fig. 4.15 in a linear-log plot. Again, the probability decreases rapidly with the contour length. Pores of contour length $c = 8$ seem to be favored, or from another point of view, pores of contour length $c = 6$ seem to be disfavored. I attribute the non-monotony to the influence of the grid on the analysis rather than to the presence of a metastable pore. To justify this assumption, I calculated the degeneracy $g(c)$ of the contour lengths c by generating systematically all possible configurations of pore-clusters (see Table 4.1)[5].

The ratio $P(c)/g(c)$, shown in Fig. 4.16 in a linear-log plot, is monotonously decreasing. Thus, the non-monotonic behavior of $P(c)$ is an artifact of the finite rectangular grid, due to the low value of $g(c)$ for $c = 6$.

---

[5] The algorithm generates systematically all pore-clusters on a two dimensional grid, and counts the ones with the expected contour length. This is very time-consuming.
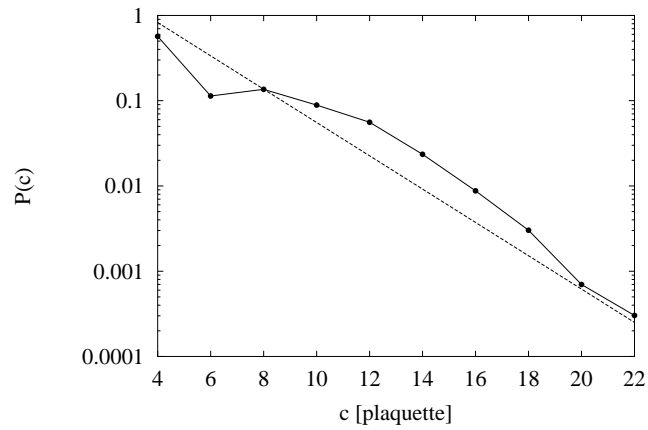
Figure 4.15: Distribution of the contour of the holes in a semi-log plot. The dashed line is simply an exponential decrease, as a guide for the eyes.

c	4	6	8	10	12	14	16
g(c)	1	2	9	36	168	715	2000 (?)

Table 4.1: Degeneracy of the contour length c of clusters of pixels connected by at least one vortex. All the positions of the grid are indistinguishable; x- and y-directions are distinguishable. Because of the high cost of such calculations, the value are exact only up to $c = 14$. The value for $c = 16$ is an estimate.
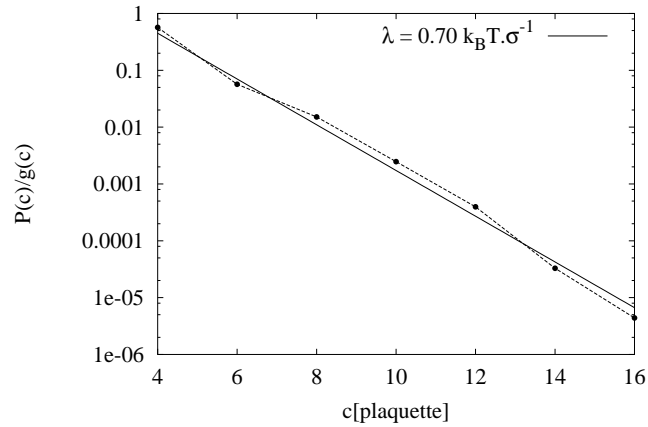
Figure 4.16: Probability distribution function of the contour of the holes, divided by the degeneracy of the contour length (linear-log plot) given in Table 4.1.

Line tension of the pore edge

To interpret the probability distributions, and eventually estimate the line tension of the pores, I make the following assumptions:

- As the simulation algorithm imposes a zero surface tension on the bilayers ($\gamma = 0$), the relevant energetic parameter is the contour length c rather than the area a of the pores. The free energy of a single pore, F, depends explicitly on the contour length of the pore. It depends only implicitly on the area:

$$F(c, a) = F(c).$$

- The pores do not interact. The probability distribution is approximated by the Boltzmann distribution

$$P(c) = e^{-F(c)/(k_B T)} = g(c)e^{-E(c)/(k_B T)}, \tag{4.4}$$

where $E(c)$ is the energy of a single pore of contour c, and $g(c)$ is the degeneracy of the contour length c.

- The effective energy $E(c) = -k_B T \ln[P(c)/g(c)]$ is modeled by a linear function of the contour length $E(c) = E_0 + \lambda c$, where λ gives an estimation of the line tension of the edge of the pore, in accordance with Eq. 4.1.

In Fig. 4.16, we can observe that the energy $E(c)$ is well described by a linear function. The line tension resulting from a linear fit is $\lambda = 0.7 \pm 0.1 \, k_B T \cdot \sigma^{-1}$ ($\sim 5 \cdot 10^{-12} \, J \cdot m^{-1}$) which agrees with the values calculated by May [115] for the excess free energy of the packing rearrangement of amphiphiles in the edge. Previous results report line tensions in the range of $10^{-11} \, J \cdot m^{-1}$ to $3 \cdot 10^{-11} \, J \cdot m^{-1}$ [210, 127, 124], *i.e.* larger than the present value. In these references, the line tension includes also the excess free energy necessary to transfer the amphiphiles from a reservoir to the edge of pore. This contribution (typically $10^{-11} \, J \cdot m^{-1}$) is proportional to the surface tension of the bilayer [127, 115] and vanishes in the present case.

As a conclusion, the size distributions computed with the simulations are compatible with the usual mesoscopic model of pores energetics and permit to compute the approximate line tension of the pore edge.

Shape of the pores

To characterize the shape of the pores, I have studied their two-dimensional gyration matrix (see Eq. 4.3). The two (positive) eigenvalues of the gyration matrix are noted ρ_1^2 and ρ_2^2, The sum of the eigenvalues $R_g^2 = \rho_1^2 + \rho_2^2$ is the square of the radius of gyration of the pore, and the relative difference $\alpha = |\rho_1^2 - \rho_2^2|/R_g^2$, its asymmetry. The asymmetry is zero for a circular pore and tends towards one when the pore is being elongated in one direction.

Fig. 4.17 represents the radius of gyration of the pores as a function of their area. As expected, the square of the radius of gyration increases linearly with the area of the
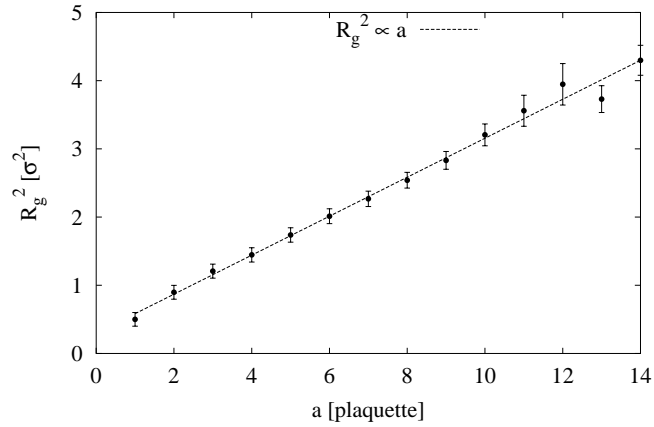
Figure 4.17: Square of the radius of gyration of the pores, as a function of their area.

pores: a linear fit yields $R_g^2 \sim 0.17a + 0.29$ (both in units of σ^2). The proportionality factor 0.17 is slightly larger than the proportionality factor obtained for a homogeneous disc ($[2\pi]^{-1} \sim 0.15$).

As illustrated in Fig. 4.18, the asymmetry of the pores does not vary significantly with the size of the pores, except for the smallest pores, whose asymmetry is imposed by the finite mesh size of the grid. This suggests that only one length-scale is sufficient to
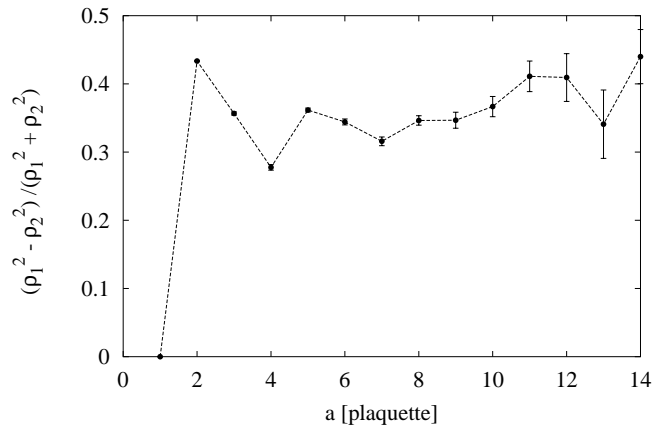
Figure 4.18: Asymmetry of the pores as function of their area.

describe the pore dimension. Notably, the average asymmetry is not zero (0.35 ± 0.05). In fact, since the bilayers are flaccid, there is no reason why the pores should be circular.

Correlation between area and contour length

Using Monte Carlo simulations of triangulated surfaces containing pores, Shillcock *et al.* [177] showed that for large pores, the area a scales with the perimeter c like $a \propto c^{3/2}$. Due to the following results, they suggested a formal analogy between pores in membranes, two dimensional flaccid vesicles, and two-dimensional ring polymers:

(i) Flory [58] showed that in two dimensions, the radius of a self-avoiding polymer R_{F2} scales with the number N of monomers as $R_{F2} \propto N^{3/4}$ when N tends to infinity.

(ii) Leibler *et al.* [103] found the same scaling law with Monte Carlo simulations of two-dimensional vesicles. The vesicles are modeled by closed, planar, tethered chains of length N, with a bending energy and a pressure difference between the inside and outside of the vesicles. For the particular case of no bending rigidity and no pressure difference, the enclosed area follows the scaling laws $a \propto R_g^2 \propto N^{3/2}$.

(iii) Shillcock *et al.* [175, 177] investigated the growth of thermally induced pores in a two-dimensional fluid membrane with Monte Carlo simulations. The membrane is represented by a triangulated surface. Pores appear by an activated process; their subsequent growth is controlled by an edge energy per unit length, which is a parameter of the model. For low line tension and barrier of formation, they observe two scaling laws: the area a scales with the perimeter L like $a \propto L^2$ for small holes, and like $a \propto L^{3/2}$ for large holes.

The analogy between polymers, vesicles and pores is clear when these objects are modeled as closed, self-avoiding, planar random-walks whose energy depends only on the number of steps. Interestingly, the present molecular approach supports the mesoscopic models [103, 177]. Fig. 4.19 shows the pore area a as a function of the contour length c in a log-log representation. The simulation data are well fitted by the scaling law $a \propto c^{3/2}$.
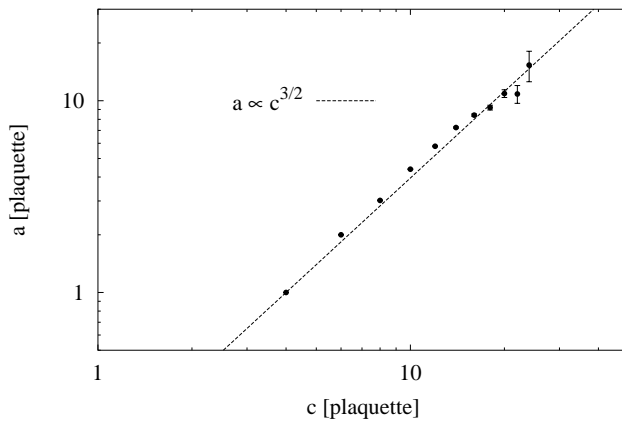
Figure 4.19: Area of the pores as a function of their contour length (log-log plot).

To summarize, I investigated the size and shape distributions of the pores in the

bilayers. An approximate value for the line tension of the pore edge was deduced from the distribution function of the contour length. The pores are not circular: The scaling law $a \propto c^{3/2}$, linking the area a to the contour length c, describes well the simulation data.

4.3.4 Time evolution

The following Section discusses the dynamics of the pores in the bilayers.

First, we shall look at the dynamics of the total area of the pores, the total contour length, and the total number of pores. The correlation times of these averaged observables give a first estimate of the time-scale of individual pore dynamics.

Then, the algorithm used to trace the time evolution of the positions and sizes of each pore is presented. It permits to obtain the life-time of the pores, their trajectory and the time evolution of their size. I interpret the time evolution of the contour length c of the pores as a biased random walk in one dimension, and characterize the transition probabilities of this random walk. This approach permits to compare the life-time distribution of the pores to a theoretical prediction obtained for a random walk in a linear potential [90].

Time scale of the pore dynamics

As a first approach, the averaged variables describing the pores are studied: the number of pores, their total area and total contour length. The time evolution of the total number of pores is plotted in Fig. 4.20. To investigate the time autocorrelation function
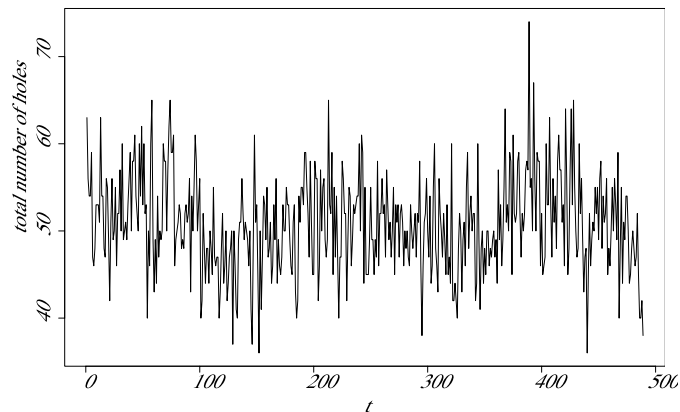
Figure 4.20: Time evolution of the total number of pores in a stack of five bilayers (time unit: τ).

of the pore number, it is instructive to separate the contributions of the different pore sizes. For example, Fig. 4.21 displays the autocorrelation functions of the total number of pores with an area of one plaquette ($a = 1$), of two plaquettes ($a = 2$) and of more than

two plaquettes ($a \geq 3$). For pores of the smallest area (one plaquette, or about $1.7\,\sigma^2$),
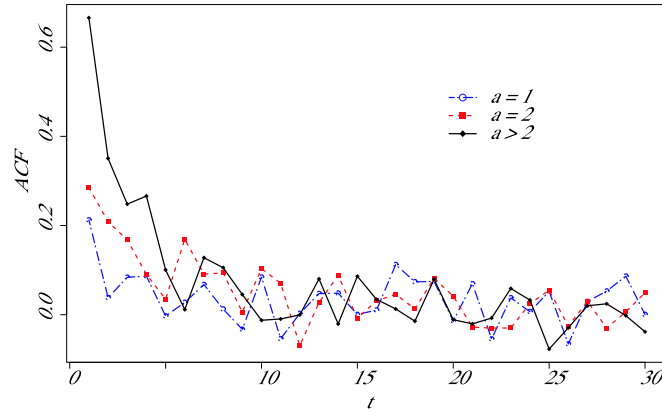
Figure 4.21: Autocorrelation functions of the total numbers of pores with an area of one plaquette ($a = 1$), of two plaquettes ($a = 2$) and of more than two plaquettes ($a \geq 3$). The time unit is τ.

the correlation time seems to be smaller than the observation time ($1\,\tau$). Actually, the data are rather noisy because of the difficulty to distinguish between a small pore and a fluctuation of the bilayer thickness. The correlation time of the number of pores however increases up to about $2\,\tau$ when the smallest pores are not taken into account ($a \geq 3$).

Similar correlation-times are found for the total contour length and total area of the pores (see Fig. 4.22).
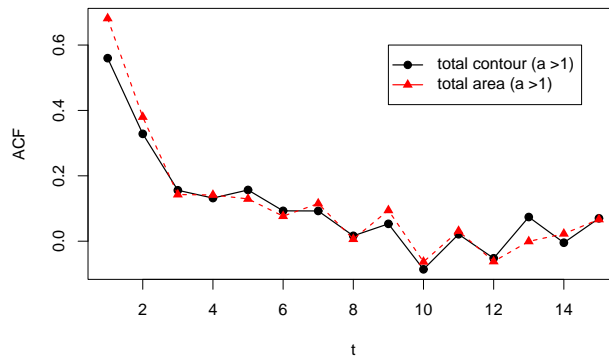
Figure 4.22: Autocorrelation functions of the total areas and contour lengths as a function of time (time unit: τ). The pores of area $a = 1$ are not included in the analysis.

As a conclusion, the time interval used to follow the pore dynamics should be smaller than a few time units. I have chosen the upper limit $dt = 1\,\tau$ to reduce the computational cost.

Details of the algorithm

This section presents the algorithm developed to describe the time evolution of individual pores. The numbers, positions, sizes and shapes of the pores are computed as described in Section 4.2 for each configuration.

The algorithm links iteratively the pores at time t to their descendants at time $t + dt$, then the pores at time $t + dt$ to their descendants at time $t + 2dt$, *etc.*. If there are no descendants, the pore "dies". Analogously, a pore without antecedents is "new born". The life-time $\mathcal{T}$ of a pore is the time interval between the "birth time", where the pore is detected for the first time, and the "death time", when the pore disappears. If a pore disappears, and reappears later at the same place, it is considered as a new, different pore.

The relationship between a pore and its descendants has to be chosen. For physical reasons, the position of a pore is expected to vary continuously with time. A "natural" choice is therefore to take as descendant the nearest pore of the parent pore (see Fig. 4.23).

parent pores (t)   descendants (t + dt)
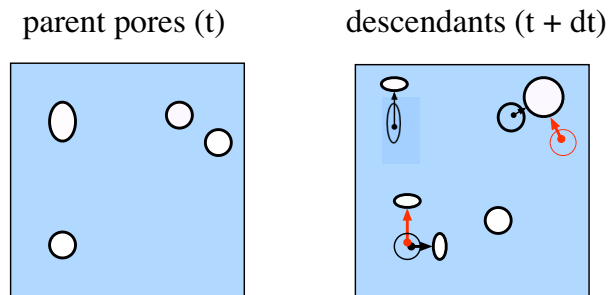
Figure 4.23: Scheme of the time evolution of pores within a bilayer. The pores are represented by ellipses, the displacements during the interval of time by small arrows. Red arrows show displacements that are not accepted because of the "nearest neighbor criterion": when two descendants are in the vicinity of the parent pore, the nearest descendant is chosen. Similarly, when two parent pores compete for the same descendant, the nearest parent is chosen.

Additionally, the maximal displacement of one pore during the time dt is limited to $\sim 2.8\,\sigma$, *i.e.* larger than the mesh of the grid of the analysis ($\sim 1.3\,\sigma$) and smaller than the typical distance between two pores ($\sim 5\,\sigma$).

A representative example of the dynamics of a pore is illustrated by Fig. 4.24. Both the contour length and the area take only discrete values, because the pores are defined on a grid with a finite mesh size. The minimal jump amplitudes are $|da| = 1$ for the area

and $|dc| = 2$ for the contour length. The amplitude of the jumps of contour length and area are limited (see Fig. 4.24). Consequently, the "nearest neighbor"criterion should give results similar to other criteria based on the continuity of the contour legnth or area of the pore.
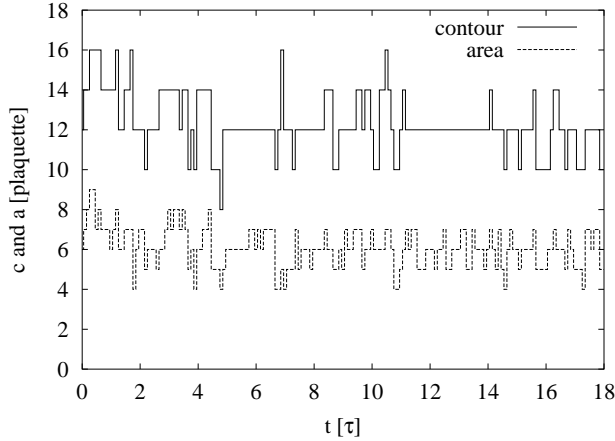
Figure 4.24: Example of the time evolution of the contour and area of one of the pores, with a time of observation $dt = 0.1\tau$.

A priori, a pore may have several descendants and several parents. In other words, we expect some fusions or divisions of pores (see Fig. 4.25). Such situations complicate
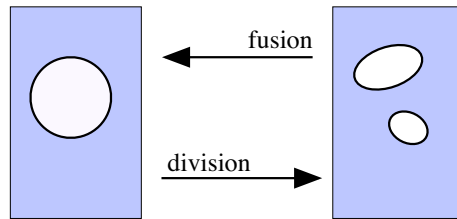
Figure 4.25: A fusion is defined as the association of pores into a pore at least as big as each of them, and a division as the dissociation of a pore into two pores which are both at least as small as the initial one.

the study of the data because the time evolution of a pore is then not uniquely defined. The algorithm intrinsically neglects the fusions and divisions because a single "parent-descendant"pair is registered at each time-step dt. It turns out that in more than 99,0% of the cases, the descendant pore could be determined unambiguously[6]. In the remaining 50 cases, approximatively 20 cases were fusions or divisions. The other cases were neither fusions nor divisions. For example, a big pore may fuse with a small one to become a small pore. Such unphysical situations may be due to the noise related to the pores

---

[6]All other pores were at a distance at least twice the distance of the nearest one.

of size $a = 1$. To conclude, given the quality of the data, neglecting the fusions and divisions of pores seems justified.

In the following Sections, the time-evolution of individual pores is discussed.

Diffusion of the pores within a bilayer

As the bilayers of the L_α phase are fluid, the pores may diffuse within the bilayers. In Section 4.2, we defined the position of a pore as the "center of mass"of the plaquettes of the pores. Fig. 4.26 shows typical trajectories of pore centers, projected on a plane parallel to the bilayers.
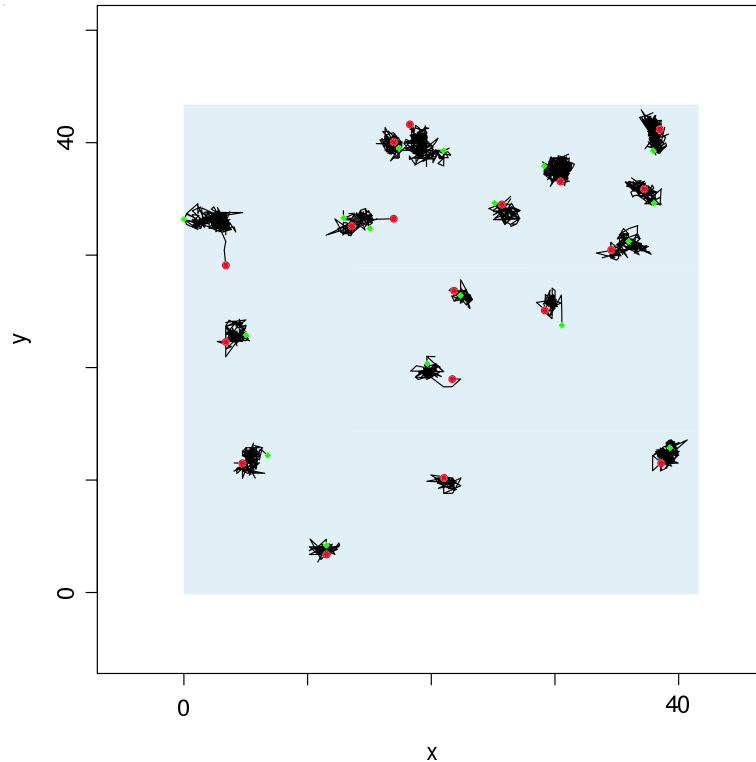
Figure 4.26: Examples of trajectories of the center of pores with the time of observation $dt = 1\,\tau$. Green points show the initial positions, red points the final positions. The effect of the noises of the data can be observed on some pore trajectories, which have a strange "tail"at their beginning or at their end. The figure is a superposition the trajectories of pores belonging to different bilayers.

The trajectories seem rather compact: the diffusion of a pore is limited by its small life-time. This phenomenon does not come from the algorithm. Indeed, the algorithm presupposes that the displacement during one time interval is smaller than $3\,\sigma$ to avoid "random correlation", but this distance is much larger than the actual displacement of

the pores.

Stochastic interpretation of pore growth

Next, we study the dynamical evolution of the pore size. The following description focuses on the dynamics of the contour length c, because we assumed that the free energy of the pores depends explicitly only on the contour length (see Sections 4.3.3). The degeneracy of the contour length is nevertheless taken into account in the effective potential $F(c) = F_0 - k_B T \ln P(c)$, where P is the probability distribution function of c.
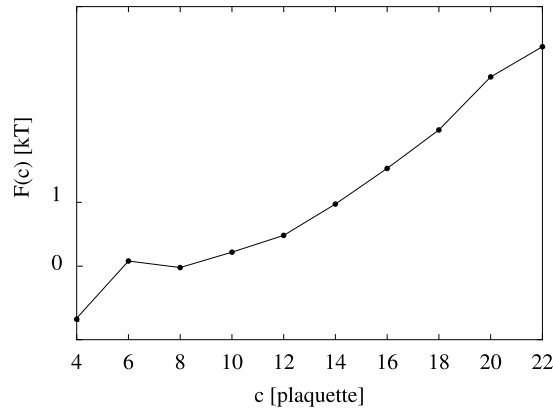
Figure 4.27: Effective free energy of the contour length calculated from the probability distribution function shown in Fig. 4.15 (F_0 is taken arbitrarily).

The numbers of jumps from c to $c + dc$, during the interval dt of time, denoted by $\Omega(c, dc, dt)$, characterize the dynamics of the contour length. The comparison between $\Omega(c, dc, dt)$ is easier if the results are normalized by the total number of jumps with an initial contour length c:

$$P(c, dc) = \frac{\Omega(c, dc, dt)}{\sum_{dc \neq 0} \Omega(c, dc, dt)}.$$

In Fig. 4.28, the probability $P(c, dc)$, that a jump with the initial contour length c has the amplitude dc ($dt = 1\,\tau$) is shown.

As the contour length of the pore is a continuous variable of time, the jump probability $P(c, dc)$ decreases when the amplitude of the jump $|dc|$ increases. 80% of the observed jumps correspond to the amplitude $|dc| = 2$.

One expects that if the time of observation is small enough, we should observe exclusively jumps of the smallest amplitudes $|dc| \leq 4$[7]. In fact, even for the observation time $dt = 0.1\,\tau$, jumps with an amplitude $|dc| \geq 6$ appear. The frequency of jump may be broadly distributed.

---

[7]It is possible that the contour length increases by 4 when only one pixel is added to the pore-cluster.
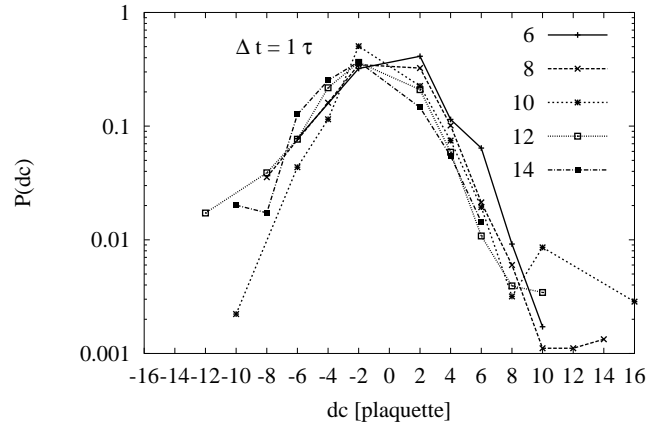
Figure 4.28: Probability of jumps from c to $c + dc$ as a function of dc for the possible values of the initial contour length c (linear-log scale).

Life time distribution

The probability distribution of life-time $P(\mathcal{T})$ decreases very rapidly with $\mathcal{T}$ (see Fig. 4.29). No preferred life-time is observed in the available range. An exponential decrease
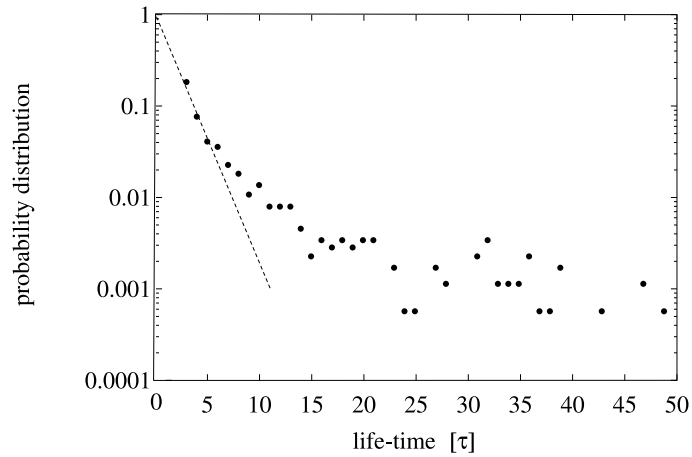
Figure 4.29: Life-time distribution of the pores with an observation time $dt = 1\,\tau$ (linear-log plot). The total number of pores is about $10\,000$. The dashed line is a simple decreasing exponential law, as if the pores had a fixed probability p^* to disintegrate during the time of observation dt. For life-time larger than $50\,\tau$, the number of pores is so low that the probability distribution is no longer significant.

does not fit the simulation data over the whole range of life-times (see, for example,

the dashed line in Fig. 4.29). The probability distribution is broad, with a long tail indicating particularly stable pores. The probability of disintegration of the pore seem to decreases when the life-time increases. This effect may emerge through a correlation between the life-time and the size of the pores.

To test this hypothesis, I plotted the mean contour length of the pores as a function of the life-time of the pore (see Fig. 4.30). No averaging was performed: each pore
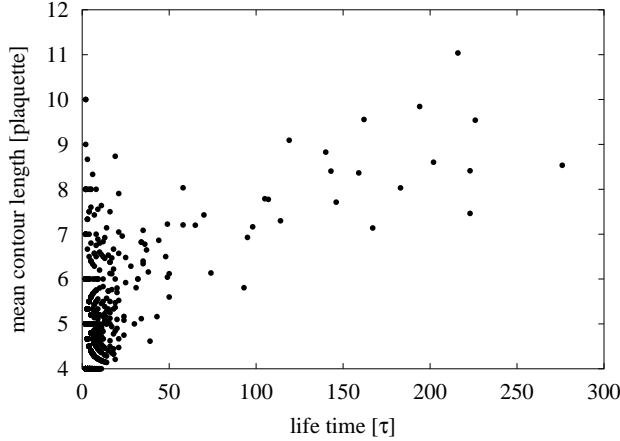
Figure 4.30: Contour lengths of the pores averaged over their respective life-times, as a function of their life-times. The motifs obtained for small life times are due to the discretization of both the life-times and the contour lengths of the pores.

is represented by one point in Fig. 4.30. For small life-times, no correlation can be observed. For life-times larger than $10\,\tau$, a correlation appears: the larger the pore, the longer it lives.

Mean life-time of the pores

The time-evolution of the pore contour-length is complex, and the form of the life-time distribution is not obviously interpreted. In the following, the time evolution of the contour length c (*e.g.* Fig. 4.24) is compared to a very simple model: a random walk in a linear potential (RW-LP model). This model reproduces one particular feature of the simulation data: the disintegration probability depends on the life-time. Moreover, the probability distribution of the life-times is known [90].

The RW-LP model describes a random walk in a semi-infinite one-dimensional space with discrete states labeled $n = 0, 1, 2, ..., \infty$. The variable n represents one half of the contour length. The trajectories consist of discrete jumps between nearest neighbors, at an average rate W. The probability to hop towards the upper neighbor $(n \rightarrow n+1)$ is $p^+ = (1-b)/2$. In the other direction $(n \rightarrow n-1)$, it is $p^- = (1+b)/2$. The bias $0 \leq b \leq 1$ measures the tendency to walk towards $n = 0$, where the walker dies

(absorbing boundary). Physically, the parameter b increases the line tension of the pores.

The life-time is then defined as the time needed for a walker starting at $n_0 = 1$ to reach the absorbing boundary $n = 0$ for the first (and last!) time. The probability $Q(n, t|n_0)$ that a walker starting from the state n_0 reaches the state $n = 0$ for the first time after having walk during the time t is [90]

$$Q(n, t|n_0) = \frac{n - n_0}{t} \left(\frac{1+b}{1-b}\right)^{\frac{n-n_0}{2}} e^{-Wt} I_{n-n_0}\left(Wt\sqrt{1-b^2}\right), \qquad (4.5)$$

where $I_\nu, (\nu \geq 1)$ is the modified Bessel Function of the first kind, W and b the two parameters of the model. The time t of Eq. 4.5 corresponds to the life time of the pores.

Of course, the simulation data are more complicated than the RW-LP model:

- About 20% of the jump dc observed in the simulation data have an amplitude larger than $|dc| = 2$. These jumps are not taken into account in the RW-LP model.

- The effective potential is not linear (see Fig. 4.27).

Despite the simplicity of the model, Eq. 4.5 describes the non-exponential decrease of the life-time distribution. For life-times larger than $5\,\tau$, the values $n_0 = 1, n = 0, b = 0.2, W = 0.5\,\tau^{-1}$ are reasonable (see Fig. 4.31).
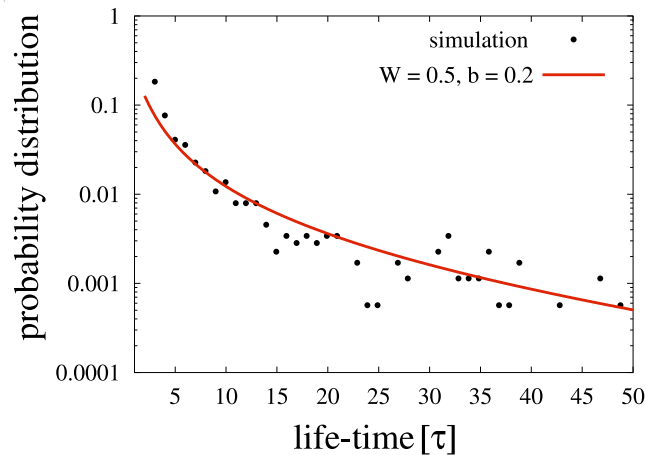
Figure 4.31: Life-time distribution of the pores (same data as Fig. 4.29, log-log scale). The solid line represents the probability predicted by Eq. 4.5, with $n_0 = 1$, $n = 0$, $W = 0.5\,\tau^{-1}$, and $b = 0.2$.

For small life-times, where the correlation between the probability of disintegration and the size of the pore disappears, the model does not fit our data. Eq. 4.5 yields the mean life-time [90]

$$\langle \mathcal{T} \rangle = \frac{n_0 - n}{Wg},$$

which yields $\langle \mathcal{T} \rangle = 10\,\tau$, or about 10 picoseconds. This is an over-estimate because it neglects pores with small life-times, but the order of magnitude is in agreement with atomic molecular simulations of a single pore in a DPPC bilayer published by Marrink *et al .* [112, 113].

Experimentally, such transient pores cannot be observed directly, but they may have an influence on the permeability of the bilayer towards protons. The permeation coefficient of protons (10^{-6} to $10^{-4}\,cm \cdot s^{-1}$) is 6 to 8 orders of magnitude larger than that of other cations. The molecular mechanism of the proton permeation is not well understood, but Nichols and Dreamer [132], and Paula [140] proposed that they permeate through water pores. The transport of a proton through a wire of water molecules can be as fast as five water molecules per picosecond! The transport mechanism, similar to the one occurring in protein channels, includes hydrogen-bond hoppings and molecular reorientations. The typical time needed for a proton to cross a bilayer of thickness 40 $\mathring{A}$ through a water wire is a few picoseconds. The mean life-time is therefore sufficient for several protons to permeate.

In addition, we have seen that a minimum pore-size is required for the solvent to span the inner part of the membrane. Only the pores with a large radius and a long life-time would therefore be leaky. The simulations also showed that larger pores do not diffuse in the bilayers. This may have a strong influence on the kinetics of permeation. For example, the diffusion of protons towards the leaky pores, or the formation of the pores may determine the kinetics of the permeation.

4.4 Conclusion

The results presented in this chapter would benefit from further investigations: the study of the pore dynamics, for example, demands more data to improve the quality of the statistical analyses. Nevertheless, the simulation results permitted to bridge different theoretical approaches of pore formation.

On the one hand, the computed mean life-time of the pores, of the order of the picosecond, agrees with all-atoms simulations [113, 207]. On the other hand, thanks to the coarse-graining of the model, we could observe the spontaneous formation of many transient pores in the bilayers, even without surface tension. We have seen that the pores scarcely diffuse during their life-time, which may help to describe more precisely the pore-mechanism of ion permeation.

Additionally, the simulations confirm underlying assumptions of mesoscopic models, describing the membrane as an undulating surface with a line tension. The simulation results on the life-time distribution of pores are compatible with the stochastic approaches traditionally used to describe electroporation or rupture of amphiphilic bilayers [62].

Finally, in the simulated bilayers without surface tension, the pores are not circular. Even though the shape fluctuations of the pores are rarely taken into account in theoretical studies, the asymmetry of the pores may become important under particular conditions. For example, recent numerical simulations [133, 126] suggest that the breaking of circular symmetry is necessary to describe the mechanism of membrane fusion.

4.5 Appendix: Minkowski functionals

This section presents the main idea leading to the algorithm calculating the Minkowski functionals, published by Michielsen [122]. More details can be found in [116, 122]. Additionally, I present some results for the Minkowski analysis of random distribution of points for several densities, and discuss the finite size effects appearing in the analysis.

Minkowski functionals are defined for d-dimensional Euclidean spaces: they associate a real number to a set of points $K \in \mathbb{R}^d$. Following the presentation of Michielsen [122], I shall first describe the Minkowski functionals of a convex body, then those of a convex ring and finally we shall deal with the particular case of a pattern on a two dimensional grid.

The Minkowski functionals are motion invariant, additive and continuous (with Hausdorff metric), as described in the Eqs. 4.6,4.7,4.8 where g is a translation or rotation in $\mathbb{R}^d$, and ϕ a functional.

$$\forall K \in \mathbb{R}^d: \quad \phi(gK) = \phi(K) \tag{4.6}$$

$$\forall K_1, K_2 \in \mathbb{R}^d: \quad \phi(K_1 \cup K_2) = \phi(K_1) + \phi(K_2) - \phi(K_1 \cap K_2) \tag{4.7}$$

$$\forall \{K_l\} \in \mathbb{R}/ \lim_{l \to \infty} K_l = K: \quad \lim_{l \to \infty} \phi(K_l) = \phi(K) \tag{4.8}$$

The importance of the Minkowski functionals in physics and chemistry is that any motion invariant, additive and continuous functional in d dimensions can be decomposed in a real linear combination of the (d+1) Minkowski functionals. Many physical observables have those properties.

Compact sets of points

A collection of points (a set) K in the d-dimensional Euclidean space $\mathbb{R}^d$ is called a **convex set** if for every pair of points in K, the entire line segment joining them also lies in K. For example, in $\mathbb{R}$ the segments $[0, 1]$, $]0, 1[$, and $]0, 1]$ are convex.

A convex set $K \in \mathbb{R}^d$ is called an **open set**, if for any point in K there exists a real positive ϵ such that the ϵ-neighborhood of the point is included in K. For example, in $\mathbb{R}$ the segments $]0, 1[$, and $[-\infty, 1[$ are open. A set K is a **closed set** if the complement of K is open. For example, in $\mathbb{R}$ the segment $[0, 1]$ is closed.

A convex set which is bounded (with finite boundaries) and closed is a **compact set**. The class of compact sets is denoted by $\mathbb{K}$.

Minkowski functionals of a closed or open set

Given a compact set $K \in \mathbb{K}$, we define **the parallel set** K_r which is the union of all closed balls of radius r whose center are points of K. The volume of this parallel set $v^{(d)}(K_r)$ depends on r and and the size and shape of K. Fig. 4.32 shows the parallel sets of simple compact sets in one and two dimensions. In d dimensions, (d+1) **Minkowski**
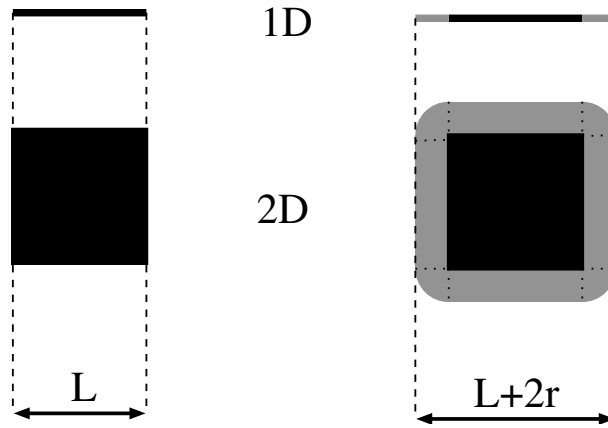
Figure 4.32: Examples of compact sets (left) and their parallel set (right), in one and two dimensions.

functionals of the convex set K, denoted by $W_\nu^{(d)}(K)$, are defined in Eq. 4.9 by the general expression of $v^{(d)}(K_r)$:

$$v^{(d)}(K_r) = \sum_{\nu=0}^{d} \binom{d}{\nu} W_\nu^{(d)}(K) \; r^\nu \tag{4.9}$$

In one dimension ($d = 1$), an example of compact set K is a segment of length $L(K)$. The ball of radius r is a segment of length 2r. The parallel set K_r is the segment of length $L(K) + 2r$. The length of the parallel set of K is $L(K) + 2r$, and the two Minkowski functionals are

$$W_0^{(1)}(K) = L(K) \text{ and } W_1^{(1)}(K) = 2.$$

In two dimensions ($d = 2$), I have chosen a closed square as an example of a compact set. The parallel set is the union of the square, plus four quaters of discs of radius r, plus four rectangles of dimension $L \times r$. The area of the parallel set of K is $L(K)^2 + 4L(K)r + \pi r^2$, and three Minkowski functionals are proportional to $L(K)^{d-\nu}$:

$$W_0^{(2)}(K) = L(K)^2 \; ; \; W_1^{(2)}(K) = 2L(K) \text{ and } W_2^2(K) = \pi. \tag{4.10}$$

This can be generalized: **in two dimensions, $W_0^{(2)}$is the area of the compact set, $W_1^{(2)}$ is twice the contour length, and $W_2^{(2)}$ is proportional to the Euler characteristic**. The definition of Euler characteristic is

$$\forall K \in \mathbb{K}, \chi(K) = \begin{cases} 0 & \text{if } K = \emptyset \\ 1 & \text{if } K \neq \emptyset \end{cases} . \tag{4.11}$$

The last Minkowski functional, $W_d^{(d)}(K)$, is proportional to the Euler characteristic whatever the dimension of the Euclidean space is. The proportionality constant is denoted by ω_d, and is defined by the volume $v(B_d(r))$ of a ball of radius r in $\mathbb{R}^d$, *i.e.* with

$v(B_d(r)) = \omega_d r^d$.

$$W_d^{(d)}(K) = \omega_d \ \chi(K) = \frac{\pi^{d/2}}{\Gamma(1+d/2)} \ \chi(K), \tag{4.12}$$

where the Gamma function is $\Gamma(z) = \int_0^\infty t^{z-1} \exp(-t) \mathrm{d}t$. Minkowski functionals can also be calculated for the interior of a n-dimensional set K of $\mathbb{R}$, denoted by $K/\partial K$, or $\check{K}$. Mecke showed that the Minkowski functionals of the interiors $\check{K}$ are plus or minus those of the compact sets K.

$$W_\nu^{(d)}(\check{K}) = (-1)^{d+n-\nu} W_\nu^{(d)}(K) \text{ for } \nu = 0, ..., d. \tag{4.13}$$

Minkowski functionals of a union of convex bodies

The subclass of convex sets $A \in \mathbb{R}^d$ which can be written as finite union of convex subsets K_i,

$$A = \bigcup_{i=1}^l K_i \text{ with } K_i \in \mathbb{K} \text{ and } l < \infty, \tag{4.14}$$

forms the convex ring $\mathcal{R}$. We are interested in this case because the patterns we analyze are unions of "pixels", and each "pixel"is a compact set of points. For a set $A \in \mathcal{R}$, the Euler characteristic is defined as

$$\chi(A) = \sum_i \chi(K_i) - \sum_{i<j} \chi(K_i \cap K_j) + ... + (-1)^{l+1} \chi(K_1 \cap ... \cap K_l). \tag{4.15}$$

This definition is independent of the finite decomposition of A into subsets $\{K_i\}$. In two dimensions, $\chi(A)$ is the number of objects, minus the number of holes in A. It is additive and motion invariant. This Euler functional is used to define the Minkowski functionals on the convex rings of $\mathcal{R}$. The first d functionals are defined as

$$W_\nu^{(d)}(A) = \int_{\mathcal{G}} \mathrm{d}g \ \chi(A \cap gE_\nu) \text{ for } \nu = 0, ..., d-1, \tag{4.16}$$

where E_ν is a ν-dimensional hyper-plane in $\mathbb{R}^d$, $\mathrm{d}g$ the motion-invariant kinematical density [170], and the integration runs over $\mathcal{G}$, the group of translations and rotation in $\mathbb{R}^d$. The last functional $W_d^{(d)}(A)$ is proportional to Euler functionals, exactly as for $K \in \mathbb{K}$, in Eq. 4.12.

Minkowski functional on a 2D lattice

To analyze a 2D-pattern numerically, one digitizes it into a two dimensional image composed of black and white pixels only. This image is considered as a finite union of black pixels, *i.e.* a compact set of $\mathbb{R}^2$. As the closed pixels do intersect along the edges and vertices of the lattice, the calculation of Minkowski functionals with the additivity equation (Eq. 4.15) has to take into account all the intersections.

To optimize the calculation, Michielsen proposed to decompose the pattern, denoted by A, into a disjoint collection of $n_2(A)$ interiors of pixel, the interior of $n_1(A)$ edges of the pixels, and $n_0(A)$ vertices, as in Fig. 4.33. The interiors of pixels are denoted by $\check{N}^2$, the interior of edges by $\check{N}^1$ and the vertices by $\check{N}^0$.
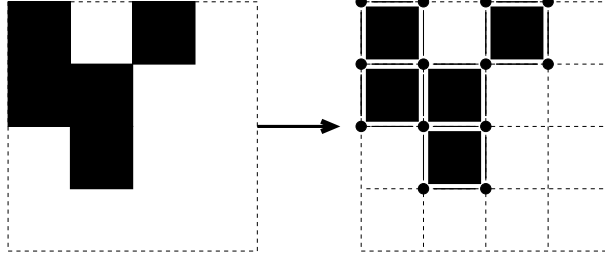
Figure 4.33: Decomposition of a pattern into a disjointed union of 5 pixels, 17 edges and 13 vertices.

$$A = \bigcup_{k=1}^{n_2(A)} \check{N}_k^2 \ \bigcup_{j=1}^{n_1(A)} \check{N}_j^1 \ \bigcup_{i=1}^{n_0(A)} \check{N}_i^0$$

As the different sets do not overlap, the additivity property (Eq. 4.17) simplifies to

$$W_\nu^{(2)}(A) = n_2(A)W_\nu^{(2)}(\check{N}^2) + n_1(A)W_\nu^{(2)}(\check{N}^1) + n_0(A)W_\nu^{(2)}(\check{N}^0). \tag{4.17}$$

The Minkowski functionals of the interiors $\check{N}^2, \check{N}^1, \check{N}^0$ are known from Eq. 4.13. The calculation of Minkowski functionals of a black an white image is thus reduced to the calculation of the number of pixels, edges and vertices composing the pattern.

Algorithm

Michielsen proposes an algorithm to calculate the number of edges and vertices [123]: one stepwise constructs the pattern, adding pixel after pixel. During this procedure, one integrates the number of new pixels, edges and vertices appearing at each addition. The number of steps of the algorithm equals the number of pixels of the pattern.

The calculation is performed on a pattern stored as a two-dimensional matrix A, with $A_{ij} = 0$ for white pixels (the background) and $A_{ij} = 1$ for black pixels (the picture). As already mentioned, the pattern is constructed by adding one pixel after the other. At each step, one obtained a "temporary" pattern T. The complementary pattern of T is called C and is defined by

$$C_{i,j} = 1 - T_{i,j}.$$

When a pixel is added at the place (i, j) on the pattern T, the increase in the number

of pixel, edges and vertices are

$$\Delta n_2 = 1, \tag{4.18}$$

$$\Delta n_1 = \sum_{\alpha=-1,+1} C_{i+\alpha,j} + C_{i,j+\alpha}, \tag{4.19}$$

$$\Delta n_0 = \sum_{\alpha,\beta=-1,+1} C_{i+\alpha,j+\beta} \, C_{i+\alpha,j} \, C_{i,j+\beta} \tag{4.20}$$

For pixels that are beyond of the boundaries of the pictures, we impose $C_{i,j} = 0$. In other words, we do not apply periodic boundary conditions but add a simple white background all around the pattern.

When the last pixel is added, the numbers n_2 of pixels, n_1 of edges and n_0 vertices, are known. The additivity equation (Eq. 4.17) is applied using the values given in Table 4.2.

	$\check{N}^0$	$\check{N}^1$	$\check{N}^2$
W_0	0	0	l^2
W_1	$2l$	l	$-2l$
W_2	$-\pi$	$-\pi$	π

Table 4.2: Minkowski values for the interiors of a pixel ($\check{N}^2$), of an edge ($\check{N}^1$), and od a vertice ($\check{N}^0$) on a lattice of mesh l.

Principle of the analysis of a distribution of points

I repeat here the principle of the analysis already described in Section 4.12.

The principle of the analysis is sketched in Figs. 4.34 and 4.12. A so-called germ is "attached" to each point. This germ is a geometrical form with a characteristic length l and orientation θ. I have chosen a square of area l^2 with a fixed orientation. Those

POINTS   GERMS   PATTERN
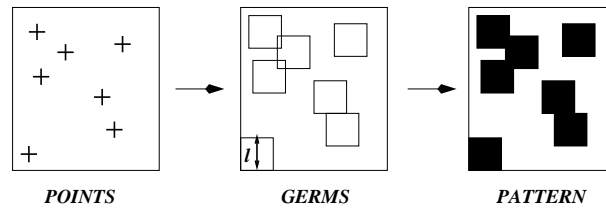
Figure 4.34: Principle of the construction of the pattern from the point distribution. The germs are oriented squares.

squares compose a pattern which is analyzed with Minkowski functionals. In two dimensions, three Minkowski functionals are defined: the area A the contour length U and the Euler characteristic χ (see Fig. 4.35). In two dimensions, the Euler characteristic is
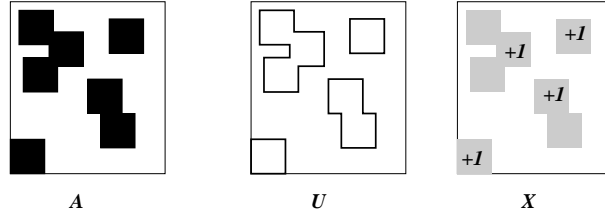
Figure 4.35: Illustration of the three Minkowski functionals of the two-dimensional pattern of Fig. 4.11: the area A, the contour length U and Euler characteristic χ.

the number of connected components minus the number of holes in those clusters. The dependence of the Minkowski functionals on the length l contains information about the distribution of points.

Results for random sets of points

In some particular distribution of points, it is possible to calculate the results of the analysis with Minkowski functionals. For a random distribution of positions and a random orientation distribution of the points in the area A_{tot}, a germ of area a^*, contour length u^* and Euler characteristic g^* is attached with a random orientation, to each of the N randomly-distributed points.

The mean values of the Minkowski functionals normalized by the number of points N depend only the density of points $\rho = N/A_{tot}$ and the nature of the germ:

$$\left\langle \frac{W_0^{(2)}}{N} \right\rangle (\rho) = \frac{1}{\rho}(1 - e^{-\rho a^*}) \tag{4.21}$$

$$\left\langle \frac{2W_1^{(2)}}{N} \right\rangle (\rho) = u^* e^{-\rho a^*} \tag{4.22}$$

$$\left\langle \frac{W_2^{(2)}}{\pi N} \right\rangle (\rho) = \left(g^* - \frac{(u^*)^2 \rho}{16} \right) e^{-\rho a^*} \tag{4.23}$$

The brackets $\langle \cdot \rangle$ denote averages over many independent distributions. I have chosen germs of area $a^* = l^2$, contour length $u^* = 4l$ and genus $g^* = 1$. The results are plotted with the dimensionaless m_0, m_1, m_2

$$\begin{aligned}
m_0(x) &\doteq \left\langle \frac{\rho W_0^{(2)}}{N} \right\rangle &=& \quad 1 - e^{-x}, \\
m_1(x) &\doteq \left\langle \frac{2\sqrt{\rho} W_1^{(2)}}{N} \right\rangle &=& \quad 4\sqrt{x} e^{-x}, \\
m_2(x) &\doteq \left\langle \frac{W_2^{(2)}}{\pi N} \right\rangle &=& \quad (1 - x) e^{-x},
\end{aligned} \tag{4.24}$$

functions of the adimensional coverage factor $x = l^2 \rho$.

Minkowski functionals are sensitive to the anisotropy of the lattice. In the case of anisotropic germs (*e.g.* oriented squares), Minkowski functionals depend not only on the spatial distribution of the germs, but also on their orientational distribution. Eqs. 4.24 happen to be valid for a random distribution of orientation, and for a fixed orientation [116].

Density effects

To test whether Eqs. 4.24 obtained for random distributions of points could be directly compared to the simulation data, I analyzed random sets of points with different densities. The investigation of density effects is important here because the number of holes per bilayer is very small.

The results are shown in Fig. 4.36. Both the the Minkowski analysis of random distributions and Eqs. 4.24 are plotted. Obviously, the results strongly depend on the density.

Correlation effects

The main aim of the Minkowski analysis is to determine whether the holes are randomly distributed. Therefore I investigated the effects of self-avoidance on the Minkowski analysis. So-called "random self-avoiding "sets (RSA) were generated on a grid `N_x`×`N_y` with the following algorithm (not in a real programming language):

```
i <- 0;
initialize(template,NX,NY,FREE)
   while(i<NPOINTS){
      xi = NX*random()
      yi = NY*random()
      if(template(xi,yi) = FREE) {
         set_occupied(template,xi,yi,min_dist)
         i <- i+1
}
}
```

where `random()` is a random number generator whose output ranges between 0 and 1. Here, the `template(x,y)` is a two dimensional matrix of booleans, with the indices `x` and `y`. Each boolean `template(x,y)` can take the value `FREE` or `OCCUPIED`. The function `set_occupied(template,xi,yi,min_dist)` attributes the label `OCCUPIED` to all the sites of the `template` around the site (`xi,yi`). It can be sketched as:

```
function set_occupied(template,x,y,min_dist){
   for(i=-min_dist to i = min_dist)
      for(j=-min_dist to j = min_dist)
         template(x+i,y+j) <- OCCUPIED
}
```

Finally, the points, whose coordinates are determined by a random number generator, are separated at least by `min_dist` pixels in the two dimensions.

The results of Minkowski analysis for several minimum distances between the points are presented in Fig. 4.37. The self-avoidance clearly influences the results. The density effects and self-avoidance effects can *a priori* be distinguished (see Figs. 4.36 and 4.37).
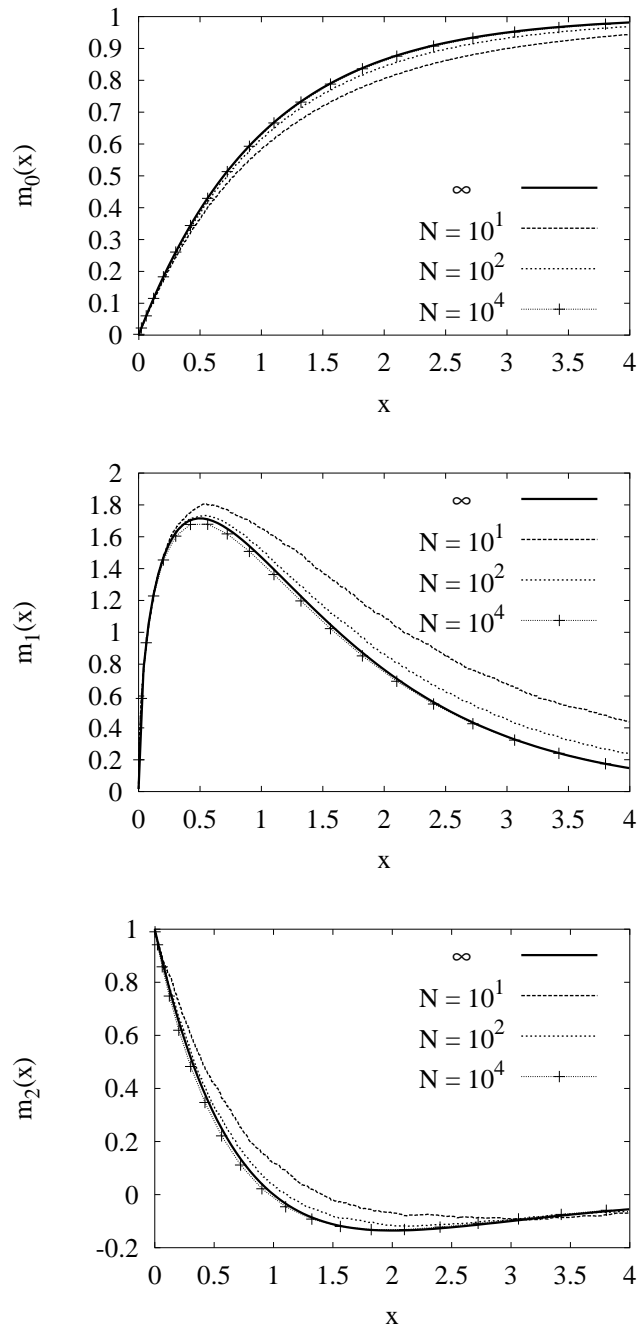
Figure 4.36: Minkowski functionals of 10 ensembles of $N = 10, 10^2, 10^4$ points on a surface of 1000×1000 pixels compared to the theoretical prediction solution for an infinite system (Eq. 4.24). The crosses are added for the system with $N = 10^4$ points to distinguish this curve from the one with $N = \infty$.
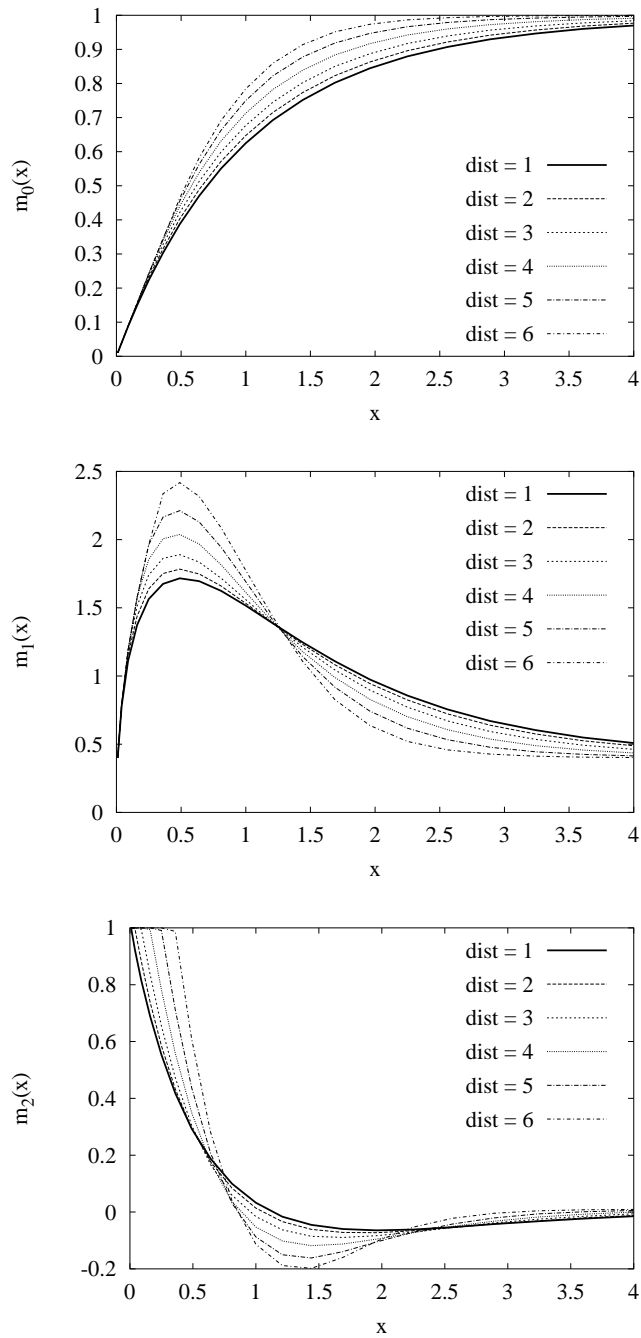
Figure 4.37: Minkowski analysis of 1000 ensembles of $N = 10^2$ points on a surface of 100×100 pixels with different minimum distances between the points.

5 Insertion of a polymer between the bilayers

The theoretical and experimental knowledge of soft condensed matter has nowadays reached a state where the properties of a solution of polymers, colloids, or surfactants are designed and synthesized to reach our goals. Even more, complex fluids including two classes of colloidal entities have appeared. For example, solutions containing colloidal particles and surfactants are often used in the formulation of cosmetics, paintings, medicaments, *etc.* These mixed colloidal systems are obtained by introducing doping molecules or particles into a self-assembled complex fluid (*e.g.*, mixtures of rods and polymers [45], nematics containing magnetic particles [11]). Under favorable circumstances, the mixture may self-assemble into a single phase that combines the structure and the stability of the complex matrix with the chemical or physical properties of the inclusions.

This chapter deals with a *solvent-soluble, flexible homopolymer* inserted in a L_α lamellar phase of amphiphiles. The aim of this work is to study the interactions between a lamellar phase and macromolecules. Two situations are then encountered: the polymer adsorbs onto the bilayer, or it does not. Both have been studied experimentally [105, 18, 17] and theoretically [23, 147]. The simulations provide data about the conformations of the polymers and about the defects of the bilayers - data which are difficult to obtain experimentally.

This Chapter is organized as follows.

In Section 5.1, background information is given on the polymer-L_α complexes: the motivation to study them, some experimental and theoretical results.

In Section 5.2, I shall follow the scaling arguments used by Ligoure and coworkers [18, 17] to explain what is meant by "dilute regime" and "confined regime" in the case of a non-adsorbing polymer confined in the lamellar phase. After this general approach, I shall restrict myself to the case of a single polymer chain (dilute regime).

Then, details on the simulations are provided (Section 5.3). As a first step, single polymer chains have been simulated: one polymer which adsorbs onto the bilayers, and one which does not. We shall compare their conformations, and their influences on the lamellar phase (Sections 5.4 and 5.5).

5.1 Lamellar phases containing polymers

The lamellar phase of amphiphilic molecules is a good experimental and theoretical model to study the physics of biological membranes. The polymer-L_α complexes are

used to understand the interaction of polymers with amphiphilic bilayers [152] and the confinement of polymers in thin slits [105].

Stability of lamellar phases containing polymers

Large amounts of polymers have been incorporated into lamellar phases without causing a phase separation. Among the numerous experimental studies of lamellar phase doped by linear homopolymers, one can distinguish between (i) neutral polymers inserted in an electrostatically stabilized L_α phase [104, 55, 57, 10, 206, 18, 17, 178, 56, 208, 43, 44, 42], (ii) polyelectrolytes inserted in an electrostatically stabilized L_α phase [94, 10, 205, 150, 149, 166, 165], and (iii) polymers inserted in neutral L_α phase [145]. Electrostatic interactions contribute to the stability of the polymer-L_α complexes but they do not always prevail: under specific conditions, anionic polyelectrolytes can even be included in lamellar phases of anionic amphiphiles [95].

The details of the phase diagram depend on the specific interactions between the polymers and the bilayers of the smectic. Brooks and Cates [23] studied theoretically the stability of lamellar phases doped with a semidilute solution of flexible polymers. They distinguished two types of lamellar phase: bound or unbound. In the so-called unbounded regime, the interlamellar distance is fixed by the global concentration of amphiphiles [188]. Conversely, a bound lamellar phase cannot be indefinitely diluted; it expels excess solvent beyond a certain maximal dilution.

According to Brooks and Cates' theory, an *adsorbing* polymer always enters the lamellar phase. Small amounts of adsorbing polymer cause the system to become bound, with expulsion of excess solvent. This agrees with many experimental and theoretical results. For example, so-called "lipoplexes"are obtained by spontaneous complexation of DNA with both cationic and neutral lipids. They have been extensively investigated because of their possible application to gene therapy [150, 149, 166, 165, 161, 93]. The formation of the complex is then driven by the release of small counterions that were "condensed"on the highly charged DNA or lipids [76].

Also, a *non-adsorbing* polymer may enter an *unbound* lamellar phase with very flexible bilayers if the repulsion between the bilayers is sufficiently large. But a semidilute solution of non-adsorbing polymers and a *bound* lamellar phase demix.

These theoretical predictions concerning the non-adsorbing polymer are in agreement with experimental results of Ligoure and coworkers [104, 105, 146, 18, 17]. They showed that the presence of a non-adsorbing polymer in the solvent of an anionic lamellar phase softens the interactions between bilayers. It destabilizes the lamellar phase: If the repulsions between the bilayers are not strong enough to stabilize the lamellar phase -*e.g.* if salt is added to the solvent of the cationic lamellar phase, the non-adsorbing polymer may cause a phase separation (L_α/L_α or L_α/polymer).

Effective interactions between the bilayers

Two observables are usually measured to study the effective interactions between the bilayers of the lamellar phase: the interlamellar distance, and the smectic compressibility

modulus.

The interlamellar distance between the bilayers measured by X-ray scattering was reported to decrease or to remain unchanged [147, 18, 17]. Brooks *et al.* predicted that the interlamellar distance diminishes.

Procar *et al.* [147] showed with small angle X-ray scattering measurements and freeze-fracture micrography that the insertion of *non-adsorbing polymers* strongly modifies the texture of the lamellar phase without affecting the smectic periodicity. The peaks emerging from the smectic arrangement broaden when the polymer concentration increases. Their form nevertheless remains well-described by smectic scattering models. The broadening is generally attributed to a decreasing smectic compressibility modulus B. Ligoure and coworkers developed a theory which describes quantitatively B^{poly}, the polymer contribution to the compressibility modulus B [105, 18, 17]. For a non-adsorbing flexible polymer, B^{poly} is negative, so that the compressibility modulus effectively decreases in the presence of the polymer. Different polymer-L_α complexes show the same behavior [64, 178, 151, 42].

In the case of *adsorbing polymers* (*e.g.* lipid-DNA complexes [165, 166]), the scattering spectra of the doped lamellar may be so perturbed, that the usual smectic model no longer fits the experimental data.

Defects

In Fig. 5.1, the freeze fracture micrographs [147] of a two-solvents lamellar phase in the absence and in the presence of doping polymers are compared. The left image (without polymer) is typical of a lamellar phase with a perfect stacking of flat bilayers. The right image (with polymer) shows that the presence of polymer changes the spontaneous curvature of the bilayers and triggers defects. Defects were also reported by Singh about a different doped lamellar phase [178].

Location of the doping molecules

The structure of the polymer-L_α complexes depends on the interactions of the polymer with the solvent and with the bilayers. Indeed, even a "simple" linear homopolymer can be confined between the solvent layers [178, 104, 208, 17], be incorporated in the bilayers [151, 152], or adsorb partially on them [89, 55, 57].

Orientational ordering of the doping molecules

The anisotropy of the lamellar phase impedes the free rotation of inclusions.

This effect was used for Nuclear Magnetic Resonance measurements [160, 9]. The method is based on the fact that lamellar phases orient in the magnetic field. As the molecules included in the anisotropic solvent are oriented relative to the bilayers, they are also oriented relative to the magnetic field. This permits to measure intramolecular dipolar couplings between pairs of nuclei of a doping molecule.

For semiflexible polymers, the confinement in the lamellar phase may even impose a long-range, orientational order. For instance, in lipoplexes, the DNA strands confined in
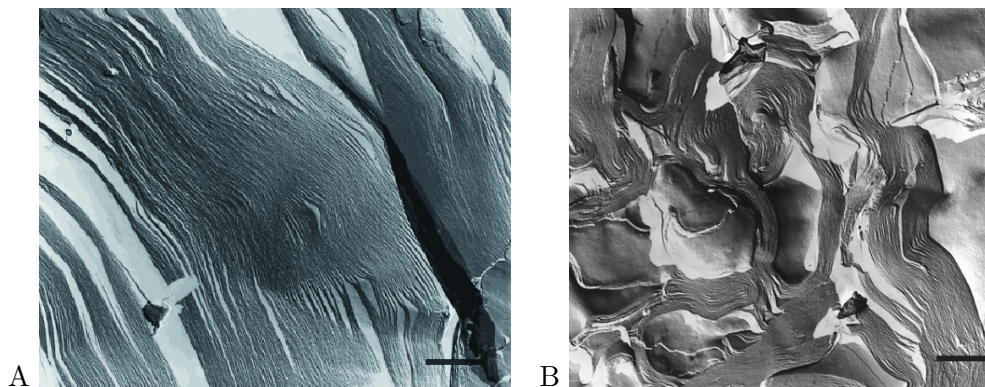
Figure 5.1: Freeze-fracture micrographs of a cationic lamellar phase (triton X/ cetylpyri-
dinium chloride/water/decane) without polymer (A) and with 5% in volume
of neutral, non-adsorbing polyvynilpyrrolidone (B). Reproduced from [147]
(length of the bar = 460 nm).

the solvent layers align, forming in each solvent layer a two-dimensional liquid-crystalline phase. This order could be investigated by X-ray scattering [165, 166, 145], and theoretically [134, 135, 145, 147].

5.2 Confinement of a flexible polymer between two parallel planes

Relatively few theoretical studies of polymer chains between *flexible* walls have been reported [46], but the simpler case of a single polymer chain between two *planar, rigid* walls has received more attention. In the following, I shall recall the scaling approaches of the dilute and confined regimes of a single chain between two planar walls, and discuss afterwards what may happen with flexible walls. In this chapter, the thickness of the walls, or bilayers, is neglected. The polymer is confined in a solvent slit of thickness d.

5.2.1 Non-adsorbing polymer

The shape of polymer chains confined between two parallel repulsive plates in good or poor solvent was investigated by several authors [39, 20, 194, 204, 21, 197, 24, 196, 154, 23, 120, 38, 121, 34, 35] using scaling arguments, renormalization group methods, variational methods as well as computer simulations. Here, I discuss mainly the scaling arguments.

We have seen in Section 1.1 that the simulated polymer is in a good solvent. The radius of the polymer coil shall be approximated by the formula proposed by Flory for a self-avoiding polymer, in D dimensions $(1 \leq D \leq 4)$[58]

$$R_{FD} \overset{N \to \infty}{\simeq} a \cdot N^{\frac{3}{D+2}}, \tag{5.1}$$

where N is the number of monomers and a their size and the symbol $\simeq$ denotes a proportionality relation, with a proportionality factor close to unity.

Bouglet, Ligoure *et al.* [105, 17] have used scaling laws to describe four regimes for the non-adsorbing polymer in the lamellar phase. The stability of these regimes depends on two parameters (see Fig. 5.2):

Φ_p The volume fraction of polymer. It depends on the monomer concentration c and the monomer size a according to $\Phi_p = a^3 c$.

d/a The ratio between the thickness d of the confining slit and the monomer size a.

3D Dilute and semidilute regimes

Different values of the polymer volume fraction Φ_p distinguish the dilute and semidilute regimes of unconfined polymer solutions. In the dilute regime (D), the polymer chains do not interact. In the semidilute regime (SD) the polymer coils interpenetrate, but the correlation length between polymer chains is still larger than the monomer size. The boundary between these two regimes is classically chosen at the concentration of monomers c^*, for which the global monomer concentration c of the solution equals the concentration of monomers in the unperturbed swollen polymer coils found in the dilute regime (see Fig. 5.3):

$$c_{3D}^* \simeq N/(R_{F3})^3. \tag{5.2}$$

Inserting Flory's radius (Eq. 5.1 with $D = 3$) in Eq. 5.2 yields

$$\Phi_p = a^3 c_{3D}^* \simeq N^{-4/5}. \tag{5.3}$$

In the unconfined semidilute solution, the typical length is the mesh size of the polymer network, denoted ξ_{3D}[1]. De Gennes [40] introduced the assumption that for length-scales much smaller than ξ_{3D}, the conformations are not perturbed by the other chains and remain analogous to self-avoiding random walks. According to Flory's theory, the size ξ_{3D} of these unperturbed portions of polymer corresponds to an ensemble of $g_{3D} \simeq (\xi_{3D}/a)^{5/3}$ monomers (a "blob"). For length-scales larger than ξ_{3D}, the interactions between the chains strongly modify the chain conformations. The semidilute solution can be seen as a dense packing of blobs of size ξ_{3D} in which the global monomers concentration c equals g_{3D}/ξ_{3D}^3. This allows us to calculate

$$\xi_{3D} \simeq a^{-5/4} c^{-3/4} = a \Phi_p^{-3/4}. \tag{5.4}$$

For the case of the doped lamellar phase, if the thickness of the solvent d is much larger than R_{F3}, the dilute and semidilute regimes are identical to the unconfined ones. They are denoted 3D-D and 3D-SD in Fig. 5.2. Using Flory's expression for the polymer radius R_{FD}, the boundary between these regimes, denoted (1), is defined by Eq. 5.3.

---

[1] I use here the usual notation for the correlation length ξ. Note that it is different from the in-plane correlation length also usually noted ξ introduced in Chapter 3.
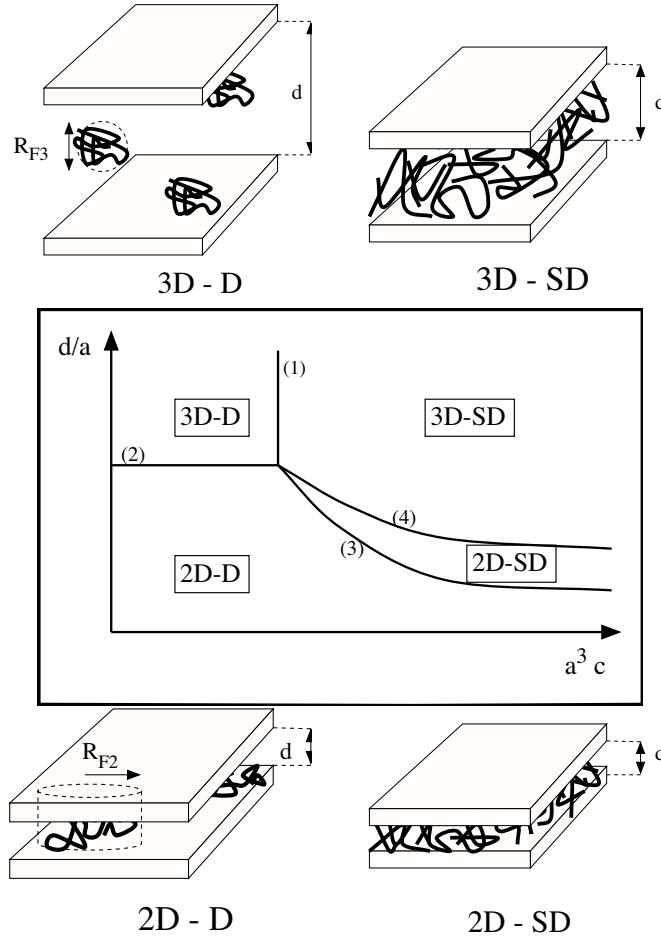
Figure 5.2: Sketches of the confinement regimes of the polymer as a function of the confinement thickness (d) divided by the monomer size (a), and of the polymer volume fraction $\Phi_p = a^3 c$. The four regimes are: the three-dimensional dilute regime (3D-D), the two-dimensional dilute regime (2D-D), the three-dimensional semidilute regime (3D-SD), and the two-dimensional semidilute regime (2D-SD). The boundaries correspond to: (1) $\phi_p = a^3 c_{3D}^*$, (2) $d = R_{3F}$, (3) $\phi_p = a^3 c_{2D}^*$, (4) $d = \xi_{3D}$. See text for more explanation. Inspired by [105, 17].

2D dilute and semidilute regimes

If the solvent layer is too thin, some polymer conformations are forbidden.

In the dilute regime, the polymer coils are deformed when the thickness d is decreased down to the radius of the swollen polymer coil R_{F3}. The boundary between the 3D and 2D dilute regimes is defined by the equation $d = R_{F3}$, and is represented by the line (2) in Fig. 5.2. In the semidilute regime, the polymer chains are deformed when the
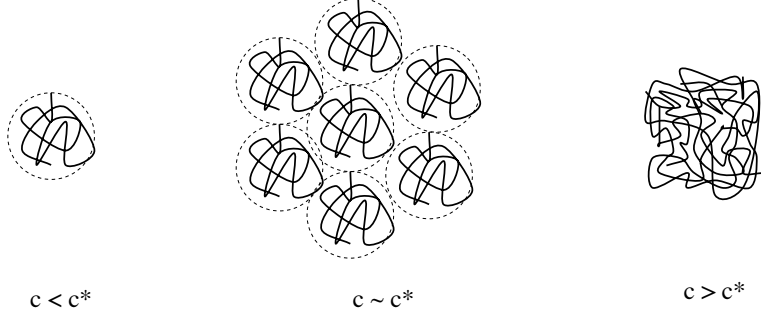
Figure 5.3: Illustration of the dilute ($c \leq c^*$), and the semidilute ($c^* \leq c$) polymer solutions. The limiting case $c \sim c^*$ is represented schematically by a dense packing of coils.

thickness d is decreased down to the mesh size ξ_{3D}. The equation $d = \xi_{3D}$ corresponds to the curve (4) in Fig. 5.2.

Daoud and de Gennes [39] have described single chains in the 2D-D regime as pancakes of thickness d, and of radius R_{F2}. The polymer conformations are assimilated to two-dimensional self-avoiding random walks of blobs, whose radius is imposed by the confinement thickness d (see Fig. 5.4). Each blob contains $g_{2D} \simeq (d/a)^{5/3}$ monomers,
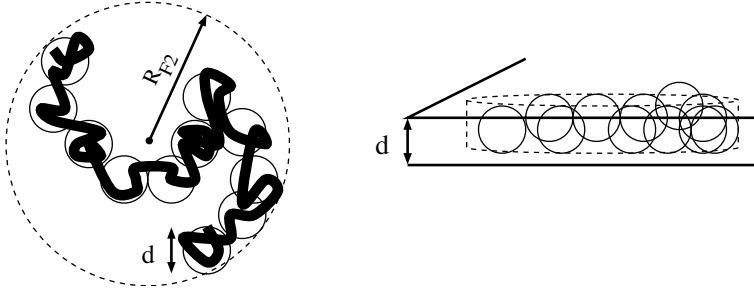
Figure 5.4: Top and side views of a polymer confined between two planes. The polymer is represented by a thick line, and the blobs by thin solid circles [20].

and each pancake contains $n_b = N/g_{2D}$ blobs. Using Eq. 5.1 for the size of a two-dimensional self-avoiding random walk with n_b steps, one finds the extension of the polymer in the plane of the solvent:

$$R_{F2} \simeq a^{5/4} d^{-1/4} N^{3/4}. \tag{5.5}$$

The boundary between the dilute (2D-D) and semidilute (2D-SD) regimes is chosen similarly to the three-dimensional case: the concentration of monomers in a pancake of volume $R_{F2} d$ equals the global concentration of monomers: $c_{2D}^* \simeq N/(R_{F2} d)$. Using the Flory Eq. 5.5, we obtain the value of the polymer volume fraction delimiting the

2D-D and 2D-SD regimes:

$$\Phi_p = a^3 c_{2D}^* \simeq (d/a)^{-1/2} N^{-1/2}. \tag{5.6}$$

In Fig. 5.2, this boundary is depicted by the curve (3).

In the following, we shall restrict ourselves to the dilute, confined regime (2D-D).

Cross-over between 3D-D and 2D-D regimes

In cross-over regions, complex behaviors that are not predicted by scaling arguments may appear. Several authors [197, 196, 120, 38, 121, 35, 34] studied the dilute regimes of a polymer confined between repulsive walls by variational methods or Monte Carlo simulations. The end-to-end distance of the polymer, R_e, turns out to be a non-monotonic function of the confinement factor d/R_{F3} (see Fig. 5.5). For the small and large values
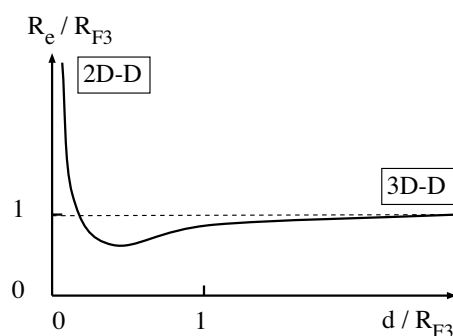
Figure 5.5: Plot of the ratio of mean end-to-end distance R_e to that of the non-confined Flory radius R_{F3} (soft repulsive walls and good solvent). The observed minimum becomes more pronounced as walls are more and more repulsive. Inspired by [38].

of d/R_{F3}, the behaviors corresponding to the $2D - D$ and $3D - D$ regimes are found. In an intermediate regime, the chains get squeezed, and the three eigenvalues of the polymer gyration matrix decrease.

5.2.2 Adsorbing polymer

Only few theoretical studies of the confinement of a *single* adsorbing polymer chain between two planes have been published [199, 86, 87]. So-called bridges appear: the polymer is adsorbed on both walls at the same time. The number of bridges depend on the ratio between the loop extension *le* and confinement thickness *d* (see Fig. 5.6). In Fig. 5.6, case A corresponds to a system with strongly adsorbing surfaces, such that there are relatively few bridges. These are stretched. The largest part of the chain is tightly adsorbed to the surface in short loops. Case B occurs when the surfaces are less adsorptive. It is characterized by a large number of slightly stretched bridges, and
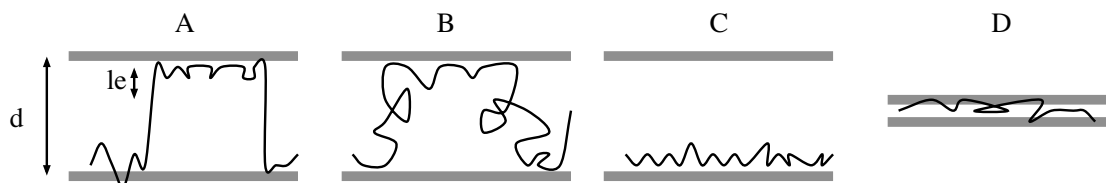
Figure 5.6: Sketches of a flexible adsorbing single polymer chain confined between planar walls (inspired partially by [87]). *A*: Strong adsorption. *B*: Weak adsorption. *C*: Limit of strong adsorption and large interlamellar distance. *D*: Limit of strong adsorption and small interlamellar distance.

fewer but larger loops. In the limit of large separation and adsorption energy, the chain adsorbs only onto one wall (case *C*). In the limit of short separation, the monomers interact with both walls at the same time (case *D*).

For the simulations of this chapter, the confinement thickness is of the same order of magnitude as the loop extension (case *D*).

5.2.3 Effects of the undulations and defects of the bilayers

The aforementioned theories of the polymer confinement assume that the polymer is strictly confined between two parallel plates. In amphiphilic lamellar phase, the bilayer may bend to relax the constraint imposed by the inclusion of a polymer. Such a possibility was suggested by Radlinska *et al.* [152, 151]. On freeze fracture micrographs of a doped lamellar phase, they observed both wormlike and globular polymers, depending on the charge fraction of the polymer. They suggested that the polymer is in the solvent layer, and locally deforms the lamellar structure.

Fig. 5.7 sketches some possible conformations of single confined polymers. The case
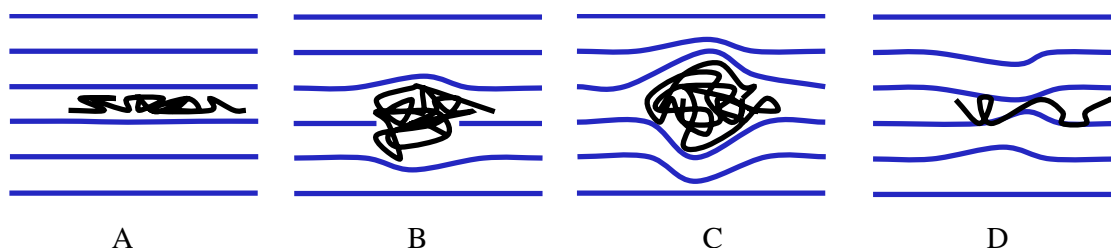
Figure 5.7: Sketches of a flexible non-adsorbing single polymer chain confined in the lamellar phase. *A*: Planar bilayers. *B*: The polymer globule makes a pore and deforms the lamellae. *C*: The non-adsorbing polymer deforms the lamellar without making holes. *D*: The adsorbing polymer deforms the lamellar without making holes.

A corresponds to the pancake configurations proposed by Daoud and de Gennes [39].

The theory based on this assumption was verified by Ligoure and coworkers for polymer concentrations from 3% to 15% in volume [17], *i.e.* in the semidilute regime.

The cases B, C and D are possible thanks to the flexibility and defects of the bilayers. In the case B, both the lamellae and the polymer deform to relax the constraint. In the cases C, the constraint due to the presence of the polymer deforms the lamellar phase, while the polymer remains in a three-dimensional state. Singh *et al.* [178] proposed the model C to interpret qualitatively the decrease of the interlamellar spacing and smectic compressibility modulus observed in scattering spectra. Interestingly, the modification of the interlamellar distance increases when the polymer is more *diluted*.

These scenarios are compared to the simulation results in Sections 5.4 and 5.5.

5.3 Description of the simulations

The simulated system is composed of a single polymer chain inserted in a stack of five bilayers. First, let us verify that the simulations presented here are in the two-dimensional dilute regime, which is defined by the inequalities: $d \leq R_{F3}$ and $\Phi \leq \Phi_p^* = (dN/a)^{-1/2}$.

In the simulated lamellar phase, the thickness t of the inner part of the bilayers is approximately $2.4\,\sigma$ (see Fig 2.10), and the periodicity of the smectic is $d = 6.4\,\sigma$. Therefore, the confinement thickness $d - t$ is approximately $4\,\sigma$. I have chosen to insert a polymer of length $N = 100$, whose radius of gyration in the pure isotropic solvent is $6.7\,\sigma$. The polymer is confined $((d - t)/R_g \leq 1)$.

To compare the simulations with the theory by Bouglet *et al.* (see Section 5.1), I approximate the volume fraction of the polymer with the bead fraction of the polymer in one (solvent+head groups) layer: $\Phi_p \sim 1.7\%$. The theory predicts the boundary between the 2D-D dilute and 2D-SD regimes at $\Phi_p^* = (dN/a)^{-1/2}$ (Eq. 5.6), which is approximately $\Phi_p^* = 4\% \geq \Phi_p$. So the regime is diluted. As the criterion used here neglects the prefactors, some care has to be taken. In fact, it can be seen on some snapshots (Figs. 5.8 and 5.9) that the end-to-end distance of the polymer is not much smaller than the size of the simulation box. The interactions between the polymers may be not totally negligible.

In the direction of the director, there is one polymer every fifth bilayer. This may be considered as a "very dilute" regime, because some solvent layers contain no polymer. This influences the local structure of the doped lamellar phase because the pressure exerted by one polymer chain on one side of a bilayer is not compensated by an other polymer on the other side of the bilayer.

The initial configuration of the simulation was constructed by hand, by introducing covalent bonds between neighboring solvent beads in an equilibrated stack of five bilayers. These bonds were introduced with a Monte Carlo procedure, so that the initial configuration of the polymer is energetically reasonable[2], and looks like a two-dimensional

---

[2]The Monte Carlo algorithm is not described in the thesis. It constructs iteratively the polymer, adding bonds after bonds between neighboring solvent beads. See for example Ref. [201, 63].

random walk. The simulation was continued in the $N, P, T, \gamma = 0$-ensemble during more than $100\,000\,\tau$, with the typical parameters described in Section 1.1 .

The adsorption is modeled by a polymer-head attraction which is stronger than the polymer-solvent attraction. We shall compare the following cases:

1. $\epsilon_{PS} = \epsilon_{PH} = 1.1\,k_B T$.
   The polymer does not absorb onto the bilayers.

2. $\epsilon_{PS} = 1.1\,k_B T$ and $\epsilon_{PH} = 1.3\,k_B T$.
   The polymer adsorbs onto the bilayers.

Non-absorbing polymer.

Fig. 5.8 shows snapshots of the *non-adsorbing* polymer at $3\,000\,\tau$, $13\,000\,\tau$ and $59\,000\,\tau$ after its introduction in the lamellar phase (as in the whole thesis, τ is the time unit). The positions $h_n(x, y)$ of the two neighboring membranes are added.

During the first $10\,000\,\tau$, the polymer remains confined between two lamellae. The shape of the polymer evolves from a relatively extended structure (Fig. 5.8 A) into a compact, two-dimensional globule (Fig. 5.8 B). During this time, the polymer happens to break through one membrane, but the pores reseal. Around $20\,000\,\tau$, the polymer spans one membrane. During the rest of the simulation time, it remains in a pore, with approximately half of its beads on each side of the bilayer.

Absorbing polymer.

Fig. 5.9 shows snapshots of the *adsorbing* polymer $30\,000\,\tau$ after its insertion in the lamellar phase. The polymer remains confined between two lamellae. In contrast to the non-adsorbing polymer, the shape of the polymer remains in a relatively extended structure. The polymer does not pass through the neighboring membranes, and the pores nucleating spontaneously around the polymer close rapidly.

In the following, the simulation data are described more quantitatively. Inspired by the results exposed in Section 5.1, I have chosen to compare the behavior of a non-adsorbing and an adsorbing polymer embedded into the simulated lamellar phase. We shall study (i) the conformations of the adsorbing and non-adsorbing polymers confined in the bilayers, (ii) the distribution of interlamellar distances between the bilayers, (iii) the defects in the bilayers of the lamellar phase.

5.4 Non-adsorbing polymer: simulation results

5.4.1 Confinement of the polymer

The size of a flexible polymer is classically described by its radius of gyration R_g. Fig. 5.10 displays the time evolution of R_g^2 (Eq. 1.3) during the simulation.

I distinguish two stages in the simulations: for $t \leq 40\,000\,\tau$ the polymer size decreases towards its equilibrium value, and for $t \geq 40\,000\,\tau$, the polymer has relaxed its shape.
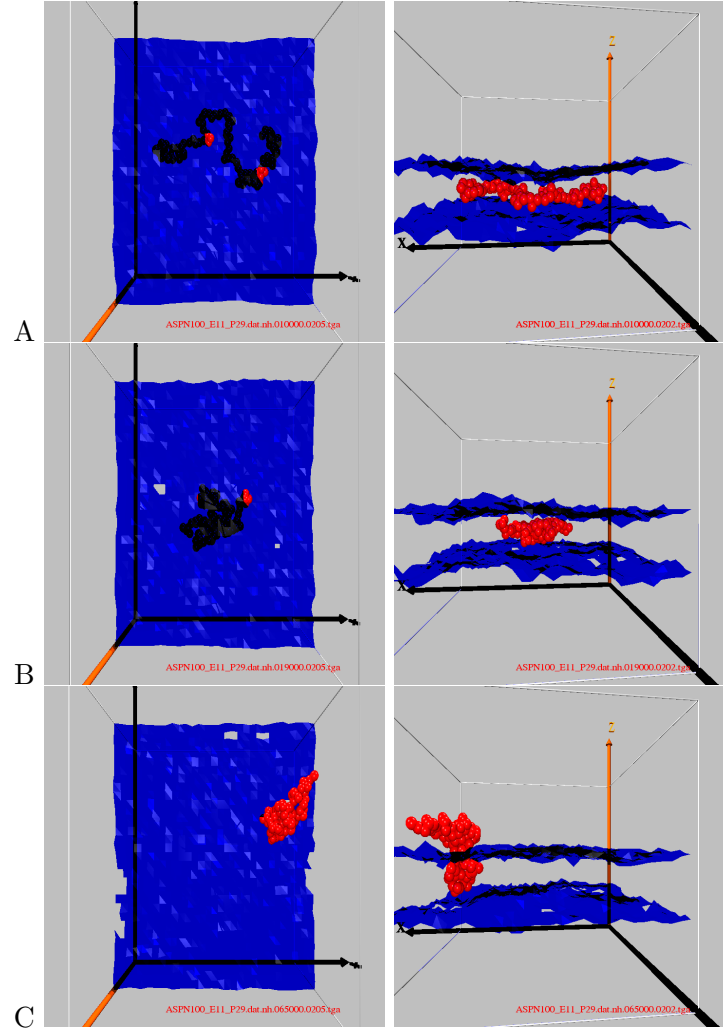
Figure 5.8: Side and top views of the polymer in the lamellar phase after $3\,000\,\tau$ (A), $13\,000\,\tau$ (B) and $59\,000\,\tau$ (C) (the polymer was inserted in the lamellar phase et $t = 7\,000\,\tau$). For clarity, only the two lamellae around the polymer are represented (in blue), but the simulation box contains five lamellae. The pores are represented by holes in the blue surfaces. The red polymer beads appear black when they are behind the blue lamellae.

The two-dimensional conformation does not seem to be a stable state. The final squared radius of gyration is approximatively $8\,\sigma^2$, which is much smaller than in the isotropic solvent ($\langle R_g^2 \rangle_0 = 42 \pm 2\,\sigma^2$, where the subscript 0 denotes the value obtained in pure solvent - see Section 1.1.3).

The transition from an extended to a globular object is also detected via the analysis
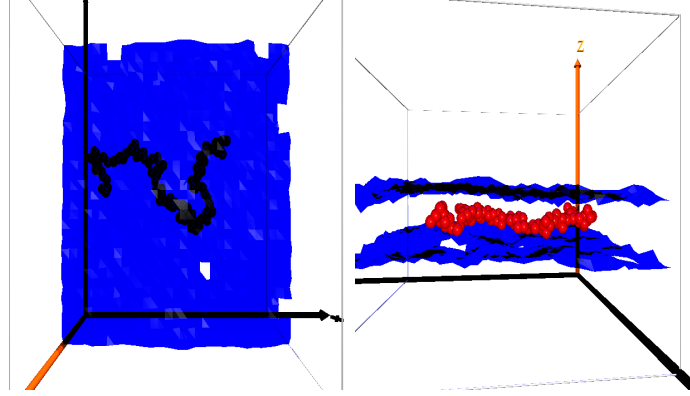
Figure 5.9: Side and top views of the absorbing polymer in the lamellar phase after $30\,000\,\tau$.
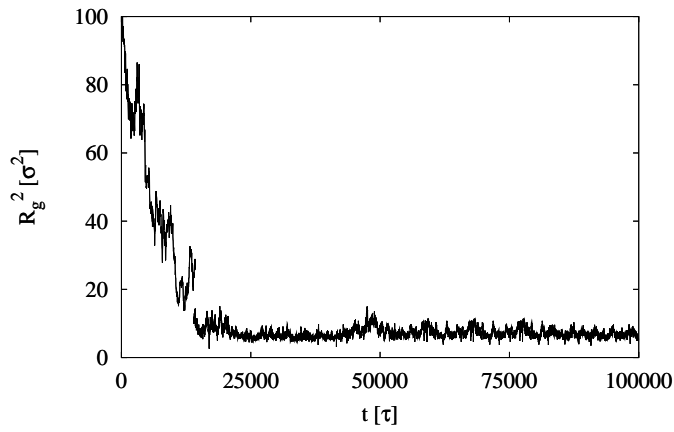
Figure 5.10: Square of the radius of gyration *vs.* simulation time (non-adsorbing polymer).

of the polymer gyration matrix $\hat{G}$ [203, 202] :

$$\hat{G}_{\alpha\beta} = \frac{1}{N} \sum_{i=1}^{N} (\mathbf{r}_i - \mathbf{r}_{CM})^\alpha (\mathbf{r}_i - \mathbf{r}_{CM})^\beta \quad \text{with} \quad \alpha, \beta \in \{x, y, z\}, \tag{5.7}$$

where $\mathbf{r}_{CM}$ is the position of the center of mass of the polymer (Eq. 1.3). The sum of the three (positive) eigenvalues of the gyration matrix is the radius of gyration

$$R_g^2 = L_1^2 + L_2^2 + L_3^2. \tag{5.8}$$

I computed the asphericity δ^* and acylindricity S^* proposed by Aronowiz [5].

$$\delta^* = 1 - 3 \; \frac{L_1^2 L_2^2 + L_2^2 L_3^2 + L_1^2 L_3^2}{R_g^4}. \tag{5.9}$$

$$S^* = \frac{(3L_1^2 - R_g^2)(3L_2^2 - R_g^2)(3L_3^3 - R_g^2)}{R_g^6}. \tag{5.10}$$

The asphericity δ^* ranges between 0 (sphere) and 1 (rod). The acylindricity S^* ranges between -0.25 for an oblate object (*e.g.* a pancake), and 2 for a prolate object (*e.g.* a cigar), with the particular value of 0 for the sphere. Fig. 5.11 displays the time evolution of the asphericity and acylindricity of the polymer.
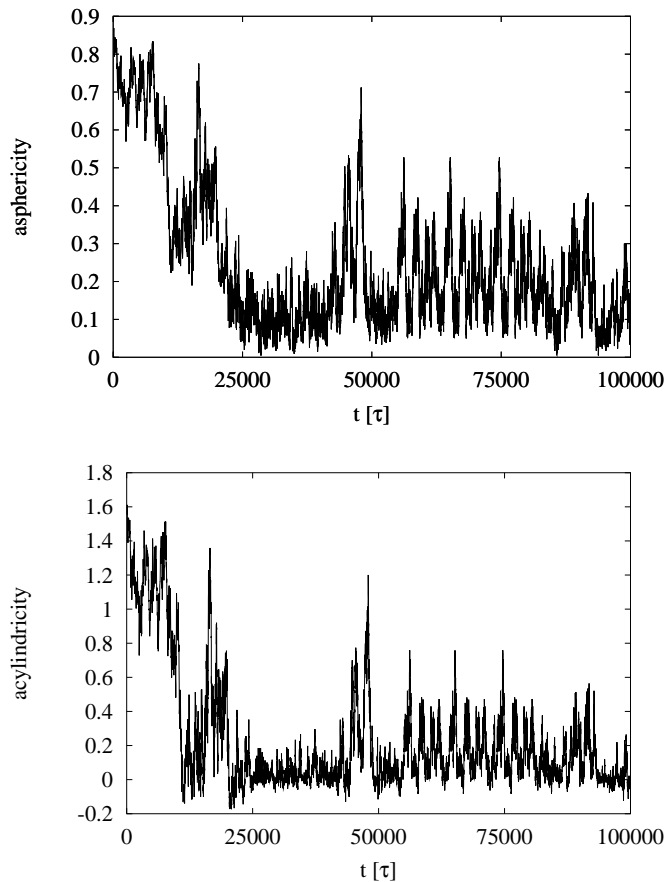
Figure 5.11: Asphericity (top) and acylindricity (bottom) *vs.* simulation time (non-adsorbing polymer).

Again, we distinguish two stages in the evolution of the polymer. At the very beginning of the simulation ($t \leq 10\,000\,\tau$), the polymer is in an extended and asymmetric state

($\langle\delta^*\rangle = 0.70 \pm 0.05$ and $\langle S^*\rangle = 1.1 \pm 0.1$). In the first stage ($t \leq 40\,000\,\tau$), the form of the polymer becomes more spherical. In the final part of the simulation ($t \geq 40\,000\,\tau$), the asymmetry of the conformations is much less pronounced: $\langle\delta^*\rangle = 0.15 \pm 0.02$ and $\langle S^*\rangle = 0.19 \pm 0.01$. The final polymer conformations are even more spherical than in the pure solvent: $\langle\delta^*\rangle_0 = 0.43$ and $\langle S^*\rangle_0 = 0.54$[3]. Fig. 5.12 emphasizes the difference between the distributions of $\{\delta^*, S^*\}$ in the isotropic pure solvent (A) and in the lamellar phase (B).

We conclude that despite the presence of good solvent, the polymer precipitates into a globular state. The decrease of the polymer size in an intermediate confinement regime agrees qualitatively with previous simulations of a single chain between two planar repulsive walls [38, 35]. But the analogy with those results should be made with care: in the present case, the shrinkage is much more important. Here, the polymer is spherical, which is not the case in Refs. [38, 35].

To determine the orientation of the polymer relative to the bilayers, I projected the main axis of the polymer gyration matrix **u** onto the director **n** of the smectic. The absolute value of the projection, $|u_z|$, is displayed in Fig. 5.13 as a function of time. Fig. 5.13 confirms the previous interpretations: during the first part of the simulation, the polymer's main axis is perpendicular to the director ($\langle|u_z|\rangle = 0.034 \pm 0.025$ for $t \leq 20\,000\,\tau$). The polymer is parallel to the solvent layers. During the second part of the simulation ($t \geq 40\,000\,\tau$), the main axis is almost aligned along the director ($\langle|u_z|\rangle = 0.67 \pm 0.25$), as the snapshot represented in Fig. 5.8 C already suggested.

The simulations therefore reveal a different scenario from what is often suggested in the literature: the polymer is a prolate globule with its main direction along the director of the lamellar. Furthermore, the constraint on the polymer due to the lamellae is partially released by a pore.

5.4.2 Effect of the polymer on bilayer fluctuations

The distribution of distances $dh = |h_n(x,y) - h_{n+\Delta n}(x,y)|$ ($n = 1, ..., N$ and $\Delta n = 1, ..., N/2$) between the bilayers in the absence of polymer has already been presented (see Section 3.2). In the stack of five bilayers, two peaks are obtained, corresponding to the distances between membranes separated by one or two solvent layers.

The analysis of the configuration in the presence of the polymer were performed as follows: For each configuration, the distributions of interlamellar distances dh were averaged on all the grid-positions (x,y) distant of r from the center of mass of the polymer[4]. If the position (x,y) corresponds to a hole in the membrane, no distance is registered. The results are based on the second part of the simulation, ($t \geq 40\,000\,\tau$), when the polymer has relaxed its shape. In Fig. 5.14, the distributions of interlamellar

---

[3]These values, obtained by a simulation of the polymer in pure solvent, agree with other numerical simulations and theoretical predictions. For an athermal self-avoiding random walk on a tetrahedral lattice, Zifferer *et al.* computed $\langle\delta^*\rangle_0 = 0.433 \pm 8.10^{-5}$, $\langle S^*\rangle_0 = 0.5447 \pm 2.10^{-4}$, see [211] and references in it.

[4]The squared distance in the plane of the bilayer is $r^2 = \Delta x^2 + \Delta y^2$, where $\Delta x = (x - x_{CM})$ and $\Delta y = (y - y_{CM})$. The couple (x,y) denotes a grid-position on the bilayer and (x_{CM}, y_{CM}) denotes the projection of the center of mass of the polymer on the midplane of the bilayer.
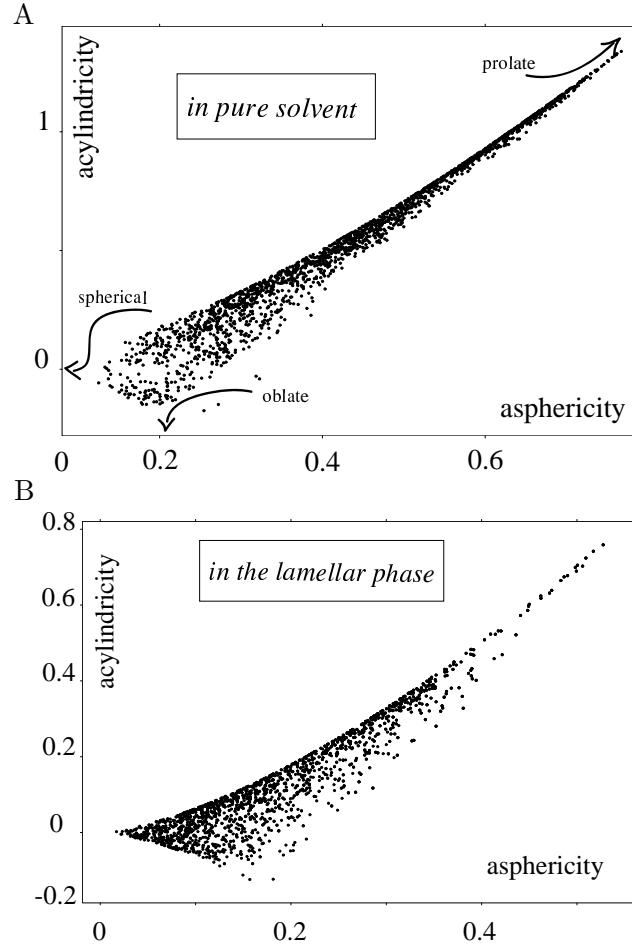
Figure 5.12: Scatter plots of the asphericity *vs.* acylindricity of the polymer chain (note the scale differences). Both plots contains 2 000 points corresponding to single configurations separated by $10\,\tau$. For the polymer in the lamellar phase, data are in the domain $t \geq 40\,000\,\tau$. *A*: in pure solvent (see Section 1.1.3). *B*: in the lamellar phase.

distances for $r \sim 2\,\sigma$ and $r \sim 17\,\sigma$ are displayed. The curve for $r \sim 0$ is not available because the polymer center of mass is in a pore.

The distributions of distances without polymer and far from the polymer are similar; the mean values of the interlamellar distances are equal. Effectively, the dimensions of the simulation box are not modified by the presence of the polymer. In particular the dimension along the director, $\langle L_z \rangle$, is $43.4 \pm 0.1\,\sigma$ in both cases. One effect is notable: the interlamellar distance distribution is broader in the presence of the polymer.

A clear influence of the polymer is observable for $r \leq 6\,\sigma$. In the vicinity of the polymer, the distribution of distances is shifted toward small distances. In other words,
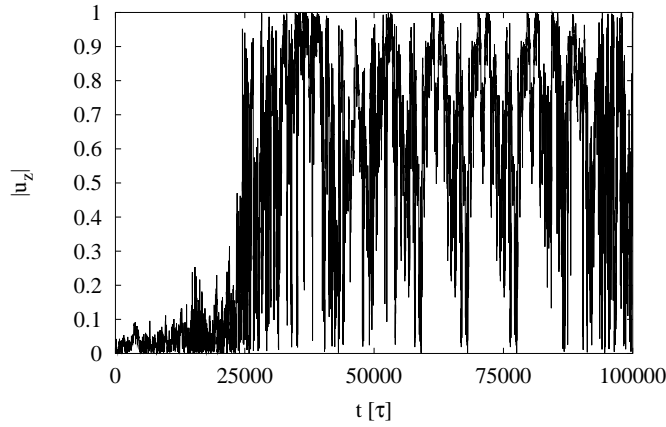
Figure 5.13: Projection of the polymer axis on the director of the smectic, $|u_z| = |\mathbf{u} \cdot \mathbf{n}|$, *vs.* simulation time (non-adsorbing polymer).
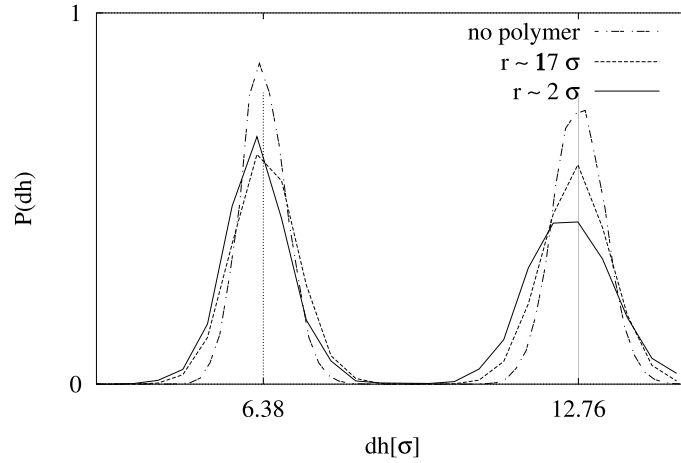
Figure 5.14: Probability distributions $P(dh)$ of the interlamellar distances $dh = |h_n(x, y) - h_{n+\Delta n}(x, y)|$ for $\Delta n = 1, 2$ (non-adsorbing polymer). The area beneath each peak is normalized to 1.

the polymer compresses the lamellae locally. As the box dimension along the director is not modified, the change in the mean value of the interlamellar distance must be attributed to the presence of pores. The interlamellar distance distribution broadens even more in the vicinity of the polymer.

5.4.3 Nucleation of defects around the polymer

Correlations between the polymer and the pores.

We have seen that the non-adsorbing polymer is globular, and located in a pore of the bilayer. Does the polymer increase the number of pores? Does it increase the size of pores? Where are these pores?

The total area of the pores and total number of pores per bilayer are collected in Tab. 5.1. Note that the values are divided by the values obtained in the stack of five bilayers without polymer (approximately 10 pores and a surface of $30\,\sigma^2$ for bilayers of area $\sim 1850\,\sigma^2$). The bilayers are sorted according to their distance to the center of mass of the polymer

$$dz = |z_{CM} - \bar{h}_n|,$$

where z_{CM} is the coordinate of the polymer center of mass along the z-axis, and $\bar{h}_n$ the height of the bilayer mid-plane. As the polymer center of mass is almost in the mid-plane of the bilayer, the distances dz are close to $0, d$, and $2d$. The effect of the polymer on

$\langle dz \rangle$	0	d	$2d$
area	1.75	0.90	0.95
number	0.65	0.90	0.95

Table 5.1: Total area and number of pores in one bilayer, in the presence of a non-adsorbing polymer, relative to the case without polymer. The variable dz is the approximate distance along the director between the polymer center of mass and the midplane of the bilayer. The variable d is the interlamellar distance.

the pore number and area is relatively strong in the bilayer which it perforates ($dz \sim 0$), but almost insignificant in the other bilayers (the errors on the ratios are approximately 0.05). For $dz \sim 0$, the polymer increases the total area of the pores, and decreases the number of pores. We deduce that some of the pores are larger in the presence of polymer. The reduction of the number of pores in the membrane may be due to the limited simulation time. As the diffusion of the amphiphiles from one bilayer to the next one is not observed, the area per amphiphile may diminish in the bilayer in which the polymer is located. This would hinder the nucleation of pores around the polymer.

To analyze the local influence of the polymer on the pore formation, we shall study the pair correlation functions between the pore positions and the polymer bead positions. I have chosen to use the positions of every polymer bead to locally investigate the correlations. The analyses were done as follows: For each configuration and each bilayer, the height difference between the polymer center of mass and the membrane, dz is measured. The two-dimensional pair correlation function $g(r)$ between the n^{pore} pore centers and n^{poly} polymer beads is computed using the formula

$$g(r) = \frac{n^{pairs}(r, dr)}{n^{poly} \cdot n^{pore}} \frac{A}{2\pi r dr}, \tag{5.11}$$

where $n^{pairs}(r, dr)$ is the number of pairs {pore center, polymer bead} separated by a distance between r and $r + dr$, A the total area of the bilayer, and dr the interval of r on

which the pair correlation function is averaged. The correlation function obtained for all the configurations are averaged for $|dz| \leq 0.25\,\sigma$, $|dz - d| \leq 0.25\,\sigma$ and $|dz - 2d| \leq 0.25\,\sigma$. Fig. 5.15 shows the pair correlation function between the polymer beads and the pore centers. As expected, the polymer and the pores are strongly correlated for $dz \sim 0$:

s
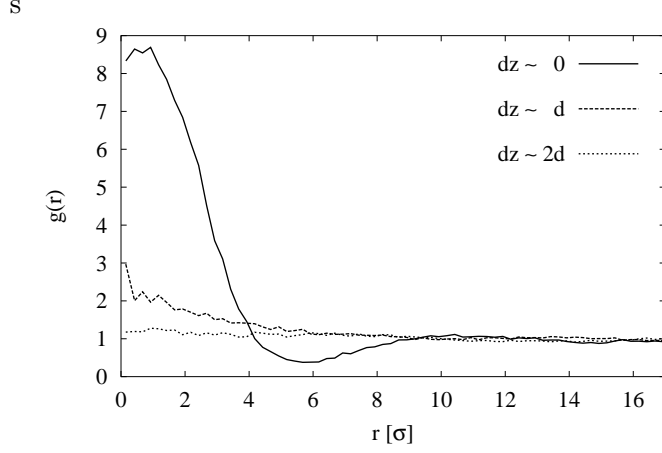
Figure 5.15: Pair correlation function between the polymer-beads and the centers of the pores (see Fig. 5.16 A). The parameter dz is the height difference between the polymer center of mass and the bilayer midplane.

we observe a peak at $r = 0$. The correlation extends up to the distance $r \sim 4\,\sigma$. The polymer also induced pores in the other bilayers ($dz \sim d$ and $2d$), but the correlation is lower than for the bilayer at $dz \sim 0$. For $r \geq 10\,\sigma$, the correlation between the polymer beads and the pore centers is no longer significant. For $r \sim 6\,\sigma$ and $dz \sim 0$, the probability to find a pore is relatively low. This depletion might be interpreted by the short-ranged repulsion between pores: two pores cannot be closer than twice the thickness of the pore rim ($\sim 3.5\,\sigma$).

The same analysis was also done with the positions of the grid where a pore was detected (which I call "pore positions", as opposed to "pore centers"). The pore positions, as in the whole thesis, are defined on a grid of mesh $1.3\,\sigma$. Fig. 5.16 illustrates the difference between the two correlation functions computed in this section.

For each bilayer, the two-dimensional pair correlation $g_B(r)$ between the n^{pp} pore-positions and n^{poly} polymer-beads (Fig. 5.16 B) is computed using the formula

$$g_B(r) = \frac{n^{pairs}(r, dr)}{n^{poly} \cdot n_0^{pp}} \frac{A}{2\pi r dr}, \tag{5.12}$$

where $n^{pairs}(r, dr)$ is the number of pairs {pore position, polymer bead} separated by a distance between r and $r + dr$, and n_0^{pp} the number of pore-positions obtained in the simulations of the lamellar phase without polymer.

The correlation B is plotted in Fig. 5.17. The correlation peak for r close to zero

pore centers   polymer beads   pore positions   polymer beads
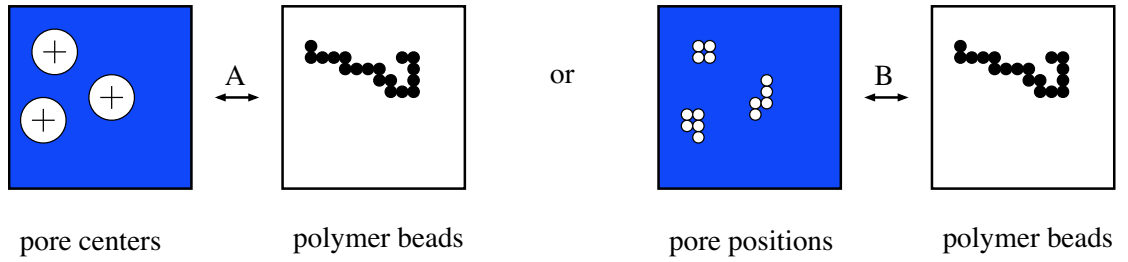
Figure 5.16: Sketch of the two types of correlations between the pores and the polymer. Each disk represents one position {x,y} used to calculate the correlation between the pores (white disks) and the polymer beads (black disks).
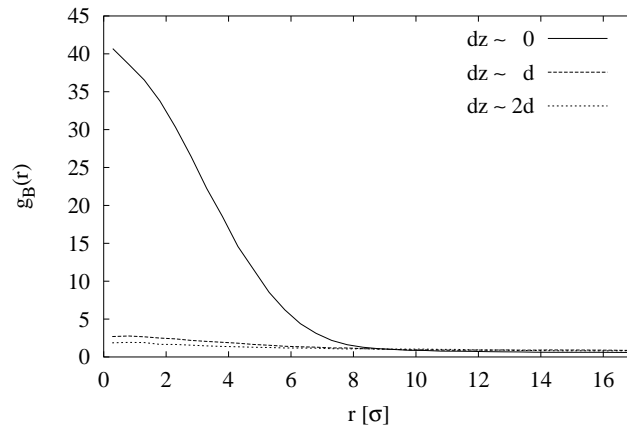
Figure 5.17: Pair correlation functions between the polymer-beads and the pore-positions (positions of the bilayer where the a pore is detected). See Fig. 5.16 B.

is larger than the one obtained with the correlation A, because the correlation B is reweighed in favor of the large pores, which are near $r = 0$. Furthermore, the depletion effect around $r \sim 5\,\sigma$ disappears: pore positions do not repel each other. Notably, the pair correlation function $g_B(r)$ computed for $dz \sim 0$ does not tend towards 1 for large distances, but towards a lower value ($g_B(r) \sim 0.5$ for $r = 20\,\sigma$). In the bilayer containing the polymer, for $r \geq 8\,\sigma$, the presence of pores is less probable that in the lamellar phase without polymer. As already discussed, this effect is probably due to the finite size and the limited time of the simulation.

5.4.4 Summary.

The non-adsorbing polymer inserted in the lamellar phase becomes globular. It forms a pore in one bilayer, and remains stuck in this pore during the whole simulation. In

the plane of the bilayers, the range of the perturbation due to the polymer is approximately the end-to-end distance of the polymer. Along the director of the bilayer, the polymer induces a compression of the bilayers, and triggers the formation of pores even in the next-neighbor bilayers. Among the different scenarios described in Fig. 5.7, the simulation data fit case B, where the stress induced by the polymer inclusion is shared between the polymer and the lamellar phase.

5.5 Adsorbing polymer: simulation results

5.5.1 Confinement of the polymer

Fig. 5.18 shows the time evolution of the squared radius of gyration of the adsorbing polymer in the lamellar phase.
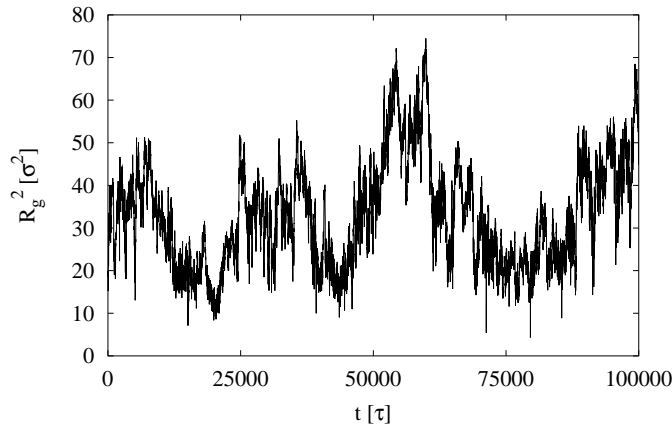
Figure 5.18: Square of the radius of gyration *vs.* simulation time (adsorbing polymer).

For the adsorbing polymer, no qualitative change in the conformation of the polymer appears. The chain remains confined in the solvent layer, with a mean square radius of gyration of $86 \pm 10\,\sigma^2$, which is greater than the value obtained in the pure isotropic solvent $(42 \pm 2\,\sigma^2)$[5]. Similar increases of the radius of gyration were found for single polymers confined in a very thin slit between two planar walls (see Fig. 5.5) [6]. The confinement also deforms the shape of the polymer coil. The mean asphericity and the mean acylindricity $\{\langle \delta^* \rangle, \langle S^* \rangle\} = \{0.65, 0.98\} \pm \{0.02, 0.05\}$ are larger than the values in the pure solvent: $\{\langle \delta^* \rangle_0, \langle S^* \rangle_0\} = \{0.43, 0.54\}$. Notably, the asphericity of the adsorbing polymer is also larger than the value computed for two-dimensional self-avoiding random walks [14] ($\langle \delta^* \rangle_{2D} = 0.53$). The projection of the polymer axis along

---

[5]The value of $86 \pm 10\,\sigma^2$ is obtained for $20\,000\,\tau \le t \le 100\,000\,\tau$, with a correlation time of $\sim 10\,000\,\tau$.

[6]I suppose here that, for a confinement thickness equal to the size of the monomers, the size of the polymer should not depend too much on the interaction with the walls.

the director is low, $\langle |u_z| \rangle = 0.027 \pm 0.002$, which confirms that the polymer main axis is aligned with the bilayer.

5.5.2 Effect of the polymer on bilayer fluctuations

As in Section 5.4, the influence of the polymer on the bilayer fluctuations is characterized by the distribution of distances $dh = |h_n(x,y) - h_{n+\Delta n}(x,y)|$, for several distances r relative to the polymer center of mass. Fig. 5.19 displays the distribution of dh at the distances $r \sim 2\,\sigma$ and $r \sim 17\,\sigma$ from the adsorbing polymer center of mass. In the stack of five bilayers, two peaks are obtained, corresponding to the distances between membranes separated by one or two layers of solvent.
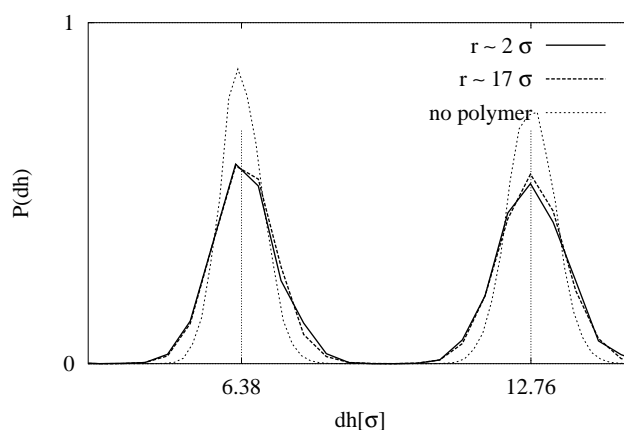
Figure 5.19: Probability distributions $P(dh)$ of the interlamellar distances in the presence of an adsorbing polymer. The solid curve is obtained in the vicinity of the center of mass of the adsorbing polymer ($r \sim 2\,\sigma$), the dashed curve is obtained further away from the polymer ($r \sim 17\,\sigma$). The dotted curve corresponds to the result in the lamellar phase without polymer. The area beneath each peak is normalized to 1.

We cannot see any significant influence of the polymer on the mean interlamellar distance, not even in the vicinity of the polymer, let alone further away. As observed experimentally by X-ray scattering, the standard deviation of the peaks is broader than in the case without polymer. Among the different scenarios described in Fig. 5.7, the simulation results suggest case D, where the stress induced by the polymer inclusion is shared between the polymer and the lamellar phase, but there is no proliferation of pores.

5.5.3 Nucleation of defects around the polymer

We have seen that the adsorbing polymer remains between two bilayers. Nevertheless, its presence may induce the formation of pores in the neighboring bilayer.

The changes of the total areas and numbers of pores per bilayer due to the presence of polymer are summarized in Tab. 5.2. As in Tab. 5.1, the values are divided by the total area and number of pores obtained in the simulations without polymer. The absorbing

$\langle dz \rangle$	$d/2$	$3d/2$
area	0.98	0.93
number	0.98	0.95

Table 5.2: Total area and number of pores in one bilayer in the presence of polymer, divided respectively by the total area and total number of pores obtained in the simulations without polymer. The distance $\langle dz \rangle$ is the averaged height difference between the polymer center of mass and the midplane of the bilayer. The errors on the ratios are about 0.05.

polymer does not show any particular tendency to perforate the bilayers.

This interpretation is confirmed by the pair correlation functions between the pore centers and the polymer beads (see Fig. 5.20). The polymer center of mass is in the solvent layer, between two bilayers; the typical distances $dz = |z_{CM} - \bar{h}_n|$ between the polymer center of mass and the mid-plane of the bilayers are then $d/2$ and $3d/2$.
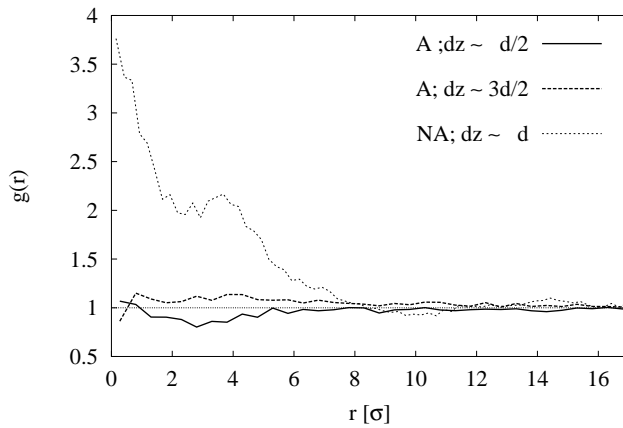
Figure 5.20: Pair correlation functions between the polymer-beads and the pore-centers (see Fig. 5.16 A) for the adsorbing polymer (A), and the non-adsorbing polymer (NA).

The correlation functions between the pore-center and the adsorbing polymer-beads (A) deviate slightly from 1. For comparison, the pair correlation obtained in the case of the non-adsorbing polymer (NA) is also plotted. I have chosen the curve with $dz \sim d$, so that the correlation between the non-adsorbing polymer and the pore in which it is located is not considered here. In comparison to the non-absorbing polymer, the absorbing polymer does not show any particular tendency to perforate the bilayers.

5.6 Discussion

Single polymer chains confined in the solvent layers of the L_α lamellar phase have been simulated. The simulations describe a very dilute polymer solution: in the solvent layers the polymer chains do not interact, and along the director, they are separated by five bilayers.

The simulations presented here are not equilibrated, in the sense that we could not investigate the whole phase space of the confined polymer and the smectic phase. For example, the time of translocation of the polymer through a pore in the membrane is proportional to N^{-2} [185]. Using the (overestimated) value of the diffusion constant of the solvent through a pore of about $10^{-2}\,\sigma^2\cdot\tau^{-1}$, one finds that the diffusion of the polymer through a pore in the membrane takes at least $10^7\,\tau$, whereas the present simulations lasted about $10^5\,\tau$. Similarly, the simulation time is too small to consider the amphiphile diffusion in the direction of the director[7]. Nevertheless, the simulations presented in this chapter describe a "local" equilibrium, in which the differences of behaviors between the adsorbing and non-adsorbing polymers are substantial.

We have seen that the adsorbing polymer confined in the lamellar phase does not trigger pores in the bilayers. The polymer remains confined between the bilayers, with a stretched planar conformation. We cannot see any change in the interlamellar spacing before and after the insertion of the adsorbing polymer, but this may due to the fact that the solvent thickness is only a few times the monomer size. The only significant influence of adsorbing polymer on the lamellar phase is a broadening of the interlamellar-distance distribution, *i.e.* an effective softening of the bilayer interactions. These observations agree qualitatively with experimental results [178].

By contrast, a non-adsorbing polymer does not remain confined between the lamellae. The polymer condenses into a globule, and makes a pore in which it remains during the whole simulation time. This can be interpreted as a local phase separation of the polymer. In the vicinity of the polymer globule, a local compression of the bilayers and a broadening of the interlamellar-distance distribution are discernible. The constraint exerted by the globule on the lamellar phase is partially released by the formation of a pore around the polymer. Nevertheless, the non-adsorbing polymer perturbs several bilayers along the director of the smectic phase.

The mechanism of membrane fusion was already investigated with numerical simulations of a coarse-grained model of amphiphilic bilayers [126]. The authors proposed a new mechanism, involving the creation of two facing pores in the parallel fusing bilayers. The ability of polymers to trigger pores demonstrated in this chapter is a possible explanation for their ability to facilitate membrane fusion.

---

[7]One can consider simulating the system using Monte Carlo methods rather than molecular dynamics in order to describe the translocation of the polymer and the diffusion of the amphiphiles. Monte Carlo steps describing the "slithering" of the polymer in the solvent, and the addition/destruction of bonds were implemented, but the code has not been used yet.

Conclusions and outlook

This thesis deals with the pure and polymer-doped L_α phase of amphiphilic molecules in aqueous solution. The investigation focuses on the local structure of a model L_α phase, in particular on the position fluctuations of bilayers and on the transient pores appearing in the bilayers.

Molecular dynamics simulations permitted to study how collective motion emerge from microscopic molecular interactions in a mixture of amphiphiles and solvent. The algorithm used in this thesis was optimized to study the lamellar phase in the isobaric isothermal ensemble without surface tension ($N, P, T, \gamma = 0$). The simulations provided information about the structure of the bulk lamellar phase at time-scales and length-scales of the order of ten picoseconds and ten nanometers.

About the position fluctuations

In the present work, stacks of five and fifteen bilayers have been studied to investigate the interlamellar interactions. The position fluctuations of the bilayers in the lamellar phase were studied, and confronted to the predictions of the "Discrete Harmonic" model [80, 144, 102, 141, 110] for the elasticity of smectic A, in which the bilayers are treated as continuous undulating surfaces. It turns out that the simulation results obtained with a stack of fifteen bilayers agree reasonably well with the theory. To compute the two elasticity constants from numerical simulations of the lamellar phase, a method similar to recent analyses of X-ray scattering spectra of highly aligned L_α-phase [110, 168] was proposed. The compressibility modulus of a smectic phase could be obtained for the first time with molecular dynamics simulations.

The fluctuation spectra obtained for free undulating membranes are usually characterized by the position fluctuation spectrum $s_0(q_\perp) \propto q_\perp^{-4}$ [68, 200, 107, 176]. One of the important results of this work is that we did not observe this regime for the bilayers in the lamellar stack. Within the continuous theory of smectic elasticity, the free-membrane regime ($s_0(q_\perp) \propto q_\perp^{-4}$) is expected only for wavelength smaller than the in-plane correlation length ξ ($q_\perp \ll \xi^{-1}$). In the simulated stack of bilayers, the in-plane correlation length ξ is small ($\xi \sim 2.35\ \sigma$). The reason is that this correlation length ξ is closely related to the interactions between membranes, which are characterized by the compressibility modulus B ($\xi = (K_c/B)^{1/4}$). For free, non-interacting membranes, the correlation length ξ is infinite. For confined membranes, ξ becomes finite. In the present simulations, the bilayers are very close to each other, it is therefore not surprising that ξ is of the order of the size of the molecules. As a consequence, the validity

of the continuum model breaks down at wavevectors larger than $q_\perp \sim \xi^{-1}$, before the free-membrane regime can be observed.

About the pores in the bilayers

In a second part, pores appearing spontaneously in the bilayers were studied. The molecular structure of the pores of area larger than $4\sigma^2$ shows that the amphiphiles situated in the rim of the pore reorient: the hydrophilic heads shield the hydrophobic tails from the solvent. The thickness of the pore edge may be at the origin of the short-range repulsion between the pores, which could be observed in the spatial pair correlation function of the pores, and in the Minkowski analyses.

Without surface tension, the pores are not circular. The relationship between the area a of the pores and their contour-length c is well described by the scaling law $a \propto c^{2/3}$. This scaling was found for other two-dimensional objects, whose energy depends only on their contour length (models of flaccid vesicles [103] and of self-avoiding ring-polymers[14]). The classical expression of the excess energy due to a single pore is $E = E_0 - \gamma a + \lambda c$, where λ is the line tension and γ the surface tension. Since the simulated bilayers undergo no surface tension ($\gamma = 0$), it seems justified to consider that the energy E of a pore depends on the contour length c only, and simplifies to a linear function. The effective free energy was therefore computed from the distribution of the contour-lengths c of the pores. It is not linear, and even non-monotonous for small contour lengths. This non-monotony was attributed to the fact that the analysis is done on a finite rectangular grid, rather than to the presence of metastable pores. Taking into account the effects of the grid on the analysis, it was possible to estimate the line tension of the pores: $\lambda = 5 \cdot 10^{-11} \, J \cdot m^{-1}$, which is in agreement with the theoretical predictions by May [115].

The time-dependent analyses of the pores showed that they nucleate and close off before diffusing within the membranes. The life-time distribution $P(\mathcal{T})$ decreases relatively slowly with the life-time $\mathcal{T}$ (it can be fitted, for example, by the power law $\mathcal{T}^{-2}$). To interpret this trend, I compared the time evolution of the pore contour-lengths to a simple model: a one-dimensional random walk in a linear potential (RW-LP) [90]. Despite its simplicity, this model reproduces one important feature observed in the simulations: the life-times of the pores are correlated to their mean contour-lengths. The prediction of the RW-LP model reproduces nicely the long tail of the life-time distribution observed for the pores. The resulting order of magnitude of the mean life-time of the pores agrees with all-atoms molecular dynamics simulations [113, 112, 207].

About the polymer between the bilayers

Finally, we investigated the interaction of a polymer with the lamellar phase.

Previous works on doped lamellar phase often study the structure of one component only, neglecting the deformations of the other one. For example, if one focuses on the conformations of the confined polymer, the bilayers are treated as planar walls [23]. On the other hand, if one focuses on the deformations of the lamellar phase, the doping

polymer is seen as a point [172]. Theories which neglect the coupling between the polymer and the lamellar phase deformations have indeed proven to be useful to interpret scattering data of doped lamellar phase [23, 16].

The present work adopts a complementary point of view: it treats the doped lamellar phase as a global system, where both components (the smectic phase, and the polymer) are considered explicitly with many internal degrees of freedom. This approach was instructive: in the simulations, both the polymer and the lamellar phase were modified in the doped lamellar phase.

The insertion of the polymer broadens the interlamellar distance distribution, as observed in X-ray scattering spectra of doped lamellar phase. In addition, a non-adsorbing polymer is able to modify locally the interlamellar distance (here, the mean interlamellar distance decreases in the presence of polymer).

The polymer conformations are strongly influenced by the confinement. Interestingly, the behaviors of adsorbing and non-adsorbing polymers were radically different: the adsorbing polymer remained confined between the bilayers, while the non-adsorbing polymer condensed into a globule, and created a large pore in a neighboring membrane. Within the limited time of the simulations (100 000 time units), the polymer remained stuck in this pore. The globular conformation of the non-adsorbing polymer is radically different from the pancake conformation assumed in the traditional scaling approach. This condensed conformation obtained by simulations in the isobaric isothermal ensemble (N,P,T,γ) may reflect the fact that, with the simulation parameters used in this thesis, the non-adsorbing polymer is not soluble in the lamellar phase. Simulations in the semi-grand canonical ensemble or grand canonical ensemble would help to verify this interpretation.

About future work

These encouraging results permit to envisage further investigations on the L_α phase and its interaction doping macromolecules. Here are some of the numerous possibilities to continue the work:

- The results about the pores merit some further investigations. First, the time-dependent analyses of the pores should be more precise to become really convincing. Second, the study of spatial distribution of pores treated the correlations of pores within each bilayer. I did not present results about the spatial distribution of pores between membranes. Preliminary results, and a related work [127] show that there are correlations between the pores of neighboring bilayers. The simulation data presented in this thesis can be exploited to study these correlations, and to understand how they are influenced by the presence of a doping polymer.

- The lamellar phase presented in this thesis is composed of short amphiphiles (tetramers). One could test whether the pores triggered by the polymeric inclusion would also appear in thicker bilayers.

- In order to compare our results with experiments, it would be informative to study

the several confinement regimes of the non-adsorbing polymer, obtained for different values of the confinement parameter d/a and the polymer volume fraction Φ_p. An first step could be to simulate a system where there is one polymer in each solvent layer, with no interactions among the polymers of the same solvent layer.

- The orientational distribution of guest molecules in the lamellar phase is anisotropic. The simulations presented here can be generalized to inclusions different from a flexible homopolymer, for example semi-flexible polymers, amphiphilic polymers, membrane inclusions...

Acknowledgments

Acknowledgments

138

Bibliography

[1] M. Allen and D. Tildeslay, *Computer Simulation of liquids*, Oxford University Press, Oxford, 1987. 5, 6, 10, 14, 20

[2] H. Andersen, *Molecular dynamics simulations at constant pressure and/or constant temperature*, Journal of Chemical Physics (1980), **72**, *4*, pp. 2384–2393. 13, 24, 28

[3] L. Antanovskii, *Microscale theory of surface tension*, Physical Review E (1996), **54**, *6*, pp. 6285–6290. 21

[4] K. Aoki and F. Yonezawa, *Constant pressure molecular-dynamics simulations of the crystal-smectic transition in systems of soft parallel spherocylinders*, Physical Review A (1992), **46**, *10*, pp. 6541–6549. 17

[5] J. Aronowitz and D. Nelson, *Universal features of polymer shapes*, Journal de Physique (1986), **47**, *9*, pp. 1445–1456. 122

[6] S. Asher and P. Pershan, *Parabolic focal conics and polygonal textures in lipid liquid crystals*, Journal de Physique (1979), **40**, *2*, p. 161. 69

[7] H. E. Bardouni, *Determination de la tension superficielle d'une goutte liquide par des simulations de dynamique moleculaire*, PhD thesis, Université Libre de Bruxelles, 2001. 21, 41, 42

[8] A. Barnett and J. Weaver, *Electroporation: a unified, quantitative theory of reversible electrical breakdown, and rupture*, Biolelectrochem. Bioenerg. (1991), **25**, pp. 163–182. 72

[9] L. Barruentos, K. Gawrisch, N. Cheng, A. Steven, and A. M. Gronenborn, *Structural characterization of the dilute aqueous surfactant solution of cetylpyridinium bromide/hexanol/sodium bromide*, Langmuir (2002), **18**, pp. 3773–3779. xii, 111

[10] N. Bechthold, B. Tiersch, J. Kötz, and S. Friberg, *Structure formation in polymer-modified liquid crystals*, Journal of Colloid and Interface Science (1999), **215**, p. 106. 110

[11] V. Berejnov, Y. Raikher, V. Cabuil, J. Bacri, and R. Perzynski, *Synthesis of stable lyotropic ferronematics with high magnetic content*, Journal of Colloid and Interface Science (1998), **199**, *2*, pp. 215–217. 109

Bibliography

[12] K. Binder and G. Ciccotti, eds., *Monte Carlo and Molecular Dynamics of condensed matter systems*, Società Italiana di fisica-Bologna, 1995. 10, 13

[13] K. Binder and D. Landau, *Guide to Monte Carlo Simulations in Statistical Physics*, Cambridge University Press, 2000. 10

[14] M. Bishop and C. Saltiel, *Polymer shapes in two, four and five dimensions*, Journal of Chemical Physics (1988), **88**, *6*, pp. 3976–3980. 129, 134

[15] F. Bordi, C. Canetti, and A. Naglieri, *Ionic transport in lipid bilayer membranes*, Biophysical Journal (1998), **74**, pp. 1358–1370. 70, 71

[16] G. Bouglet, *Confinement d'un polymère dans une phase lamellaire lyotrope: comportement de phase et constantes élastiques*, PhD thesis, Université de Montpellier II, 1997. 69, 135

[17] G. Bouglet and C. Ligoure, *Polymer-mediated interactions of fluid membranes in a lyotropic lamellar phase: a small angle x-ray and neutron scattering study*, European Physical Journal B (1999), **9**, pp. 137–147. xiii, 45, 54, 109, 110, 111, 113, 114, 118

[18] G. Bouglet, C. Ligoure, A. Bellocq, E. Dufourc, and G. Mosser, *Bending moduli of a non-adsorbing-polymer-containing lyotropic lamellar phase: An experimental study*, Physical Review E (1998), **57**, *1*, p. 57. 109, 110, 111

[19] Y. Bouligand, *Remarks on the geometry of micelles, bilayers and cell membranes*, Liquid Crystals (1999), **26**, *4*, pp. 501–515. 49, 69

[20] F. Brochard and P.-G. D. Gennes, *Conformation of molten polymers inside small pores*, Journal de Physique France Lett. (1979), **40**, pp. L399–L401. 112, 115

[21] F. Brochard-Wyart and E. Raphael, *Scaling theory of molten polymers in small pores*, Macromolecules (1990), **23**, p. 2276. 112

[22] U. Brodatzki and K. Mecke, *Simulating stochastic geometries: morphology of overlapping grains*, Computational Physics Communication (2002), **147**, *1-2*, pp. 218–221. 81

[23] J. Brooks and M. Cates, *The role of polymer added in dilute lamellar surfactant phases*, Journal of Chemical Physics (1993), **99**, p. 5467. 45, 109, 110, 112, 134, 135

[24] J. T. Brooks, C. Marques, and M. Cates, *The effect of adsorbed polymer on the elastic moduli of surfactant bilayers*, Journal de Physique II (France) (1991), **1**, pp. 673–690. 112

[25] F. Buff, *Spherical interface.2.molecular theory*, Journal of Chemical Physics (1955), **23**, *3*, pp. 419–426. 21

140

[26] A. Caillé, *X-ray scattering in smectic a*, Rapports de l'Académie des Sciences (1972), **274B**, *14*, p. 891. 57

[27] P. Canham, *Minimum energy of bending as a possible explanation of biconcave shape of human reed blood cell*, Journal of Theoretical Biology (1970), **26**, p. 61. 45, 47

[28] P. Chaikin and T. Lubenski, *Principles of condensed matter physics*, Cambridge University Press, London, 1995. 33, 51, 69

[29] D. Chandler, *Introduction to Modern Statistical Mechanics*, Oxford University Press, New York, 1987. 10

[30] S. Chandrasekhar, *Liquid crystals*, Cambridge University Press, London, 1977. 32, 33, 51, 69

[31] S. Chiu, M. Clark, V. Balai, S. Subramanian, H. Scott, and E. Jakobsson, *Incorporation of surface tension into molecular dynamic simulation of an interface: a fluid phase lipid bilayer membrane*, Biophysical Journal (1995), **69**, *4*, pp. 1230–1245. 22

[32] S. Chiu, E. Jakobsson, S. Subramaniam, and J. Scott, *Combined monte carlo and molecular dynamics simulation of fully hydrated dioleyl and palmitoyl-oleyl phosphatidylcholine lipid bilayers*, Biophysical Journal (1999), **77**, *5*, pp. 2462–2469. 1, 2

[33] A. Ciach, *Phase diagram in a lattice model of surfactant solutions*, Journal of Chemical Physics (1990), **93**, *7*, p. 5322. 2

[34] P. Cifra and T. Bleha, *Anisotropy in the dimensional and elastic parameters of confined macromolecules*, Macromolecular Theory and Simulations (1999), **8**, *6*, p. 603. 112, 116

[35] ――――, *Concentration dependence of the global and anisotropic dimensions of confined macromolecules*, Macromolecular Theory and Simulations (2000), **9**, *8*, p. 555. 112, 116, 123

[36] C. J. Clark and K. L. Wooley, *Polymerization of organized polymer assemblies*, Current Opinion in Colloid and Interface Science (1999), **4**, p. 122. xii

[37] D. Constantin and P. Oswald, *Diffusion coefficients in a lamellar lyotropic lamellar phase: evidence for defects connecting the surfactant structure*, Physical Review Letters (2000), **85**, *20*, pp. 4297–4300. 39, 69, 70

[38] C. Cordeiro, M. Molisana, and D. Thirumalai, *Shape of confined polymer chains*, Journal de Physique II (France) (1997), **7**, pp. 433–447. 112, 116, 123

[39] M. Daoud and P.-G. de Gennes, *Statistics of macromolecular solutions trapped in small pores*, Journal de Physique II (France) (1977), **38**, *1*, pp. 85–93. xii, 112, 115, 117

[40] P.-G. de Gennes, *Scaling Concepts in Polymer Physics*, Cornell University Press, New York, 1995. 113

[41] P.-G. de Gennes and J. Prost, *The Physics of Liquid Crystals*, Oxford University Press, London, 1993. 33, 51, 53, 69

[42] B. Demé, M. Dubois, and T. Zemb, *Swelling of a lecithin lamellar phase induced by small carbohydrate solutes*, Biophysical Journal (2002), **82**, *1*, p. 215. xiii, 110, 111

[43] B. Demé, M. Dubois, T. Zemb, and B. Cabane, *Effect of carbohydrates on the swelling of a lyotropic lamellar phase*, Journal of Chemical Physics (1996), **100**, p. 3828. 110

[44] ——, *Coexistence of two lyotropic lamellar phases induced by a polymer in a phospholipid-water system*, Colloids and Surfaces A (1997), **121**, *2-3*, p. 135. xiii, 110

[45] Z. Dogic and S. Fraden, *Development of model colloidal liquid crystals and the kinetics of the isotropic-smectic transition*, Philosophical Transactions of the Royal Society London A (2001), **359**, pp. 997–1015. 109

[46] T. Dotera and Y. Suzuki, *Polymer confinement in undulated membrane boxes and tubes*, Physical Review E (2000), **62**, *4*, p. 5318. 112

[47] B. Dünweg and K. Kremer, *Microscopic verification of dynamic scaling in dilute polymer solutions: a molecular-dynamics simulation*, Physical Review Letters (1991), **66**, *23*, pp. 2996–2999. xiii, 3, 5, 9

[48] ——, *Molecular dynamics of a polymer chain in solution*, Journal of Chemical Physics (1993), **99**, *9*, pp. 6983–6997. 9

[49] D. Evans and H. Wennerström, *The colloidal domain*, J. Wiley and Sons, second ed., 1999. xi, 53

[50] E. Evans and R. Kwok, *Mechanical calorimetry of large dimyristoylphosphatidylcholine vesicles in the phase transition region*, Biochemistry (1982), **21**, pp. 4874–4879. 45, 46

[51] E. Evans and W. Rackwicz, *Entropy driven tension and bending elasticity in condensed-fluid-membranes*, Physical Review Letters (1990), **64**, p. 2094. 46

[52] S. Feller, *Molecular dynamics simulations of lipid bilayers*, Current Opinion in Colloid and Interface Science (2000), **5**, *3-4*, p. 217. 1

[53] S. Feller, R. Pastor, and Y. Zhang, *Computer simulation of liquid/liquid interfaces.ii. surface tension-area dependence of a bilayer and monolayer*, Journal of Chemical Physics (1995), **103**, *23*, pp. 10267–10276.   21, 22

[54] S. Feller and R. W. Pastor, *Constant surface tension simulation of lipid bilayers: the sensitivity of surface areas and compressibility*, Journal of Chemical Physics (1999), **111**, *3*, pp. 1281–1287.   21, 22

[55] M.-F. Ficheux, A.-M. Bellocq, and F. Nallet, *Experimental study of a lyotropic lamellar phase swollen with polymer solutions*, Journal de Physique II (France) (1995), **5**, p. 823.   110, 111

[56] ——, *Effect of two water soluble polymers on the stability of the aot-h$_2$0-lamellar phase*, Colloids and Surfaces A (1997), **123-124**, p. 253.   110

[57] ——, *Elastic properties of polymer-doped dilute lamellar phases: a small-angle neutron scattering study*, European Physical Journal E (2001), **4**, p. 315.   xiii, 110, 111

[58] J. Flory, *Principle of polymer chemistry*, Cornell Univ. Pr., 1953.   9, 87, 112

[59] L. Forrest and K. MacConnell, *Membrane simulations: bigger and better?*, Current Opinion in Structural Biology (2000), **10**, *2*, p. 174.   1

[60] J.-B. Fournier, *Microscopic membrane elasticity and interactions among membranes inclusions: interplay between the shape, dilation, tilts and tilt-difference modes*, European Physical Journal B (1999), **11**, p. 261.   xii

[61] J.-B. Fournier, A. Ajdari, and L. Peliti, *Effective-area elasticity and tension of micromanipulated membranes*, Physical Review Letters (2001), **86**, *21*, pp. 4970–4973.   46, 47

[62] S. Freeman, M. Wang, and J. Weaver, *Theory of electroporation of planar bilayer membranes: predictions of the aqueous area, change in capacitance, and pore-pore separation*, Biophysical Journal (1994), **67**, pp. 42–56.   70, 72, 73, 97

[63] D. Frenkel and B. Smit, *Understanding Molecular Simulation*, Academic-New York, first ed., 1996.   5, 6, 10, 13, 14, 25, 26, 118

[64] E. Freyssingeas, D. Antelmi, P.Kekitchev, P. Richetti, and A.-M. Bellocq, *Softening of the interactions between surfactant bilayers in a lamellar phase due to the presence of a polymer*, Eur. Phys. J. B (1999), **9**, pp. 123–136.   xiii, 111

[65] C. Gardiner, *Handbook of stochastic methods*, Springer Verlag, Berlin, second ed., 1990.   10

[66] R. Gennis, *Biomembranes: molecular structure and function*, Springer Verlag, 1989.   ix, 39

Bibliography

[67] R. W. Glaser, S. Leikin, L. Chernomordik, V. Pastushenko, and A. I. Sokirko, *Reversible electrical breakdown of lipid bilayers: formation and evolution of pores*, Biochemical et Biochimica Acta (1988), **940**, pp. 275–287. xiii, 70, 72, 77

[68] R. Goetz, G. Gompper, and R. Lipowski, *Mobility and elasticity of self-assembled membranes*, Physical Review Letters (1999), **82**, *1*, pp. 221–224. 48, 133

[69] R. Goetz and R. Lipowsky, *Computer simulation of bilayer membranes: self-assembly and interfacial tension*, Journal of Chemical Physics (1998), **108**, *17*, pp. 7397–7409. 2, 3, 33, 41

[70] H. Goldstein, *Classical mechanics*, Addison-Wesley, 1980. 10

[71] G. Gompper and D. Kroll, *Membranes with fluctuating topology: Monte carlo simulations*, Physical Review Letters (1998), **81**, pp. 2284–2287. 3

[72] N. Goulaiev and J. Nagle, *Simulation of interacting membranes in the soft confinement regime*, Physical Review Letters (1998), **81**, *12*, pp. 2610–2613. 45, 52, 53

[73] G. Grest and K. Kremer, *Molecular dynamics simulation for polymer in the presence of a heat bath*, Physical Review A (1986), **33**, *5*, pp. 3628–3631. xiii, xiv, 3

[74] H. Guo, *private communication*. The direction of the tetramers *hhtt* can also be chosen along the vector linking the middle of the *hh* bond to the middle of the *tt* bond of the tetramers. The results are similar. 33

[75] H. Guo, K. Kremer, and T. Soddemann, *Non-equilibrium molecular dynamics simulation of shear-induced alignment of amphiphilic model systems*, Physical Review E (2002), **66**, *061503*. xiii, 3, 17

[76] D. Harries, S. May, W. Gelbart, and A. ben Shaul, *Structure, stability and thermodynamics of lamellar dna-lipid complexes*, Biophysical Journal (1998), **75**, p. 159. 110

[77] G. Hed and S. Safran, *Initiation and dynamics of hemifusion in lipid bilayers*, cond-mat preprint (2002), *0211186*. 70

[78] W. Helfrich, *Elastic properties of lipid bilayers - theory and possible experiments*, Zeitung Naturforschung (1973), **28**, *11-1*, pp. 693–703. 45, 47, 54

[79] H. Heller, M. Schaefer, and K. Schulten, *Molecular dynamics simulation of a bilayer of 200 lipids in the gel and in the liquid crystal phases*, Journal of Physical Chemistry (1993), **97**, pp. 8343–8360. 1

[80] R. Holyst, *Laudau-peierls instabilities, x-ray diffraction patterns, and surface freezing in thin smectic films*, Physical Review A (1991), **44**, *6*, pp. 3692–3709. xv, 45, 51, 52, 53, 133

144

[81] R. Holyst and W. T. Gozdz, *Fluctuating euler characteristics, topological disorder line and passages in the lamellar phase*, Journal of Chemical Physics (1997), **106**, *11*. 69, 70, 75

[82] J. Irving and J. Kirkwood, *The statistical mechanical theory of transport processes.4. the equation of hydrodynamics*, Journal of Chemical Physics (1950), **18**, *6*, pp. 817–829. 41

[83] J. Israelachvili, *Intermolecular and surface forces*, Academic Press, 1985. 53, 54

[84] K. Jacobs, S. Herminghaus, and K. Mecke, *Thin liquid polymer films rupture via defects*, Langmuir (1998), **14**, pp. 965–969. 81

[85] F. Jähnig, *What is the surface tension of a bilayer ?*, Biophysical Journal (1996), **71**, p. 1348. 21, 22, 48

[86] H. Ji, D. Hone, P. Pincus, and G. Rossi, *Polymer bridging between 2 parallel plates*, Macromolecules (1990), **23**, *3*, p. 698. 116

[87] J. Jimenez, J. de Joannis, I. Bitsanis, and R. Rajagopalan, *Bridging of an isolated polymer chain*, Macromolecules (2000), **33**, p. 7157. 116, 117

[88] V. John, B. Simmons, G. McPherson, and A. Bose, *Recent developments in materials synthesis in surfactant systems*, Current Opinion in Colloid and Interface Science (2002), **7**, *5-6*, p. 288. ix

[89] P. Kekicheff, B. Cabane, and M. Rawiso, *Macromolecules dissolved in a lamellar lyotropic mesophase*, Journal of Colloid and Interface Science (1984), **102**, *1*, pp. 51–70. 111

[90] M. Khanta and V. Balakrishnan, *First passage time distribution for finite one-dimensional random walks*, Pramana (1983), **21**, *2*, pp. 111–122. 88, 95, 96, 134

[91] A. Kolb and B. Dünweg, *Optimized constant pressure stochastic dynamics*, Journal of Chemical Physics (1999), **111**, *10*, pp. 4453–4459. 14, 22, 28

[92] I. Koltover, T. Salditt, J. Rädler, and C. Safinya, *An inverted hexagonal phase of cationic liposome-dna complexes related to dna release and delivery*, Science (1998), **281**, p. 78. xii, xiii

[93] I. Koltover, T. Salditt, and C. Safinya, *Phase diagram, stability and overcharging of lamellar cationic lipid dna self assembly complexes*, Biophysical Journal (1999), **77**, p. 915. 110

[94] J. Kötz, I. Brühl, S. Kosmella, J. Reiche, and B. Tiersch, *polyelectrolyte complex formation in lamellar liquid crystalline systems*, Journal of Colloid and Interface Science (1997), **186**, p. 141. 110

[95] J. Kötz and S. Kosmella, *Polymers in lyotropic liquid crystals*, Current Opinion in Colloid and Interface Science (1999), **4**, p. 348. 110

[96] R. Koynova and M. Caffrey, *Phase and phase transitions of phosphatidycholines*, Biochemical et Biochimica Acta (1998), **1376**, p. 91. xii

[97] K. Kremer, G. Grest, and I. Carmesian, *Crossover from rouse to reptation dynamics: A molecular-dynamics simulation*, Physical Review Letters (1988), **61**, *5*, p. 566. xiii, 3

[98] R. Kubo, *Statistical Physics II, Non equilibrium statistical mechanics*, Springer Verlag, Berlin, second ed., 1991. 10

[99] Y. Lansac, M. Glaser, and N. Clark, *Microscopic structure and dynamics of a partial bilayer smectic liquid crystals*, Physical Review E (2001), **64**, *051703*. 1

[100] R. G. Larson, *Monte carlo simulations of microstructural transition in surfactant systems*, Journal de Physique II (1996), **6**, p. 1441. 2

[101] R. Lawaczeck, *Defect structures in membranes: routes for permeations of small molecules*, Ber. Benenges. Phys. Chem. (1988), **92**, pp. 961–963. 70, 72

[102] N. Lei, C. Safinya, and R. Bruinsma, *Discrete harmonic model for stacked membranes: theory and experiment*, Journal de Physique II (1995), **5**, pp. 1155–1163. xv, 45, 52, 53, 57, 67, 133

[103] S. Leibler, R. Singh, and M. Fisher, *Thermodynamic behavior of two-dimensional vesicles*, Physical Review Letters (1987), **59**, *18*, pp. 1989–1992. 2, 3, 87, 134

[104] C. Ligoure, G. Bouglet, and G. Porte, *Polymer induced phase separation in lyotropic smectics*, Physical Review Letters (1993), **71**, *21*, pp. 3600–3603. 110, 111

[105] C. Ligoure, G. Bouglet, G. Porte, and O. Diat, *Smectic compressibility of polymer-containing lyotropic lamellar phases: An experimental tool to study the thermodynamics of polymer confinement*, Journal de Physique II (France) (1997), **7**, pp. 473–491. xii, 109, 110, 111, 113, 114

[106] E. Lindahl, *Computational Modeling of biological membrane and interface dynamics*, PhD thesis, Royal institute of Technology of Stockholm, 2001. xiv

[107] E. Lindahl and O. Edholm, *Mesoscopic undulations and thickness fluctuations in lipid bilayers from molecular dynamics simulations*, Biophysical Journal (2000), **79**, p. 426. 133

[108] ——, *Spatial and energetic-entropic decomposition of surface tension in lipid bilayers from molecular dynamics simulations*, Journal of Chemical Physics (2000), **113**, *9*, pp. 3882–3893. 21, 41

[109] J. Lister, *Stability of lipid bilayers and red blood cell membranes*, Physics Letters (1975), **53A**, pp. 193–194.   73

[110] Y. Lyatskaya, Y. Liu, S. Tristam-Nagle, J. Katsaras, and J. F. Nagle, *Method for obtaining structure and interactions from oriented lipid bilayers*, Physical Review E (2000), **63**, *011907*, pp. 1–9.   xv, 45, 53, 57, 133

[111] J. Mahanty and B. Ninhan, *Dispersion forces*, Academic Press, London, 1976.   54

[112] S. Marrink, F. Jähning, and H. Berendsen, *Proton transfer across transient single-file pores in a lipid membrane studied by molecular dynamics simulations*, Biophysical Journal (1996), **71**, pp. 632–647.   70, 73, 97, 134

[113] S. Marrink, E. Lindahl, O. Edholm, and A. Mark, *Simulation of the spontaneous aggregation of phospholipids into bilayers*, Journal of the American Chemical Society (2001), **123**, p. 8638.   1, 70, 73, 97, 134

[114] S. Marrink and A. Mark, *Effect of undulation on surface tension in simulated bilayers*, Journal of Chemistry B (2001), **105**, pp. 6122–6127.   1, 22, 48, 51, 64

[115] S. May, *A molecular model for the line tension of lipid membranes*, European Physical Journal E (2000), **3**, p. 37.   70, 73, 77, 85, 134

[116] K. Mecke, *Additivity, convexity, and beyond: Applications of minkowski functionals in statistical physics*, Lectures Notes in Physics (2000).   81, 98, 104

[117] W. Meier, *Nanostructure synthesis using surfactants and copolymers*, Current Opinion in Colloid and Interface Science (1999), **4**, p. 6.   xii

[118] K. Melikov, V. Frolov, A. Shcherbakov, A. Samsonov, Y. Chizmadzhev, and L. Chernomordik, *Voltage-induced non-conductive pre-pores and metastable single pores in unmodified planar lipid bilayer*, Biophysical Journal (2001), **80**, p. 1829.   xiii, 70, 72

[119] K. Merz, *Molecular dynamics simulations of lipid bilayers*, Current Opinion in Structural Biology (1997), **7**, *4*, pp. 511–517.   22

[120] A. Milchev and K. Binder, *Dynamics of polymer chains confined in slit-like pores*, Journal de Physique II (France) (1996), **6**, p. 21.   112, 116

[121] ——, *A polymer chain between two parallel repulsive walls: A monte-carlo test of scaling behavior*, European Physical Journal B (1998), **3**, p. 477.   112, 116

[122] K. Milchielsen and H. D. Raedt, *Integral-goemetry morphological image analysis*, Physics Reports (2001), **347**, *6*, pp. 462–538.   81, 98

[123] K. Milchiesen and H. D. Raedt, *Morphological image analysis*, Computational Physics Communication (2000), **132**, pp. 94–103.   101

Bibliography

[124] J. D. Moroz and P. Nelson, *Dynamically stabilized pores in bilayer membranes*, Biophysical Journal (1997), **72**, *2*, pp. 2211–2216.   73, 85

[125] D. Morse and S. Miller, *Absence of the nematic phase in symmetric dibloc copolymers*, Physical Review E (1993), **47**, *2*, pp. 1119–1125.   36

[126] M. Müller, K. Katsov, and M. Schick, *Mechanism of model membrane fusion*, Journal of Chemical Physics (2002), **116**, *6*, p. 2342.   xiv, 2, 43, 70, 73, 77, 97, 132

[127] M. Müller and M. Schick, *Structure and nucleation of pores in polymeric bilayers: A monte carlo simulation*, Journal of Chemical Physics (1996), **105**, *18*, pp. 8282–8292.   2, 70, 73, 77, 85, 135

[128] D. Needham and E. Evans, *Structure and mechanical properties of giant lipid (dmpc) vesicle bilayers from 20 degrees to 10 degrees above the liquid crystal-crystalline phase transition*, Biochemistry (1988), **27**, pp. 8261–8269.   46

[129] P. Nelson, G. Rutledge, and T. A. Hatto, *On the size and shape of self-assembled micelles*, Journal of Chemical Physics (1997), **107**, *24*, p. 10777.   2

[130] R. Netz and J. Joanny, *Adsorption of semiflexible polyelectrolytes on charged planar surfaces: Charge compensation, charge reversal, and multilayer formation*, Macromolecules (1999), **32**, *26*, pp. 9013–9025.   54

[131] R. Netz and M. Schick, *Pore formation and rupture in fluid bilayers*, Physical Review E (1996), **53**, pp. 3875–3885.   70, 73

[132] J. Nichols and D. Deamer, *Net proton-hydroxyl permeability of large unilamellar liposomes measured by an acid-base titration technique*, Proc. Natl. Acad. Sci. USA (1980), **77**, pp. 2038–2042.   71, 97

[133] H. Noguchi and M. Takasu, *Fusion pathways of vesicles: a brownian dynamics simulation*, Journal of Chemical Physics (2001), **115**, pp. 9547–9551.   97

[134] C. O'Hern and T. Lubensky, *Nonlinear elasticity of the sliding columnar phase*, Physical Review E (1998), **58**, *5*, p. 5948.   112

[135] ——, *Sliding columnar phase of dna-lipid complexes*, Physical Review Letters (1998), **90**, *19*, p. 4345.   112

[136] M. Parrinello and A. Rahman, *Crystal structure and pair potentials : a molecular-dynamics study*, Physical Review Letters (1980), **45**, *14*, p. 1196.   23, 24

[137] ——, *Crystal structure pair potentials: a molecular-dynamics study*, Physical Review Letters (1980), **45**, *14*, p. 1196.   17

[138] ——, *Polymorphic transition in single crystals: a new molecular dynamics method*, Journal of Applied Physics (1981), **52**, *12*, pp. 7182–7190.   17

[139] S. Paula, A. Volkov, and D. Deamer, *Permeation of halide anions through phospholipid bilayers occurs by the solubility-diffusion mechanism*, Biophysical Journal (1998), **74**, pp. 319–327. 71

[140] S. Paula, A. Volkov, A. V. Hoeck, T. Haines, and D. Deamer, *Permeation of protons, potassium ions and small polar molecules through phopholipid bilayers as a function of bilayer thickness*, Biophysical Journal (1996), **70**, pp. 339–348. 70, 71, 72, 97

[141] H. I. Petrache, N. Goulaiev, S. Tristam-Nagle, R. Zhang, R. M. Suter, and J. F. Nagle, *Inter bilayer interactions from high-resolution x-ray scattering*, Physical Review E (1998), **57**, *6*, pp. 7014–7024. xv, 45, 52, 53, 57, 133

[142] C. Pierleoni and J.-P. Ryckaert, *Relaxation of a single chain molecule in good solvent conditions by molecular-dynamics simulation*, Physical Review Letters (1991), **66**, *23*, pp. 2992–2995. 9

[143] ———, *Molecular dynamics investigation of dynamics scaling for dilute polymer solution in good solvent conditions*, Journal of Chemical Physics (1992), **96**, p. 8539. 9

[144] R. Podgornik and V. Parsegian, *Thermal-mechanical fluctuations of fluid membranes in confined geometries: the case of soft confinement*, Langmuir (1992), **8**, *2*, p. 557. xv, 45, 52, 53, 133

[145] T. Pott, A. Colin, L. Navailles, and D. Roux, *Dna intercalation in neutral multilamellar membranes: experiments and theory*, Interface Science (2003), **11**, p. 249. 110, 112

[146] L. Procar, C. ligoure, and J. Marignan, *layer compression modulus of electrostatically stabilized lamellar phases revisited: application to the quantitative analysis of a polymer induced critical sma-sma phase separation*, Journal de Physique II (France) (1997), **7**, *3*, p. 493. 110

[147] L. Procar, J. Marignan, and C. Ligoure, *Effect of a non-adsorbing polymer on the stability of a two-solvent lamellar phase: Experimental and theoretical study of critical points of lamellar/lamellar phase separations*, Langmuir (2000), **16**, p. 2581. 109, 111, 112

[148] M. Pütz and A. Kolb, *Optimization techniques for parallel molecular dynamics using domain decomposition*, Compt. Phys. Commun. (1998), **113**, *2-3*, pp. 145–167. 6

[149] J. Rädler, I. Koltover, A. Jamieson, T. Salditt, and C. Safinya, *Structure and interfacial aspects of self-assembled cationic lipid-dna gene carrier complexes*, Langmuir (1998), **14**, *15*, pp. 4272–4284. 110

Bibliography

[150] J. Rädler, I. Koltover, T. Salditt, and C. Safinya, *structure of dna-cationic liposome complexes dna intercalation in multilamellar membranes in distinct interhelical packing regime*, Science (1997), **275**, p. 810. xiii, 110

[151] E. Radlinska, T. Gulik-Krzywick, L. Lafuma, D. Langevin, W. Urbach, C. Williams, and R. Ober, *Polymer confinement in surfactant bilayers of a lyotropic lamellar phase*, Physical Review Letters (1995), **74**, *21*, p. 4237. 111, 117

[152] E. Radlinska, T. Gulik-Krzywicki, F. Lafuma, D. Langevin, W. Urbarch, and C. Williams, *Modification of the lamellar phase in $c_{12}e_5$/water/ system by a random hydrophilic-hydrophobic polyelectrolyte*, Journal de Physique II (France) (1997), **7**, p. 1393. xii, xiii, 110, 111, 117

[153] R. Rand, *Interacting phospholipid-bilayers - measured forces and induced structural changes*, Ann. Rev. Biophys. Bioeng. (1981), **10**, pp. 277–314. 53

[154] E. Raphael and P. Pincus, *Scaling theory of polymer solutions trapped in small pores: the θ-solvent case*, Journal de Physique II (France) (1992), **2**, pp. 1341–1344. 112

[155] W. Rawicz, K. Olbrich, T. MacIntosh, D. Needham, and E. Evans, *Effect of chain length and instaturation on elasticity of lipid bilayers*, Biophysical Journal (2000), **79**, *1*, pp. 328–339. 39, 46, 47, 73

[156] J. Ray, *Molecular dynamics equations of motion for systems varying in shape and size*, Journal of Chemical Physics (1983), **79**, *10*, pp. 5128–5130. 24

[157] J. Ray and A. Rahman, *Statistical ensembles and molecular dynamics studies of anisotropic solids*, Journal of Chemical Physics (1984), **80**, *9*, pp. 4423–4428. 24

[158] H. Risken, *The Fokker-Planck equation*, Springer, Berlin, second ed., 1989. 10

[159] D. Roux and C. Rafinya, *A synchrotron x-ray study of competing undulation and electrostatic interlayer interactions in fluid multimembranes lyotropic surfaces*, Journal de Physique II (France) (1988), **49**, *2*, pp. 307–318. 54

[160] M. Rückert and G. Otting, *Alignment of biological macromolecules in novel nonionic liquid crystalline media for nmr experiments*, Journal of the American Chemical Society (2000), **122**, p. 7793. xii, 111

[161] C. Safinya, I. Koltover, and J. Rädler, *Dna at membrane surfaces: an experimental overview*, Current Opinion in Colloid and Interface Science (1998), **3**, *1*, p. 69. 110

[162] S. Safran, T. Kuhl, and J. Israelachvili, *Polymer-induced membrane contraction, phase separation, and fusion via marangoni flow*, Biophysical Journal (2001), **81**, pp. 859–666. xii, 70

[163] S. A. Safran, *Statistical thermodynamics of surfaces, interfaces, and membranes*, Addison-Wesley Publishing Compagny, 1994.   47, 49, 51, 55

[164] T. Salditt, *Structure and fluctuations of highly oriented phospholipid membranes*, Current Opinion in Colloid and Interface Science (2000), **5**, *1-2*, p. 19.   69

[165] T. Salditt, I. Koltover, J. Rädler, and C. Safinya, *Two-dimensional smectic ordering of linear dna chains in self assembled dna-cationic liposomes mixtures*, Physical Review Letters (1997), **73**, *13*, p. 2582.   110, 111, 112

[166] ———, *Self assembled dna-cationic lipid complexes : two-dimensional smectic ordering, correlations and interactions*, Physical Review E (1998), **58**, *1*, p. 889.   110, 111, 112

[167] T. Salditt, C. Muenster, J. Lu, W. Fenzl, and A. Souvorov, *Specular and diffuse scattering of highly aligned phopholipid membranes*, Physical Review E (1999), **60**, *6*, p. 7285.   69

[168] T. Salditt, M. Vodel, and W. Frenz, *Thermal fluctuations and positional correlations in oriented lipid membranes*, Physical Review Letters (2003), **90**, *178101*.   53, 133

[169] O. Sandre, L. Moreaux, and F. Brochard-Wyart, *Dynamics of transient pores in stretched vesicles*, Proc. Natl. Acad. Sci. USA (1999), **96**, pp. 10591–10596.   xiii, 70

[170] S. Santalo and L. Antonio, *Integral geometry and geometric probability*, Addison Wesley, 1976.   100

[171] U. Seifert, *Configurations of fluid membranes and vesicles*, Advances in Physics (1997), **46**, pp. 13–137.   49

[172] P. Sens and S. Safran, *Inclusions induced phase separation in mixed lipid film*, European Physical Journal E (2000), **1**, p. 237.   xii, 135

[173] J. Shelley, M. Shelley, R. Reeder, S. Bandyopadhyay, P. B. Moore, and M. Klein, *Simulations of phospholipids using a coarse grain model*, Journal of Chemical Physics B (2001), **105**, pp. 9785–9792.   2

[174] J. Shelley, M. Y. Shelley, R. C. R. S. Bandyopadhyay, and M. L. Klein, *A coarse grain model for phospholipid simulations*, Journal of Chemical Physics B (2001), **105**, pp. 4464–4470.   2, 3

[175] J. Shillcock and D. Boal, *Entropy-driven instability and rupture of fluid membranes*, Biophysical Journal (1996), **71**, pp. 317–326.   3, 73, 87

[176] J. Shillcock and R. Lipowsky, *Equilibrium structure and lateral stress distribution of amphiphilic bilayers from dissipative particle dynamics simulations*, Journal of Chemical Physics (2002), **117**, pp. 5048–5061.   xiv, 39, 41, 133

Bibliography

[177] J. Shillcock and U. Seifert, *Thermally induced proliferation of pores in a model fluid membrane*, Biophysical Journal (1998), **74**, pp. 1754–1766.   3, 73, 87

[178] M. Singh, R. Ober, and M. Kleman, *Polymer in a lyotropic lamellar system: an experimental study*, Journal of Physical Chemistry (1993), **97**, *42*, p. 11109.   110, 111, 118, 132

[179] S. Singh, *Phase transitions in liquid crystals*, Physics Reports (2000), **324**, pp. 107–269.   32

[180] B. Smit, P. Hilbers, K. Esselink, L. Rupert, N. Os, and A. Scjlijper, *Structure of water/oil interfaces in the presence of micelles: a computer simulation study*, Journal of Physical Chemistry (1991), **95**, pp. 6361–6368.   2

[181] T. Soddemann, *Non-equilibrium molecular dynamics study of an amphiphilic model system*, PhD thesis, University of Mainz, 2001.   17

[182] T. Soddemann, B. Dünweg, and K. Kremer, *A generic computer model for amphiphilic systems*, European Physical Journal E (2001), **6**, *5*, pp. 409–419.   xiii, xiv, 3, 6, 7, 17, 36

[183] A. Sonneleitner, G. Schütz, and T. Schmidt, *Free brownian motion of individual lipid molecules in biomembranes*, Biophysical Journal (1999), **77**, pp. 2638–2642.   39

[184] I. Souza and J. Martins, *Metric tensor as the dynamical variable for variable-cell-shape molecular dynamics*, Physical Review B (1997), **55**, *14*, pp. 8733–8742.   23

[185] W. Sung and P. Park, *Polymer translocation through a pore in a membrane*, Physical Review Letters (1996), **77**, *4*, p. 783.   xii, 132

[186] ——, *Dynamics of pore growth in membranes and membrane stability*, Biophysical Journal (1997), **73**, pp. 179–1804.   xii, 73

[187] V. Talanquer and D. W. Oxtoby, *Nucleation of pores in amphiphilic bilayers*, Journal of Chemical Physics (2003), **118**, *2*, pp. 872–877.   70, 73

[188] N. Taulier, C. Nicot, M. Waks, R. Hodges, R. Ober, and W. Urbach, *Unbinding-binding transition induced by molecular snaps in model membranes*, Biophysical Journal (2000), **78**, p. 857.   110

[189] J. L. Thomas and D. Tirell, *Polymer-induced leakage of cations from dioleylphosphatidylcholine and phosphatidylglycerol liposomes*, Journal of Controlled Release (2000), **67**, pp. 203–209.   70

[190] D. Tobias, K. Tu, and M. Klein, *Atomic-scale molecular dynamics simulations of lipid membranes*, Current Opinion in Colloid and Interface Science (1997), **2**, *1*, pp. 15–26.   1

[191] K. Tu, D. Tibias, and M. Klein, *Constant pressure and temperature molecular dynamics simulation of fully hydrated liquid crystalline phase dipalmitoylphosphatidylcholine bilayer*, Biophysical Journal (1995), **69**, pp. 2558–2562. 22

[192] M. Tuckerman, *Ab initio molecular dynamics: basic concepts, current trends and novel applications*, Journal of Physics: Condensed Matter (2002), **14**, *50*, pp. R1297–R1355. 10

[193] M. Tuckerman and G. Martyna, *Understanding modern molecular dynamics: Techniques and applications*, Journal of Chemical Physics B (2000), **104**, *2*, pp. 159–178. 10

[194] L. Turban, *Conformation of confined macromolecular chains - crossover between slit and capillary*, Journal de Physique II (France) (1984), **45**, *2*, pp. 347–353. 112

[195] M. Turner and P. Sens, *Interactions between particulate inclusions in a smectic-a liquid crystal*, Physical Review E (1997), **55**, *2*, p. R1275. xii

[196] J. van Vliet, M. Luyken, and G. ten Brinke, *Scaling behavior of dilute polymer solutions confined between parallel plates*, Macromolecules (1992), **25**, *14*, pp. 3802–3806. 112, 116

[197] J. van Vliet and G. ten Brinke, *Orientation and shape of a polymer in a slit*, Journal of Chemical Physics (1990), **93**, pp. 1436–1441. 112, 116

[198] F. Varnik, J. Baschnagel, and K. Binder, *Molecular dynamics results on the pressure tensor for polymer films*, Journal of Chemical Physics (2000), **113**, *10*, pp. 4444–4453. 40, 41, 42

[199] L. Vega, A. Z. Panagiotopoulos, and K. Gubbins, *Chemical potentials and adsorption isotherms of polymers confined between parallel plates*, Chemical Engineering Science (1994), **49**, *17*, p. 2921. 116

[200] M. Venturoli and B. Smit, *Simulating the self-assembly of model membranes*, Phys. Chem. Comm. (1999), **10**. 41, 133

[201] T. Vlugt, *Adsorption and diffusion in zeolites: a computational study*, PhD thesis, Amsterdam University, 2000. 1, 118

[202] K. Šolc, *Shape of a random-flight chain*, Journal of Chemical Physics (1971), **55**, *1*, p. 335. 121

[203] K. Šolc and W. Stockmayer, *Shape of a random flight chain*, Journal of Chemical Physics (1971), **54**, *6*, p. 2756. 121

[204] Z. Wang, A. Nemirovsky, and K. Freed, *Polymer with excluded volume in various geometries: Renormalization group methods*, Journal of Chemical Physics (1987), **86**, pp. 4266–4279. 112

Bibliography

[205] Y. Yang, R. Prudhomme, K. McGrath, P. Richetti, and C. Marques, *Confinement of polysoaps in membrane lyotropic phases*, Physical Review Letters (1998), **80**, *12*, p. 2729. 110

[206] Y. Yarovoy and M. Labes, *Effect of chiral polymers on lyotropic liquid crystals*, Journal of the American Chemical Society (1997), **119**, p. 12109. 110

[207] D. Zahn and J. Brickmann, *Molecular dynamics study of water pores in a phospholipid bilayer*, Chem. Phys. Lipids (02), **352**, pp. 441–446. 70, 73, 97, 134

[208] K. Zhang and P. Linse, *Solubilization of polymer in the lyotropic lamellar phase: the aot/peo/water system*, Journal of Chemical Physics (1995), **99**, p. 9130. 110, 111

[209] Y. Zhang, S. Feller, R. Pastor, and B. Brooks, *Constant pressure molecular dynamics simulation: the langevin piston method*, Journal of Chemical Physics (1995), **103**, *11*, pp. 4613–4621. 22

[210] D. V. Zhelev and D. Needham, *Tension-stabilized pores in giant vesicle: determination of pore size and line tension*, Biochemical et Biochimica Acta (1993), **1147**, pp. 89–104. xiii, 70, 73, 85

[211] G. Zifferer, *Shape distribution and correlation between size and shape of tethahedral lattice chains in athermal and theta systems*, Journal of Chemical Physics (1998), **109**, *9*, pp. 3691–3698. 123

154

Lebenslauf

Claire LOISON

1976	geboren in Paris
1990-93	Lycée Marcelin Berthelot
1993	Baccalauréat
1993-95	Classes Préparatoires aux Grandes Ecoles (Lycée Marcelin Berthelot) ($\sim$ Vordiplom)
1995-1999	Hauptstudium, Ecole Normale Supérieure de Lyon
1998	Agrégation de Sciences Physiques ($\sim$ Lehramtsprüfung)
1999	Magistère des Sciences de la Matière de l'ENSL ($\sim$ Diplom)
1999-2003	Doktorarbeit ("cotutelle")
	$\rightarrow$ Centre Européen de Calcul Atomique et Moléculaire , Ecole Normale Supérieure de Lyon - 15 Monate
	$\rightarrow$ Universität Bielefeld - 15 Monate
	$\rightarrow$ Max Planck Institut für Polymerforschung, Mainz - 10 Monate